Advanced Proteomics of Skeletal Muscles: Spatial and Single Fiber Insights into Metabolic Diversity

Inaugural-Dissertation

zur

Erlangung des Doktorgrades

der Mathematisch-Naturwissenschaftlichen Fakultät

der Universität zu Köln

vorgelegt von

Luisa Marie Schmidt

aus Kempten

Köln, 2024

Berichterstatter:	Prof. Dr. Marcus Krüger
(Gutachter)	
	Prof Dr. Matthias Hammerschmidt
Tag der mündlichen Prüfung:	29.10.2024

Content

Abstract

In recent years, the importance of muscle health for overall body function has gained increasing recognition. Although whole proteome methods with protein extraction and LC-MS analysis provide accurate insights into different cell types and protein composition, the localization of specific proteins, including the extracellular matrix (ECM) and intercellular junctions, is limited. Here, we present a novel approach that preserves tissue spatial organization. By employing thin cryosectioning followed by LC-MS/MS analysis, we spatially map proteins across the tissue. This method enabled us to characterize the myotendinous junction (MTJ) in the soleus and diaphragm muscles, revealing 32 new marker proteins and the significant role of the renin-angiotensin system (RAS) in the muscle-tendon transition zone.

Our approach facilitated the spatial characterization of 33 known marker proteins of the neuromuscular junction (NMJ) along the diaphragm axis and identified approximately 140 potential NMJ proteins, which we deconvoluted to either neuronal or muscle origin. Utilizing the generated protein profiles for a distance-based network analysis, we identified spatial structural changes in aged mice, such as NMJ broadening and loss of connectivity. Applying this method to TDP43 dependent ALS mouse models uncovered NMJ structural changes that traditional methods would have missed. Using our new approach, we identified around 10,000 proteins in skeletal muscle, generating more than 3,500 protein profiles across the skeletal muscles which will be a comprehensive repository for researchers focusing on skeletal muscle biology and related diseases.

Additionally, isolating single muscle cells from the mouse soleus muscle in response to a high-fat diet (HFD) administration revealed significant metabolic impacts on different fiber types. Fast fibers were particularly affected by nutrient overexposure, leading to a loss of peripheral mitochondria throughout the muscle, as demonstrated by immunohistochemistry (IHC).

Single-cell analysis of muscle fibers from bears during hibernation and active periods demonstrated evolutionary adaptations to minimize energy expenditure. Hibernating bears showed reduced myosin ATPase activity, decreased mitochondrial protein levels, and altered myosin light chain kinase (MYLK2) activity, suggesting mechanisms to preserve muscle function and prevent wasting during inactivity.

Zusammenfassung

Muskelgesundheit hat in den letzten Jahren an Bedeutung für das allgemeine Wohlbefinden des Körpers gewonnen. Obwohl Proteinanalysen durch Isolierung und LC-MS-Analyse einen präzisen Einblick in verschiedene Zelltypen und Proteinkompositionen ermöglichen, bleibt die Lokalisierung spezifischer Proteine, sowie die extrazelluläre Matrix (ECM) und interzelluläre Verbindungen, unklar. Hier wird ein neuartiger Ansatz vorgestellt, der die räumliche Organisation und Struktur des Gewebes bewahrt. Durch die Anwendung dünner Kryoschnitte, gefolgt von LC-MS/MS-Analysen, ermöglichen wir die räumliche Kartierung von Proteinen im Gewebe.

Mit dieser Methode ermöglichten wir die Charakterisierung der Muskel-Sehne Übergangszone (MTJ) im Soleus- und Zwerchfellmuskel und identifizierten 34 neue Markerproteine. Zusätzlich zeigten wir die bedeutende Rolle des Renin-Angiotensin-Systems (RAS) in der MTJ. Darüber hinaus wurden 33 bekannte Markerproteine der neuromuskulären Übergangszone (NMJ) entlang der Zwerchfellachse charakterisiert und ~140 potenzielle NMJ-Proteine identifiziert, die entweder neuronaler oder muskulärer Herkunft zugeordnet wurden. Mit einer distanzbasierten Netzwerkanalyse wurden die generierten Proteinprofile zur Identifizierung räumlich-strukturellen Veränderungen bei gealterten Mäusen genutzt, wie die Verbreiterung der NMJ und der Verlust von Verbindungen zwischen den Proteinen. Die Anwendung dieser Methode auf frühe ALS-Mausmodelle offenbarte strukturelle Veränderungen in der NMJ, die mit traditionellen Methoden übersehen worden wären. Mithilfe dieses neuen Ansatzes wurden ~10.000 Proteine im Skelettmuskel identifiziert und mehr als 3.500 Proteinprofile generiert, die eine willkommene und hilfreiche Ressource für Forscher sein werden, die sich auf die Muskelbiologie konzentrieren.

Durch die Isolierung einzelner Muskelzellen aus dem Soleusmuskel der Maus und anschließender LC-MS/MS Analyse wurden signifikante metabolische Auswirkungen auf verschiedene Fasertype nach einer fettreichen Diät (HFD) nachgewiesen. Insbesondere waren schnelle Fasern von Nährstoffüberbelastung betroffen, was zu einem Verlust an peripheren Mitochondrien im gesamten Muskel führte, wie durch Immunohistochemie (IHC) belegt wurde.

Zusätzliche Einzelzellanalysen von Muskelfasern in Bären während des Winterschlafs und aktiver Phasen legte evolutionäre Anpassungen zur Minimierung des Energieverbrauchs

offen. Bären während des Winterschlafs zeigten eine verringerte Myosin-ATPase-Aktivität, reduzierte Level an mitochondrialen Proteinen und veränderte Aktivität der Myosin-Leichtketten-Kinase (MYLK2), was auf Mechanismen hinweist, die die Muskelfunktion erhalten und den Muskelschwund während der Inaktivität verhindern sollen.

Acknowledgements

Words cannot fully express the depth of my gratitude to all the people who have contributed to making this PhD journey possible. To all my colleagues, friends, and family, thank you for your unwavering support and encouragement.

First and foremost, I would like to thank my supervisor, Prof. Dr. Marcus Krüger, for his invaluable mentorship and countless hours of fruitful discussions. Your openness to my ideas and opinions has been an essential aspect of my growth as a researcher, and I am immensely grateful for your support.

I also extend my sincerest appreciation to my thesis committee members, Prof. Dr. Matthias Hammerschmidt and Prof. Dr. Günther Schwarz, for taking the time to assess my work. Thank you to my TAC committee members, Prof. Dr. Jan Riemer and Prof. Dr. Tessa Lühmann, for your contributions and guidance throughout this journey.

My heartfelt thanks go out to my collaborators, with a special thanks to Christian Høgsbjerg, Abigail Mackey, Leonardo Nogara, Bert Blaauw, and Philipp Antczak. Your friendship, support, and the dynamic exchange of ideas have not only enriched my work but have also fostered a strong sense of community.

Thank you to all the (and former) Krügis, Micha, Angela, Lena, Uli, Kerstin, Andreas, Bibi, Saskia, Pegi, Sebastian, Nitin, Pengyu, and Minhaz, without you nothing of this would have been possible. Thank you for the game evenings, for open hearts and ears, for scientific and non-scientific discussions, and helping me at the darkest times.

To my family, thank you for your love, encouragement, and steadfast belief in my abilities throughout the years. Your unwavering support has been a fundamental pillar of my success, and I am grateful for your presence in my life.

Finally, with tears in my eyes, I want to extend my profound gratitude to my extraordinary friends, who have become family to me. Your laughter, dancing, gaming, and shared adventures have carried me through both the highs and lows of this experience. You have cheered me on at every stage and lifted me up when I needed it the most. Your unyielding love and encouragement have been a constant source of strength and inspiration, and for that, I thank you with all my heart.

Thank you all for your invaluable contributions and unwavering belief in my abilities. Your collective support has been the bedrock of my journey, and I am immensely grateful to have had such an exceptional group of individuals by my side.

List of publications

Schmidt, L.; Antczak, P. Krüger, M. (2024) **Protocol for generating protein profiles and distance-based network analysis of tissue slices**, in revision in STAR Protocols

De Napoli, C.$; **Schmidt, L.$,** Montesel, M.; Cussonneau, L.; Sanniti, S.; Marucci, L.; Germinario, E.; Kindberg, J.; Evans, A.; Gauqueline-Koch, G.; Bertile, F.; Lefai, E.; Krüger, M.; Blaauw, B.; Nogara L. (2024) **Reduced ATP turnover during hibernation in relaxed skeletal muscle**, in revision in Nature Communications

Schmidt, L.; Saynisch, M.; Hoegsbjerg, C.; Schmidt, A.; Mackey, A.; Lackmann, J.; Müller, S.; Koch, M.; Brachvogel, B.; Kjaer, M.; Antczak, P.; Krüger, M. (2024) **Spatial proteomics of skeletal muscle using thin cryosections reveals metabolic adaption at the muscle-tendon transition zone**, Cell Reports, https://doi.org/10.1016/j.celrep.2024.114374

Kraszewska, I.; Sarad, K.; Andrysiak, K.; Kopacz, A.; **Schmidt, L**.; Krüger, M.; Dulak, J.; Jaźwa-Kusior A. (2023) **Casein kinase 2 activity is a host restriction factor for AAV transduction**, Mol Ther S1525-0016(23)00611-1. doi: 10.1016/j.ymthe.2023.11.010.

Andrysiak, K.; Ferdek, P.; Sanetra, A.; Machaj, G.; **Schmidt, L**.; Kraszewska, I.; Sarad, K.; Palus-Chramiec, K.; Lis, O.; Targosz-Korecka, M.; Krüger, M.; Lewandowski, M.; Ylla, G.; Stępniewski, J.; Dulak, J. (2024) **Upregulation of utrophin improves the phenotype of Duchenne muscular dystrophy hiPSC-derived cardiomyocytes**, Molecular Therapy - Nucleic Acids, https://doi.org/10.1016/j.omtn.2024.102247.

Wolkersdorfer, A.; Bergmann, B.; Adelmann, J.; Ebbinghaus, M.; Günther, E.; Gutmann, M.; Hahn, L.; Hurwitz, R.; Lühmann, T.; Schueler, J.; **Schmidt, L**.; Teifel, M.; Meinel, L. (2024) **PEGylated Recombinant Aplysia punctata Ink Toxin Depletes Arginine and Lysine and Inhibits the Growth of Tumor Xenografts**, ACS Biomaterials Science & Engineering Article ASAP, DOI: 10.1021/acsbiomaterials.4c00473

List of figures

List of tables

Abbreviations

ACACA	acetyl-CoA carboxylase alpha
ACADVL	acyl-CoA dehydrogenase very long chain
ACAT	acetyl-CoA acetyltransferase
ACC	acetyl-CoA carboxylase alpha
ACE	angiotensin converting enzyme
ACh	acetyl choline
AChE	acetyl choline esterase
AChR	acetyl choline receptor
ACLY	ATP citrate lyase
ACN	acetonitril
ACTN4	Actinin-4
AEBP1	AE binding protein 1
ADH1	alcohol dehydrogenase 1
ADP	adenosine diphosphate
AGT	angiotensinogen
AGTRAP	type-1 angiotensin II receptor-associated protein
AKT2	protein kinase B
AP2	adaptor protein complex 2
AP2S1	AP-2 complex subunit sigma
ALDH	aldehyde dehydrogenase
ALS	amyotrophic lateral sclerosis
ANOVA	one-way analysis of variance
ANPEP	aminopeptidase N
ANT	adenine nucleotide translocase
ATP	adenosine triphosphate
ATP1A3	ATPase Na^+/K^+ transporting subunit alpha 3
AUC	area under the curve
BCAM	basal cell adhesion molecule
BChE	butyryl cholinesterase
BDNF	brain-derived neurotrophic factor
BMAL2	basic helix-loop-helix ARNT like 2
BMD	Becker muscular dystrophy
BMI	body mass index
BNIP1	BCL2 interacting protein 1
C9orf72	chromosome 9 open reading frame 72
CACNA2D1	calcium voltage-gated channel auxiliary subunit alpha 2 delta 1
Ca^{2+}	calcium ions
CAA	Chloro acetamide
$CaCl_2$	calcium chloride
CCS	collision cross section
CD	control diet
CD9	Tetranspanin-29
CD63	Tetranspanin-30
CD151	Tetranspanin-24
CDK2	cyclin-dependent kinase 2
CHAD	Chondroadherin

CID	collision-induced dissociation
CILP	cartilage intermediate layer protein
CK	creatine kinase
CLU	Clusterin
CMA1	chymase 1
CMS	congenital myasthenic syndrome
CODEX	co-detection by indexing
CNP	2',3'-cyclic nucleotide 3' phosphodiesterase
CNS	central nervous system
COL	collagen
COLQ	acetylcholinesterase collagenic tail peptide
COMP	cartilage oligomeric matrix protein
COX20	cytochrome C oxidase assembly factor COX20
CPNE	Copine 3
CPT	carnitine palmitoyltransferase
CRK	CT10 regulators of kinase
CRYAB	Crystallin alpha-B
CTGF	connective tissue growth factor
CTTN	Cortactin
DAB	DAB adaptor protein
DARS2	aspartyl-tRNA synthetase 2
DBI	diazepam binding inhibitor
DCM	dilated cardiomyopathy
DGC	dystrophin-glycoprotein complex
DHPR	dihydropyridine receptor
DIA	data-independent acquisition
DIA-NN	data-independent-neural networks and interference correction
DMD	dystrophin gene
DMD	Duchenne Muscular Dystrophy
DMEM	Dulbecco's modified eagle medium
DNA	deoxyribonucleic acid
DNAJC11	DnaJ heat shock protein family member C11
DNML2	Dynamin 2
DOK7	downstream of kinase 7
DPYSL2	dihydropyrimidinase-like 2
DRP1	dynamin-related protein 1
DRX	disordered relaxed state
ECD	electron capture dissociation
ECM	extracellular matrix
EDTA	ethylenediaminetetraacetic acid
EGFR	epidermal growth factor receptor
EHD4	EH domain-containing protein 4
EIF4A1	Eukaryotic initiation factor 4A-I
ENPEP	glutamyl aminopeptidase
ENTPD2	ectonucleoside triphosphate di phosphohydrolase 2
EPB	erythrocyte membrane protein
EPP	endplate potential
ESI	electrospray ionization
EXOC	exocyst complex component

FA	formic acid
FACIT	fibril-associated collagens with interrupted triple helices
FAP	fibro-adipogenic progenitor
FASN	epidermal growth factor receptor
FBN	fibulin
FBS	fetal bovine serum
FDR	false discovery rate
FERMT2	FERM domain containing kindlin 2
FFPE	formaldehyde-fixed paraffin-embedded tissue
FIS	fission protein
FLN	filamin
FMOD	Fibromodulin
FUS	fused in sarcoma
GJP3	GAP junction protein gamma 3
GLUT1/SLC2A1	glucose transporter type 1
GSK3	glycogen synthase kinase
GuHCL	guanidinium hydrochloride
HADH	hydroxyacyl-CoA dehydrogenase
HARS2	histidyl-tRNA synthetase
HAT	histone acetyltransferase
HDAC1/2–NuRD	nucleosome remodeling and deacetylase complex
HFD	high-fat diet
HGF	hepatocyte growth factor
HSPA12A	heat shock protein family A member 12A
IFM	interfibrillar mitochondria
IHC	immunohistochemistry
IL	Interleukin
IGF-1	insulin-like growth factor 1
IGSF8	immunoglobulin superfamily member 8
iRT peptides	indexed retention time peptides
ITGA	integrin
ITIH	inter-alpha-trypsin inhibitor heavy chain
ITSN1	intersectin 1
LAMA	laminin
LC	liquid-chromatography
LC3	microtubule-associated protein light chain 3
LFQ	label-free quantification
LMD	laser-microdissection
LOESS	locally estimated scatter smoothing
LRP4	low-density lipoprotein receptor-related protein 4
K^+	potassium ions
KPNA1	karyopherin subunit alpha 1
MAG	myelin associated glycoprotein
MATN4	Matrilin 4
MBP	myelin binding protein
MeCP2	methyl CpG binding protein 2
MFN	mitofusin
MG	myasthenia gravis

MIM	mitochondrial inner membrane
MMP	matrix metalloproteinase
MOM	mitochondrial outer membrane
MPZ	myelin protein zero
MRF5	myogenic regulatory factor 5
MS	mass spectrometry
MTATP8	mitochondrially encoded ATP synthase membrane subunit 8
MTCO2	mitochondrially encoded cytochrome C oxidase II
MTFP1	mitochondrial fission process 1
MTJ	myotendinous junction
MuSC	skeletal muscle satellite cell
MuSK	muscle-specific receptor tyrosine kinase
MYH	myosin heavy chain
MYL	myosin light chain
MYLK	myosin light chain kinase
MYOC	Myocilin
MYOD	myogenic differentiation
MYOZ	Myozenin
m/z	mass-to-charge ratio
Na^+	sodium ions
NAALAD2	N-acetylated-alpha-linked acidic dipeptidase 2
NCAM1	neural cell adhesion molecule 1
NEF	neurofilament
NGF	nerve growth factor
NGR1	nogo receptor 1
NID	Nidogen
NMJ	neuromuscular junction
NSF	N-ethylmaleimide sensitive factor, vesicle fusing ATPase
NT	Neurotrophin
OCT	optimal cutting temperature
OPA1	optic atrophy 1
p75NTR	p75 neurotrophin receptor
PA2G4	proliferation-associated protein 2G4
PALM	paralemmin
PASEF	pParallel accumulation serial fragmentation
PAX7	paired box protein 7
PC	phosphatidylcholine
PCYT1A	phosphate cytidylyltransferase 1A
PDGFRA	platelet derived growth factor receptor alpha
PECAM1	platelet and endothelial cell adhesion molecule 1
PICALM	phosphatidylinositol binding clathrin assembly protein
PLP1	proteolipid protein 1
PNS	Peripheral nervous system
POSTN	periostin
PPARγ	peroxisome proliferator-activated receptor gamma
PPP2RA1	protein phosphatase 2
PRR33	proline rich 33
PRAF2	PRA1 domain family member 2
PRX	Periaxin

PTGFRN	prostaglandin F2 receptor negative regulator
RAB	Ras-related protein
RAS	renin-angiotensin system
RNA	ribonucleic acid
ROS	reactive oxygen species
RTN4R	reticulon-4 receptor
RYR	ryanodine receptor
SAM	significance analysis of microarrays
SDS	sodium dodecyl sulfate
SERCA	sarcoplasmic/endoplasmic reticulum Ca^{2+}-ATPase
SLC	solute carrier proteins
SMMCs	smooth muscle myosin cells
SMYD2	N-lysine methyltransferase SMYD2
SNAP-25	synaptosomal-associated protein 25
SNARE	soluble N-ethylmaleimide-sensitive factor attachment protein receptor
SOD	superoxide dismutase
SORBS	sorbin and SH3 domain
SP3	single-pot solid-phase sample-preparation
SPD	samples per day
SPTAN	Spectrin
SR	sarcoplasmic reticulum
SRX	super relaxed state
SSM	subsarcolemmal mitochondria
STX1	Syntaxin 1
STXBP	Syntaxin binding protein
SYT	Synaptotagmin
TCA	tricarboxylic acid
TCEP	tris(2-carboxyethyl) phosphine
TDP43	TAR DNA-binding protein 43
TFA	trifluoroacetic acid
TFAM	mitochondrial transcription factor
TGF-β	transforming growth factor-beta
THBS4	Thrombospondin 4
TIMS	trapped ion mobility spectrometry
TNC	tenascin c
TNN	troponin
TOF	time-of-flight
TOM20	translocase of outer mitochondrial membrane 20
TPM	tropomyosin
TRK	tropomyosin receptor kinase
UMAP	uniform manifold approximation and projection
USP5	ubiquitin-specific peptidase 5
VAT1L	vesicle amine transport 1 like
VCAM1	vascular cell adhesion molecule 1
VDAC	mitochondrial anion channel
VWF	von willebrand factor
XIRP2	xin actin-binding repeat-containing protein 2

1. Introduction

1.1. Skeletal muscle physiology

More than 40% of the human body is composed of muscles, which contain 50-75% of all body proteins.[1] Muscle tissue is highly dynamic, depending on a fine-tuned balance between protein synthesis and degradation. These processes are extremely sensitive to factors such as food availability, physical exercise, neurodegenerative diseases, and metabolic activity.[2] Muscles are grouped into cardiac, smooth, and skeletal muscle. Cardiac muscles pumps blood through the heart, ensuring proper oxygenation for the body, whereas smooth muscles transport various contents though these systems via their contractile force in vessels. Skeletal muscles maintain the posture, control movement, and most importantly serve as an energy source for the whole body.[3]

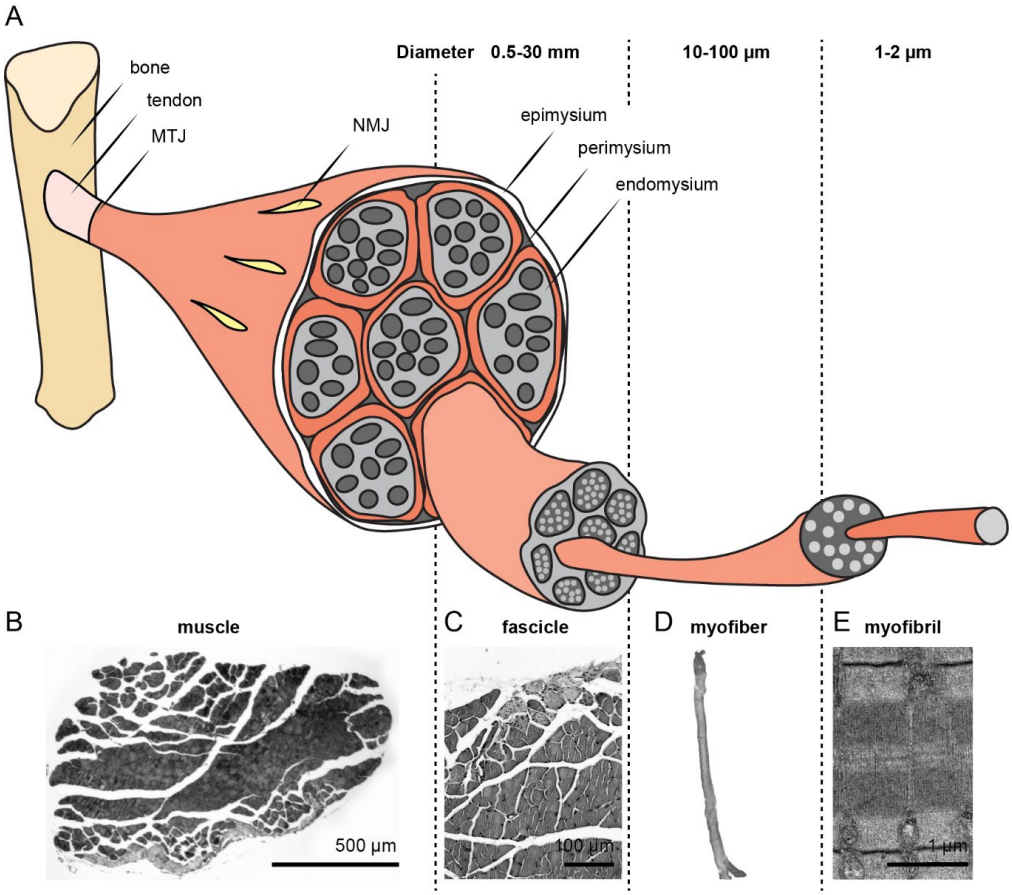

Figure 1 Skeletal muscle anatomy. A-E) Schematic overview of the skeletal muscle architecture (**A, B**). Fascicles (**C**) consists of myofibers (**D**) and in their smallest unit of myofibrils (**E**). MTJ, myotendinous junction; NMJ, neuromuscular junction.

Mammalian skeletal muscle is a heterogenous tissue, comprising various cell populations, including different skeletal muscle fiber types, stem cells, fibroblasts, endothelial cells, pericytes, immune cells and adipocytes. In addition, specialized fasciae are formed with extracellular matrix (ECM) proteins to maintain the integrity and stability of skeletal muscle (**Figure 1A, B**). The tissue is hierarchically organized into parallel bundled fascicles (**Figure 1C**) made up of elongated, cylindrical, and multi-nucleated myofibers (**Figure 1D**). These muscle cells are acting as the functional units of skeletal muscle and vary in size depending on their location and function, with diameters from 10-100 µm and lengths from 5.7-7.6 mm in both human and mice.[4, 5] Myofibers consist of myofibrils with repeating sarcomeres, the smallest contractile units, each measuring 2.1 µm in length (**Figure 1E**).[6]
The endomysium, perimysium, and epimysium encapsulate the myofibers, fascicles, and whole muscle, respectively, providing structural support while aiding in force transmission and synchronous contraction. Next to the connective tissue, the skeletal muscle is connected to the tendons, which attaches the muscle to the bone. Another function of the tendon is to transfer the muscle force generated to the bone in order to initiate movement. In particular, ECM areas such as the myotendinous junction (MTJ) connecting muscle fibers with the tendon.[7] Another unique structure is the neuromuscular junction which connects nerves and muscle fibers (**Figure 1A**).[8] Overall, the skeletal muscle tissue shows a remarkable spatial complexity, characterized by the presence of multiple cell types and matrices, each specialized to fulfill distinct roles essential for muscle function and maintenance.

1.2. The muscle as heterogeneous tissue – different cell populations

Among all cells in the human body, skeletal muscle myocytes and fibers contribute to ~50% of the whole-body mass and support the other organs with energy (ATP), hormones (myokines) and small molecules. Skeletal muscle cells are responsible for contraction and force generation, enabling movement and stability. Muscle stem cells (MuSCs, also known as satellite cells) are crucial for muscle repair and regeneration in response to injury.[9] Vital components of the skeletal muscle maintenance are muscle-resident cells such as fibro-adipogenic progenitors (FAPs), macrophages, and endothelial cells.[10-12]

The cells related to the connective tissue, like tenocytes and fibroblasts, produce extracellular matrix components that provide structural support and facilitate communication between cells such as MuSCs and FAPs.[13] This cellular diversity is a result of the muscle tissue's need to perform complex, dynamic functions and maintain homeostasis under varying physiological conditions.

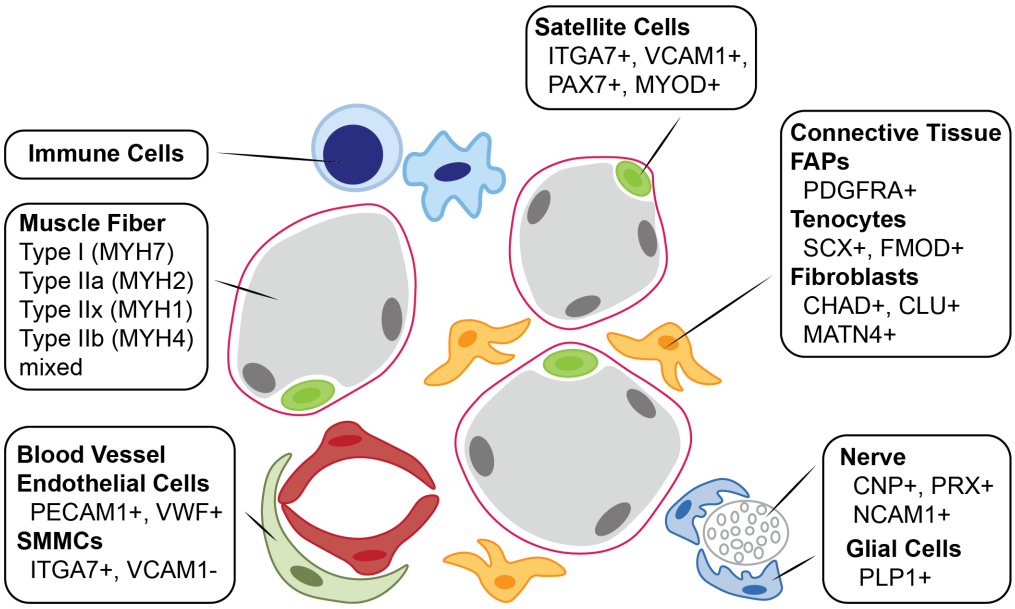

Figure 2 Schematic overview of different cell types in the skeletal muscle. The skeletal muscle contains various cell types including Satellite Cells, Cells related to the connective tissue, Immune Cells, Muscle Fiber, and Nerve Cells with differential expressed marker proteins. CHAD; Chondroadherin; CLU, Clusterin; CNP; 2',3'-Cyclic Nucleotide 3' Phosphodiesterase; FMOD, Fibromodulin; ITGA, Integrin Subunit Alpha 7; MATN4, Matrilin 4; MYH, Myosin Heavy Chain; MYOD, myogenic differentiation; NCAM, Neural Cell Adhesion Molecule 1; PAX7, Paired box protein 7; PECAM1, platelet and endothelial cell adhesion molecule 1; PDGFRA, Platelet Derived Growth Factor Receptor Alpha; PLP1, Proteolipid Protein 1; PRX, Periaxin; VCAM1, Vascular Cell Adhesion Molecule 1; VWF, Von Willebrand Factor. Adapted from Giordani et al., 2019.[14]

1.2.1. Muscle fibers, the force generator of the muscle

The skeletal muscle fibers exhibiting specialized structural and functional characteristics tailored to their role in force production (**Figure 2**). The contractile unit of the fiber are sarcomeres, composed of two main protein filaments and segmented into the A-band, I-band, Z-disc, and M-line (**Figure 3A**). The A-band contains thick filaments made of myosin, while the I-band contains thin filaments of actin and lies between two thick filaments. The Z-disc connects two actin filaments and transverse the I-bands. The sarcomere is also defined as the area between two Z-discs, with the M-line marking its center (**Figure 3B, C**).

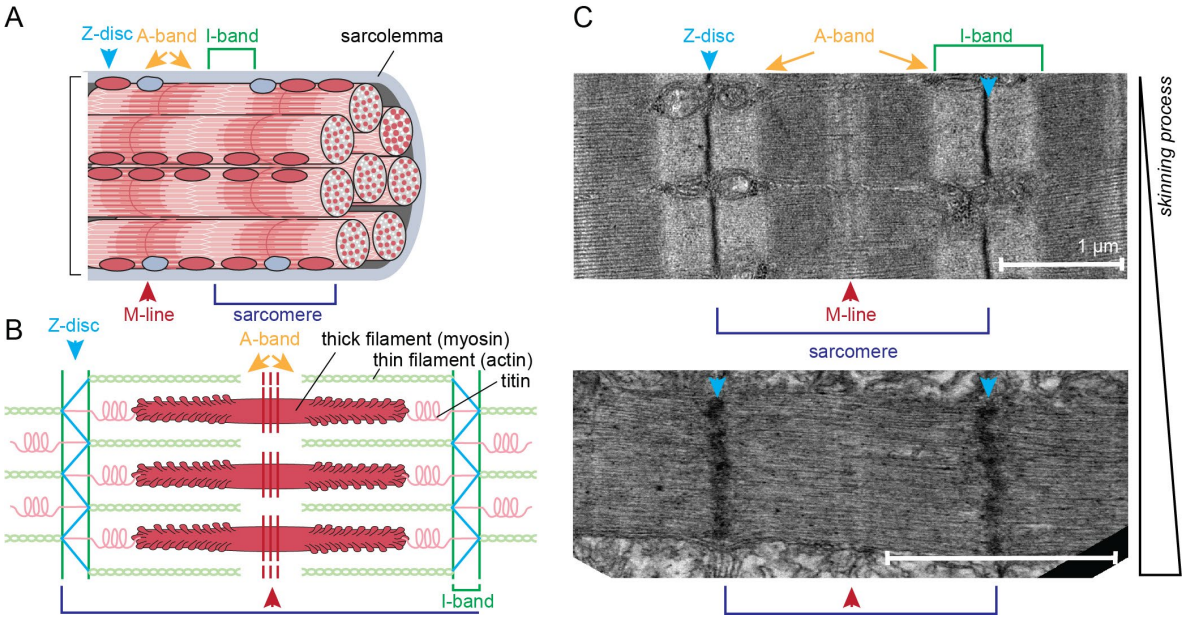

Figure 3 Structure of the myofibers contractile unit. A) Structural overview of the myofiber segmented into the Z-disc, A-band, M-line, and I-band. **B**) Schematic overview of the contractile proteins within one sarcomere. **C**) Electron microscopy picture of one sarcomere with and without a skinning process.

At the cellular level, myocytes generate force through the coordinated interaction of the contractile proteins actin, myosin, tropomyosin, and troponins within the sarcomeres. This process, described by the sliding filament theory[15, 16], involves myosin heads cyclically binding to and pulling along actin filaments, powered by adenosine triphosphate (ATP) hydrolysis.

The process begins with an action potential triggering the release of calcium ions (Ca^{2+}) from the sarcoplasmic reticulum into the cytoplasm of the muscle fiber. Ca^{2+} binds to troponin, causing a conformational change in tropomyosin that exposes the binding sites on the actin filament. Energized myosin heavy chain (MYH) heads then bind to these exposed sites, forming cross-bridges (**Figure 3**). The power stroke occurs as the myosin heads pull the actin

filaments toward the center of the sarcomere. ATP binding to the myosin head leads to its detachment from the actin filament. Subsequent hydrolysis of ATP to adenosine diphosphate (ADP) and inorganic phosphate, the myosin head is re-tensioned and prepared for a further cycle of cross-bridge formation and power stroke. Muscle relaxation follows the active re-transportation of Ca^{2+} by sarco(endo)plasmic reticulum Ca2+-ATPase (SERCA) pump back into the sarcoplasmic reticulum, which leads to the covering of the actin binding sites by tropomyosin, preventing further cross-bridge formation. This intricate interplay between myosin, actin, troponin, and tropomyosin complexes ensures precise control of muscle contraction and relaxation.[17]

The activity of actin-activated myosin ATPase varies depending on the isoform of myosin, troponin, and tropomyosin present.[18] Muscles with a higher consumption rate of ATP exhibit step-wise activation, while those with a lower consumption rate show a linear relationship between contraction and activation. This distinction classifies muscle fibers as either fast-twitch or slow-twitch.[19] Slow-twitch fibers, also known as type I fibers, are characterized by the expression of the myosin heavy chain 7 (MYH7) isoform and an oxidative metabolism for energy production. Conversely, fast-twitch fibers mainly express MYH2 (type IIa), MYH1 (type IIx) and MYH4 (type IIb) isoforms and display a wide range of oxidative (type IIa) and glycolytic (type IIb) activities (**Figure 2**). It is important to note that type IIa fast fibers have significantly more mitochondria compared to the other type II fibers and primarily use oxidative metabolism. Further fiber subtypes are formed through mixed MYH isoform expression, thus expanding the metabolic variability of skeletal muscle tissue. Each fiber type shows distinct metabolic characteristics how it stores and utilizes energy during muscle contraction and how it processes metabolites like glucose, fatty acids and lipids. Type I fibers are adapted for endurance and sustained contractions, relying predominantly on aerobic metabolism. These fibers are rich in mitochondria, myoglobin, and oxidative enzymes, facilitating efficient ATP production through oxidative phosphorylation. The high mitochondrial density and capillary supply ensure a continuous delivery of oxygen, enabling prolonged activity without rapid fatigue. Additionally, slow-twitch fibers store significant amounts of triglycerides, serving as a readily available energy reserve for prolonged aerobic metabolism.

In contrast, fast-twitch fibers are specialized for rapid, high-intensity movements. Type IIa fibers, also known as intermediate fibers, exhibit a mixture of oxidative and glycolytic

capabilities, allowing for both aerobic and anaerobic ATP production. While slow-twitch fibers generally contain a higher number of mitochondria compared to fast-twitch fibers, type IIa fibers have the highest mitochondrial content among all fiber types. Type IIx and IIb fibers, on the other hand, rely predominantly on anaerobic glycolysis, characterized by a higher concentration of glycolytic enzymes and lower mitochondrial density compared to type I and IIa fibers.[20] This reliance on anaerobic pathways enables quick bursts of power and speed but also leads to rapid accumulation of metabolic byproducts such as lactate, contributing to faster fatigue. Fast-twitch fibers also have a greater store of glycogen to fuel glycolysis during intense activity.[21] The diverse and specialized nature of muscle fibers is essential for adapting to various metabolic and environmental changes.

1.2.1. Activated muscle stem cells form new muscle fibers by fusion of myoblasts

MuSCs are essential for the growth, repair, and regeneration of skeletal muscle tissue. During development, myofibers form through the fusion of mesoderm progenitors known as myoblasts. In the neonatal and juvenile stages, each myofiber grows through the fusion with the postnatal stem cell population MuSCs, while the number of myofibers remains constant.[9] These mononucleated cells are located between the basal lamina and sarcolemma of muscle fibers and only sporadically fuse with myofibers under normal conditions to compensate for muscle turnover caused by daily wear and tear (**Figure 2**). In response to muscle injuries, stress, or diseases, MuSCs are activated, proliferate, differentiate, and either fuse with each other to form new myofibers or with existing damaged fibers to facilitate repair.

Under normal conditions, the MuSCs remain quiescent and are characterized by the expression of paired box transcription factor paired box 7 (PAX7), which is essential for their maintenance and self-renewal. PAX7 is highly expressed in quiescent MuSC and continues to be expressed during the early stages of activation and proliferation. In addition, PAX7 regulates the expression of genes necessary for MuSC maintenance and prevents premature differentiation. The main purposes of the proliferative capability of MuSCs are for the replenishment of a stem cell pool and generation of myoblasts for muscle regeneration. In contrast, the myogenic regulatory factor 5 (MYF5) and myoblast determination protein 1 (MYOD1) are one of the earliest key markers in MuSC activation and myogenic commitment, driving the differentiation of myoblasts into myotubes, respectively. Another MRF family member, myogenin, is also essential for later stage differentiation of MuSCs and promotes the fusion of myoblasts into myotubes.[9, 22] The crosstalk between MuSCs and

other cells like FAPs, endothelial, or immune cells from the stem cell niche is mediated by transmembrane proteins, cell adhesion molecules, and inter-cell contact pathways play a pivot role in the activation of MuSCs. The Notch-Signaling pathway for example is a key regulator of MuSC activation and quiescence. Direct contact between MuSCs and neighboring cells, such as myofibers or other MuSCs, facilitates the interaction between Notch receptors on MuSCs and ligands, like delta-like 1 (DLL1) or jagged1 (JAG1), on neighboring cells. Activation of the Notch pathway typically maintains MuSCs in a quiescent state, but upon muscle injury or stress, changes in this signaling can lead to MuSC activation and entry into the cell cycle.[23] Cell-cell interactions are also communicated via the calcium-dependent homophilic cell-to-cell adhesion molecule M-cadherin and vascular adhesion protein-1 (VCAM-1). Both proteins are expressed on proliferating myoblasts and MuSCs and interactions are necessary for fusion of derived myoblasts with existing fibers. The inhibition or ablation of VCAM-1 leads in cell culture to a reduced number of nuclei within myotubes and a transient delay of fiber growth post injury *in vivo*.[24, 25] Other transmembrane receptors of the integrin family mediate the attachment between MuSCs and the ECM resulting in an important role in MuSC activation, migration, and proliferation. For example, integrin α7β1 is particularly important in MuSCs, facilitating their attachment to the ECM via laminins[26] and influencing intracellular signaling pathways that regulate cell behavior.[27]

1.2.2. Fibro-adipogenic progenitors (FAPs) and specialized fibroblasts in muscle repair and regeneration

Fibro–adipogenic progenitors (FAPs) are multipotent stromal cells located in muscle tissue, capable of differentiating into fibroblasts and adipocytes (**Figure 2**). They are activated during muscle injury, leading to their proliferation and secretion of cytokines and growth factors that influence the muscle repair process. Immune cell infiltration and inflammatory signals from damaged tissue trigger FAP activation. In response to immune cells, FAPs secrete factors such as interleukin-4 (IL-4), IL-6, IL-13, and hepatocyte growth factor (HGF), creating a pro-regenerative environment that enhances MuSC activation and myogenesis. Conversely, MuSCs can affect FAP behavior through paracrine signaling, ensuring a coordinated repair response. Platelet-derived growth factor receptor alpha (PDGFRα), a cell surface receptor tyrosine kinase, is a crucial marker for FAPs. PDGFRα signaling influences FAP proliferation and differentiation into fibroblasts.[28] These fibroblasts express collagens, elastin, and other ECM proteins, providing a scaffold that supports muscle cells and

maintains tissue architecture. The ECM is vital for transmitting mechanical forces generated during muscle contraction.[29] Fibroblasts also play a key role in wound healing and cell migration to injury sites to replace damaged tissue. The newly formed matrix is later remodeled into mature scar tissue and restores the muscle's structural integrity. In addition to secreting pro-regenerative signaling molecules, fibroblasts release cytokines and growth factors that modulate the inflammatory response. Released signaling molecules help recruit immune cells to the injury site and regulate inflammation, facilitating the transition from the inflammatory phase to the repair phase.[28]

Activation of proliferator-activated receptor gamma (PPARγ) and its downstream pathways by pro-inflammatory cytokines, such as tumor necrosis factor alpha (TNF-α) and IL-6, can induce adipogenesis of FAPs. Factors that upregulate PPARγ expression or activity in FAPs promote adipogenic differentiation. The differentiation into adipocytes supports muscle repair by secreting insulin-like growth factor 1 (IGF-1), which aids muscle cell proliferation and differentiation, and anti-inflammatory cytokines that help resolve inflammation and create a conductive environment for muscle regeneration. Adipocytes also release adipokines such as adiponectin and leptin, which have systemic effects enhancing muscle metabolism and insulin sensitivity, thereby supporting overall muscle health and recovery.

Similar to fibroblasts, adipocytes are involved in ECM remodeling by secreting matrix ECM-modulating enzymes like metalloproteinases (MMPs) and lysyl oxidase (LOX). Small amounts of 2-5% of fat within muscle tissue can provide structural cushioning and support, maintaining tissue integrity during the repair process.[30]

In addition to muscle fibroblasts, specialized fibroblastic cells known as tenocytes are primarily found in tendons. Tenocytes are essential for maintaining tendon health, repairing tendon injuries, and ensuring the structural integrity of the musculoskeletal system. They produce type I collagen, the main structural protein in tendons, which provides tensile strength and flexibility. Additionally, tenocytes synthesize other ECM components such as elastin, proteoglycans, and glycoproteins. Continuous ECM remodeling is necessary to maintain the tendon's structural integrity and adaptability to mechanical stress, involving both the synthesis and degradation of ECM components. Following tendon injury, tenocytes proliferate and migrate to the injury site, playing a crucial role in the initial phase of tendon healing by producing new ECM to replace damaged tissue. While scar formation is necessary for healing, excessive scar tissue can lead to fibrosis, reducing tendon elasticity and function. Tendons have a limited regenerative capacity, and chronic injuries can result in

tendinopathies, characterized by pain, swelling, and reduced function due to degenerative changes in the tendon structure. The inflammation and tendon repair processes are tightly controlled by various secreted factors, including transforming growth factor-beta (TGF-β) and connective tissue growth factor (CTGF, also known as connective tissue growth factor CCN2). These signaling molecules coordinate the activities of other cells involved in the repair process, including fibroblasts and immune cells.[31] While muscle tissue contains various cell populations with an extensive crosstalk, their specific functions are driven by the location within the tissue.

1.3. Specialized extracellular matrix (ECM) regions are key interfaces in muscular function

1.3.1. The myotendinous junction (MTJ) as stabilizing area for force transmission and structural integrity

The MTJ is a specialized tissue that forms the interface between muscle fibers and tendon, transmitting the force generated by muscle contractions to the skeletal system, thereby enabling the force transmission from skeletal muscles to bones.[32] Understanding the MTJ requires examining its morphometric architecture, the cellular and molecular interactions, and its physiological function under normal and disease-related conditions.

The MTJ is characterized by its complex interface between muscle fibers and tendon collagen fibers (**Figure 4A**). At the cellular level, this junction features the interdigitation of muscle fiber membranes with tendon collagen fibers and the invagination of muscle fibers, which creates a large surface area for force transmission and ensures a strong connection. These invaginations are filled with complex ECM components, such as laminin, fibronectin, and integrins, which anchor the muscle fiber membrane to the tendon. This complex architecture ensures that the generated forces are evenly distributed and transmitted without causing damage to the muscle fiber membrane.[33]

Molecular components supporting this structure are integrins, dystrophin-glycoprotein complex (DGC) members, sarcoglycans and sarcospan, cell adhesion proteins and different collagen members. Integrins and the DGC attach myofibers to the basement membrane and are expressed throughout the sarcolemma, with enrichment at force-regulating and force-transducing sites.[34] Integrins also transduce signals to control actin dynamics and link the cytoskeleton with the ECM through associated proteins like talin (TLN1) and integrin-linked

kinase (ILK).[35] This process involves both inside-out and outside-in activation mechanisms: inside-out activation occurs when intracellular signals regulate integrin affinity and activation state, allowing them to interact more effectively with the ECM; outside-in activation happens when integrins bind to ECM components, triggering intracellular signaling pathways that modulate actin dynamics and cytoskeletal organization.[36] Ablation of integrin α7β1 and α5 leads to muscular dystrophy characterized by reduced myoblast adhesion, reduced proliferation and impaired MTJs. This underscores the important role of integrin signaling in MTJ function.[37, 38] Important members of the DGC are dystrophin, dystrophin-associated proteins (like syntrophin), dystrophin-associated glycoproteins (like α-dystroglycan), sarcoglycans, and sarcospan which serves as stabilizer of the muscle cell membrane and connects the cytoskeleton of the muscle fiber to the ECM.[39] During the contraction of the fiber, the DGC contribute to maintain the stability and integrity of the muscle cell membrane. Mutations on or the absence of dystrophin are leading to structural defects at the MTJ including a reduction in lateral associations between thin filaments and the MTJ membrane in prenecrotic and regenerated mice skeletal muscle.[40] A major part of the tendon structure that is interdigitating with the muscle membranes are collagen fibers, primarily structured by collagen I and III. The FACIT (fibril-associated collagens with interrupted triple helices) collagen XXII was identified as cell adhesion ligand for fibroblasts and is found to be enriched at the MTJ.[41] Other published MTJ marker are the xin actin-binding repeat-containing protein 2 (XIRP2) and cartilage intermediate layer protein (CILP).[42, 43]

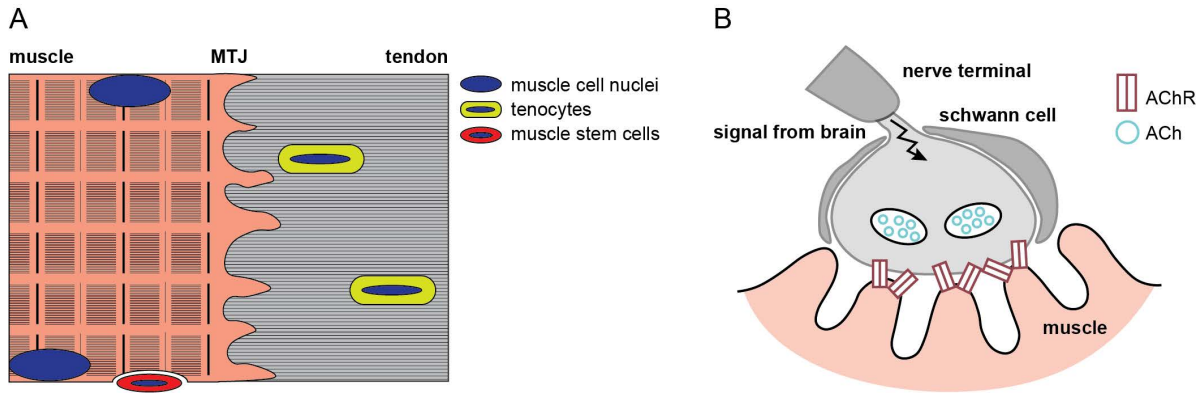

Figure 4 Simplified structure of the myotendinous and neuromuscular junction. A) Myotendinous junction as the interdigitation between muscle and tendon. **B**) Neuromuscular junction as the connection point between nerve and muscle. ACh, acetyl choline; AChR, acetyl choline receptor; MTJ, myotendinous junction. Adapted from Charvet et al. 2012[44] and Pratt et al 2020[45].

In addition to its function as a force transmitter, the MTJ is also essential for coordinated movement and stability. Any disruption in its structure or function can lead to significant impairments, like reduced force transmission, muscle weakness, and muscle dystrophy. Injuries to the MTJ, such as strains or tears, are common in response to excessive physical activity. Chronic overuse or repetitive strain can lead to tendinopathies, characterized by pain, inflammation, and degeneration of the tendon. In addition to mechanical injuries, genetic disorders affecting components of the MTJ can lead to muscular dystrophies and other myopathies. For instance, mutations in the genes encoding integrins or components of the DGC can disrupt the stability of the muscle-tendon interface, leading to progressive muscle weakness and degeneration. For example, mutations in *ITGA7* cause myopathy in humans[46] as well as in mice[37].

A critical point of the MTJ is the neuronal innervation, involving nerve fibers that interact with both muscle and tendon tissues. This neuronal activity contributes to the regulation of muscle function and proprioception to sense self-movement. Important types of the sensory nerve fibers are the Golgi tendon organ (GTO) and mechanoreceptors, which are monitoring tension and force exerted by the muscle[47] and responding to mechanical changes such as stretch or pressure within the MTJ[48].

1.3.2. The neuromuscular junction (NMJ) as communication interface between neuronal and muscle cells

The NMJ is another critical anatomical structure, serving as the synapse or communication point between a motor neuron and a skeletal muscle fiber. It is essential for the initiation and regulation of muscle contraction and enables both voluntary and reflex activation

The NMJ consists of three key components: the presynaptic terminal, synaptic cleft, and postsynaptic membrane (motor endplate) (**Figure 4B**). The presynaptic terminal, at the end of the motor neuron axon, synthesizes and stores neurotransmitter in synaptic vesicles. The synaptic cleft is the gap between the presynaptic terminal and the muscle fiber membrane, filled with extracellular fluid and molecules that facilitate neurotransmitter diffusion. The motor endplate, like the MTJ, is highly interdigitated to increase the surface area for neurotransmitter reception.[49] This specialized region of the muscle fiber contains acetylcholine receptors (AChRs), ligand-gated ion channels that respond to acetylcholine by allowing sodium influx and initiating depolarization. Acetylcholinesterase (AChE), located

in the synaptic cleft, rapidly degrades acetylcholine (ACh), terminating the signal and allowing the muscle fiber to repolarize.

The process of communication between the synapse and the muscle can be described in the following steps:

An action potential originates in the cell body of a motor neuron in the spinal cord and travels to the presynaptic terminals. This action potential leads to a depolarization of the presynaptic membrane and opens voltage-gated calcium channels. The influx of Ca^{2+} triggers synaptic vesicles containing ACh to merge with the presynaptic membrane, releasing ACh into the synaptic cleft via exocytosis. Proteins associated with synaptic vesicles, such as synaptotagmin (SYT) and soluble *N*-ethylmaleimide-sensitive factor attachment protein receptor (SNARE) complexes, mediate vesicle fusion and neurotransmitter release.[50, 51] The neuronal SNARE complex includes synaptobrevin-2 (SYB2) on the synaptic vesicle membrane and syntaxin 1 (STX1) and synaptosomal-associated protein 25 (SNAP-25) on the plasma membrane.

The released ACh binds to AChRs on the motor endplate and leads to the flow of sodium ions (Na^{+}) into the muscle cell via opening ligand-gated sodium channels. This influx of sodium causes depolarization of the muscle membrane, generating an endplate potential (EPP). A great EPP of 20-30 mV triggers an action potential in the muscle fiber that travels along the sarcolemma and into the T-tubules, promoting the release of Ca^{2+} from the sarcoplasmic reticulum (SR), an internal calcium store, into the cytoplasm of the muscle cell. The increase in cytoplasmic calcium concentration initiates the interaction between actin and myosin filaments within the sarcomeres, the contractile units of the muscle. This interaction, facilitated by the sliding filament mechanism and regulated by the proteins troponin and tropomyosin, results in muscle contraction. The signal is terminated by the rapidly enzymatic breakdown of acetylcholine in the synaptic cleft by AChE. Choline is taken back up into the nerve terminal for the synthesis of new acetylcholine molecules. Ca^{2+} are pumped back into the sarcoplasmic reticulum by SERCAs, decreasing the cytoplasmic calcium concentration and leading to muscle relaxation as the actin-myosin interaction ceases. This sequence of events ensures precise control of muscle contraction and relaxation, enabling coordinated movement and response to neural stimuli.[52]

Next to the vesicle proteins, neurotransmitters, and their receptors, also the class of neurotrophins, such as agrin, neuregulin, nerve growth factor (NGF), brain-derived neurotrophic factor (BDNF), neurotrophin-3 and 4 (NT-3, NT-4), are functional for signal

transmission at the NMJ. They control the survival, development, and function of neurons, regulating the clustering of AChRs and other postsynaptic components, thus playing crucial roles in the development and maintenance of the NMJ.[53] Neurotrophins exert their effects through binding to specific receptors on the surface of neurons and muscle cells. The primary receptors for neurotrophins are the tropomyosin receptor kinase (TRK) family of receptors and the p75 neurotrophin receptor ($p75^{NTR}$). High-affinity neurotrophins preferentially bind to a specific TRK receptor (e.g., NGF to TrkA) and triggers intracellular signaling pathways that promote survival, growth, differentiation, and synaptic plasticity. In contrast, the low-affinity receptor $p75^{NTR}$ binds all known mammalian neurotrophins (proNGF, NGF, BDNF) and modulates their effects by interacting with TRK receptors or activating distinct signaling pathways involved in cell survival and apoptosis.[54, 55]

Another protein involved in neurotransmission is the proteoglycan agrin, which is secreted from the nerve terminal of a spinal motor neuron. Its receptors, the low-density lipoprotein receptor-related protein 4 (LRP4) and muscle-specific receptor tyrosine kinase (MuSK), are located at the postsynaptic muscle membrane. The agrin-LRP4 pathway activates the receptor tyrosine kinase MuSK through phosphorylation at position Y553 and Y750.[56, 57] Subsequently, the cytoplasmic adapter protein downstream of kinase 7 (DOK7) binds to MuSK and recruits proteins like CT10 regulators of kinase (CRK and CRK-L) and sorbin and SH3 domain (SORBS) which, stabilizes the AChR clusters.[52]

While it's known that the NMJ is most commonly sitting at the muscle side, several studies also show that tenocytes express neurotransmitter receptors, suggesting that they can interact with the nervous system. This interaction may play a role in pain perception and modulation during tendon injuries and inflammation.[58, 59]

Since the NMJ and MTJ are critical structures in skeletal muscle, an injury or pathological change in these structures is significant for overall skeletal muscle function.

1.4. Stratification of muscle related diseases

Skeletal muscle diseases can be classified into primary and secondary categories. The primary diseases directly affect the muscles, leading to weakness, degeneration, and functional impairments. They can be further sub-categorized into myopathies, neuromuscular junction disorders, and neurogenic disorders. In the secondary category, skeletal muscles are affected by systemic disorders, like diabetes, that primarily impact other organs.

In both primary and secondary diseases, muscle energy metabolism can be compromised and includes defects in muscle carbohydrate and lipid metabolism. In addition, mitochondrial electron transport and abnormalities in purine nucleotide metabolism contribute to muscle weakness.

Furthermore, muscle wasting leads to a significant decline in muscle mass, caused by muscle necrosis, atrophy, or the replacement of functional muscle tissue with fat and connective tissue. This progressive deterioration adversely affects maximal oxygen uptake and mitochondrial activity, crucial for sustaining physical performance. Moreover, the impact on anaerobic muscle performance is notable, with severity of muscle weakness and atrophy directly influencing overall endurance and strength. Additionally, intrinsic muscle dysfunction, along with abnormalities in the central nervous system, motor nerves, or neuromuscular junctions, can impair the proper activation of muscle contraction and relaxation.[60]

The following chapters detail examples of muscle diseases which are leading to muscle loss and weakness.

1.4.1. Muscle dystrophy – Genetic causes for muscle degeneration

Muscular dystrophies are genetic disorders marked by progressive muscle degeneration and weakness. Traditionally, these conditions were classified based on clinical and pathological criteria, but modern classification relies predominantly on genetic factors. Among the muscular dystrophies, Duchenne Muscular Dystrophy (DMD) is the most common and severe form, particularly affecting young boys (**Figure 5**). Affected males typically present motor symptoms and enlarged calves in early childhood. DMD is caused by “out-of-frame” or nonsense mutations in the X-linked *dystrophin* (*DMD*) gene.[61] These mutations have an altered reading frame by a premature stop codon, which results in the production of a truncated, not functional dystrophin protein. Conversely, “in-frame” mutations maintain the reading frame and still express a shorter dystrophin, leading to a milder disease and is called Becker muscular dystrophy (BMD).[62]

Dystrophin is a critical protein that maintains muscle fiber integrity by protecting muscle cells against the forces generated during contraction. It achieves this by interacting with a complex network of proteins at specialized sites on the muscle cell membrane called costameres. Dystrophin plays a vital role in organizing the DGC at these costameres, which forms a crucial connection between the internal cytoskeleton and the ECM. This stabilizes

the muscle cells during contraction. The DGC is a key structural component of the sarcolemma, facilitating the transmission of force both laterally and longitudinally from the contractile apparatus to the ECM. It also helps maintaining the alignment of sarcomeres in adjacent myofibers. By dispersing the forces of contraction away of myofibers, dystrophin and the DGC protect muscles from injury caused by contracting, thereby preserving the structural integrity of the sarcolemma.[63] In the absence of dystrophin, the sarcolemma becomes more prone to damage during muscle contractions, especially at MTJ, where force transmission is highest. This increases susceptibility to micro-tears and injuries, particularly with repeated muscle use. As a result, efficient force transmission from muscle to tendon is compromised, leading to weaker and less effective muscle contractions. Damage to MTJs results in chronic inflammation, which can trigger fibrosis (scar tissue formation), further stiffen the MTJ, reducing its flexibility and making it more prone to re-injury.[64]

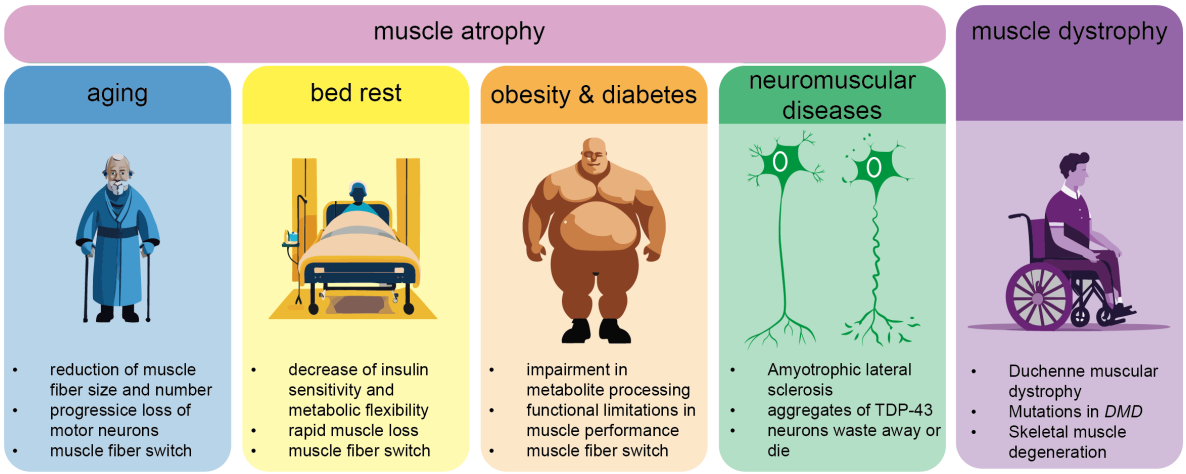

Figure 5 Muscle diseases. Muscle diseases can be categorized into muscle dystrophies (right) and muscle atrophy (left). Examples of muscle atrophy are aging, bed rest, obesity & diabetes, and neuromuscular diseases. TDP43, TAR DNA-binding protein 43; *DMD*, dystrophin.

The study of MTJs in DMD patients is essential for understanding the full scope of muscle degeneration in this condition. This is particularly important due to the higher concentration of dystrophin at the MTJ and the role that the MTJ plays in transmitting force from muscle to tendon and bone.[33] Ongoing research and targeted therapies hold promise for mitigating the effects of dystrophin deficiency at these critical sites of muscle-tendon interaction.[40]

A widely used animal model to study DMD are MDX mice, which harbors a UAA premature stop codon in exon 23 of *DMD* gene, leading to the absence of functional dystrophin protein, similar to the condition in humans. Barton-Davis, 1999 #639} MDX mice exhibit critical hallmarks of human DMD, including high susceptibility to contractile-induced damage,

significant degree of muscle fiber degeneration and regeneration, and increased fibrosis later in life.[65, 66] However, MDX mice show a milder phenotype to human DMD, particularly with respect to lifespan and cardiac involvement. This indicates the presence of compensatory mechanisms, such as the upregulation of utrophin (a dystrophin homolog), which allows for the initial formation of MTJs despite the absence of dystrophin.[67]

Regardless of these differences, MDX mice remain vital for research into MTJs in the absence of dystrophin and for studying dystrophin's role as a structural link between thin filaments and the membrane. For instance, in MDX mice, treatment options like read-through therapy for nonsense mutations, which bypasses the premature stop codon, have been extensively studied. One example includes the administration of aminoglycosides, which suppress stop codons in cell culture. These were first tested on MDX mice and showed dystrophin expression and localization at the membrane in MDX myotubes.[68] New approaches, such as gene therapy for DMD, are based on insights from the milder phenotype observed in Becker Muscular Dystrophy (BMD), where a full-length dystrophin is not obligatory to slow down the disease. Gene transfer using a non-pathogenic adeno-associated viral vector (AAV) has been explored, though the AAV's limited size of 4.7 kb restricts the use to a shorter version of dystrophin. The resulting mini- or micro-dystrophins have shown clinical potential, with several trials demonstrating promising results.[69]

1.4.2. Muscle atrophy – Non-genetic causes for muscle degeneration

Muscle atrophy refers to the wasting and degeneration of muscle tissue and leads to a decrease in muscle size and strength. In contrast to genetic related disorders which induce muscle dystrophy, muscle atrophy is mainly caused by a lack of physical activity[2], aging[70], malnutrition[2], certain medical conditions[71], and prolonged immobilization[72]. Symptoms are muscle loss and weakness, early fatigue, difficulty in maintaining balance, and increased strain on joints. The most common cause is disuse atrophy, arising due to prolonged immobilization, such as from bed rest, sedentary lifestyle, or casting after a fracture. Another important factor is the uptake of nutrition, and a reduced caloric consumption can lead to muscle wasting conditions also described as anorexia nervosa. In addition, gastrointestinal disorders (for example liver cirrhosis and inflammatory bowel diseases) can cause this skeletal muscle atrophy. Additionally, malnutrition or excessive food consumption that leads to higher body mass index (BMI) and obesity can cause muscle wasting by increasing the amount of lipid storage in adipocytes and muscle fibers.

Sarcopenia describes the decline of muscle mass and strength during aging. This process can be accelerated by a sedentary lifestyle and poor nutrition. One of the most sever atrophies are the neurogenic atrophies that are caused by injury or disease affecting the nerves that connect to muscles, such as spinal cord injury, amyotrophic lateral sclerosis (ALS), or peripheral neuropathies. While disuse atrophy is a process over a longer period, the loss of neuronal innervation leads to a rapid muscle loss.

1.4.3. The neurodegenerative disease Amyotrophic Lateral Sclerosis (ALS)

ALS, also known as Lou Gehrig's disease, is a progressive neurodegenerative disorder that affects motor neurons in the brain and spinal cord (**Figure 5**). These motor neurons are responsible for controlling voluntary muscle movements, and their degeneration leads in the early stages to muscle weakness in the hands, arms, and legs. Further symptoms are skeletal muscle twitching, cramping, and reduced fine motor tasks. At the advanced stages, ALS patients typically lose voluntary control over their muscles and often die of respiratory failure caused by weakness in diaphragm and chest muscle. The precise cause of ALS is not completely understood, but the ALS disease is associated with several genetic and environmental factors. About 5-10% ALS cases are inherited and show mutations of the superoxide dismutase type 1 (SOD1), chromosome 9 open reading frame 72 (C9orf72), TAR DNA-binding protein 43 (TDP43), and fused in sarcoma (FUS) genes. Besides familial ALS, the majority cases are sporadic ALS, with no clear family history and detectable genetic alterations. The exact causes are unclear, but they may involve a combination of genetic predisposition and environmental risk factors such as toxins, smoking, military service, and physical trauma. However, the evidence for these factors is not entirely clear yet.[73]

Although the exact pathological mechanisms of ALS are still unknown, it is assumed that familial and sporadic ALS share some common mechanisms due to their molecular changes, including oxidative stress, mitochondrial dysfunction, glutamate excitotoxicity, disrupted protein trafficking, neuroinflammation, and RNA metabolism alterations.[74] The cellular by-products superoxide radical anion, hydrogen peroxide, and hydroxyl radical are summarized under the term of reactive oxygen species (ROS) and are generated through enzymatic and nonenzymatic reactions. One of the most contributing sites for intracellular ROS production are the mitochondria due to their primary role in oxidative ATP production. In this process, molecular oxygen is reduced to water within the electron transport chain.[75] The elevated ROS levels are leading to oxidative damage to proteins, lipids, and deoxyribonucleic acid (DNA).

This oxidative stress is a significant contributor to motor neuron death. One of the involved proteins is SOD1. The most common mutations at G93A, D90A and L144S in SOD1 lead to a toxic gain of function and are responsible for the loss of motor neurons.[76, 77] However, it is not clear whether increased ROS and oxidative damage are the primary cause or a secondary consequence of this disease.[78, 79] It was reported that mitochondrial abnormalities like swelling and vacuolation occur together with an increased oxidative damage. Similar, mitochondria in ALS-affected neurons show structural abnormalities, reduced ATP production, and increased susceptibility to apoptosis.[79]

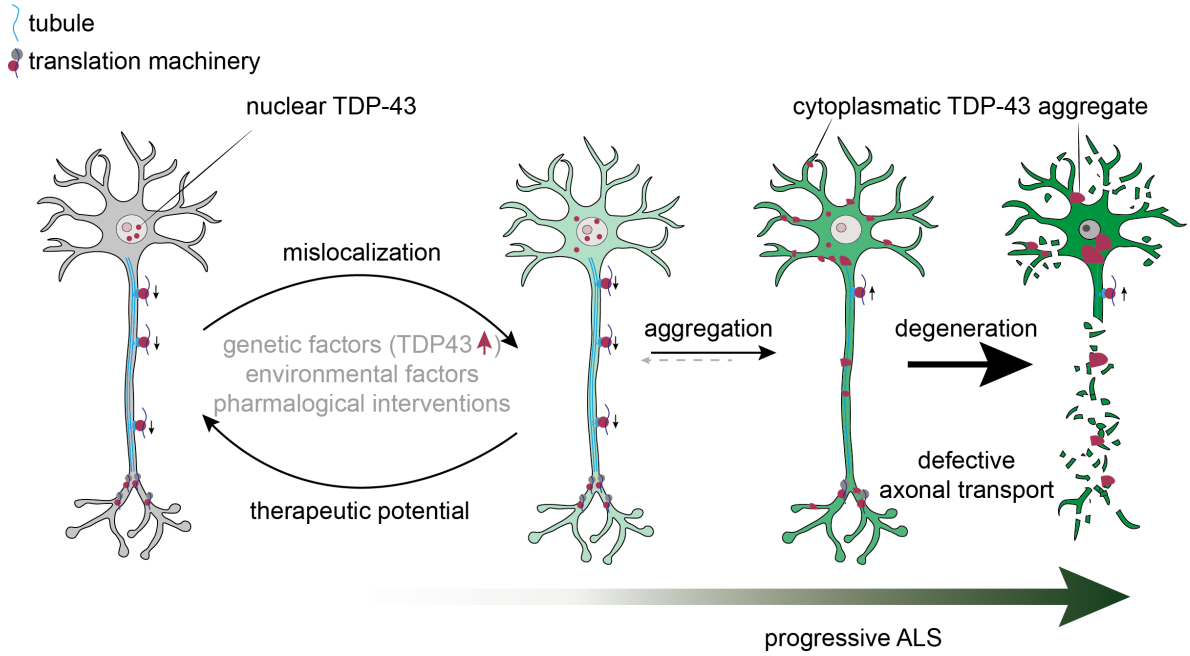

Figure 6 Progressive ALS related to cytoplasmatic aggregation of TDP43. On the left side, an intact healthy neuron with nuclear TDP43 that is transported to the axons via tubule. Mislocalization of TDP43 because of genetic and environmental factors leads to a progressively aggregation of TDP43 in the cytosol leading to the degeneration of the neuron and defective axonal transport. ALS, Amyotrophic Lateral Sclerosis; TDP43, TAR DNA-binding protein 43. Adapted from Nilaver et al..[80]

Another important factor is the aggregation of molecules like glutamate and the protein TDP43. Reasons for protein aggregation are misfolded proteins, impaired proteastasis, transport mechanisms, and impaired glutamate uptake. An insufficient glutamate uptake by astrocytes results in excessive glutamate in the synaptic cleft, which leads to overactivation of glutamate receptors on motor neurons and subsequent toxic overload of calcium influx.[81] The assembly of stress granules is closely linked to the presence of stress granule assembly factors 1 and 2 (G3BP1/2), which are commonly used as marker proteins for these aggregates. Without G3BP1/2, stress granule formation is inhibited, while their overactivation promotes the assembly of these granules.[82] While autophagy and proteasome

dysfunction, responsible for degrading misfolded proteins, can result in the accumulation of toxic protein aggregates, also the mutation in proteins like TDP43 and FUS can lead to misfolding and relocalization. TDP43 and FUS are DNA-/ribonucleic acid (RNA)-binding proteins that aggregate abnormally in ALS, disrupting RNA processing and transport. In 90% of ALS patients, insoluble protein aggregates of the nuclear protein TDP43 are found in the cytoplasm of neurons and glial cell (**Figure 6**). TDP43 is an essential DNA-/RNA-modulating protein, with the primary function in RNA processing, including transcription regulation, alternative splicing, mRNA stability, and transport. In cases where TDP43 is mislocalized outside the nucleus, it disrupts RNA processing by binding RNA-binding proteins and interferes with transport processes, promoting neurodegeneration. In particular, TDP43 mutations localized at the phosphorylation sites (Ser 379, Ser 403/404, Ser 409/410) causes changes in the localization and protein interactions.[83] Possible causes for the accumulation of protein aggregates in axons is disturbed trafficking of mitochondria towards the proximal axon areas. In addition, local protein synthesis and proteolysis of TDP43 can be imbalanced. In humans TDP43 based ALS pathology is described as a gain of toxic function driven by mislocalization and accumulation of TDP43 in the cytoplasm. A recently described ALS mouse model describes an overexpression of TDP43 which lacks the nuclear localization signal, providing insights into the molecular understanding of TDP43 accumulation and mislocalization.[83, 84]

1.4.3.1. Sarcopenia – The effects of aging and obesity on muscles

Aging is marked by a gradual deterioration of biological functions, leading to increased vulnerability to diseases and ultimately death. One of the hallmarks of aging is cellular senescence, defined by stable exit from the cell cycle in response to cellular damage and stress. The accumulation of senescent cells with age contribute to tissue dysfunction and results in loss of repair and regeneration. Other metabolic health implications during muscle loss are associated with insulin resistance and increased risk of type 2 diabetes.[2, 85, 86]

The aging process in muscles by themselves is quite severe, after the age of 30 the human body lose ~1% of the muscle mass each year. Mechanisms of skeletal muscle aging results from a combination of factors including hormonal changes (decrease of testosterone and IGF-1), inflammation, and decreased physical activity (**Figure 5**).

Muscle mass and fiber size is regulated by the processes of protein synthesis and protein degradation, summarized as protein turnover.[87] The pathway which controls protein turnover

is primarily regulated by the insulin-like growth factor IGF1 and its downstream effector protein kinase B (AKT2). AKT2 is a central kinase regulating downstream proteins such as mammalian target of rapamycin (mTOR) and forkhead box O protein (FOXO). Interestingly, in aged mice, the proteolytic system is not activated via FOXO; instead, there is an increased activation of the mTOR complex 1 (mTORC1).[88] This observation also explains the longer lifespan associated with caloric restriction, which is linked to decreased mTOR activation.[87, 88] Another pathway related to protein degradation is the ubiquitin-proteasome system (UPS), modulated by key E1, E2 and E3 ubiquitin ligases. The main E3 ligases involved in protein degradation are atrogin-1 (FBXO32)[89] and muscle RING-finger protein-1 (MURF1).[90] With aging, FBXO32 levels increase.[89] However, studies have shown that inactivation of FBXO32 can lead to muscle pathology and reduced lifespan, indicating that completely blocking protein degradation pathways might accelerate, rather than mitigate, sarcopenia.[87]

Another consequence of aging is a reduced mitochondrial function in skeletal muscle tissue. This causes reduced ATP production, and increased ROS levels and enhanced oxidative stress. Aging also significantly affects the NMJ, where structural and functional changes contribute to sarcopenia (**Figure 7**). Axonal degeneration and remodeling are caused by a reduced number of motor neurons leading to a reinnervation of denervated fibers by surviving axons. These motor units often become enlarged and less efficient. Structural changes are also observed at the synaptic site, including fragmentation of the postsynaptic membrane and a reduction in synaptic vesicles at the presynaptic terminal. These alterations disrupt the normal transmission of nerve impulses to muscle fibers. Correlating to the architecture changes at the postsynaptic membrane, also the density of AChRs decreases. The functional consequences of the cumulative structural changes are decreased synaptic transmission efficiency, increased fatigue, and impaired motor control.[91]

Next to changes of motor neurons at the NMJ alterations in skeletal muscle fiber types can also be observed during the aging process. These changes impact muscle performance, metabolic efficiency, and overall physical capabilities. Based on morphological observations, fast-twitch fibers appear smaller and flatter during aging. Moreover, the number of fast fibers and their cross-sectional area (CSA) decreases. In contrast, the number and CSA of slow-twitch fiber increases with aging.[92, 93]

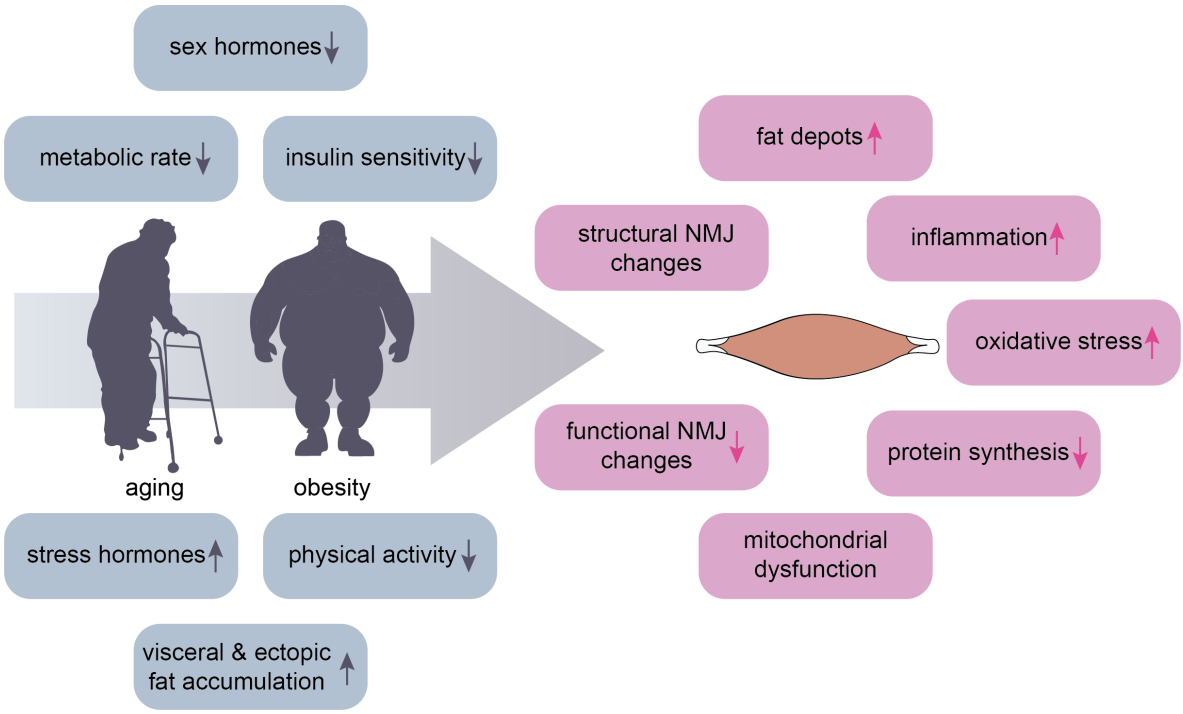

Figure 7 Causes and consequences of aging and obesity on muscles. Factors like a decrease of sex hormones, metabolic rate, insulin sensitivity, and physical activity and the increase of stress hormones and visceral and ectopic fat accumulation influences the muscle healthy. Consequences are structural and functional changes at the NMJ, a mitochondrial dysfunction, an increase of fat depots, inflammation, and oxidative stress, as well as a reduced protein synthesis. NMJ, neuromuscular junction.

Another pathological effect on the skeletal muscles is caused by increased food intake and the associated obesity (**Figure 7**). Skeletal muscle is responsible for almost 70% of insulin-stimulated glucose processing and therefore represents the body's largest energy reservoir. It is thus obvious that changes in food intake influence the activity of skeletal muscles. For example, skeletal muscles of individuals with severe obesity and type 2 diabetes mellitus show impaired glucose metabolism and a reduced mitochondrial activity (**Figure 5**).[94] Both obesity and type 2 diabetes lead to decreased insulin sensitivity, which impairs the recruitment of glucose transporter type 4 (GLUT4) to the cell membrane, resulting in reduced glucose uptake and energy supply.[95] Additionally, insulin resistance disrupts the Akt signaling pathway, crucial for muscle protein synthesis, leading to decreased muscle growth and increased muscle degradation, which contributes to muscle weakness.[96, 97] Mitochondrial activity is further compromised due to increased production of reactive oxygen species (ROS), driven by intracellular glucose overload that intensifies the glycolytic pathway and the tricarboxylic acid cycle.[98]

The processing of glucose, fatty acids and lipids in the muscle is closely related to its fiber type composition. Since each fiber type has unique metabolic characteristics that determine

how it stores and utilizes energy during muscle contraction, a potential shift of fiber types has a significant impact for the energy homeostasis of the whole body. Previous studies have shown that the proportion of slow muscle fibers (type I) is inversely related to obesity, while the number of glycolytic type IIx fibers increases.[85] Similar to other metabolic disorders and aging, also the nutrient excess leads to mitochondrial dysfunction leading to altered lipid and glucose metabolism. One potential reason for mitochondrial dysfunction can be an imbalance of the formation of mitochondrial network through fusion and fission. At the molecular level the mitochondrial outer membrane GTPase proteins mitofusins 1 and 2 (MFN1 and MFN2) mediates mitochondrial fusion[99], while mitochondrial fission is regulated by dynamin-related protein 1 (DRP1)[100]. Another fission factor is the inner membrane protein mitochondrial fission process 1 (MTFP1/MTP18). Genetic ablation of the *Mtfp1* gene in cell culture and in mouse cardiomyocytes reduces mitochondrial fission. The observation of reduced OXPHOS efficiency might be caused by the increased proton leak via the adenine nucleotide translocase (ANT).[101, 102]

Due to the increasing number of obese and older individuals in our society, more attention should be drawn to possible changes in skeletal muscles.

1.5. Liquid tandem mass spectrometry (LC-MSMS) as promising tool for unbiased identification and quantification in metabolic challenged muscles

1.5.1. Dynamic range as bottle neck for large scale and low input studies of skeletal muscle

In recent years, tandem mass spectrometry (MS/MS) has emerged as a powerful analytical technique for the identification and characterization of molecules based on their mass, charge, and collision cross section (CCS). Analytes in these studies may include metabolites (metabolomics), lipids (lipidomics), and proteins (proteomics).

In bottom-up proteomics, proteins are enzymatically digested into peptides, simplifying the analysis by reducing the complexity of the protein structures to peptides of 7-19 amino acids length. These peptides are then matched against sequence libraries to identify and quantify the corresponding proteins.

Peptides are separated based on their hydrophobicity using a reversed phase liquid-chromatography (LC) system, which effectively reduces sample complexity before MS analysis. Peptides are ionized through electrospray ionization (ESI), facilitating the transfer

of ions from the solution into the gas phase by the dispersion of charged droplets, solvent evaporation, and an ion ejection of highly charged droplets. These ions are subsequently transferred and trapped in the MS instrument. The peptides are selected for fragmentation based on their mass-to-charge ratio (*m/z*); an initial step defined as MS1. The selected precursor ions are isolated and fragmented using higher-energy collisional dissociation (HCD), collision-induced dissociation (CID) or electron capture dissociation (ECD). The resulting fragment ions are further sent to the mass analyzer to determine the *m/z* and receive amino acid sequence information about the selected precursor. Compared to other proteomic methodologies, such as antibody- or gel-based techniques, LC-MS/MS offers high sensitivity in an unbiased manner, enabling the detection of low-abundance compounds and facilitating both qualitative and quantitative analysis through ion intensity measurements. Proteomic approaches uniquely reveal the functional state of the cell through protein analysis, contrasting with genomics (DNA) and transcriptomics (mRNA), which primarily elucidate genetic variations and gene expression profiles.[103] A significant challenge in proteomics is the dynamic range of protein concentrations. For example, in blood or skeletal muscle tissue, a few proteins such as albumin or myosin heavy chain isoforms (MYH) constitute a large amount of the total protein mass.

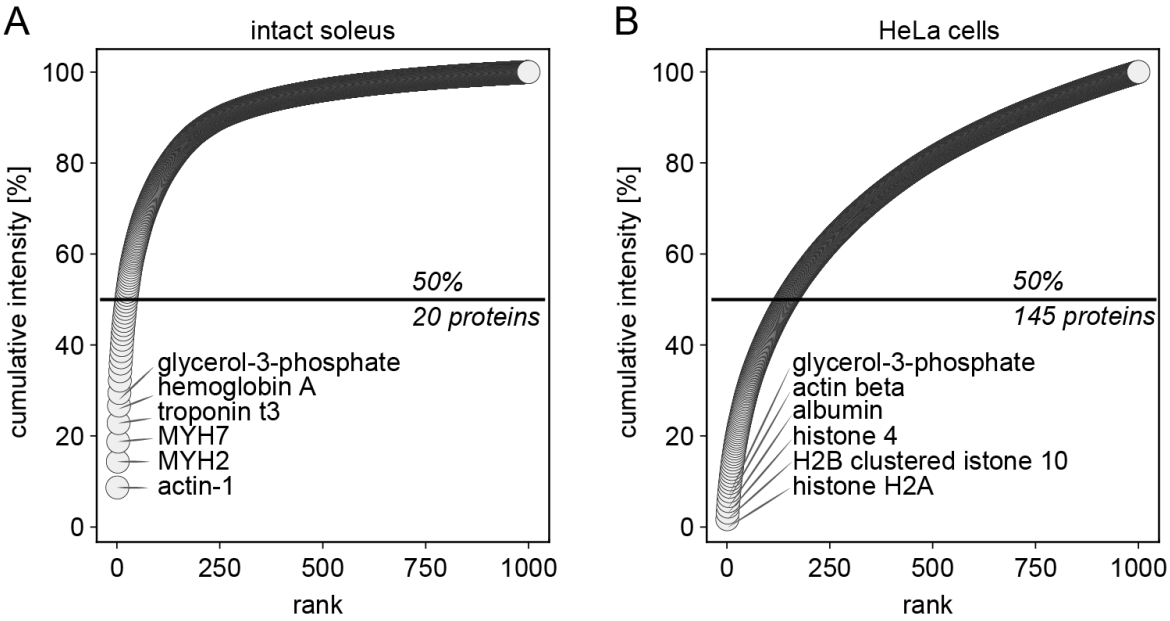

Figure 8 Dynamic range in intact soleus muscle, soleus muscle fiber, and HeLa cells. A, B) Cumulative intensity of the first 1,000 proteins identified with LC-MSMS ranked by intensity in intact soleus tissue (**A**) and HeLa cell lysate (**B**).

In intact muscle tissue (**Figure 8A**), the 20 most abundant proteins account for 50% of the total intensity. In stark contrast, the protein ranking revealed that in HeLa cell lysates 145 proteins contribute to the top 50% of all proteins (**Figure 8B**). In muscle tissue, the most abundant proteins include MYH isoforms, actin-1, troponins, and tropomyosins, while in HeLa cells, histone isoforms dominate the protein composition.

The requirement for substantial peptide input (standard MS instrument 200-500 ng) and the relatively low throughput of proteomic analyses presents bottlenecks for low-input and large-scale studies. Recent advancements in LC and MS instrumentation have significantly enhanced analytical capabilities, including speed and sensitivity. The EvoSep LC system, featuring partial elution and minimal gradient overhead, markedly increases high-throughput sample measurements. The timsTOF MS represents a cutting-edge instrument combining time-of-flight (TOF) mass spectrometry with trapped ion mobility spectrometry (TIMS). This hybrid technology provides enhanced resolution and enables the in-depth analysis of complex biological samples. The incorporation of TIMS facilitates four-dimensional separation including LC, MS, MS/MS and CSA. The TIMS device can accumulate and concentrate ions based on their m/z and mobility, enhancing peak capacity and confidence in compound characterization. This process, termed parallel accumulation serial fragmentation (PASEF), involves ion accumulation in the initial part of the dual TIMS device, followed by sequential ion release according to their ion mobility.[104]

1.5.2. Proteomic analysis of pre-diabetic skeletal muscle tissue revealed only minor changes in fatty acid metabolism

Numerous studies have investigated skeletal muscle alterations due to disease, exercise, or aging in both human and animal models. For instance, Giebelstein et al. reported increased glycolytic enzyme levels and mitochondrial protein changes in insulin-resistant humans.[105] Proteomic analysis on skeletal muscle of the db/db genetic diabetic mice models, were so far not reported, but administration of a high-fat diet (HFD) for 20 weeks, skeletal muscles showed a modest response with 56 differently expressed proteins. Affected pathways were fatty acid metabolism, including beta-oxidation in these obesity mouse model.[106] Similar pathways were involved in the type 2 diabetes *ob/ob* mouse model. Ob/Ob mice show increased body weight, more slow fibers and an increase in mitochondria content in skeletal muscle tissue.[107] Experiments on exercised and aged skeletal muscle have shown that non-contractile proteins in skeletal muscle are predominantly affected. In addition, skeletal

muscle has been analyzed using LC-MS/MS by chromatographic fractionation techniques of intact skeletal muscle samples to decrease complexity or applying long LC-MS gradients of more than two hours.[105, 108, 109] Although these studies highlight metabolic changes in the intact skeletal muscle, they often lack insights into the individual fiber type composition and the activity of the individual fiber types under disease related conditions. A more focused view of the skeletal muscles was achieved by analyzing individual muscle fibers.[108] So far, single muscle fibers have been studied using either long LC-MS gradients exceeding 60 min or very short 5-min LC-MS gradients.[108, 110] Although long LC-MS gradients result in higher numbers of proteins hits, the disadvantage is the limited number of samples which can be measured in a reasonable time period. Therefore, a high throughput fiber type analysis can only be realized with short LC-MS gradients.

Despite several studies on skeletal muscle cell populations, like myofibers[108], MuSC[111], and FAPs[112], there is still a need for spatial proteomics to decipher skeletal muscle protein localization and the analysis of intact ECM structures.

1.6. Aims of this thesis

Although several skeletal muscle proteomics studies have been performed, a spatial skeletal muscle proteome has not yet been established. This work includes the publications and manuscripts for protocols to characterize longitudinal protein profiles of the soleus skeletal muscle and diaphragm. The aim of these profiling studies was to spatially characterize skeletal muscle fibers, the MTJ, NMJ and tendon regions. In addition, this work focuses on the development of short LC-MS gradients for the mass spectrometric analysis of individual skeletal muscle fibers. The aim was to perform a large-scale analysis of single skeletal muscle fibers from mice treated with a normal and high-fat diet (HFD).

Publication (I): While the intact muscle and the individual cell populations were already intensively studied, spatial protein profiling of the skeletal muscle is still lacking. In particular, ECM structures like the MTJ were so far only isolated based on their morphological features. Here, we used the mouse soleus skeletal muscle and performed thin cryosections and to analyze each individual slice via short LC-MS Gradients. By bioinformatic analysis more than 3000 protein profiles were generated and 206 novel MTJ candidates were detected. Additionally, we aimed to spatially characterize the MTJ using network analysis and other bioinformatic approaches.

Preprint Publication/in revision (II): Since we have shown in **Publication (I)** the use of the generation of protein profiles for the spatial characterization, we aimed to generate a standardized protocol that can be transferred to other tissues like brain, kidney, or skin. Additionally, we detailed the bioinformatic approach of using sliding windows for imputation and the distance-based network analysis.

Prepared manuscript (III): Here, we used the diaphragm to generate longitudinal protein profiles to monitor proteins associated to the formation of the NMJ. In addition to wildtype animals, we also used aged mice and a TDP43-dependent ALS model to visualize changes in the NMJ structure. Comparing the area under the curve of the NMJ of aged mice and using a distance-based network analysis, we could show a broadening of the NMJ as well as a loss of connectivity between the core NMJ proteins during aging and in the ALS model.

Prepared manuscript (IV): Metabolic changes that come along with obesity are well studied on intact skeletal muscle tissue. Here, we are focusing on specific fiber types and their adaptation during the administration of an HFD for 16 weeks. The aim of this study is to understand how different fiber types switch their MYH isoform expression and metabolic

activity. Therefore, we compared normal and HFD treated skeletal muscle fibers of the soleus skeletal muscle by LC-MS analysis. Because of a high heterogeneity of fiber types within a skeletal muscle, we extended the MYH-based classification method to a broader panel of ~50 fiber type-specific proteins. For the mitochondrial protein MTFP1, we observed a lower intensity in peripheral regions of type IIa skeletal fibers treated with an HFD compared to control fibers. This could indicate an imbalance of mitochondrial fission and fusion after HFD.

Preprint Publication/in revision (V): Similar to obesity and aging, bed rest or reduced mobility has a great impact on the skeletal muscle performance and induces muscle loss. As an exception we wanted to study hibernating animals like the brown bear to decipher protective mechanisms to reduce muscle loss over their winter rest. Therefore, we analyzed single muscle fiber of bears in active and hibernating states via LC-MSMS, IHC, EM, and complemented with biochemical approaches like ATPase chase assays. Here, we observe a reduction of ATPase activity in skeletal muscle myosin, suggesting a new energy saving mechanism during extreme situations. These results further indicate a role of myosin ATPase activity in other conditions of muscle wasting, particularly those affected by major modulations of muscle metabolism.

2. Results

2.1. Publication (I): Spatial proteomics of skeletal muscle using thin cryosections reveals metabolic adaptation at the muscle-tendon transition zone

Luisa Schmidt[1], Michael Saynisch[1], Christian Hoegsbjerg[2], Andreas Schmidt[3], Abigail Mackey[2], Jan-Wilm Lackmann[1], Stefan Müller[1], Manuel Koch[4], Bent Brachvogel[5], Michael Kjaer[2], Philipp Antczak[1, 6, $], Marcus Krüger[1, 6, $]

[1] Institute for Genetics, Cologne Excellence Cluster on Cellular Stress Responses in Aging-Associated Diseases (CECAD), Cologne, Germany
[2] Institute of Sports Medicine Copenhagen, Department of Orthopedic Surgery, Copenhagen University Hospital - Bispebjerg and Frederiksberg, Copenhagen, Denmark (Part of IOC Research Center Copenhagen) and Department of Clinical Medicine, Faculty of Health and Medical Sciences, University of Copenhagen, Denmark
[3] Bruker Daltonics GmbH & Co. KG, Bremen, Germany
[4] Institute for Dental Research and Oral Musculoskeletal Biology, Center for Biochemistry, Medical Faculty, University of Cologne, Cologne, Germany
[5] Department of Pediatrics and Adolescent Medicine, Experimental Neonatology, Medical Faculty, University of Cologne, Cologne, Germany and Center for Biochemistry, Medical Faculty, University of Cologne, Cologne, Germany.
[6] Center for Molecular Medicine (CMMC), University of Cologne, 50931 Cologne, Germany
$ Correspondence: PA Philipp Antczak (pantczak@uni-koeln.de) and MK Marcus Krüger (marcus.krueger@uni-koeln.de)
Lead Contact: Marcus Krüger, marcus.krueger@uni-koeln.de

Published as Resource Article in Cell Reports, 2024

2.1.1. Summary publication I

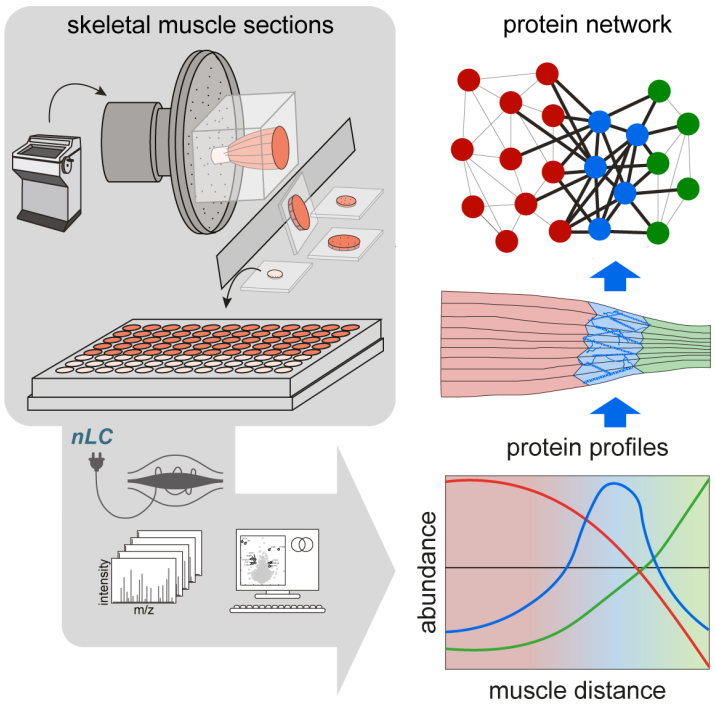

Figure 9 Graphical abstract publication I. The workflow to acquire protein profiles over the skeletal muscle starts with cutting thin cryotome sections of embedded muscles placing them into a 96-well plate. The samples are prepared for orbitrap LC-MS analysis followed by intensive bioinformatic analysis to generate ascending and descending protein profiles and profiles exhibiting a central maximum revealing MTJ proteins. The protein profiles resolved an extensive MTJ network validated by a generated distance-based network analysis.

LC-MS, liquid-chromatography-mass spectrometry; *m/z*, mass/charge.

Morphological studies of skeletal muscle tissue typically focus on the architecture of muscle fibers, surrounding cells, and the extracellular matrix (ECM). However, a comprehensive spatial proteomics analysis, especially of the muscle-tendon transition zone, has been missing. In this study, we prepared cryotome sections of the mouse soleus muscle and analyzed each slice using short LC-MS gradients. This approach generated 3,000 high-resolution protein profiles, which served as the basis for a network analysis to uncover the complex architecture of the muscle-tendon junction (**Figure 9**). Our findings revealed that certain protein profiles increased from muscle to tendon, including those related to neuronal activity, fatty acid biosynthesis, and the renin-angiotensin system (RAS). Notably, blocking the RAS in cultured mouse tenocytes using losartan led to a reduction in ECM synthesis.

Overall, our spatial proteome analysis of thin cryotome sections of skeletal muscle highlighted the role of the RAS as an additional regulator of the matrix within muscle-tendon junctions.

2.1.2. My contribution to publication I

My contribution as first author of the paper included the isolation, preparation, sectioning, and digestion of the muscles. Together with Andreas Schmidt, Jan-Wilm Lackmann, and Stefan Müller, we optimized the MS instrumentation and method set up as well as ensured stable data acquisition. Implementation of the bioinformatic analysis workflow and distance-based network analysis was performed by me and Philipp Antczak. Immunohistochemistry staining, imaging, and figure preparation of longitudinal muscle sections were performed by Christian Hoegsbjerg, Abigail Mackey, and Michael Kjaer. Tenocytes were kindly gifted by Gil Oreff and Florien Jenner and maintained, treated, and harvested by Michael Saynisch. MS sample preparation and phosphorylated peptide enrichment was performed by me. I assembled all figures, handled the revision process, and assisted Marcus Krüger in writing the manuscript.

2.1.3. Introduction

The mouse is one of the most widely used animal models to study musculoskeletal systems under normal and disease-related conditions. To handle the high tensile forces and loads, skeletal muscles have developed a specialized extracellular matrix (ECM) that surrounds and stabilizes contractile muscle fibers.[113] The myotendinous junction (MTJ), a junction area between the tips of muscle fibers and tendons that transmits muscle force to the bone, is another spatially defined region of skeletal muscle.[114] Earlier anatomical studies showed that the MTJ consists of interacting tendon fibers and terminal myocytes that form finger-like structures, resulting in strong bonds between tendons and muscle fibers. However, the MTJ is the weakest part of the muscle-tendon-bone axis, and a high muscle load often leads to injuries of the MTJ in humans. [115] Another interesting feature of the MTJ is its neuronal innervation and the presence of pain receptors. Neuronal sensory units within the MTJ, such as the Golgi tendon organs, may also play a role in muscle and tendon regeneration processes.[116]

At the molecular level, the MTJ exhibits specific protein expression patterns compared to neighboring muscle and tendon areas. For example, some proteins—including xin-actin binding repeat protein 2 (XIRP2), the FACIT collagen type XXII (COL22), and tenascin c (TNC) are enriched at the MTJ.[41, 43, 117]

So far, several quantitative proteomics studies have demonstrated a specific protein expression pattern of the MTJ in mouse[118], horse[119] and human samples.[42, 43] In particular, analysis of human semitendinosus muscle-tendon samples revealed approximately 112 proteins are enriched in the MTJ, including COL22, tetraspanin-24 (CD151), and the cartilage intermediate layer protein 1 (CILP1).[43] The separation of muscle, MTJ, and tendon regions based on morphological features has provided a comprehensive overview of protein expression; however, unbiased spatial mapping of skeletal muscle fibers and associated tendons has not yet been conducted.

Since the sensitivity of mass spectrometers has improved significantly in recent years, it is now possible to analyze proteins in samples with low protein concentrations. For example, sensitive mass spectrometers identified more than 1000 proteins from individual muscle fibers of humans[120] and mice[121, 122].

In this study, we aimed to develop a method for high-resolution mapping of proteins in skeletal muscle fibers, the MTJ, and tendons. We isolated the soleus muscle from the mouse hind leg and analyzed single thin cryosections with a thickness of 20 µm using short LC-MS gradients to generate a spatial protein profile along the longitudinal muscle fiber-tendon axis. On average, we detected ~2000 proteins per cryo slice by LC-MS and identified more than 7200 proteins in the whole dataset. Based on the 3000 spatial protein profiles generated, we created a complex protein network and demonstrated increased network connectivity within the MTJ transition zone. We discovered that the expression of the renin-angiotensin system (RAS), which is involved in blood pressure regulation and modulation of the extracellular matrix, is significantly elevated in the MTJ and adjacent tendon areas compared to muscle. This is an unbiased approach to study the protein patterns within skeletal muscle and we demonstrate the high sensitivity of our workflow by detecting multiple transcription factors, signaling molecules, and matrix proteins.

2.1.4. Results

2.1.4.1. Manual dissection of soleus skeletal muscle based on morphological features only partially identifies the myotendinous junction (MTJ)

First, we isolated soleus muscles (n = 4) from the hind leg of mice and dissected the muscle based on macroscopic features into three parts: central muscle, muscle-tendon, and tendon (**Figure 10A and S1A-C**). In total, we identified 4120 protein groups with a false discovery rate (FDR) below 1% at the protein and peptide level. Comparison of all three parts revealed 3164 common proteins and 252 proteins with restricted protein expression in tendons (**Figure 10B and S1D**; **Table S1**). Principal component analysis of the soleus showed clear separation between the tendon and muscle samples, whereas the MTJ and muscle samples were barely separated (**Figure 10C**). Hierarchical clustering and gene ontology (GO) analysis of 896 significant proteins (ANOVA) also revealed enhanced expression of matrix proteins in the tendon compared to the muscle and MTJ samples (**Figures S1E and S1F)**. In total, we identified 1260 significantly altered proteins between the MTJ and tendon (**Figures S1G-I and Table S1**). However, a volcano plot showed no significant outliers between the MTJ and muscle samples (**Figure S1J**). Thus, we conclude that manual dissection of muscle, MTJ, and tendon areas is helpful but does not enable clear delineation of the MTJ and muscle tissue. Therefore, there is a need for an unbiased method to spatially analyze the muscle-tendon transition.

2.1.4.2. Study design, quality control, and optimization of protein identification rates from thin cryotome sections using short LC-MS gradients

To map protein expression along the longitudinal muscle-tendon area, we cryo-embedded soleus muscles and prepared consecutive cross-sections from the central to distal areas using a cryotome (**Figure 10D**). The distal (tendon) slices have an area of less than ~0.2 mm^2 and yield less than 1 µg protein (**Figures S2A-C)**; therefore, we first tested comparable amounts of protein from muscle lysates using different lengths of LC-MS gradients combined with a 15 cm reverse-phase column. Approximately 1900 protein hits were achieved with 100 ng input and 30 min LC-MS gradients (**Figures S2D-G)**. We also used 100 ng HeLa cell lysates as control and identified ~5000 proteins (**Figures S2H-K**). Finally, we measured central and distal muscle slices with thicknesses of 10–30 µm and detected an average of ~2000 proteins per 20-µm-thick slice (**Figures S2L and S2M**).

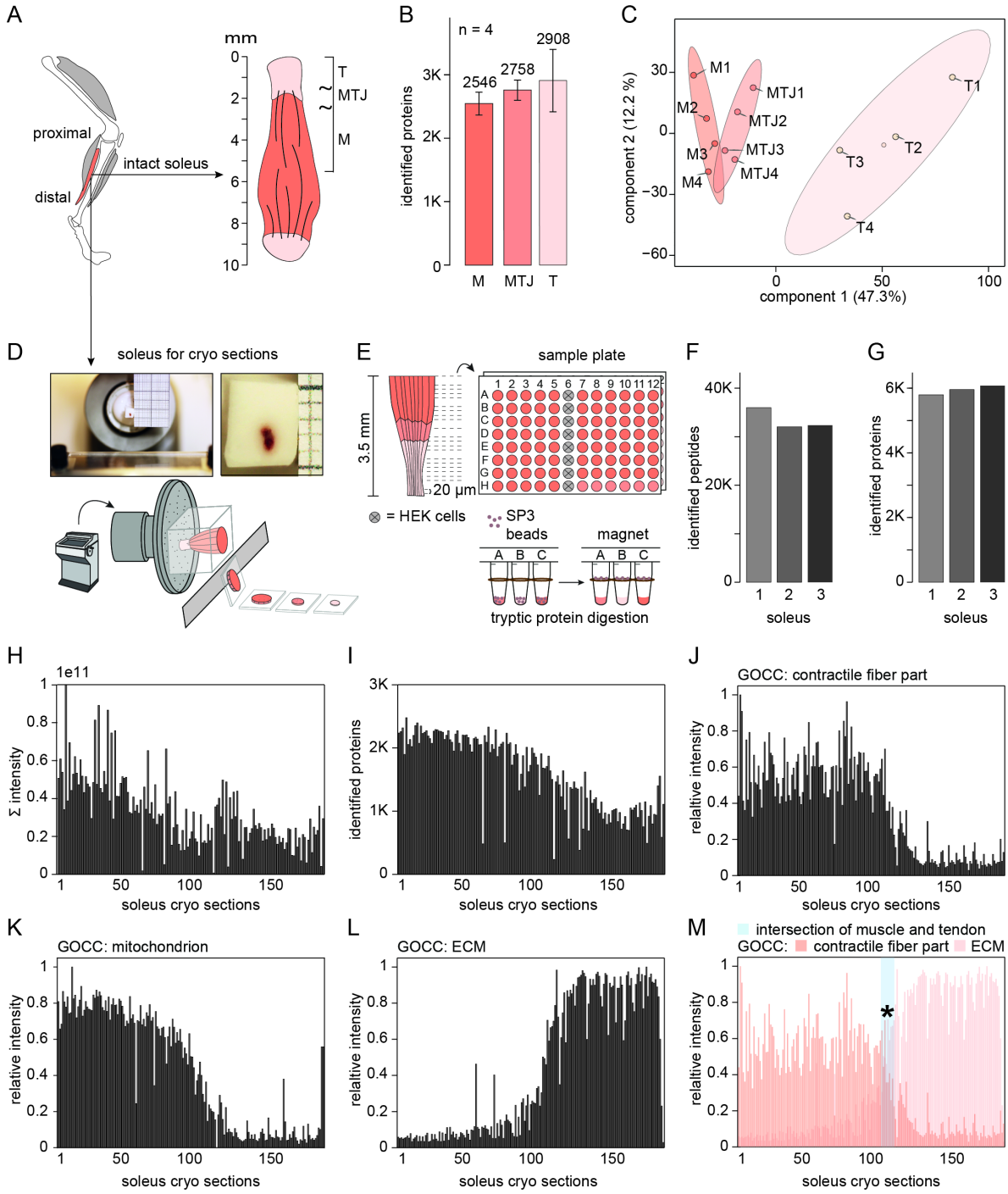

Figure 10 Distinct protein profiles along the longitudinal muscle-tendon axis. A) Overview of the soleus muscles and the position in the hindlimb with indicated areas of muscle, MTJ and tendon. **B**) Average number of proteins ± SEM identified from manually dissected skeletal muscle, MTJ, and tendon areas of the soleus (*n* = 4). **C**) Principal component analysis of protein expression patterns from manually dissected muscle, MTJ, and tendon samples. **D-E**) Overview of the experimental workflow. **F**) Identified precursors and **G**) proteins in the three profiling experiments (*n* = 3 muscles). H-M) Bar plots for the sectioned soleus samples, starting from the left side section 1 (central muscle area) to right side section 175 (tendon area), showing **H**) sum intensity of identified proteins, **I**) number of proteins identified per section, **J**) relative intensity of gene ontology terms enriched in contractile fiber part, **K**) mitochondria, and **L**) ECM and **M**) an overlay of the relative intensity of the contractile fiber part and ECM GO terms. ECM: extracellular matrix, GOCC: gene ontology cellular component, M: muscle, MTJ: myotendinous junction, SP3: single-pot solid-phase sample-preparation, T: tendon. Blue line indicates the muscle-tendon transition.

2.1.4.3. Protein normalization and implementation of missing values to generate complete protein profiles

We prepared approximately 175 20 µm-thick cryotome slices, representing a total length of around 3.5 mm of tissue, covering the area between the central muscle and the proximal tendon areas (**Figure S1A**, upper part). Single cryotome slices were transferred to 96-well-plates and subjected to tryptic digestion according to the SP3 protocol (**Figure 10E**).[123] To ensure high data completeness, we chose a data-independent acquisition (DIA) approach and identified an average of ~6000 proteins per muscle profile (n = 3 muscles; **Figure 9F** and **1G**). As a control, we used HEK293T cell lysates and identified ~4000 proteins, demonstrating constant instrument performance and high technical reproducibility during the MS analysis period of ~11 days (**Figure 10E,** column 6 and **S3A).** In addition, we observed virtually no carry-over of contractile MYH peptides in blank runs **(Figure S3B)** and the peptide retention times were monitored by adding non-naturally occurring peptides (**Figures S3C and S3D**).[124] To obtain reliable protein profiles, we filtered the generated datasets for proteins that were identified based on at least two peptides and protein intensities > 10^4 and each protein had to be detected in at least two out of the three biological replicates (**Figure S3E**).

As the muscle and tendon slices exhibited different protein intensities (**Figure 10H** and **1I**), we normalized the data by dividing the individual protein intensities by the sum of the protein intensity per slice and performed z-score normalization. As an example, we plotted the intensities of tenascin C (TNC), alcohol dehydrogenase 1 (ADH1), and myosin heavy chain 2 (MYH2) before and after normalization (Figures S4A-C). Although the DIA approach leads to a high degree of data completeness, we observed missing intensities for proteins with low abundances and for proteins that have restricted expression in muscle or tendon. Hence, to generate a complete protein profile, we used sliding windows covering adjacent sections to fill in the missing protein intensities. When we detected a missing protein intensity on a section, we selected the protein intensities of the same protein from the 10 sections before and 10 sections after the missing value and used a linear model to impute the protein intensity for that section (**Figure S4D**). For proteins that were only found in the muscle and not in the tendon, the protein intensities of the lowest 5% of all protein intensities in the dataset were used to replace the missing values in the tendon sections (**Figure S4E**). To include proteins with local expression in our profiling dataset, we accepted profiles that had at least 70% data completeness in a range of 200 µm from the total length of 3500 µm (**Table S2**).

We observed a slight profile shift between the three muscles, indicating different starting points for the sections within the central muscle areas or a slight variation in muscle size. To obtain congruent protein profiles across the three solei, we first calculated the probability distribution for every protein in each experiment using a bootstrap analysis. Based on this analysis, each protein profile was correlated to the same randomized sample set to exclude any bias, variances, and predicted errors. Every protein that had a probability distribution with a d-score higher than 5 was selected as a protein with a significantly increasing or decreasing intensity profile from muscle to distal (tendon) end.[125] Using these proteins, we then calculated the offset and performed a shift for all other profiles (**Figure S4F**). Finally, all profiles were combined using locally estimated scatter smoothing (LOESS) to obtain a representative profile for each individual protein (**Figure S4G**). In total, we generated ~3000 protein profiles from three independent soleus muscles (**Table S2**).

2.1.4.4. Protein profiles of sarcomeric and matrix proteins reflect the position of the MTJ in the muscle

The protein profiles were assessed using systematic gene ontology term (GO) analysis. As expected, we mainly observed GO terms associated with components of contractile fibers and mitochondria in the central muscle areas (**Figure 10J** and **1K**), while the tendon area showed enrichment of terms connected to ECM organization (**Figure 10L**). Since we observed an intersection between contractile and matrix proteins at the junction between the muscle and tendon, we suggest that this intersection may represent the MTJ (**Figure 10M,** blue line). A heatmap of the enriched GO terms also substantiated the distinct biological functions of the muscle and tendon (**Figures S5A-D**). To demonstrate how protein expression profiles change along the muscle-tendon axis, we plotted the z-score normalized protein profiles of sarcomeric (**Figure 11A**), Ca^{2+} handling (**Figure 11B)**, and mitochondrial proteins (**Figure S6A**). These proteins show high expression in central muscle areas and steadily decrease in the transition zone between muscle and tendon, indicating the end of the muscle fiber unit. Conversely, the most abundant matrix proteins, including collagen 1 (COL1A1), chondroadherin (CHAD), and tenascin c (TNC) showed a marked increase in expression towards the proximal end of the skeletal muscle, reflecting the start of the tendon area (**Figure 11C** and **2D**).

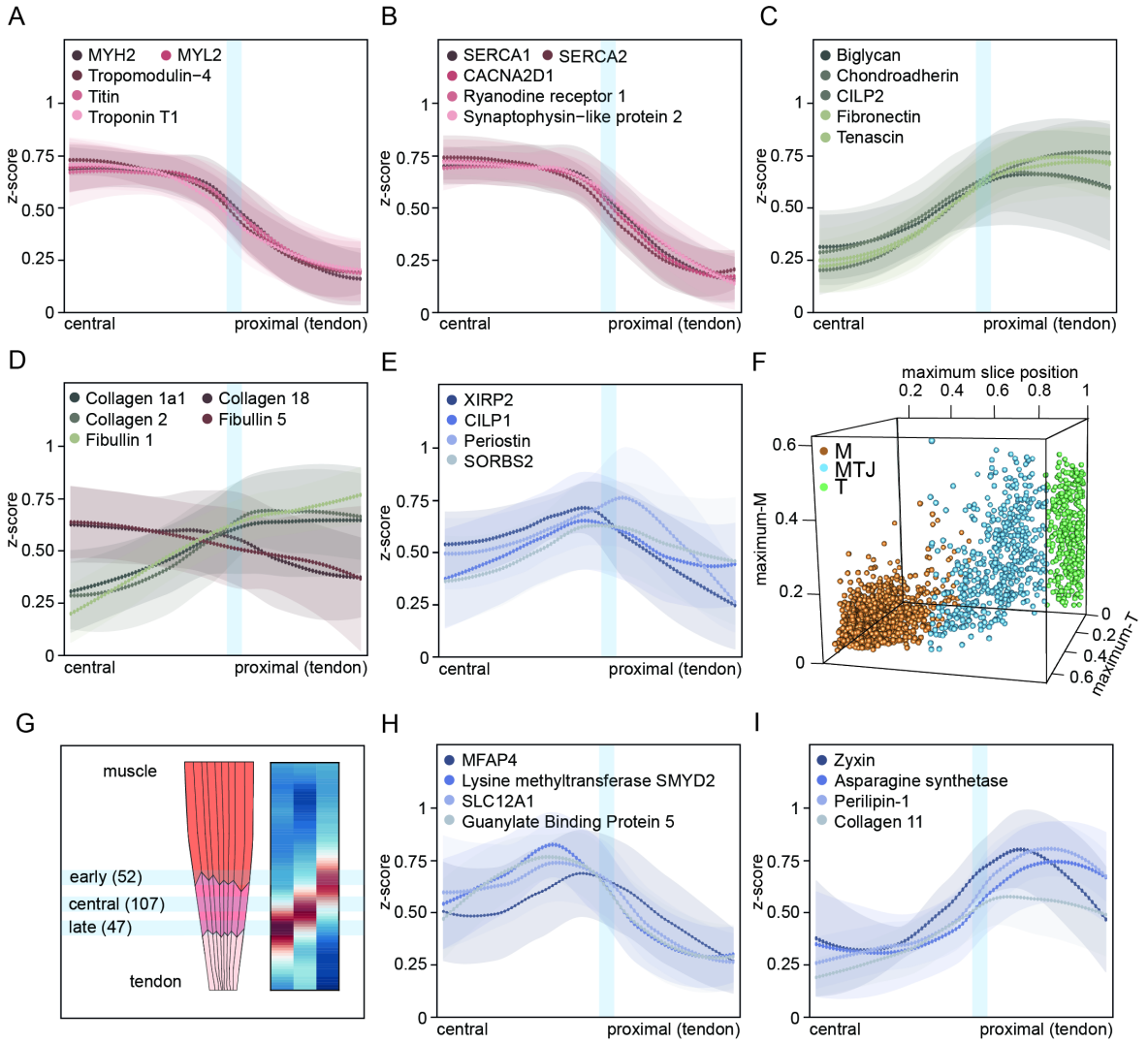

Figure 11 Proteomic profiling of soleus muscles reveals additional MTJ marker proteins. A-E) Protein expression profiles along the longitudinal muscle-tendon axis of **A)** selected sarcomeric proteins, **B)** selected calcium housekeeping proteins, **C, D)** selected ECM proteins, and **E)** selected MTJ proteins. **F**) 3-Dimensional plot of proteins localized at muscle, MTJ, and tendon areas. Each dot represents the maximum of one protein profile. The *x*-, *y*-, and *z*-axes show the spatial orientation of the maxima of the protein profiles in the muscle (orange), MTJ (blue), and tendon (green) area, and the differences in protein abundance between the maxima and the muscle and tendon. **G)** Summary of identified proteins with early, central, and late maxima in the MTJ area. **H)** Selected protein expression profiles with early and **I)** late maxima in the MTJ area. ECM: extracellular matrix, GOCC: Gene Ontology cellular component, M: muscle, MTJ: myotendinous junction, T: tendon. Blue line indicates the muscle-tendon transition.

In addition to the change in the muscle fiber-matrix ratios along the longitudinal axis, we also observed intracellular proteins with increasing profiles from muscle to tendon, possibly representing specific cell populations such as tenocytes, tendon-derived stem cells, or other fibroblasts.[126] For example, the detection of different isoforms of creatine kinase (CK) and filamins confirmed these cellular changes; we also observed high intensities of the muscle- and mitochondria-specific (CKM, CKMT2) isoforms in skeletal muscle, while the brain isoform (CKB) exhibited a reciprocal pattern (**Figure S6B**). Similarly, the filamin c (FLNC) isoform showed a similar decreasing profile from muscle to tendon, whereas filamin B (FLNB) increased towards the MTJ. Together, the isoform profiles of CK and filamins demonstrate the presence of different cell populations in the muscle and tendon areas.[127-129] Of note, the intersections of the CK and filamin isoform profiles with the GO terms for sarcomere and matrix proteins are congruent, supporting the suggested position of the MTJ. Selected protein profiles with constant protein abundances along the muscle-tendon axis, including collagen 4, are shown in **Figure S6C** as a control. Systematic k-means clustering revealed 10 clusters with 143 constant, 646 ascending, and 1850 descending protein profiles (**Figures S7A-J**). The large number of proteins with descending profiles reflects the high number of proteins in skeletal muscle fibers.

Next, we investigated the profiles of previously described MTJ proteins, including xin actin-binding repeat-containing protein 2 (XIRP2), periostin (POSTN), cartilage intermediate layer protein (CILP), and SORBS2.[118, 130] These MTJ candidates exhibited maximum intensities at the interface between muscle and matrix proteins (blue line), which further substantiates the position of the MTJ (**Figure 11E**). For example, the profiles of XIRP2 and CILP1 showed increased intensities in ~13 slices, corresponding to a distance of ~260 µm. To systematically identify potential MTJ proteins in our dataset, we determined the profile maximum for each protein and subtracted the average intensity of the same protein in muscle and tendon slices. Proteins with a ≥ 1.5-fold increase in their maximum intensity in the MTJ compared to the average intensity in muscle and tendon were categorized as potential MTJ proteins. Three-dimensional plotting of all protein maxima and slice positions illustrated the distribution of the muscle, MTJ, and tendon proteins (**Figure 11F)**. The separation of the different muscle areas was additionally visualized by PCA of three muscle profiles (**Figures S8A-C**). Using this approach, we identified 206 proteins with maximum intensities around the central

MTJ (**Table S2**), including 52 protein profiles with early maxima, 107 protein profiles with central maxima, and 47 protein profiles with late maxima at the MTJ (**Figure 11G**).

Comparison of the 206 MTJ protein profiles generated from analysis of the soleus sections and our analysis of the manually dissected M, MTJ, and T samples (**Figure 10**) revealed a congruent pattern for six proteins (**Figure S10A**). We detected an overlap on either the muscle or tendon side for 93 proteins and 107 proteins were only partially or not detectable in the intact muscle samples compared to our protein profiling. This demonstrates the high sensitivity of our profiling approach and significantly expands the catalogue of potential MTJ proteins. One example of a potential early MTJ protein is extracellular microfibril-associated glycoprotein 4 (MFAP4), which binds to collagen in elastic fiber-rich regions (**Figure 11H**). A study of protein expression profiles in human muscle across the lifespan found that MFAP4 is one of the most underrepresented proteins during aging.[131] Therefore, the expression of MFAP4 within the MTJ might be involved in the correct arrangement of elastic fibers and stabilize the transition zone. Another protein with an early maximum is the lysine methyltransferase SMYD2, which methylates chaperones outside the nucleus and interacts with myosin heavy chains and titin.[132,133] Whether the increased expression of SMYD2 at the MTJ also contributes to the stability of the compound by methylating chaperones and/or sarcomere-associated proteins remains unclear and needs to be investigated in future experiments. MTJ protein profiles with late maxima include collagen 11 and the focal adhesion protein zyxin (**Figure 10I**). Next, we performed immunostaining of longitudinal sections of mouse soleus muscles with anti-MYH pan, anti-collagen 22, and anti-tenascin C antibodies, which substantiated the location of the muscle, MTJ, and tendon area, respectively (**Figure 12A**). Similarly, to COL22, the MTJ marker protein periostin also localized at the MTJ (**Figure 12B**). The spatially restricted expression of COL11 within the muscle-tendon transition zone is shown in **Figure 12C**. Other proteins with transient maxima at the MTJ that have not previously been described include immunoglobulin superfamily member 8 (IGSF8), myosin light chain kinase, and smooth muscle (MYLK) **(Figure 13A)**. Furthermore, we detected several proteins with ascending protein expression profiles from the muscle to tendon, including the clock gene BMAL2 and the secreted protein *connective tissue growth factor* (CTGF, also known as CCN2) (**Figure 13B**).[134]

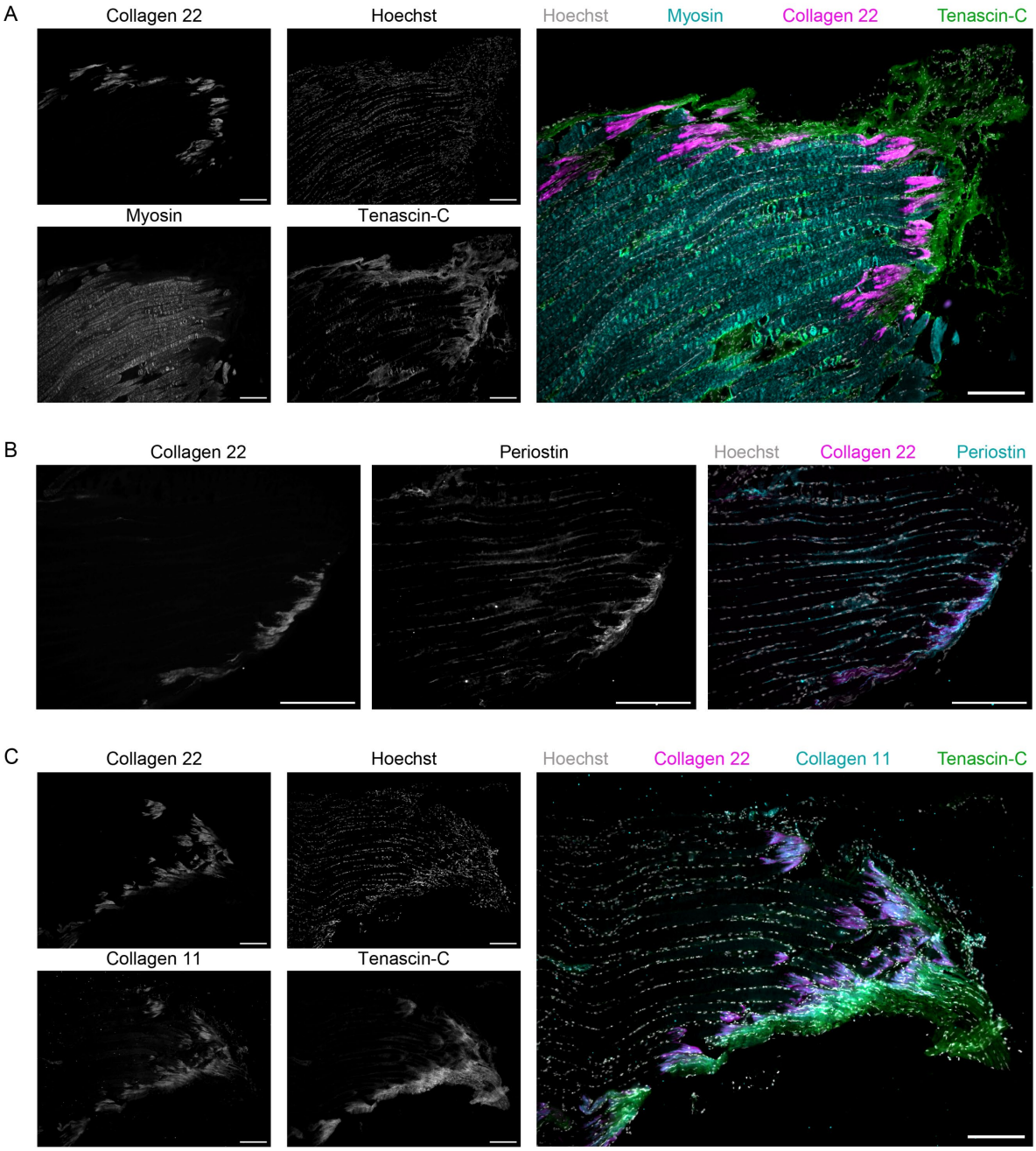

Figure 12 Microscope images and immunostaining of potential MTJ candidates. Immunostaining of collagen 22, MYH, tenascin-C**, A)** periostin **B),** and collagen 11 **C)** in longitudinal mouse soleus sections. Muscle is stained using MYH and tendon is stained using tenascin-C. Collagen 22 is used as MTJ marker. Periostin and collagen 11 staining overlap with Collagen 22 staining. Two biological replicates were performed for each staining. Scale bar = 200 µm. MTJ: myotendinous junction, MYH: myosin heavy chain.

Integrins are cell adhesion receptors that bind extracellular matrix proteins, such as collagen, laminin, and fibronectin. We found enhanced levels of integrin ITGα11 and ITGβ4 in the tendon area (**Figure S6D**). We also observed constant or descending profiles for the detected laminin isoforms (laminin α2, α4, α5, β1, β2, and basal cell adhesion molecule (BCAM) from muscle to tendon (**Figures S6E and S6F-H)**. Interestingly, neuronal marker proteins such as neurofilaments (NEFL) and myelin proteins (MBP, MPZ, MAG) showed biphasic profiles, with high levels in the central muscle sections and second maxima at the MTJ (**Figure 13C**). The dyslexia-associated KIAA0319-like protein also exhibited a similar profile as the neuronal marker proteins. KIAA03191-like protein is known to be involved in brain development and neuronal migration.[135 136] Overall, our protein profiling demonstrates a heterogeneous profile of membrane, adhesion, and matrix proteins along the longitudinal muscle-tendon axis[116, 130] and highlights the distinct cellular composition along the longitudinal muscle-tendon axis.

2.1.4.5. The MTJ and tendon areas show increased abundances of enzymes related to *de novo* fatty acid synthesis and the renin-angiotensin system (RAS)

Since skeletal muscle fibers contain high numbers of mitochondria, we also observed descending profiles for most mitochondrial proteins starting at the MTJ, reflecting the end of the skeletal muscle fiber unit (**Figure S6A**). Accordingly, similarly to mitochondrial proteins, we also detected descending profiles for 11 members of the SLC25 family, including SLC25A11 and SLC25A12 (**Figure 13D**). Solute carrier proteins (SLC25) transport molecules across mitochondrial membranes and are involved in a variety of cellular processes.[137] Interestingly, however, we observed increasing profiles from muscle to tendon for some mitochondrial proteins, such as the tricarboxylate transporter SLC25A1 (also known as CTP) (**Figure 13D**). This suggests a higher cytoplasmic content of citrate, which is used as the main carbon source for the biosynthesis of fatty acids, in the distal muscle-tendon area. It is important to note that a number of enzymes involved in the conversion of citrate to acetyl-CoA and fatty acids, such as ACLY, ACC, and FASN, were also upregulated in the MTJ and tendon compared to muscle areas (**Figure 13E and 4F**).

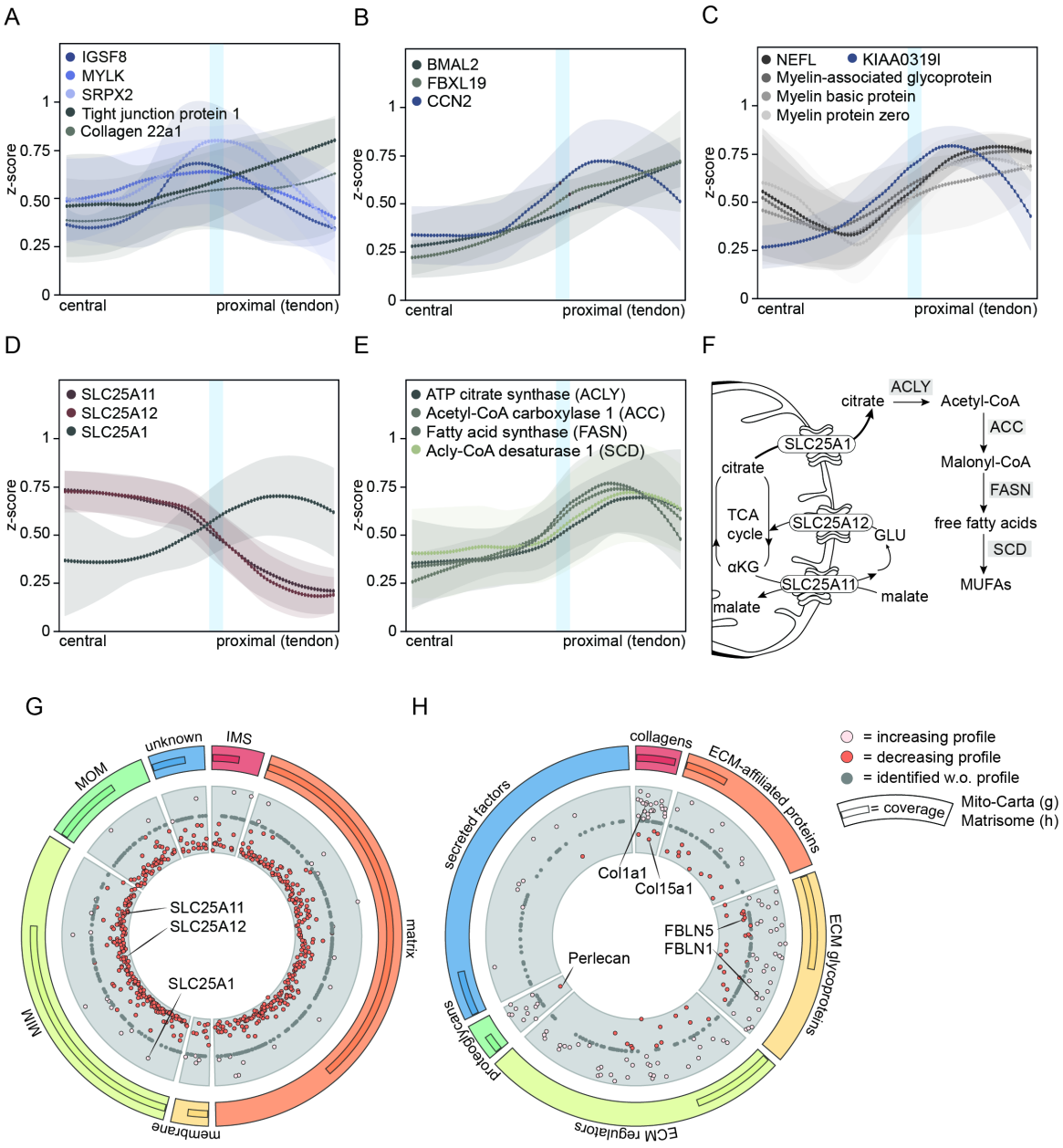

Figure 13 Protein expression profiles identify different pathways related to metabolic and neuronal activity along the longitudinal muscle-tendon axis. A, B) Protein expression profiles of proteins not previously described as MTJ markers and showing maximal protein intensities in the MTJ area. **C**) Selected protein expression profiles of neuronal factors showing biphasic profiles with maxima at the central muscle and distal MTJ-tendon areas. **D**) Mitochondrial solute carrier proteins of the SLC25A family exhibit descending (SLC25A11, SLC25A12) or ascending (SLC25A1) profiles. **E**) Protein expression profiles of selected members of the fatty acid synthesis pathway. **F**) Mitochondrial TCA cycle and fatty acid synthesis pathway. **G, H)** Hamilton plots of mitochondrial proteins and ECM proteins based on Mitocarta entries and the mouse matrisome.[138] Blue line indicates the muscle-tendon transition.

The solar protein expression profile plot of mitochondrial proteins highlights the enhanced abundance of SLC25A1 in tendons. In contrast, most mitochondrial proteins including members of the SLC25A family showed the opposite trend, suggesting that other cell populations, such as tenocytes, express this transporter more abundantly (**Figure 13G**). We also plotted and observed increased expression of annotated ECM proteins in the matrix compared to the muscle. Extracellular proteins that exhibited the opposite trend, such as Col15, Col18, fibulin 5, and perlecan, are shown in **Figure 13H and S6G**.

The renin-angiotensin system (RAS) is closely linked to blood pressure regulation. The angiotensin converting enzyme (ACE) and serine proteinase chymase 1 (CMA1) cleave the inactive peptide angiotensin I into active angiotensin II. Both of these enzymes showed strong ascending profiles from muscle to tendon (**Figure 14A**). Similarly, other RAS proteins, including the aminopeptidase N (ANPEP) and glutamyl aminopeptidase (ENPEP), also exhibited similar ascending profiles from muscle to tendon areas. Although we did not detect the TGFβ receptor and its downstream factors SMAD2/3, we observed elevated levels of EGFR, the transforming growth factor beta-1-induced transcript 1 protein (TGFβ1l1), and connective tissue growth factor (CTGF) in the tendon area compared to skeletal muscle (**Figure 14B**). In addition, comparison of intact muscle and tendon samples revealed increased expression of angiotensinogen (AGT), type-1 angiotensin II receptor-associated protein (AGTRAP), TGFβ1, and TGFβR3 in tendons (**Figure 14C** and **5D**). LC-MS analysis of immortalized mouse tenocyte cell lines substantiated the presence of several members of the RAS (**Figure 14E**). To examine the effect of a commonly used RAS inhibitor on tenocytes, we treated immortalized tenocytes with losartan for 1–4 days. We observed significant downregulation of ECM proteins after 4 days of treatment with low (10 µM) and higher doses (50 µM) of the inhibitor (**Figure 14F** and S**9A, Table S3**). To further elucidate activation of the RAS signaling pathways, we cultivated tenocytes with 10 µM losartan for 4h. Phosphopeptide enrichment revealed altered phosphorylation of known TGFβ pathway members, including CDK2 (pY15) and TGFβ1I1 (**Figures S9B** and **S9E-G**). Similarly, gene ontology analysis showed decreased phosphorylation of terms such as cellular response to growth and TGFβ stimulus (**Figures S9C** and **S9D**). This indicates that treatment with losartan inhibits the TGFβ and RAS signaling pathways in tenocytes and thereby alters the matrix.

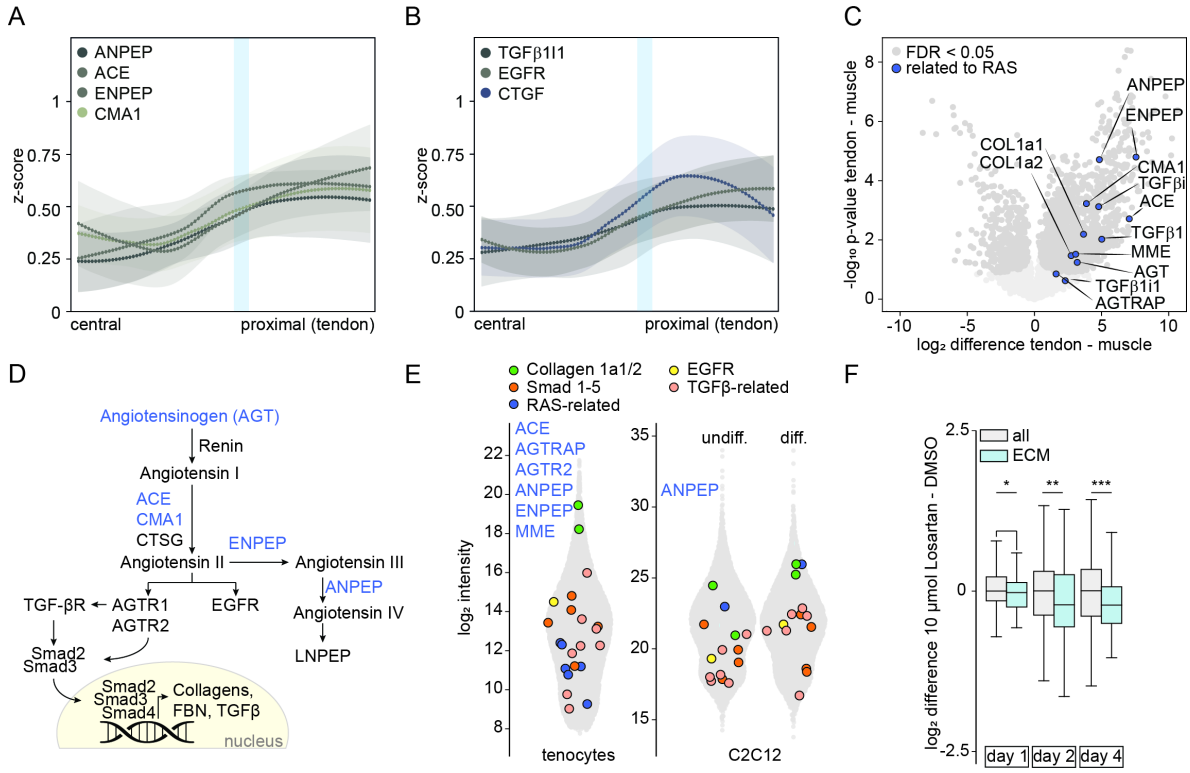

Figure 14 AGTR1 inhibitor reduces ECM proteins in isolated tenocytes. A, B) Protein expression profiles along the longitudinal muscle-tendon axis of ACE, ANPEP, CMA1, ENPEP (**A**), CTGF, EGFR, and TGFβ1l1 (**B**). **C**) Volcano plot of intact muscle and tendon samples reveals higher expression of the renin-angiotensin system (RAS)-related proteins in tendon. Differentially abundant proteins are highlighted in dark grey (Student's *t*-test: FDR < 0.05, s0 > 0.1) and RAS-related proteins in blue. **D**) Schematic overview of the RAS. Identified proteins are labelled in blue. **E**) Jitter plot of log_2 intensities of identified proteins in immortalized tenocytes and undifferentiated and differentiated C2C12 cells/myotubes. Identified proteins related to the RAS are labelled in blue. **F**) Box plot of immortalized tenocytes treated with 10 µm losartan, showing a decrease in ECM proteins. Data are represented as mean ± SEM. Asterisks denote significance (*T*-test: * < 0.05, ** < 0.01, *** < 0.001). ACE: Angiotensin-converting enzyme, ANPEP: alanyl aminopeptidase, CMA1: chymase 1, CTGF: connective tissue growth factor, ECM: extracellular matrix, EGFR: epidermal growth factor receptor, ENPEP: glutamyl aminopeptidase TGFβ1l1: transforming growth factor beta 1, RAS: Renin-Angiotensin System. Blue line indicates the muscle-tendon transition.

2.1.4.6. Network analysis of protein profiles along the muscle-tendon axis reveals the complex connectivity of the muscle-tendon junction

Since we identified ~3000 protein profiles within the soleus, we aimed to correlate the protein expression patterns to develop a soleus protein-protein connection network to better visualize the different areas of the soleus. We used the generated protein profiles to perform a delay analysis.[139, 140] Delay analysis was initially designed to identify the time delay between time-series profiles, i.e., the amount of time it takes for one feature to respond to the other. By shifting the time index of one of the features and repeating the correlation analysis, the time delay is then defined as the required shift in time to reach a maximum correlation.

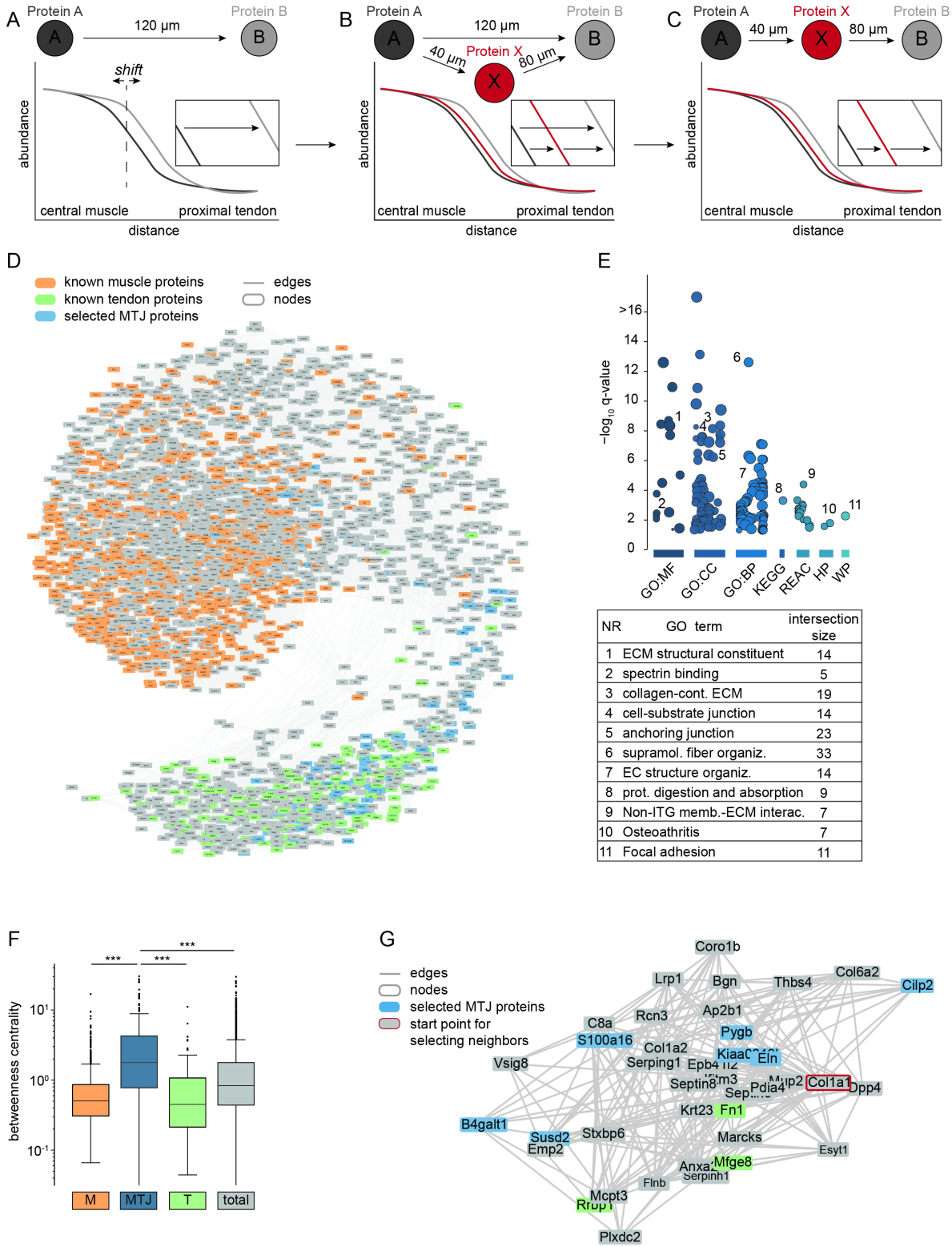

NR	GO term	intersection size
1	ECM structural constituent	14
2	spectrin binding	5
3	collagen-cont. ECM	19
4	cell-substrate junction	14
5	anchoring junction	23
6	supramol. fiber organiz.	33
7	EC structure organiz.	14
8	prot. digestion and absorption	9
9	Non-ITG memb.-ECM interac.	7
10	Osteoathritis	7
11	Focal adhesion	11

Figure 15 Spatial network analysis of the soleus muscle reveals higher connectivity at the MTJ area. A-C) Schematic workflow for creating a distance-based network using delay-analysis. **A**) The correlation between two protein profiles was calculated using distance as a variable. **B**) All correlations between two proteins were selected and added as connections. **C**) Connections with a distance shorter than 100 µm were used for visualization. **D**) Distance-based network generated using the protein expression profiles. Known muscle (orange), tendon (green), and potential MTJ (blue) proteins are marked. **E**) GO term analysis of MTJ proteins revealed enrichment of terms related to organization, binding, and junction. **F**) The betweenness score was significantly higher for the MTJ compared to muscle and tendon areas, indicating more connections between MTJ proteins than muscle and tendon proteins. Data are represented as mean ± SEM. Asterisks denote

significance (*T*-test: *** < 0.001). **G**) Direct protein connections in the network analysis using collagen 1 (COL1a1) as a starting point. GO: gene ontology, MTJ: myotendinous junction.

In our analysis, we replaced the time factor with the spatial arrangement of the slices to illustrate the distance within the muscle profile. Pairs of protein profiles were correlated, and the spatial delay to reach the maxima identified (**Figure 15A-C**). Those pairs with a delay of less than 100 µm were then subjected to a data processing inequality approach to remove indirect connections, i.e., links that occur as a result of sequential protein correlations. The resulting links between proteins were visualized using Cytoscape and arranged in a spring embedded layout. Mapping of known muscle (orange) and tendon proteins (green) enabled us to identify specific regions within the network that highlight the spatial organization of proteins (**Figure 15D** and interactive online version **https://medex.uber.space/networks/index.html#/**). Known MTJ proteins (*n*=10) and MTJ proteins identified in this study (*n*=196) localized to a specific region of the network (blue). Gene ontology term analysis of the MTJ network proteins for molecular function and cellular localization indicated enrichment of proteins associated with the terms ECM structural constituent, ECM structure organization, cell-substrate junction, and anchoring junction (**Figure 15E**). In addition, we observed a significantly higher betweenness centrality score for MTJ proteins compared to the muscle and tendon proteins, suggesting MTJ proteins are more interconnected than the proteins in the other areas (**Figure 15F**). As an example, we selected collagen 1 and observed biglycan and fibronectin 1 as direct neighbors with a correlation distance of less than 100 µm. Moreover, we observed several MTJ proteins with late maxima, including elastin, in proximity with collagen 1 (**Figure 15G**).

2.1.5. Discussion

Our comprehensive longitudinal protein profiling based on short LC-MS runs of single muscle sections allowed us to exactly localize the transition area between muscle and tendons in an unbiased manner and revealed 206 proteins have a local maximum at the MTJ. In addition, our protein network analysis shows that the MTJ has a higher level of connections compared with the muscle and tendon areas, supporting the function of the MTJ as a link between muscle fiber tips and tendon. We also observed that several members of the fatty acid synthesis pathway and RAS exhibit ascending profiles from muscle to tendons. In validation of these observations, treatment of isolated tenocytes with losartan reduced ECM protein secretion, which suggests that the RAS contributes to matrix formation within the MTJ and tendon.

In addition to the complex protein expression pattern of the MTJ, the anatomical arrangement of skeletal muscle fibers and tendons is also an important factor in muscle stability. Skeletal muscles with a bipennate shape, like the soleus, resemble a feather-like structure, with the fibers on either side of the tendon arranged at a specific angle. Manual dissection or separation of certain muscle areas such as the transition between muscle and tendon is therefore almost impossible. Our approach enabled us to determine the transition zone based on i) the intersection of GO terms for skeletal muscle and matrix proteins, ii) the profiles of specific isoforms, and iii) observation of maximal protein expression of several known MTJ marker proteins, including XIRP2 and CILP, at the intersection. Overall, the generated protein profiles clearly indicate the area of the MTJ and highlight the complex spatial architecture of the muscle and tendon regions.

2.1.5.1. Protein profiles of ECM proteins indicate tissue-specific adaptations of the matrix along the longitudinal muscle and tendon axis

Increasing profiles from muscle to tendon were observed for about 10% of all proteins identified in our dataset, and the identified proteins consist mainly of matrix proteins such as collagens, tenomodulin, and proteoglycans. Conversely, we also observed extracellular proteins exhibited the opposite trend, showing increased protein expression in muscle areas compared to tendons. For example, the basement laminin proteins LAMA2, LAMA4, and LAMA5, as well as the heparan sulphate proteoglycans perlecan and nidogen 1, were expressed at higher levels in central muscle areas compared with tendons. This reflects their function as basal lamina proteins that surround skeletal muscle fibers and interact with

collagen type IV (**Figure S6F**). In addition, higher signals for fibrillar collagen 11 were detected in the MTJ than in muscle and tendon; this finding has not been described previously. We suggest that the expression of collagen 11 at the MTJ could induce enhance fibrillogenesis and thus regulate the formation of tendon fibrils and mechanical stability at the MTJ.[141, 142]

Members of the fibulin (FBN) family are known interactors of collagens and are also involved in the organization, assembly, and stabilization of the ECM.[143] Similarly to several collagens, we observed an ascending profile from muscle to tendon for FBN1. In contrast, FBN5 was more abundant in muscle areas compared to tendon; thus, we hypothesize that FBN5 might be involved in cell adhesion and anchoring muscle fibers to the ECM through its interaction with other ECM proteins and cell surface receptors. There is also evidence to suggest that FBN5 may be involved in certain muscular dystrophies and muscle pathologies such as muscle fibrosis, a condition characterized by excessive accumulation of fibrous connective tissue in muscle.

Overall, our profiling demonstrates that muscle fibers and tendons are surrounded by specific matrix structures that provide contractility support to the muscle fibers.

2.1.5.2. Comparison of transcriptomics and proteomics datasets shows similar enrichment of known MTJ marker proteins

Comparison of three previous omics studies in mouse[118], horse[144], and human[42] muscles with our proteomics data demonstrated corresponding enrichment of 10 of 29 proteins at the MTJ, including XIRP2, SORBS2, periostin, and CILP (**Figure 11E and Table S2**). For the other 19 proteins that were previously described to be enriched in the MTJ, we observed increasing protein profiles from muscle to tendon, which possibly indicates these proteins function within the MTJ and adjacent tendon areas. One reason for the low extent of overlap between these datasets could be that the correlation between mRNA and protein expression is poor due to variations in the half-lives of proteins and post-transcriptional regulation. Moreover, accumulation of proteins in the extracellular matrix cannot be detected at the mRNA level. As indicated earlier, skeletal muscles undergo various morphological and functional adaptations, depending on their location in the body. The isolation of different skeletal muscles from mice, horses, and humans could be another possible explanation for the high variation in the MTJ candidates identified to date (**Figures S10B and S10C**). In addition, recent RNAseq profiling of single myonuclei identified 291 genes that were enriched in MTJ

myonuclei. Comparison with our proteomics data revealed an overlap of 115 proteins, including seven proteins that we defined as MTJ marker proteins.[145] To determine the spatial and cellular localization of these MTJ candidates more precisely, immunostaining based on co-detection by indexing (CODEX) could be used in future experiments.[146, 147]

2.1.5.3. The biphasic profiles of several neuronal factors indicate neuronal innervation of distal muscle tissue

We also found several proteins related to neuronal activity with biphasic maxima at the central muscle area and MTJ-tendon transition zone (**Figure 13C**). For example, the maxima of neurofilament (NEFL) and myelin proteins (MBP, MAG, MPZ) in the central muscle area are probably due to neuronal innervation of the muscle fibers and indicate the presence of motor end plates. Although the MTJ and tendon are primarily responsible for connecting muscles and bones, they are also innervated by neurons and contain several mechanoreceptors (**Figures S10D-F**).[116] These neurons convert mechanical energy into electrical signals that are then used by the central nervous system to control body movements. Studies on the skeletal muscles of fish, mice, and horses confirmed the presence of sensory nerve endings and neuronal marker proteins, proving that the MTJ acts as a hub for mechanosensing and pain reception.[130, 144] Since more than 4% of the thousand most abundant tendon proteins are neuronal factors (**Figures S10G and 10H**), we suggest that the influence of neuronal innervation and mechanoreceptors at the muscle-tendon junction has a greater impact than previously assumed.

A neuronal protein with a biphasic profile is the dyslexia-associated protein KIAA0319-like protein (**Figure 13C**). KIAA0319l might be involved in neuronal migration and is thought to influence the formation of neural circuits involved in language processing. KIAA0319l also interacts with reticulon-4 receptor (RTN4R), also known as nogo receptor 1 (NGR1), which is an axon guidance receptor.[148] A protein with a similar function is neuronal cell adhesion molecule (NCAM), which also promotes neuritogenesis and neuronal migration.[149] Furthermore, NCAM has recently been identified as MTJ protein.[130] It is tempting to speculate that the interaction between RTNR4 and KIAA0319l may be related to axon guidance in the MTJ region. Thus, our spatial proteomic analysis is a useful tool to determine the extent of neuronal innervation in different areas of the skeletal muscle and could be used to study the alterations in neuronal structures under stress or disease-related conditions.

2.1.5.4. Network analysis of our protein profiles showed higher connectivity within the MTJ than the muscle or tendon areas

Our network analysis revealed significantly higher betweenness centrality at the MTJ compared to the other skeletal muscle or tendon sections and therefore suggests more cellular connections occur at the junction between muscle fiber tips and matrix proteins than the centrally located muscle fibers (**Figure 14**). Betweenness centrality is also often used to find nodes in a network that serve as a bridge from one part of the graph to another. As muscle and tendon are connected by the MTJ, it is reasonable to assume that the higher connectivity observed for this area in our analysis highlights this bridging property of the MTJ. In addition, the high connectivity is supported by the identification of more than 200 protein groups with maxima at the MTJ and demonstrates the high complexity of the MTJ. Other proteins that are closely positioned near the identified MTJ area within the network may represent further MTJ candidates and require additional validation.

Compared to earlier studies, we identified similar biological processes including neuronal activity, immune regulation, cell adhesion, and various metabolic pathways are enriched at the MTJ. Although the MTJ proteins identified vary compared to the studies in other species and muscles, in many cases we identified similar isoforms of the same protein family. For example, we observed a maximum at the MTJ for the immunoglobulin superfamily 8 (ISGF8) member (**Figure 4A**), whereas the MTJ of the human hamstring muscle showed enrichment of the family member IGFS1.[130] Both proteins are cell surface proteins related to cellular signaling and the immune system. IGSF8 (also known as prostaglandin regulatory-like protein, PGRL) is associated with various cellular processes related to motility, fusion, and neuronal growth. In addition, IGSF8 interacts with the tetraspanin molecules CD9 and CD81.[150, 151] Accordingly, we also observed increasing protein abundance of the cell membrane proteins CD9 and CD81 from muscle to tendon, supporting interactions between these proteins and IGFS8. Another CD9 and CD81-interacting protein with a similar expression profile is CD9P-1, also known as prostaglandin F2 receptor negative regulator (PTGFRN) (**Figure S6I**). Genetic ablation of CD9 and CD81 reduces muscle regeneration, and both tetraspanins are expressed by centrally nucleated myofibers in response to injury. Since centrally positioned myonuclei are also detectable in myofibers near the MTJ in humans[144], we hypothesize that increased expression of cell surface proteins such as tetraspanins and members of the immunoglobulin superfamily might be involved in

regeneration, fusion, and adhesion processes within the MTJ and surrounding areas. Further study of the network, particularly the area we identify as the MTJ, may further reveal the true complexity of this important region and establish a deeper understanding of its molecular state. This could lead to further targets relevant to pathophysiology that could not be easily identified by more traditional statistical approaches.

2.1.5.5. Fatty acid metabolism and the RAS are involved in maintenance of the tendon matrix

Although most mitochondrial SLC transporters were more abundant in muscle tissue, we observed the opposite trend for SLC25A1, also known as citrate transporter protein (CTP). SLC25A1 exports citrate or isocitrate from the mitochondria into the cytosol in exchange for malate. Cytosolic citrate functions as a source of acetyl-coenzyme A for fatty acid and sterol biosynthesis and as an allosteric regulator of enzymes that control glycolysis, lipogenesis, and gluconeogenesis.[152] In addition, citrate is an essential intermediate molecule in the TCA cycle and is central to energy production, which is ultimately essential to muscle contraction. Since tendons are mainly comprised of tenocytes, fibroblasts, and myofibroblasts, we suggest that these cell populations express high levels of citrate transporters to increase the cytosolic concentration of citrate for fatty acid synthesis. Mass spectrometric analysis confirmed that citrate transporter expression was higher in isolated mouse tenocytes compared to myoblasts (**Figure S9H**). In addition, the transport of citrate and acetyl-CoA from mitochondria to the nucleus is also used by histone acetyltransferases (HATs) to transfer the acetyl group to histone residues for histone acetylation, which in turn regulates gene activity.[153] For example, the capacity of mesenchymal stem cells to express osteogenic genes is tightly regulated by the concentration of citrate and histone acetylation.[154] Hence, a high concentration of citrate transporters in tendon cells or fibroblasts may not only regulate the synthesis of fatty acids but also influence the expression of secretory proteins and matrix formation via histone acetylation. A recent study in cancer-associated fibroblasts demonstrated that increased levels of acetyl-CoA in fibroblasts induced H3K27 hyperacetylation and transcriptional activation of collagens, suggesting that acetyl-CoA is a key epigenetic regulator.[155] Overall, increased concentrations of acetyl-CoA in the cytosol of tenocytes could affect histone acetylation and thus modulate the expression of the matrix proteins responsible for matrix formation.

Another metabolic pathway closely linked to blood pressure regulation is the renin-angiotensin system. The angiotensin converting enzyme (ACE) cleaves the inactive peptide angiotensin I to produce the active peptide angiotensin II. We demonstrated ascending profiles for ACE and related enzymes from muscle to tendon (**Figures 5A-D**), suggesting enhanced levels of angiotensin II in tendons. Earlier studies showed that the RAS activates transforming growth factor beta (TGFβ) and SMAD2/3 signaling, which also play critical roles in the regulation of ECM gene expression and fibrosis.[156] In addition, administration of several medications, including agents of the renin-angiotensin system, may increase the risk of achilles tendon injury.[157, 158]

Therefore, increased expression of ACE in the MTJ and tendons may help to activate the TGFβ-SMAD signaling pathway, induce the expression of CTGF, and promote the production of collagen and other ECM components. Previous studies showed that inhibition of the RAS by losartan reduces collagen formation and CTGF secretion in various experimental models of fibrosis.[156, 159] We hypothesize that the RAS also influences the activity of the TGFβ-SMAD pathway in tenocytes and thus affects matrix formation at the MTJ and tendons. As further evidence of enhanced activation of the TGFβ-SMAD pathway, we also detected an ascending profile for DAB adaptor protein 2 (DAB2), which is required for internalization of TGFβR and subsequent activation of the SMAD pathway (**Figure S6G**).[160]

Excessive production and accumulation of ECM components in skeletal muscle induced by chronic kidney disease and Duchenne muscular dystrophy lead to contractile dysfunction, stiffness, and muscle weakness. Although the administration of ACE inhibitors prevents fibrosis of skeletal muscle and has a positive effect on muscle function, the possible adverse effects on the MTJ are completely unclear. Therefore, a detailed analysis of the RAS signaling pathways that are activated in the context of matrix formation after muscle injury could provide detailed insight into whether ACE/ACER inhibitors significantly affect the maintenance and regeneration of the muscle-tendon transition.

In conclusion, we provide a comprehensive spatial expression profile from the central to distal areas of a skeletal muscle. In addition, our protein expression profiling approach could be used to screen any tissue, such as heart or brain, to achieve a comprehensive spatial proteome. Furthermore, our results demonstrate a number of physiological differences

between the muscle fibers, MTJ, and tendon areas and the quantitative proteomic analysis highlights several proteins with previously unknown associations to the MTJ.

2.1.5.6. Limitations of the study

We provide a longitudinal profile of a mouse skeletal muscle, paving the way for future spatial proteomics studies. Although we profiled over 3000 proteins from the central muscle to tendon areas, our dataset does not have a cellular resolution. Complementary approaches such as CYTOF, CODEX, and laser capture dissection microscopy could be used to assign expression profiles to specific fiber types and cell populations. In addition, our protein profiling dataset does not include complete profiles of transcription factors expressed at low levels; in the future, targeted mass spectrometry approaches and ultra-sensitive single-cell proteomics could be used to obtain profiles of low-abundance proteins. To further increase the resolution of our protein profiles, thinner cryosections of 10 µm could be generated. The increased measurement time could be for compensated by even shorter LC-MS gradients. Finally, this analysis was limited by the fact that we only measured one type of skeletal muscle. Other muscles, and muscles from other species, could provide further insights into the molecular architecture of muscle-tendon junctions. Last, further experiments using mouse models with muscle weakness and impaired regeneration are necessary to characterize the spatial proteome of the skeletal muscle. Overall, our unbiased spatial proteomic profiling of the soleus muscle can serve as a reference for the study of specific muscle structures such as the neuromuscular and myotendinous junction and provides a valuable resource for the skeletal muscle community.

2.1.6. Acknowledgments

We thank Gil Oreff and Florien Jenner (University of Veterinary Medicine Vienna) for providing the tenocyte cell line. This work was supported by the Cologne Cluster of Excellence on Cellular Stress Responses in Aging-associated Diseases (CECAD) EXC 299/2, the RELOC graduate school GRK 2550 (DFG 411422114) and FOR2722/2 (Krüger_384170921/TP4, KR 3788/8-2; BB_FOR2722-407146744/TP1 (BR2304/12-1), 270922282 (BR2309/9-2); Koch_407164333/TP4 (KO2247/8-1). In addition, this work was supported by a major invest grant from the Deutsche Forschungsgemeinschaft (INST 216/1163-1 FUGG and INST 216/1020-1 FUGG) and the JPND2019-466-146 grant.

2.1.7. Author contributions

Conceptualization, L.S., M.K.; Methodology, L.S., M.K., Software, L.S., P.A., Validation, L.S., M.S., C.H.; Formal Analysis, L.S., P.A., Investigation L.S., Resources, M.K., M.K., A.M., J.W.L., A.S., S.M., B.B., M.K.; Writing – Original Draft, L.S., M.K., P.A.; Writing – Review & Editing, L.S., M.K., A.M., P.A., J.W.S., B.B., M.K.; Visualization, L.S., C.H.; Supervision, Project Administration M.K.; Funding Acquisition, M.K., B.B., M.K..

2.1.8. Declaration of Interests

The authors declare that they have no competing interests.

2.1.9. Experimental model

2.1.9.1. Experimental model

All animal experiments were performed in accordance with national and institutional guidelines. Three- to four-month-old male wildtype C57BL/6 mice were maintained at 22 ± 2 °, 55 ± 10% humidity, and an air exchange rate of 15 times per hour under a 12:12 h light-dark cycle and had free access to standard chow diet.

All mouse experiments were performed in accordance with the regulations stated in European, national, and institutional guidelines and were approved by local government authority Landesamt für Natur, Umwelt und Verbraucherschutz (LANUV) of North Rhine-Westphalia, Germany.

2.1.9.2. Cell lines

Immortalized murine tenocytes were kindly provided by Gil Lola Oreff (Vienna) and cultivated in minimal essential medium supplemented with 10% fetal bovine serum (FBS), 1% L-glutamine, 100 U/mL penicillin and 0.1 mg/mL streptomycin at 37 °C and 5% CO_2.

2.1.10. Method details

2.1.10.1. Intact tissue sample processing, protein digestion, and desalting

Isolated soleus skeletal muscles were manually dissected into three parts: the central part of the muscle, the MTJ, and the tendon (n = 4). Samples were snap-frozen in liquid nitrogen, ground using a mortar and pestle, resuspended in 4% SDS in PBS, homogenized by heating for 5 min at 95 °C, and sonicated with a Bioraptor sonicator; the sonication settings were 21 °C water with 10 cycles of 30 on and 30 off. Lysates were cleared by centrifugation for 10 min at 16,000 *g* and protein concentrations were determined using the Pierce Protein Assay (Thermo Scientific), then 25 µg protein extract was reduced and alkylated for 45 min at 45 °C using 5 mM TCEP and 15 mM CAA. After acetone precipitation, the protein pellet was reconstituted in 3M GuHCl in 50 mM HEPES, 2.5 mM $CaCl_2$. Proteins were digested with the protease LysC (substrate:enzyme ratio 50:1) for 3 h at room temperature followed by dilution of the GuHCl with 50 mM HEPES, 2.5 mM $CaCl_2$ to a final concentration of 0.5 M. Further protein digestion was performed with trypsin (substrate:enzyme ratio 100:1) overnight at room temperature. Samples were acidified to 1% formic acid (FA) and cleaned-up using house-made SDB-RPS tips.

2.1.10.2. Sample preparation for cryo-embedding and sectioning with a cryostat

Soleus muscles were fixed on both sides using insect needles on cork matrix, embedded in optimal cutting temperature (OCT) resin, and stored at -80 °C until further use. OCT embedded solei were cut into 10–30-µm-thick slices at -25 °C using a Reichert Jung cryostat (Leica, Nussloch, Germany) and each slice was placed individually into a well of a 96-well-plate. As controls, one column on each 96-well plate was loaded with a HEK293T protein lysate. The slices placed in the wells were mixed with 40 µL of 4% SDS in PBS containing 5 mM TCEP and 10 mM CAA. The 96-well-plates were incubated at 95 °C for 10 min followed by Bioraptor sonication at 20 °C with 10 cycles of 30 on and 30 off. Samples were digested following the standard SP3 protocol.[123] Briefly, 20 µg of washed SP3 beads were

added to each well, followed by one sample volume of acetonitrile (ACN). After incubation for 8 min and a further 2 min on a magnet, the supernatant was discarded, and the magnetic beads were washed twice with 70% EtOH and once with 100% ACN. Samples were digested with 10 µL of 20 ng LysC and 40 ng trypsin in 50 mM ammonium bicarbonate buffer at 37 °C on a rotating wheel (750 rpm) overnight, acidified by addition of 100 µL 0.1% FA, followed by clean-up with house-made SDB-RPS tips. Peptides were reconstituted in 2% ACN, 5% FA, with iRT peptides (**Table S5** for peptide sequences).

2.1.10.3. ACE inhibitor incubation and MS analysis

Immortalized murine tenocytes were provided by Gil Lola Oreff (Vienna) cultivated in minimal essential medium supplemented with 10% fetal bovine serum (FBS), 1% L-glutamine, 100 U/mL penicillin and 0.1 mg/mL streptomycin at 37 °C and 5% CO_2 until the desired number of cells were obtained. Cells were seeded at a density of $0.4x10^5$ in 24-well-plates in culture medium containing 10, 50, or 100 µmol Losartan (Sigma Aldrich) or DMSO as control and cultured for 1–4 days. The media were changed daily until harvesting and all experiments were carried out in biological triplicate (n = 3). Cells were washed with PBS, lysed with a PBS buffer containing 4% SDS, and 8 µg of protein lysate was used for digestion as described above, followed by purification with in-house prepared SDB-RPS tips.

For phosphopeptide enrichment, cells were seeded in culture medium with 1% FBS. The media was changed daily until harvesting and all experiments were carried out in biological triplicate (n = 3). Cells were washed with PBS, lysed with PBS buffer containing 4% SDS, and 8 µg of protein lysate was used for LC-MS analysis. Magnetic Ti-NTA beads (Cube BioTech) were used for phosphopeptide enrichment following the manufacturer's instructions. In brief, 250 µg of desalted peptides were reconstituted in 250 µL binding buffer (80% ACN, 5% TFA, 0.1% glycolic acid). Peptides were incubated with magnetic beads in a 1:10 ratio for 20 min at 1300 rpm. After binding, the beads were washed twice with wash buffer 1 (80% ACN, 5% TFA) and wash buffer 2 (10% ACN, 0.2% TFA). Peptides were eluted with 1% ammonium hydroxide and acidified with 10 µL FA.

2.1.10.4. LC-MS analysis

For peptide separation, an in-house made fused silica emitter (75 µm diameter, length 15–30 cm) was packed with 5 µm C18 Poroshell resin (Agilent, USA) and applied to an Easy

nLC1200 (Thermo-Fisher Scientific, Waltham, USA) with the column temperature maintained at 50 °C using an integrated column oven. Peptides were separated using a binary buffer system of buffer A (0.1% FA) and buffer B (80% ACN, 0.1% FA) on a 30 cm in-house-packed analytical column filled with 1.9 µm C18-AQ Reprosil Pur beads (Dr. Maisch, Germany). A 90 min segmented gradient of 4–32% Solvent B over 72 min, 32–55% Solvent B over 13 min and 55–95% over 2 min at a flow rate of 250 nL/min was applied to elute peptides and the peptides were measured with an Orbitrap Eclipse Tribid mass spectrometer equipped with an FAIMS-Pro interface (Thermo-Fisher Scientific, Waltham, USA). A data-independent (DIA) method was used for peptide acquisition and each acquisition cycle consisted of four scans, two full scans, and two DIA scans at CVs of -50 and -70 V, respectively, employing 25 x 22 Da windows from 350 to 1600 *m/z* with an overlap of 1 Da on each side. All scans were acquired in positive ionization mode at 15k resolution and DIA scans were acquired after peptide fragmentation at a normalized collision energy (NCE) of 30.

MS analysis of tissue sections was performed with a single CV of -50 V and a staggered-window DIA method, using a duty cycle of two sets shifted by ½ isolation window from 400 to 900 *m/z*. The MS methods and duty cycle are described in **Table S5**.

Samples from cell culture experiments were processed as described before and digested peptides were loaded on EvoTips. Pure and measured using a 44-min LC-MS gradient on an EvoSep One system coupled to a 15 cm PepSep column (Evosep, Denmark). The mobile phases were compromised of 0.1% FA as solvent A and 0.1% FA in ACN as solvent B. The HPLC system was coupled to a timsTOF pro 2 using a CaptiveSpray source (both Bruker). Samples were measured in dia-PASEF mode with daily ion mobility calibration using three ions in the Agilent ESI-Low Tuning Mix following the vendor's specifications. The DIA-PASEF window ranged in dimension from 1/k0 0.7–1.35, with 24 x 25 Th windows and in dimension from 350 to 1250 *m/z* and 1/k0 0.7–1.45, with 2 x 16 Th windows and in dimension from 400 to 1400 *m/z* for proteomics and phospho proteomics analysis, respectively.

2.1.10.5. Bioinformatic analysis

The mass spectrometry proteomics data have been deposited to the ProteomeXchange Consortium via the PRIDE partner repository with the dataset identifier PXD046596.[161] For the analysis of intact skeletal muscle samples, spectra from different CV settings were separated manually using the Freestyle software suite (Thermo-Fisher Scientific) and

analyzed with DIA-NN 1.8 using library free search against the UniProt mouse database (Sep. 2017) complemented with protein sequences from myosin heavy chain variants and collagens. Mass ranges were set according to the settings of the mass spectrometer; mass deviation was automatically determined from the first data file. Data was further processed using R (V 4.2.2), with the tidyverse, diann, data.table, magrittr, FactoMineR, factoextra, ggplot2, and gprofiler libraries. An in-house modified R-script based on the version by V. Demichev was used to calculate MaxLFQ values.[162, 163] To show identified peptides we used the term "precursor", which refers to an ion analyzed by the MS instrument. The precursor ion is fragmented into product ions and contain information about the sequence, modification status, and the charge state. Data input was filtered for unique precursor, q-value <0.01, Lib.Q.Value <0.01, PG.Q.Value < 0.01, Global.Q.Value < 0.01, Quantity.Quality > 0.7, Fragment.count >= 4; previously separated data from different compensation voltages were combined for each protein entry to the maximum value. Statistical analysis was performed with R (V 4.2.2) and Perseus (V.1.6.5.0) and visualized with Instant clue (V 0.10.10.20210315). For the analysis of the cell culture experiments and identification of phosphopeptides we used Spectronaut software (version 1.8).[164]

For the analysis of sectioned tissue, RAW data were first deconvoluted using ProteoWizard (V 3.0.21218). Files were pre-processed as described before. Further calculations were performed within R (version 4.2.2) using the diann, tidyverse, data.table, samr, vsn, ggplot2, and gprofiler libraries. All protein intensities smaller than 10^4 were replaced as missing values.

The protein intensities in each slice were normalized to the total protein intensity in each slice. Slices were arranged spatially, and proteins were filtered in a distance related manner; a sliding window was generated that covered an overall a distance of 200 µm, i.e., five sections back and five sections forward. Proteins with less than 70% coverage over one sliding window were excluded. For imputation, a pseudo-slice ID was established to capture sections for which measurement completely failed and to ensure that the sliding window always contained 10 sections before and 10 sections after the current slice. Sections close to the edge of the sample were truncated but required a minimum of three samples to be present for imputation. For windows that fulfilled the 70% limit, missing values in the windows were imputed with a normal linear imputation using 200 µm distances. The remaining missing

values were imputed with random values 1.6 points below the mean of the lower 5% of the total expression values across all proteins.

Samples from different biological replicates had to be adjusted to obtain congruent protein profiles. We normalized each muscle section by dividing each section by the length of the whole muscle. Then, each experiment was analyzed with a bootstrap approach based on the Significance analysis of Microarrays (SAM) method [125, 165] to detect gradual increases or decreases over distance for specific proteins in a linear and non-linear relationship as local minima and maxima. The reported distribution statistics (d-statistics) were further used as readout for significantly up- or downregulated proteins. The average score across all samples was calculated and proteins with a d-statistic > 5 were selected to shift the profiles required to achieve improved matching of minima and maxima within the profiles. Z-scores were calculated row-wise and the average protein profile was smoothed using a local regression function, called LOESS, in which the 95% confidence intervals were calculated as representative profiles of each protein. For ease of visualization, the representative profiles were normalized to range from 0–1 for all data.

2.1.10.6. Development of a network-based representation of the muscle tendon regions

The representative profile of each protein was used as input for a time impact analysis, replacing time with distance. This comprehensive technique is used to analyze each delay event individually in chronological order to calculate its impact and to quantify each delay based on the schedule immediately before and after the delay event took place. The delay is calculated by the highest correlation of two protein profiles. Correlation was calculated by shifting two protein profiles in both directions by up to 20% of the total distance. The reported delays were filtered for correlation scores higher than 0.7 and for distances less than 100 µm. The interactions were visualized in Cytoscape and arranged using the Spring Embedded Layout of the delay, leading to a hierarchical arrangement of the proteins over distance.

An interactive online version of the network is available using following link: **https://medex.uber.space/networks/index.html#/**. Wilcoxon t-tests of the betweenness scores and GO-term enrichment analysis were performed and visualized using R (V 4.2.2) using the packages gprofiler2 and ggplot2.

2.1.10.7. Histochemistry and immunostaining

Mouse solei were collected, embedded as described previously, cut longitudinally and transversely in 3–10 µm sections, collected on glass slides (VWR) and stored at -80 °C until further use. Slides were removed from the freezer and dried at room temperature. Two biological replicates were performed for each staining. Longitudinal sections were fixed with Histofix (Histolab) for 10 min at RT. Primary antibodies against Tenascin-C (Leica Biosystems Cat# NCL-TENAS-C, RRID:AB_564026), Myosin pan (DSHB Cat# A4.1025, RRID:AB_528356), Collagen 11a1 (Invitrogen(Zymed Custom Ab Lab), [166]), Collagen 22 (provided from Manuel Koch (Cologne)[41]), Periostin (Abcam Cat# ab14041, RRID:AB_2299859) were diluted 1:100 in 1% BSA in TBS, except Collagen 22 was used 1:500, and applied overnight at 4 °C; the following day, secondary antibodies were diluted 1:200 and Hoechst (Invitrogen, #H1399) 1:100 in TBS and applied for 60 min at RT. As secondary antibodies were used (AF568-conjugated anti-rabbit (Molecular Probes Cat# A-11036 (also A11036), RRID:AB_10563566), AF488-conjugated anti-rabbit (Thermo Fisher Scientific Cat# A-11034 (also A11034), RRID:AB_2576217), AF568-conjugated anti-guinea pig (Thermo Fisher Scientific Cat# A-11075, RRID:AB_2534119), AF488-conjugated anti-mouse IgG2b (Thermo Fisher Scientific Cat# A-21141, RRID:AB_2535778), AF680-conjugated anti-mouse IgG2a (Thermo Fisher Scientific Cat# A31563, RRID:AB_2536177)). Samples were washed twice for 10 min in TBS between all steps in the protocol. Finally, slides were mounted with coverslips using Prolong Gold Antifade Reagent (Thermo Fisher Scientific). For widefield fluorescence microscopy, images were captured using two different objectives (10x/0.3NA; 20x/0.5NA) on an Olympus BX51 microscope with a 0.5x camera (Olympus DP71, Olympus Deutschland GmBH, Hamburg, Germany) at the ISMC using the software Olympus cellSens Software (RRID:SCR_014551). Transverse sections were used for Masson Goldner Trichrome staining (Morphisto) and imaged using a Dmi8A inverse microscope (Leica). Images were further processed using ImageJ (version 1.54d; RRID:SCR_003070) and colorblind-friendly pseudo colors were applied to the composite images.

2.1.11. Quantification and statistical analysis

All experiments were carried out in at least triplicates as outlined in the methods details. One-way analysis of variance (ANOVA) was calculated within Perseus. The Permutation-based FDR and Number of randomizations was set to 0.05 and 500, respectively. For intact muscle tissue and cell culture proteome analysis Student's *T*-test was used to calculate significantly changed proteins. A protein was classified as significant with an FDR < 0.05 and s0 > 0.1. For phosphoproteome analysis the Welch's *T*-test analysis was performed and a phosphosite was classified as significant with a p-Value < 0.05 and $\log_2$ difference > |1|. GO-terms and phosphosites on a protein were compared using a *T*-test analysis and significance are indicated using asterisks (* adjusted p-value < 0.05. ** adjusted p-value < 0.01, *** adjusted p-value < 0.001). Statistical details can also be found in the according figure legends.

2.2. Preprint Publication (II): Protocol for generating protein profiles and distance-based network analysis of tissue slices

Luisa Schmidt,[1,3]*Philipp Antczak,[1,2] and Marcus Krüger[1,2,4]**

[1]Institute for Genetics, Cologne Excellence Cluster on Cellular Stress Responses in Aging-Associated Diseases (CECAD), 50931 Cologne, Germany

[2]Center for Molecular Medicine (CMMC), University of Cologne, 50931 Cologne, Germany

[3]Technical contact

[4]Lead contact

*Correspondence: luisa.schmidt@uni-koeln.de

**Correspondence: marcus.krueger@uni-koeln.de

In revision in STAR Protocols since August, 2024

2.2.1. Summary publication II

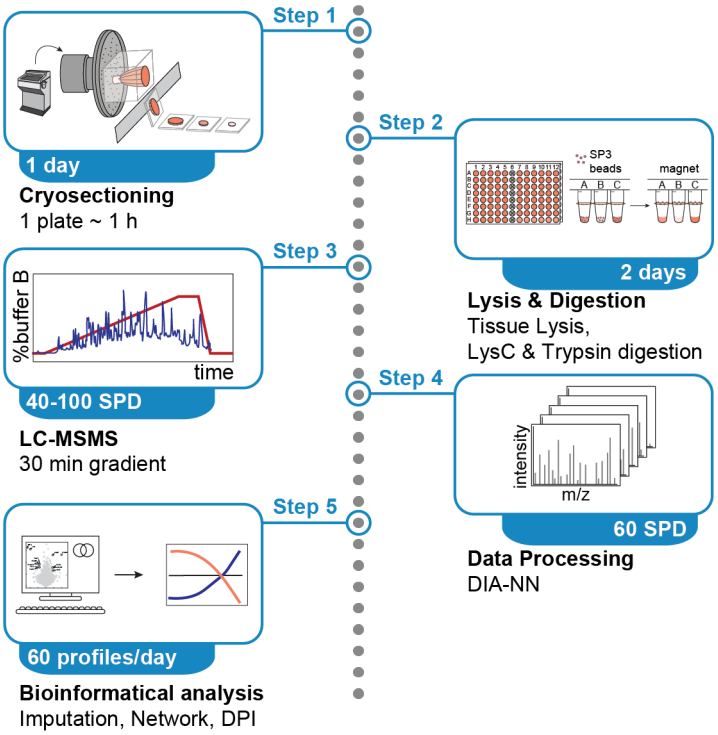

Figure 16 Graphical abstract publication II. Step wise workflow to generate protein profiles starting with the sectioning of the tissue (Step 1) and the MS sample preparation (Step 2), followed by LC-MSMS data acquisition (Step 3) and processing (Step 4). Bioinformatical analysis includes imputation, and network analysis (Step 5).

DIA-NN, data-independent data acquisition-neural network and interference correction; LC-MSMS, liquid chromatography tandem mass spectrometry; SP3, Single-pot, solid-phase-enhanced sample preparation.

We introduce a protocol for spatial proteomics using thin cryotome sections of mouse skeletal muscle tissue. We describe the steps required to prepare the muscle sections, as well as the mass spectrometric and bioinformatic analyses to generate spatial protein profiles from LC-MS measurements along the longitudinal skeletal muscle axis. A sliding-window approach is used to scan longitudinal protein profiles and replace missing data, bootstrap analysis is employed to compress or stretch biological replicates, and distance-based network analysis is performed using R packages. This protocol has also potential applications in spatial proteomics for different regions of the brain or heart.

For complete details on the use and execution of this protocol, please refer to **Schmidt et al.** (2024) https://pubmed.ncbi.nlm.nih.gov/38900641/.[167]

2.2.2. Before you begin

We developed a method for high-resolution mapping of proteins in skeletal muscle fibers, the MTJ, and tendons that is not biased by morphological features. The following protocol describes the steps required to use cryo-embedded mouse soleus muscles for spatial proteomics profiling. We describe how to isolate the soleus muscle from the mouse hind leg and analyze single thin cryosections with a thickness of 20 µm using a cryotome. Each section is placed in a 96-well-plate and the extracted proteins are subjected to tryptic protein digestion using the SP3 protocol. Each section is analyzed using short LC-MS gradients to generate spatial protein profiles along the longitudinal axis between muscle fibers and tendon. The bioinformatics approach involves an alternative normalization for samples with input variances, and a sliding window scans an area of 200 µm to filter data and impute missing values. The profiles are then subjected to distance-delay analysis to create a distance-based network.

In summary, this workflow can be used to generate protein profiles for various muscle structures and other tissues, and thus contribute to development of spatial repositories of organs and improve our understanding of spatial alterations in disease models.

2.2.3. Muscle extraction

All of our mouse experiments were performed in accordance with the regulations stated in European, national, and institutional guidelines and were approved by local government authority Landesamt für Natur, Umwelt und Verbraucherschutz (LANUV) of North Rhine-Westphalia, Germany.

Timing: 10 min per tissue

1. Adult male wildtype C57BL/6 mice were housed at 22° ± 2°, 55 ± 10% humidity, and an air exchange rate of 15 times per hour under a 12:12 h light-dark cycle and had free access to standard chow diet.
2. Isolate a skeletal muscle of interest from the hind leg of the mouse or another area of the body (**Figure 17A**).
3. Attach the skeletal muscle to a transparent silicone mat with insect needles to document the morphology and size of the muscle using a stereomicroscope and camera (**Figure 17B**).

4. To prevent muscle contraction, we attached the soleus to the cork mat with small needles (**Figure 17C**). The cork mat and the skeletal muscle is then transferred to a cryomold, which is filled with cryomatrix (Tissue-Tek O.C.T. compound) until the muscle is completely covered by the matrix (**Figure 17D**). We used the soleus skeletal muscle of the hind leg of the mouse.
5. Freeze the cryomolds on dry ice for 10 minutes, remove the needles, and store the samples at -80 °C.

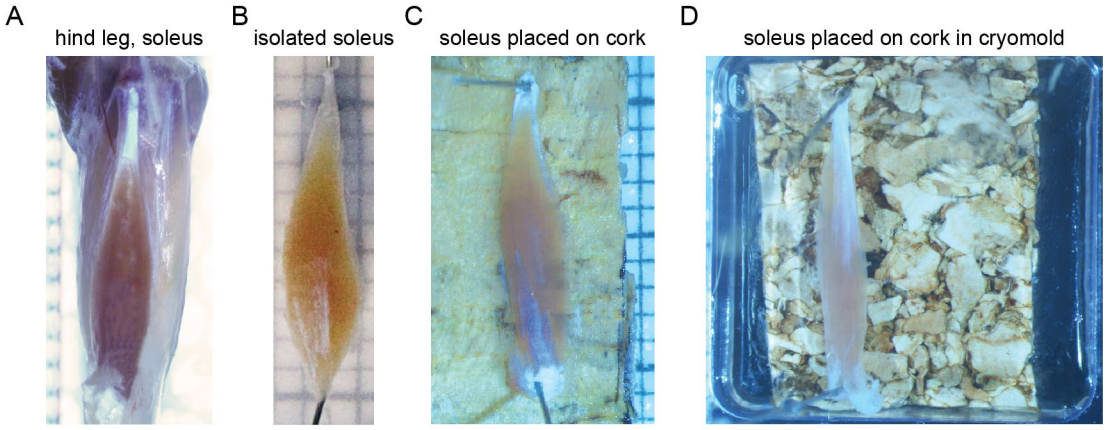

Figure 17 Preparation of the mouse soleus muscle. A) Mouse soleus skeletal muscle intact in the mouse hindleg. **B**) Isolated soleus muscle pinned on transparent silicon to calculate the length of the tissue. **C**) Pinned muscle is transferred on cork. D) Pinned muscle on cork is transferred to a cryomold.

2.2.3.1. Bioinformatic analysis

6. Next to R, further libraries should be installed:
    a. library(samr).
    b. library(vsn).
    c. library(ggplot2).
    d. library(gplots).
    e. library(slider).
    f. library(openxlsx).
    g. library(preprocessCore).
    h. library(pbapply).
    i. library(igraph).
    j. library(parallel).
7. For visualization, cytoscape should be installed.

2.2.4. Key resource table

Table 1 Key resource table.

REAGENT or RESOURCE	SOURCE	IDENTIFIER
Chemicals, peptides, and recombinant proteins		
Lysyl Endopeptidase	Wako	Cat# 129-02541
Sequencing Grade Modified	Serva	Cat# 37286.03
iRT peptides	GeneCust	NA
Ammonium bi carbonat (ABC)	Merck	207861
Tris(2-carboxyethyl)phosphine hydrochloride (TCEP)	ThermoFisher	77720
2-chloroacetamide (CAA)	Sigma	C0267-100G
Formic acid (LC grade)	VWR	64-18-6
Acetonitril (LC grade)	VWR	83640.320
Acetonitril + 0.1% FA (LC grade)	VWR	84866.290
Water (LC grade)	VWR	83645.320
Water + 0.1% FA (LC grade)	VWR	84867.320
Methanol (LC grade)	VWR	20847.320
Ethanol (>99.5%)	VWR	85033.360
SDS	VWR	151-21-3
Sera Mag beads A	VWR	44152105050250.
Sera Mag beads B	VWR	65152105050250
Tissue-Tek	Laborversand.de	TTEK
Deposited data		
C57BL/6 untargeted proteomics	This paper	ProteomeXchange (http://www.proteomexchange.org) PXD046596

Code of the spatial analysis (Sliding window for filter, imputation, k-means clustering, distance-delay analysis)	This paper	Zenodo (https://zenodo.org/) 10.5281/zenodo.10678005
Experimental models: Organisms/strains		
Mice: C57BL/6	The Jackson Laboratory	Cat#000664
Software and algorithms		
R (V 4.3.3)	The R Project	https://www.r-project.org; RRID: SCR_001905
Rstudio	Rstudio	https://www.rstudio.com
ProteoWizard (V 3.0.21218)	ProteoWizard	http://proteowizard.sour
Freestyle software suite	Thermo Fisher Scientific	RRID:SCR_022877
DIA-NN	Demichev, 2019 https://www.nature.com/articles/s41592-019-0638-x	https://github.com/vdemichev/DiaNN; RRID:SCR_022865
Cytoscape	Cytoscape Consortium	http://cytoscape.org; RRID:SCR_003032
R package: samr		NA
R package: vsn		RRID:SCR_001459
R package: ggplot2		RRID:SCR_014601
R package: gplots		RRID:SCR_025035
R package: slider		NA
R package: openxlsx		RRID:SCR_019185
R package: preprocessCore		RRID:SCR_024254
R package: pbapply		NA
R package: igraph		RRID:SCR_019225
R package: parallel		NA
Other		
Orbitrap Eclipse Tribid	Thermo Fisher	RRID:SCR_023618
Faims Pro	Thermo Fisher	NA
Ultimate 3000	Thermo Fisher	NA

Cryotome	Reichert Jung/Leica	NA
Tissue-Tek Cryomold	Sakura	(15 mmx15 mm x 5
Cork	Kork-Deko.de	NA
Needles	Bioform	Gr. 000 (0,25x38mm)
One-sided plate magnet		
SDB-RPS	Merck	66886-U

2.2.4.1. Materials and equipment setup

PBS (Phosphate Buffered Saline) (1X, pH 7.4):

Table 2 PBS buffer recipe.

Reagent	Final concentration	Amount
Sodium chloride (mw: 58.44 g/mol)	0.137 M	8 g
Potassium Chloride (mw: 74.55 g/mol)	0.0027 M	0.2 g
Sodium Phosphate Dibasic (mw: 141.96 g/mol)	0.01 M	1.44 g
Potassium Phosphate Monobasic (mw: 136.09 g/mol)	0.0018 M	0.245 g
Total	**n/a**	**1 L**

- Stock solutions:

  4% SDS(!) in PBS.

  buffer can be stored for a month on RT.

  ABC buffer: 50 mM ABC in water (pH 8.0).

  buffer can be stored for a month on 4 °C.

  550 mM 2-chloroacetamide (CAA) in milliQ water.

  0.5 µg/µl trypsin protease (dilute in milliQ water).

  0.5 µg/µl LysC protease (dilute in milliQ water).

  These buffers buffer can be aliquoted at -20 °C.

  CRITICAL: SDS, CAA and TCEP are toxic. Pipette them in a fume hood and handle with gloves.

- Bead solution: Mix 20 µL of Sera Mag beads A and 20 µl of Sera Mag beads B. Wash the beads three times with 200 µL water (LC grade), using a magnet to immobilize the beads in the tube after each wash step. Reconstitute the beads in 200 µL of water.
- Lysis buffer: 5 mM TCEP(!), 15 mM CAA(!) in 4% SDS(!) in PBS.

CRITICAL: buffer must be prepared freshly.

CRITICAL: SDS, CAA, and TCEP are toxic. Pipette these chemicals in a fume hood and handle with gloves.

- Digestion buffer: 20 ng of trypsin, 10 ng of LysC in ABC buffer.

CRITICAL: buffer must be prepared freshly.

- Buffer A: 0.1% formic acid(!) in MilliQ water.
- Buffer B: 0.1% formic acid(!) in 80% acetonitrile(!) in MilliQ water.
- Buffer R: iRT peptides, 2% formic acid(!) in 5% acetonitrile(!) in MilliQ water. buffer can be stored at 4 °C.

CRITICAL: Formic acid vapor can severely irritate the eyes, mucous membranes, and skin. When preparing this buffer, pipette under fume hood and wear gloves.

2.2.5. Step-by-step method details

2.2.5.1. Cryotome sectioning

Timing: 1 h per plate

1. Attach the embedded sample to the rotary microtome of the cryotome using cryomatrix. Align the block at a right angle to the blade (**Figure 18**). (PROBLEM 1)

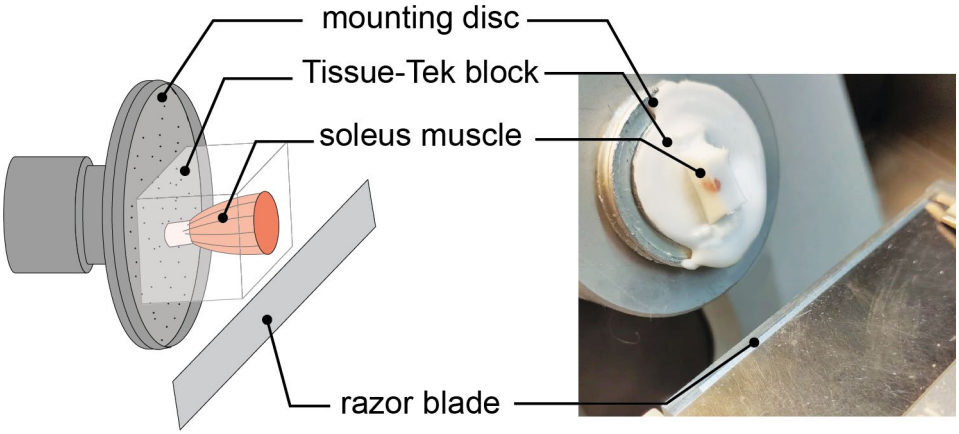

Figure 18 Correct positioning of the tissue on the mounting disk.

2. To cut the soleus skeletal muscle:
    a. Trim the sample block with a razor blade in order to transfer as little of the surrounding cryomatrix as possible when the sections are cut. Cut the block until the embedded muscle tissue becomes visible - this will be the first section to be used for analysis (**Figure 19A**).
    b. Cut the skeletal muscle from the central to the peripheral regions at a thickness of 20 µm (**Figure 19A**). Transfer each slice into a 96-well-plate using cooled tweezers (**Figure 19B**). A muscle piece with a length of 3.5 mm will result in ~175 samples.(PROBLEM 2)
    c. One column of the 96-well plate should not be filled with sections as it will be used for control samples

NOTE: Tissue sections can be cut in thinner or thicker sections to increase or decrease the resolution of the analysis. The choice of slice thickness depends on the area/size of the tissue and the sensitivity of the MS instrument and should be individually determined for each tissue.

CRITICAL: All materials for cutting, 96-well plates, tweezers, and cryo-embedded samples should be chilled at -20 °C for at least 30 min before use. Insufficient cooling

of the materials can lead to thawing of the tissue and sample loss. Importantly, the 96-well plates should also be kept in the cryotome at -20 °C during sample collection

PAUSE POINT: Samples can be stored at -20 °C until further use.

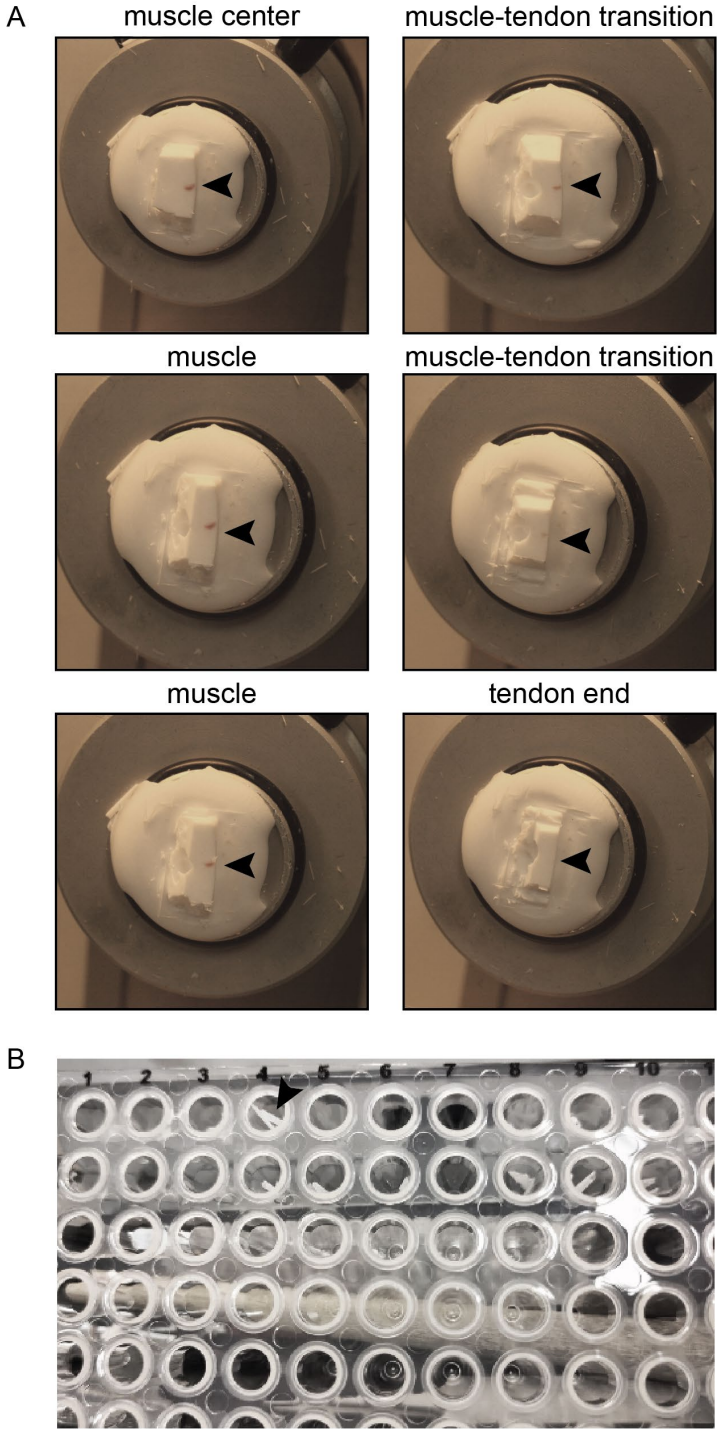

Figure 19 Tissue sampling. A) Tissue-Tek embedded muscle from central muscle to the tendon end. **B**) 20 µm sections placed in a 96-well plate.

2.2.5.2. Tissue lysis and digestion

Timing: 2 days

3. Tissue lysis.
    a. Add 40 µl lysis buffer to each well.
    b. Fill empty control wells with 40 µl human embryonic kidney 293 (HEK-293) cell lysates in the same lysis buffer.
    c. Heat the 96-well-plates to 95 °C for 5 minutes and centrifuge at 248 g for 5 minutes.
    d. Sonicate the 96-well plates for 10 minutes in a Bioruptor system using an on/off interval of 30 seconds.
    e. Heat the 96-well-plates to 70 °C for 10 min and centrifuge for 5 min at 248 g.

    NOTE: Instead of HEK cells, every other cell line can be used as quality control for digestion and sample preparation.

    PAUSE POINT: Samples can be stored at -20 °C until further use. If samples are stored, repeat 3c.
4. SP3 precipitation.
    a. Add 2 µL of the Sera-Mag bead mixture to each sample.
    b. Add 42 µL of acetonitrile and vortex carefully.
    c. Incubate the 96-well-plates for 8 min at room temperature.
    d. Place the 96-well plate on a one-sided plate magnet for 2 min.
    e. Remove the supernatant carefully.
    f. Wash the 96-well-plates twice with 100 µL of 70% ethanol
    g. Wash the 96-well-plates once with 100 µL of 100% acetonitrile.
    h. Remove the 96-well-plates from the magnet and air dry for 2 min.
5. Protein digestion with LysC and trypsin.
    a. Add 10 µl digestion buffer to each well.
    b. Incubate samples over night at 27 °C. (PROBLEM 3)
    c. Add 100 µl buffer A to stop protein digestion.

    CRITICAL: The beads must be completely reconstituted in digestion buffer. DO NOT pipette up and down, as the beads will adhere to the pipette.

6. Sample purification and desalting with stop and go extraction tips (StageTips)
    a. Place two layers of styrenedivinylbenzene reverse-phase sulfonate (SDB-RPS) on top of each other and punch them out with the help of a modified syringe as described in [168, 169].
    b. Press the two double layers out of the syringe into a 200 µL pipette tip
    c. Add 50 µL methanol to equilibrate the SDB-RPS stop and go extraction tips (StageTips) and centrifuge at 800 g for 1 min (Rappsilber, Ishihama, & Mann, 2003).
    d. Wash the StageTips with 50 µL buffer B and centrifuge at 800 g for 1 min.
    e. Wash the StageTips twice with 50 µL buffer A and centrifuge at 800 g for 1 min.
    f. Pipette the samples on top of the StageTips and centrifuge at 400 g for 5 min.
    g. Wash the StageTips with 100 µL buffer A and centrifuge at 800 g for 1 min.
    h. Wash the Stage Tips twice with 50 µL buffer B and centrifuge at 800 g for 1 min.
    i. Dry the StageTips by centrifugation at 800 g for 10 min.

PAUSE POINT: Samples can be stored at 4 °C until further use.

7. Samples elution.
    a. Place the StageTips in a tips-to-well adapter placed on a 96-well plate suitable for LC-MSMS.
    b. Add 30 µL elution buffer to each StageTip.
    c. Place the plate with the StageTips in a centrifuge equipped with an adapter for 96-well plates that are suitable for your LC-MS system.
    d. Quickly spin down the elution buffer in the StageTips for 10 s to incubate the SDB-RPS material (+ peptides) with the elution buffer.
    e. Incubate the StageTips with the elution buffer for 30 min.
    f. Centrifuge the StageTips at 400 g for 5 min.
    g. Place the 96-well plates in the SpeedVac at RT for 45 min to remove the elution buffer.
    h. Reconstitute the peptides with 6 µL buffer R.

PAUSE POINT: Samples can be stored at -20 °C until further use.

2.2.5.3. LC-MSMS measurement

Timing: 40-100 samples per day (SPD)

For a detailed description of the label-free quantitative mass-spectrometry, please view Schmidt et al.

8. The setup and usage of liquid chromatography-mass spectrometer (LC-MS) instrumentation should be conducted according to the manufacturer's instructions.
    a. Add indexed retention time peptides (iRT) to each sample and monitor the iRT

       Peptides via Skyline to ensure stable LC performance.

    b. Inject 4 µL of each reconstituted peptide sample into a 30-cm in-house-packed analytical column filled with 1.9 µm C18-AQ Reprosil Pur beads (Dr. Maisch, Germany). Analyze the sample using an Ultimate 3000 (Thermo-Fisher Scientific, Waltham, USA) with an integrated column oven coupled to an Orbitrap Eclipse Tribid mass spectrometer equipped with an FAIMS-Pro interface (Thermo-Fisher Scientific, Waltham, USA).
    c. Inject a blank sample (buffer A) every 15th sample as a control for carry over.

Table 3 Peptide sequence, m/z, and molecular mass of iRT peptides.

iRT peptide	m/z (z=2)	mass [mol]	iRT peptide	m/z (z=2)	mass [mol]
LGGNEQVTR	487.2567	2.26E-06	TPVISGGPYEYR	669.8381	1.57E-06
GAGSSEPVTGLDAK	644.8226	1.78E-06	DGLDAASYYAPVR	699.3384	1.57E-06
TPVITGAPYEYR	683.8537	1.83E-06	YILAGVENSK	547.298	2.38E-06
VEATFGVDESNAK	683.8279	1.83E-06	GTFIIDPGGVIR	622.8535	1.77E-06
LFLQFGAQGSPFLK	776.9298	1.42E-06	ADVTPADFSEWSK	726.8357	1.51E-06
GTFIIDPAAVIR	636.8692	1.89E-06			

    d. Elute the peptides from the column using mobile phases A (0.1% FA in LC-grade water) and B (0.1% FA in 80% LC-grade ACN) keeping the column at a constant temperature of 50 °C.

e. Set LC-MS parameters as follows:

- LC column.

Table 4 LC column parameters.

Elution mode	One column separation
Separation column	in-house made fused silica emitter of 75 µm diameter, 15–30 cm length packed with 5 µm C18 Poroshell resin (Agilent, USA) in-house-packed analytical column of 75 µmdiameter, 30 cm length, packed with 1.9 µm C18-AQ Reprosil Pur beads (Dr. Maisch, Germany).
Column temperature	50 °C

- LC gradient parameters.

Table 5 LC parameters.

Time [min]	Duration [min]	Composition (%B)	Flow rate (µl/min)
0	0	3	450
1:30	1:30	3	450
2:30	1:00	8	450
23:30	21:00	30	400
26:00	2:30	55	400
26:30	0:30	95	400
31:00	4:30	95	400
32:00	1:30	3	400
34:30	2:30	3	400

- MS parameters.

Table 6 MS parameters

Application Mode	Peptide
Method Duration [min]	35
Infusion Mode	Liquid Chromatography
Exected LC Peak Width (s)	8
Default Charge state	2

- FAIMS Settings.

Table 7 FAIMS settings.

FAIMS Inner Electrode Temp [°C]	99.5
FAIMS Outer Electrode Temp [°C]	85.5
Total Carrier Gas Flow	Static
Total Carrier Gas Flow [L/min]	3.7

- MS1 scan.

Table 8 MS1 scan.

Detector type	Orbitrap
Orbitrap Resolution	15,000
Scan Range [m/z]	380-900
RF Lens [%]	40
Normalized AGC Target %	250
Maximum Injection Time [ms]	20
Data Type	Centroid
Polarity	Positive

- First DIA scan.

Table 9 First DIA scan.

Precursor Mass Range [m/z]	400-850
Isolation mode	Quadrupole
Isolation window [m/z]	15
Window overlap [m/z]	2
Number of Scan Events	30
Activation type	HCD
HCD Collision Energy	Normalized
HCD Collision Energy [%]	31
Detector type	Orbitrap
Orbitrap Resolution	15,000
Scan Range [m/z]	250-1700
RF Lens [%]	40
Normalized AGC Target %	1000
Maximum Injection Time [ms]	25
Data Type	Centroid
Polarity	Positive

- DIA m/z windows.

Table 10 First DIA scan m/z windows.

m/z Range	m/z Range	m/z Range	m/z Range
399.4314-416.4392	519.486-536.4937	639.5406-656.5483	759.5952-776.6029
414.4383-431-446	534.4928-551.5006	654.5474-671.5551	774.602-791.6097
429.4451-446.4528	549.4997-566.5074	669.5542-686.562	789.6088-806.6165
444.4519-461.4596	564.5065-581.5142	684.561-701.5688	804.6156-821.6233
459.4587-476.4665	579.5133-596.521	699.5679-686.562	819.6224-836.6302
474.4656-491.4733	594.5201-611.5297	714.5747-731.5824	834.6293-851.637
489.4724-506-4801	609.5269-626.5347	729.5815-746.5829	
504.4792-521.4869	624.5338-641.5415	744.5883-761.5961	

- MS1 scan as described before.
- Second DIA scan.

Table 11 Second DIA scan.

Precursor Mass Range [m/z]	392.5-857.5
Isolation mode	Quadrupole
Isolation window [m/z]	15
Window overlap [m/z]	2
Number of Scan Events	30
Activation type	HCD
HCD Collision Energy	Normalized
HCD Collision Energy [%]	31
Detector type	Orbitrap
Orbitrap Resolution	15,000
Scan Range [m/z]	250-1700
RF Lens [%]	40
Normalized AGC Target %	1000
Maximum Injection Time [ms]	25
Data Type	Centroid
Polarity	Positive

- DIA m/z windows.

Table 12 Second DIA scan m/z windows.

m/z Range	m/z Range	m/z Range	m/z Range
391.4278-408.4355	511.4824-528.4901	631.5369-648.5447	751.5915-768.5992
406.4346-423.4424	526.4892-543.4696	646.5438-663.5515	766.5983-783.6061
421.4414-438.4492	541.496-558.5038	661.5506-678.5583	781.6052-798.6129
436.4483-453.456	556.5028-573-5106	676.5574-693.5651	796.612-813.6197
451.4551-468.4628	571.5097-588.5174	691.5642-708.572	811.6188-828.6265
466.4619-483.4696	586.5165-603.5242	706.5711-723.5788	826.6256-843.6334
481.4687-498.4765	601.5233-618.531	721.5779-738.5856	
496.4756-513.4833	616.5301-633.5379	736.5847-753.5924	

2.2.5.4. Data processing

Timing: 60 SPD

9. Process the acquired DIA spectra using software packages such as DIA-NN, MaxQuant, or Spectronaut according to the instructions as described in [170], [171], and [164].
    a. Convert RAW data into '.dia' format.
    b. Set the following parameters for RAW data analysis: digestion with trypsin/P and one missed cleavage. Select a current UniProt FASTA database (we used UniProt *Mus musculus* database Sep. 2017).
    c. Adjust precursor and fragment ion *m/z* range according to the MS settings; typical *m/z* ranges would be 400–1000 and 350–1600, respectively.
    d. Create the main output of the data and the output library in the correct directory.
    e. Set the precursor FDR to 1% and select the thread settings according to the available cores.
    f. Mass accuracy is calculated by DIA-NN.
    g. Set 'MBR', 'Heuristic protein inference', and 'No shared spectra' as active.
    h. Choose 'protein names (from FASTA)' for protein inference settings.
    i. Choose 'double-pass mode' for the neural network classifier.
    j. Choose 'high precision' for the quantification strategy.

k. Set Cross-run normalization, Library generation, and Speed and RAM to the default parameters.

l. For additional information add '--report-lib-info'option.

NOTE: The time required to process the data highly depends on the number of samples, LC-MS instrument, gradient length, and the CPU.

2.2.5.5. Bioinformatical analysis: Generation of protein profiles

Timing: 120 profiles per day

10. Data preprocessing

a. Read and subset the data to normalizing strategies

```
library(samr)
library(vsn)
library(ggplot2)
library(gplots)
library(slider)
library(openxlsx)
library(preprocessCore)
### Data reading and preprocessing
#read data and subset columns
data <- read.xlsx("Dataset1_sorted.xlsx")
data.cols <- sapply(strsplit(colnames(data),"_"),function(x) x[1])
#generate data subsets
data.x <- list(
        GENES=data[,which(data.cols == "GENES")],
        GENESnorm=data[,which(data.cols == "GENESnorm")],
        GENESquant=data[,which(data.cols == "GENESquant")],
        MaxLFQ=data[,which(data.cols == "MaxLFQ")],
        PG.Norm=data[,which(data.cols == "PG.Norm")],
        PG.Quant=data[,which(data.cols == "PG.Quant")],
        rest=data[,grep("^S",data.cols)])
```

f. Normalize data to the sum intensity in each slice. (PROBLEM 4)

```
#extract the PG Quant data, preprocess, and normalize data
tmp <- as.matrix(data.x$PG.Quant)            #ensure that table is a matrix
tmp[which(!is.finite(tmp))] <- NA  #remove any value that is not finite i.e. Inf or NaN
tmp[which(tmp < 1e4)] <- NA                  #set low intensity measures to NA
rownames(tmp) <- data$Protein.Group
cannot <- data.frame(id=colnames(tmp),soleus=sapply(strsplit(colnames(tmp),"_"),function(x)
x[2]),slice=sapply(strsplit(colnames(tmp),"slice"),function(x) as.numeric(x[length(x)])))
rownames(cannot) <- cannot$id
#calculate total remaining intensity
cannot$int <- colSums(tmp,na.rm=T)
#ensure all retained samples have an intensity
tmp <- tmp[,which(cannot$int != 0)]
#subset column annotation to same size of dataset
cannot <- cannot[which(cannot$int != 0),]
#VSN normalize the data
tmp.quant <- justvsn(as.matrix(tmp))
#correct for total intensity
tmp.norm <- tmp.quant-log2(cannot$int)
### Data reading and preprocessing END
```

11. Introduce a sliding window to evaluate missing values. (PROBLEM 5)

```
### Evaluating missings
data.full.s <- tmp.norm
cannot.s <- cannot
#calculate sample specific missing values
data.col.na <- apply(data.full.s,2,function(x) length(which(is.na(x)))/length(x))
#generate sliding window NA count
slideNA <- tapply(rownames(cannot.s),cannot.s$soleus,function(x){
        naprot <- apply(data.full.s[,x],1,function(z){
                return(slide_dbl(z,function(k) length(which(is.na(k)))/length(k),.after=10,.complete=T))
        })
        return(naprot)
})
#select proteins based on sliding Window and a 70% data rate
selectedProteins <- names(which(rowMeans(sapply(slideNA,function(x) apply(x,2,min,na.rm=T))) <= 0.3))
### Evaluating missings END
```

12. Impute missing values. (PROBLEM 6)

g. Impute all missing values using the sliding window.

```
### Imputing missing values
#imputing values across a spatial profile using sliding windows
imputeProteomics_byDistance <-
function(datax,annot,slice.width.forward=10,slice.width.backward=10,newfit.na="impute",sel=0.05, m.offset=1.6,sd.offset=0.8,
min.data.required=3){
	annot <- annot[colnames(datax),]
	newdatx <- by(t(datax),annot$soleus,function(x){
		.pos <<- x
		slice <- annot[rownames(x),"slice"]
		slicex <- seq(min(slice),max(slice),by=1)
		names(slicex)[match(slice,slicex)] <- rownames(x)
		newx <- apply(x,2,function(z){
			.pos2 <<- z
			names(z) <- rownames(x)
			if(any(is.na(z))){
				allx <-
slide(slicex,~list(start=.x[1],stop=.x[length(.x)],pos=length(na.omit(names(.x)))),.before=slice.width.backward,.after=slice.width.for
ward,.complete=F)
				allx <- allx[which(!is.na(names(allx)))]
				allxs <- data.frame(start=sapply(allx,function(x) x$start),stop=sapply(allx,function(x)
x$stop),len=sapply(allx,function(x) x$pos))
				rownames(allxs) <- names(allx)
				allx <- subset(allxs,len > min.data.required)
				allx <- allx[names(which(is.na(z))),]
				allx <- subset(allx,!is.na(start))
				allx$pos_real <- rownames(allx)
				if(nrow(allx) > 0){
					newfits <- apply(allx,1,function(l){
						.pos3 <<- l
						pos <-
na.omit(names(slicex[match(as.numeric(l[1]):as.numeric(l[2]),slicex)]))
						tmpf <- data.frame(prot=z[pos],annot[pos,])
						tmp <- subset(tmpf,!is.na(prot))
						if(nrow(tmp) >= min.data.required){
							lmr <- lm(prot~slice,data=tmp)
							pred <-
predict(lmr,newdata=data.frame(slice=tmpf$slice))
							pred[pred < min(x,na.rm=T)] <- NA
							names(pred) <- rownames(tmpf)
							return(pred[l["pos_real"]])
						}else{
							if(newfit.na == "impute"){
								zr <- range(z,na.rm=T)
								xx <- as.matrix(x)
								xm <- xx[which(xx > zr[1] & xx < zr[2])]
								return(rnorm(1,mean=mean(xm,na.rm=T)-
m.offset*sd(xm,na.rm=T),sd=sd(xm[which(xm < quantile(xm,probs=sel,na.rm=T))],na.rm=T)*sd.offset))
							}else{
								return(NA)
							}
						}
					})
					names(newfits) <- rownames(allx)
					z[names(newfits)] <- newfits
					return(z)
				}else{
					return(z)
				}
			}else{
				return(z)
			}
		})
		return(newx)
	})
	newdatx <- do.call(rbind,newdatx)
	return(t(newdatx))
}
```

h. Use only proteins with enough data points.

```
#only use proteins with enough data
data.norm <- data.full.s[match(selectedProteins,rownames(data.full.s)),]
#impute by distance and a simple linear model, forward and backward slices tell it "how far to go" on
a "per slice basis" (not on a per available sample basis)
data.norm <- imputeProteomics_byDistance(data.norm,cannot.s,slice.width.forward=10,
slice.width.backward=10,min.data.required=3,newfit.na="none")
#impute whatever couldn't be imputed to the lower 5% of the data
data.norm <- perseus.impute(data.norm)
data.norm <- data.norm[,rownames(cannot.s)]
### Imputing missing values END
```

13. Bootstrap analysis to compress or stretch biological replicates.

i. Identification of proteins changing over the tissue. (PROBLEM 7)

```
### Evaluate the need for compression ratios between samples
#identify proteins that change across slice
res <- lapply(unique(cannot.s$soleus),function(x){
        tmp <- subset(cannot.s,soleus == x)
        dat.tmp <- data.norm[,rownames(tmp)]
        data.sam <-
list(x=dat.tmp,y=tmp$slice,genenames=rownames(dat.tmp),geneid=rownames(dat.tmp),logged2=T)
        samr.obj <- samr(data.sam,resp.type="Quantitative",nperms=1000)
        delta.table <- samr.compute.delta.table(samr.obj)
        sig <- samr.compute.siggenes.table(samr.obj,1,data.sam,delta.table,all.genes=T)
        return(list(data=data.sam,samr=samr.obj,delta.table=delta.table,sig=sig))
})
names(res) <- unique(cannot.s$soleus)
scores <- lapply(lapply(res,function(x) rbind(x$sig$genes.up,x$sig$genes.lo)),function(x) { tmp <-
as.numeric(x[,4]); names(tmp) <- x[,2]; return(tmp)})
scores <- do.call(cbind,lapply(scores,function(x) x[order(names(x))]))
#assign new variables to evaluate different thresholds
data.final <- data.norm[,rownames(cannot.s)]
scores2 <- scores
#identify which proteins follow similar trajectories between samples
scores2.s <- scores2[,as.character(unique(cannot.s$soleus)),drop=F]
scores2.s <- cbind(scores2.s,abs(apply(scores2.s,1,function(x) sum(diff(x)))))
scores2.sm <- data.frame(mean=apply(scores2.s[,-ncol(scores2.s)],1,mean),absdiff=abs(apply(scores2.s[,-
ncol(scores2.s)],1,function(x) sum(diff(x)))))
scores2.sm$fscore <- scores2.sm[,1]*(1/scores2.sm[,2])
scores2.smo <- scores2.sm[order(abs(scores2.sm$fscore),decreasing=T),]
cannot.s2 <- do.call(rbind,by(cannot.s,cannot.s$soleus,function(x){ x$perc <- (x$slice2-
min(x$slice2))/(max(x$slice2)-min(x$slice2)); return(x)}))
rownames(cannot.s2) <- gsub("S\\d\\.","",rownames(cannot.s2))
#create comparison table between all samples
cmb <- combn(ncol(scores2.s)-1,2)
#setup data
cannot.s2 <- cannot.s2[order(cannot.s2$soleus,cannot.s2$perc),]
data.final <- data.final[,rownames(cannot.s2)]
```

j. Calculate the median compression ratio. (PROBLEM 8)

```
#calculate compression ratios between samples using smoothed profiles and a delay strategy
scores2.smo.s <- subset(scores2.smo,abs(mean) > 5)
bxs <- sapply(rownames(scores2.smo.s), function(dx){
	lns <- lapply(unique(cannot.s2$soleus),function(x){
		ct <- subset(cannot.s2, soleus == x)
		dd <- data.final[dx,rownames(ct)]
		los <- loess(y~x,data=data.frame(y=dd,x=ct$perc))
		prd <- predict(los,newdata=data.frame(x=seq(0,1,len=5000)))
		return(data.frame(soleus=x,x=seq(0,1,len=5000),y=prd))
	})
	lns.dat <- sapply(lns,function(x) x$y)
	colnames(lns.dat) <- sapply(lns,function(x) x$soleus[1])
	cors <- sapply(seq(-2500,-1,by=1),function(x){
		res <- c()
		for(i in 1:ncol(cmb)){
		t1 <- lns.dat[x:0,cmb[1,i]]
		t2 <- lns.dat[1:min(c(x+5000,5000)),cmb[2,i]]
		t3 <- lns.dat[x:0,cmb[2,i]]
		t4 <- lns.dat[1:min(c(x+5000,5000)),cmb[1,i]]
		res <- c(res,cor(t1,t2),cor(t3,t4))
		}
		return(res)

	})
	cors.up <- cors[seq(1,nrow(cors),by=2),,drop=F]
	cors.lo <- cors[seq(2,nrow(cors),by=2),,drop=F]
	fix.lo <- apply(cors.lo,1,function(x) seq(0,1,len=5000)[abs(seq(-2500,-1,by=1)[which.max(x)])])
	fix.up <- apply(cors.up,1,function(x) seq(0,1,len=5000)[abs(seq(-2500,-1,by=1)[which.max(x)])])
	fix <- rbind(fix.lo,fix.up)
	colnames(fix) <- apply(cmb,2,paste,collapse="-")
	return(fix)
})
#across selected proteins to identify compression ratios create a median compression ratio and select
the right stretch/compress strategy
final.fix <- rowMedians(bxs)
final.fix <- matrix(final.fix,nrow=2)
colnames(final.fix) <- apply(cmb,2,paste,collapse="-")
rownames(final.fix) <- c("lo","up")
touse <- final.fix[,grep("1",colnames(final.fix)),drop=F]
sol.names <- unique(cannot.s2$soleus)
names(sol.names) <- 1:(ncol(scores2.s)-1)
cannot.s2$perc2 <- cannot.s2$perc
for(i in 1:ncol(touse)){
	p <- which.max(touse[,i])
	#p <- 2
	n <- strsplit(colnames(touse)[i],"-")[[1]]
	n <- sol.names[as.character(n)]
	if(p == 1){
		cannot.s2$perc2[which(cannot.s2$soleus == n[2])] <-
cannot.s2$perc2[which(cannot.s2$soleus == n[2])]-touse[p,i]
	}else{
		cannot.s2$perc2[which(cannot.s2$soleus == n[2])] <-
cannot.s2$perc2[which(cannot.s2$soleus == n[2])]+touse[p,i]
	}
}
### Evaluate the need for compression ratios between samples END
```

14. Create final data. (PROBLEM 9)

```
### Create final dataset
#helper functions
myloess <- function (x, y = NULL, nsigma = 1, newdata=data.frame(x=dis), ...)
{
        xy <- xy.coords(x, y)
        x <- xy$x
        x0 <- sort(x)
        y <- xy$y
        nsigma <- as.numeric(nsigma)
        mod <- loess(y ~ x, ...)
        yfit <- predict(mod, newdata)
        r <- residuals(mod)
        modr <- loess(I(r^2) ~ x, ...)
        sd <- sqrt(pmax(0, predict(modr, newdata)))
        list(model = mod, x = x0, y = yfit, sd = sd, upper = yfit +
        nsigma * sd, lower = yfit - nsigma * sd)
}
range01 <- function(x){(x-min(x,na.rm=T))/(max(x,na.rm=T)-min(x,na.rm=T))}
adjust <- function(x,annot,norange=F){
        x <- x[,rownames(annot)]
        newx <- do.call(cbind,by(t(x),annot$soleus,function(x) t(scale(x))))
        if(!norange)
                newx <- t(apply(newx,1,range01))
        return(newx[,rownames(annot)])
}

#create final dataset
profileDat <- list(
        full.z.2=adjust(data.final[,-match(crem,colnames(data.final))],cannot.use,norange=T),
        full.zr.2=adjust(data.final[,-match(crem,colnames(data.final))],cannot.use)
)
### Create final dataset END
```

NOTE: The time is highly dependent on the data set because of the following variables: number of proteins within the data set, missing values within the data set, and biological replicates. The time is also dependent on the used CPUs. Steps are suitable for parallel processing.

2.2.5.6. Bioinformatical analysis: Generation of distance-based network

Timing: 120 profiles per day

15. Calculate distance-delay correlation (PROBLEM 10)

    a. Use multicore if possible

```
#use apply with a progressbar
library(pbapply)
#use igraph libraby for convenience
library(igraph)
#use multicore where possible
library(parallel)
#extract the specific dataset to use
dd <- profileDat[["full.zr.2"]]
#get all pairwise combinations of proteins
cmb <- combn(rownames(data),2)
cl <- makeCluster(15) #15 cores were used
#export the data to the parallel instances
clusterExport(cl,c("data","delayc"))
```

    b. Calculate delay for all protein profiles

```
#code that calculates the delay correlation
delayc <- function(x,y,delayt=length(x)/10*4.5,plot=F,method="s",delayx=0.2){
        delayt <- floor(delayt)
        cor1 <- c()
        cor2 <- c()
        for(i in delayt:length(x)){
                tmp <- cor(x[1:i],y[(length(x)-i+1):length(x)],method=method)
                tmp2 <- cor(y[1:i],x[(length(x)-i+1):length(x)],method=method)
                cor1 <- c(cor1, tmp)
                cor2 <- c(cor2, tmp2)
                if(plot){
                        par(mfrow=c(1,2))
                        plot(x[1:i],ylim=c(min(x,y),max(x,y)),type="l",main=round(tmp,3))
                        lines(y[(length(x)-i+1):length(x)])
                        plot(y[1:i],ylim=c(min(x,y),max(x,y)),type="l",main=round(tmp2,3))
                        lines(x[(length(x)-i+1):length(x)])
                        Sys.sleep(delayx)
                }

        }
        corr <- c(cor1,rev(cor2))
        #which(corr == max(corr))
        names(corr) <- c(rev(-
seq(0,floor(length(corr)/2),length=length(corr)/2)),seq(0,floor(length(corr)/2),length=length(corr)/2))
        corr <- corr[-which(names(corr) == 0)[1]]
        names(corr) <- -floor(length(corr)/2):floor(length(corr)/2)
        return(corr)
}

#calculate the delays for all proteins
dl <- pbapply(cmb,2,function(x) delayc(data[x[1],],data[x[2],],plot=F),cl=cl)
#extract those that have the highest correlation
dlx2 <- data.frame(t(cmb),delay=apply(dl,2,function(x)
as.numeric(rownames(dl)[which.max(x)])),corr=apply(dl,2,max))
```

c. Remove proteins with a delay greater than 20 μm

```
#remove any with a delay greater than 20
dlx2.s <- subset(dlx2,delay > -20 & delay < 20)
#create the inverse connection, i.e. a -> b and put in b -> a with a switched around delay
dlx3 <- rbind(dlx2.s,data.frame(X1=dlx2.s$X2,X2=dlx2.s$X1,delay=dlx2.s$delay*-1,corr=dlx2.s$corr))
dlx4 <- subset(dlx3,delay >= 0)
rownames(dlx4) <- paste(dlx4[,1],dlx4[,2],sep="-")
#use a graph representation for quick access
graph <- graph_from_data_frame(dlx4,directed=T)
#function to remove unecessary connections
#What this does is look at all possible triplet combinations
#First it identifies the neighbours in the graph of the 2 nodes passed
#Then identifies whether there is an intersect between the two suggesting that other nodes might carry more information than this connection
#Then it extracts the data and looks for delays that are greater than 0, and where the sum of delay is below the percentage of dpi added to the current delay. So if the delay is 5 it looks for whether the sum of the delay of the other 2 connections is below that. Also the correlation needs to be on average greater than the current correlation-dpi.
#It then returns whether there is a better combination of nodes than the current one (T/F)
dpi <- function(x,y,graph=gg,dat=dlx3,dpi=0.1){
        require(igraph)
        x_n <- names(neighbors(graph,x,mode="out"))
        y_n <- names(neighbors(graph,y,mode="in"))
        i_n <- intersect(x_n,y_n)
        cur_edge <- paste(x,y,sep="-")
        alt_edge1 <- paste(x,i_n,sep="-")
        alt_edge2 <- paste(i_n,y,sep="-")
        cur_d <- dat[cur_edge,"delay"]
        if(cur_d < 0)
                return(match(cur_edge,rownames(dat)))
        cur_c <- dat[cur_edge,"corr"]
        alt_d <- cbind(e1=dat[alt_edge1,"delay"],e2=dat[alt_edge2,"delay"])
        alt_c <- cbind(e1=dat[alt_edge1,"corr"],e2=dat[alt_edge2,"corr"])
        alt_d <- cbind(alt_d,s=rowSums(alt_d))
        alt_c <- cbind(alt_c,s=rowMeans(alt_c))
        sel <- which(alt_d[,1] > 0 & alt_d[,2] > 0 & alt_d[,3] < cur_d*(1+dpi) & abs(alt_c[,3]) >= abs(cur_c)-
dpi)
        if(length(sel) > 0){
                return(T)
        }else{
                return(F)
        }
}
#another cluster with more cores
#cl <- makeCluster(100) #100 core cluster
clusterExport(cl,c("graph","dlx4","dpi"))
#identify whether the current combination is ideal or whether other combinations exist that are better, TRUE means there is something better, FALSE means there isn't anything better. Hence we would like to extract all FALSE entries
res <- pbapply(dlx4,1,function(x) dpi(x[1],x[2],graph=graph,dat=dlx4),cl=cl)
#extract FALSE entries
dlx4.s <- dlx4[which(!res),]
#add an inverse delay for better plotting in cytoscape
dlx4.s$delay_inv <- 1/(dlx4.s$delay+1)
#write the file as CSV and load into cytoscape
write.csv(dlx4.s,"InteractionNetwork_2023.04.21.csv",quote=F)
```

d. Visualization was performed in cytoscape.

2.2.6. Expected outcomes

2.2.6.1. Cryotome sectioning

Cryo-embedded soleus muscles and consecutive cross-sections prepared from the central to distal areas using a cryotome (**Figure 20A, B**). For tissues with a length of 3.5 mm, there will be 175 consecutive 20 µm-thick sections.

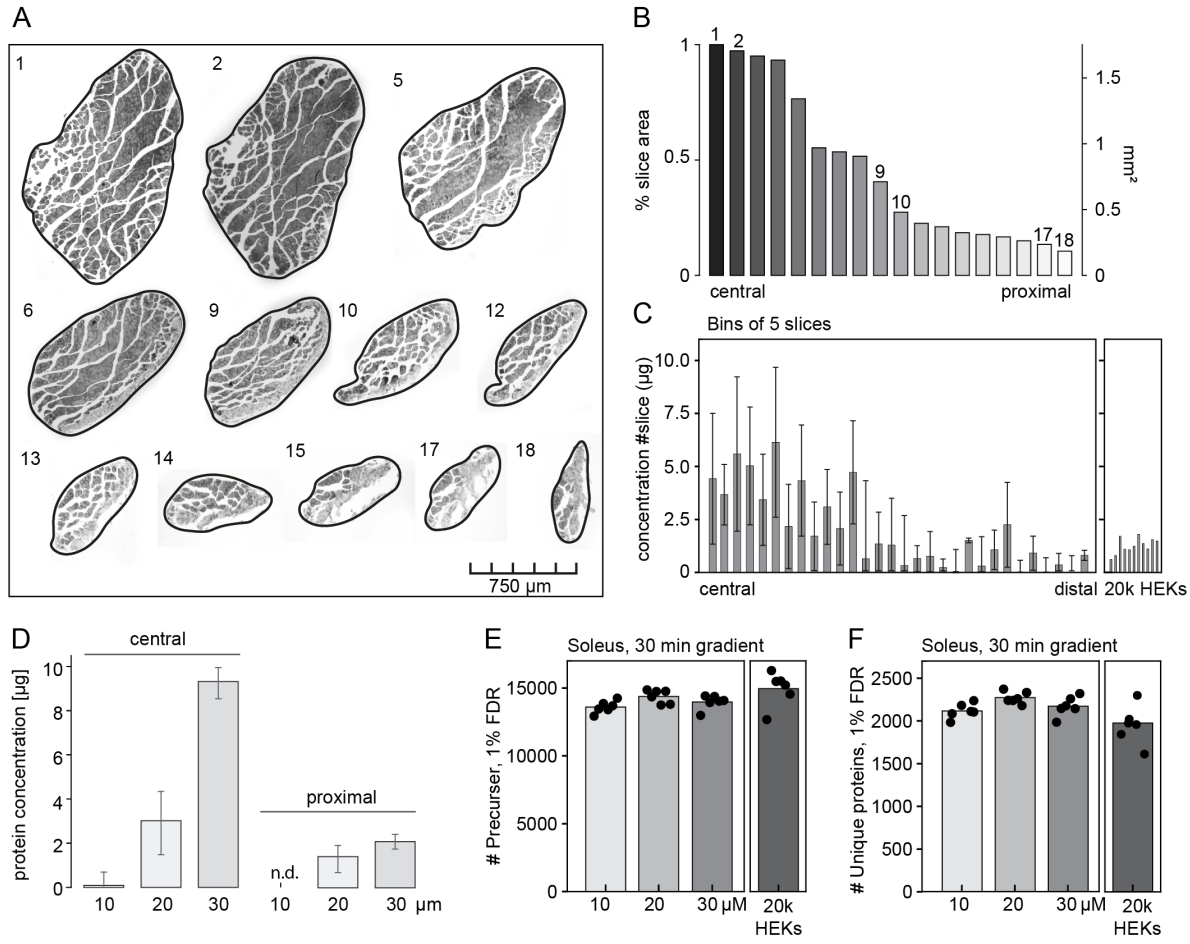

Figure 20 Expected outcomes for muscle sectioning and protein lysis. A) Muscle sections from central muscle (1) to proximal end. **B**) Slice area of central muscle to the proximal end **C**) and the correlating total protein input amount per section. **D**) Total protein input amount per 10-30 µm thick section. **E**) Identified peptides and **F**) proteins per 10-30 µm thick section.

2.2.6.2. Tissue lysis and digestion and LC-MS/MS analysis

For a 20 µm-thick tissue section with an area of approximately 1.7 mm^2, 4 µg of protein can be expected. For tissues with a smaller area, it is recommended to use thicker sections; thinner sections can be used to obtain a higher resolution over the length of the tissue. The distal (tendon) slices have an area of less than ~0.2 mm^2 and yield less than 1 µg protein (**Figure 20B-D**). Even though the input variances of 10–30 µm are relatively large, the LC-MS performance should be stable and identify in high dynamic ranged tissue around ~2000 proteins per 20-µm-thick section (**Figure 20E, F**).

2.2.6.3. Bioinformatical analysis

Depending on the tissue type, heterogeneity, and sample size, a data set of > 7,000 proteins can be expected. For tissues with high heterogeneity in terms of cell distribution, missing values are to be expected — especially between the different tissue types. Additionally, a variety between tissue lengths can be expected with slightly different protein profile lengths because of biological variability of the skeletal muscle length. Over 3,000 protein profiles can be expected depending on the sensitivity of the instrument.

2.2.6.4. Limitations

The protocol may not be ideal or particularly beneficial for all types of tissues. In cases where tissues exhibit low heterogeneity or lack distinct regions, such as in the liver, the advantages of this protocol may be minimal. The effectiveness of the protocol is highly dependent on the resolution required for the specific tissue and its regions. In some instances, limitations due to the sensitivity of the instruments used may exist. Additionally, the depth of proteomic analysis is significantly influenced by the capabilities of the mass spectrometry (MS) instrument employed.

Furthermore, biological variability within a group of replicates (animals) can be more pronounced in these studies compared to other research that focuses on intact tissues. This increased variability can complicate interpretation of the results and potentially obscure meaningful differences. Consequently, careful consideration must be given to the choice of tissue type and the specific requirements of the study to ensure that the application of this protocol is both appropriate and effective.

2.2.7. Troubleshooting

Problem 1:

The cork mat should be removed very carefully, otherwise the cryo-matrix and the tissue could be damaged.

Potential solution 1:

- Place enough cryomatrix between the tissue and the cork mat to prevent the tissue from freezing directly to the cork. It is also possible to first fill the lower half of the cryomold with Tissue-Tek and cool the cryomold until the cryomatrix is slightly frozen. Then, position the tissue on top of the frozen cryomatrix, embed the tissue completely with Tissue-Tek, and completely freeze the cyromatrix. Care must be taken here to ensure that the cryomaterial freezes evenly.
- Alternatively, the tissue can also be placed on a PDVF membrane. By pressing the tissue tightly to the membrane, the tissue is fixed in the correct position.

Problem 2:

Empty MS measurements because of sample loss during transfer or protein extraction.

Potential solution 2:

- Visually check that all the wells contain a cryosection.
- Perform an additional centrifugation step before adding lysis buffer to move the sections to the bottom of the well.
- As an alternative to Tissue-Tek, formaldehyde-fixed paraffin-embedded tissue (FFPE) can also be used. In this case, the lysis buffer can be added before the section is transferred to the plate. The protein extraction protocol should be adjusted for FFPE sections.

Problem 3:

Magnetic Sera-Mag beads stick to the wall.

Potential solution 3:

- Lysis buffer can be added several times to the tube to wash the beads from the wall of the well.

- Before the overnight digest, shake the 96-well plate on 1,300 rpm for 10 min on 37 °C.

Problem 4:

Protein input variability across the tissue samples. Since label-free quantification (LFQ) works optimally for similar samples, variation in the amount and composition of the skeletal muscle and tendon areas could interfere with the normalization and LFQ quantification.

Potential solution 4:

- Normalization can be performed by dividing the individual protein intensities by the sum of the protein intensity per slice. This ensures that all protein intensities become relative to the total intensity.
- Normalize to a housekeeping protein. If the tissue heterogeneity is minimal, normalization of the protein intensities to a house-keeping gene like actin or tubulin may be an alternative.
- Spike in heavy peptides. Isotope-labeled peptides, used in the same concentration in all samples and are detected in the MS instruments, can be used to normalize peptide and protein intensities.
- Total ion chromatogram (TIC) normalization: Samples can be measured using very short gradients in MS1 mode. The TIC can be then used to adjust the injection volume.

Problem 5:

Selection of protein profiles with missing values.

Potential solution 5:

- To generate protein profiles that are as valid and complete as possible, only proteins that were detected in at least 70% of all data points (in this case, slices) should be selected.
- For tissues with high heterogeneity, it is recommended to use a sliding window approach as described in **Schmidt et al.** The sliding window size can be adapted and can cover 5-20 sections.

Problem 6:

Imputation of missing data requires an adjustment of data points from the adjacent slices for linear modeling.

Potential solution 6:

- The minimum number of datapoints should not be less than 5 to ensure enough data points are present for imputation.

Problem 7:

We used a bootstrapping approach based on the R package samr [125] to identify which proteins can be used for alignment between the different muscles. This ensures identification of proteins with strong increasing or decreasing trends that are suitable for alignment. This procedure can be replaced by other approaches.

Potential solution7:

- Several statistical approaches have been proposed to identify features that align with various profiles. Alternative examples are: BETR (Bayesian Estimation of Temporal Regulation) [172], Mutual Information [173], correlation [173], and ANOVA [174].

Problem 8:

Protein profiles are not smooth enough.

Potential solution 8:

- When creating profiles, we use the loess function to generate local average slopes. The span parameter allows for fewer or more samples to be included, which changes the smoothness of the profiles that are generated.
- Alternative smoothing functions such as smooth, Spline, lowess, and approx within R can also be utilized.

Problem 9:

Delays between features are too high.

Potential solution 9:

- When calculating the delay between two features, the approach shifts one profile against the other. When the number of delays is too high, the number of samples included in the correlation goes towards zero, which often leads to an increase in the correlation towards 1. This issue can be handled with the *delayt* parameter within the *delayc* function.

2.2.8. Resource availability

Lead contact: Further information and requests for resources and reagents should be directed to and will be fulfilled by the lead contact, Marcus Krüger (Marcus.krueger@uni-koeln.de).

Technical contact: Technical questions on executing this protocol should be directed to and will be answered by the technical contact, Luisa Schmidt (luisa.schmidt@uni-koeln.de).

Materials availability:

- This study did not generate new unique reagents.

Data and code availability:

- The published article includes all datasets and code generated or analysed during this study.

2.2.9. Acknowledgments

This work was supported by the Cologne Cluster of Excellence on Cellular Stress Responses in Aging-associated Diseases (CECAD) EXC 299/2, the RELOC graduate school GRK 2550 (DFG 411422114) and FOR2722/2 (Krüger_384170921/TP4, KR 3788/8-2). In addition, this work was supported by a major invest grant from the Deutsche Forschungsgemeinschaft (INST 216/1163-1 FUGG and INST 216/1020-1 FUGG) and the JPND2019-466-146 grant.

2.2.10. Author contributions

Conceptualization, L.S., M.K.; Methodology, L.S., M.K., Software, L.S., P.A., Formal Analysis, L.S., P.A., Investigation L.S., Resources, M.K., Visualization, L.S., Supervision, Project Administration M.K.; Funding Acquisition, M.K..

2.3. Prepared manuscript III: Comprehensive protein profiling using spatial proteomics of the diaphragm reveals structural changes in neuromuscular junctions with increasing age and amyotrophic lateral sclerosis (ALS)

Luisa Schmidt[1], Sina Panschar[1], Christian Hoegsbjerg[2], Abigail Mackey[2], Philipp Antczak[1,3], Tal Gradus-Pery[4], Eran Perlson[4,5], Marcus Krüger[1,3$]

[1] Institute for Genetics, Cologne Excellence Cluster on Cellular Stress Responses in Aging-Associated Diseases (CECAD), Cologne, Germany
[2] Institute of Sports Medicine Copenhagen, Department of Orthopaedic Surgery, Copenhagen University Hospital - Bispebjerg and Frederiksberg, Copenhagen, Denmark (Part of IOC Research Center Copenhagen) and Department of Clinical Medicine, Faculty of Health and Medical Sciences, University of Copenhagen, Denmark
[3] Center for Molecular Medicine (CMMC), University of Cologne, 50931 Cologne, Germany
[4] Sackler Faculty of Medicine, Tel-Aviv University, Tel-Aviv, Israel
[5] Sagol School of Neuroscience, Tel-Aviv University, Tel-Aviv, Israel

$ Correspondence: MK Marcus Krüger (marcus.krueger@uni-koeln.de)
Lead Contact: Marcus Krüger, marcus.krueger@uni-koeln.de

This manuscript is so far not available September, 2024

2.3.1. Summary preprint publication III

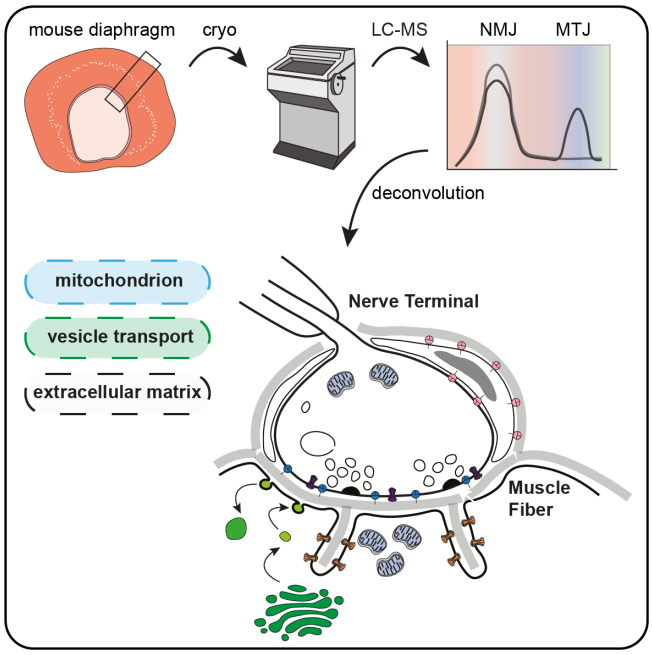

Figure 21 Graphical abstract publication III.

The workflow to acquire protein profiles over the longitudinal axis of the diaphragm skeletal muscle. The profiling starts with the isolation of the diaphragm, cryo embedding and slicing. The data for the protein profiles were generated using proteomics. This approach makes it feasible to spatially resolve protein localization at the junction between motor endplate and muscle.

LC-MS, liquid chromatography-mass spectrometry; MTJ, myotendinous junction; NMJ, neuromuscular junction.

The thoracic diaphragm contracts and flattens, being vital for respiration. Morphological studies of the diaphragm have provided a detailed view of its architecture consisting of parallel skeletal muscle fibers, a central ring of neuronal innervation, including the neuromuscular junction (NMJ) units and a muscle-tendon transition (MTJ) area. Although immunohistochemical (IHC) approaches showed the protein expression of selected candidates, there is no unbiased spatial proteomic profiling approach of the diaphragm. Here, we generated thin cryo sections of the mouse diaphragm and measured each section with short LC-MS gradients. We generated 3000 diaphragm protein profiles which allowed us to precisely localize the position and the protein expression of the NMJ and MTJ (**Figure 21**). Next, we used our profiling to investigate the molecular changes of the NMJ during aging. Compared to young control profiles, aged diaphragm shows a more widespread expression of several known NMJ marker proteins, including the myelin associated glycoprotein (MAG). To investigate the process of neurodegeneration in the diaphragm, we performed spatial proteomics of a TDP43-dependent ALS model. The elevated expression of a human TDP43 variant without the nuclear localization signal (NLS) in neurons induces an increased protein expression of proteins associated to endocytosis and protein degradation at the NMJ. Similar to the structural change of aged diaphragm, the TDP43 mouse model also showed an increased width of the NMJ. Overall, the use of thin cryotome sections and their LC-MS analysis is a versatile approach to generate a spatial proteome along the muscle-tendon axis

and the approach enabled us to characterize the molecular composition of NMJ and MTJ under normal, aged, and disease-related conditions.

2.3.2. My contributions to preprint publication III

As the first author of the preprint, I performed isolation, preparation, sectioning, and digestion of the muscles together with Sina Pascher. I optimized the MS instrumentation and method set up as well as ensured stable data acquisition. Implementation of the bioinformatic analysis workflow and distance-based network analysis was performed by Philipp Antczak and me. Immunohistochemistry staining, imaging, and figure preparation of longitudinal muscle sections were performed by Christian Hoegsbjerg, Abigail Mackey, and me. I assembled all the figures and wrote the manuscript together with Marcus Krüger.

2.3.3. Introduction

The diaphragm, the skeletal muscle of the respiratory system, is located between the thorax and the abdominal cavity and ensures rhythmic respiratory movement. Due to its continuous contraction, the diaphragm has a higher density of neuromuscular junctions (NMJs) compared to other skeletal muscles of the limbs.[175] The phrenic nerve, a bilateral structure that innervates the diaphragm, plays a key role by providing motor innervation and sensory feedback, particularly to the central tendon of the diaphragm.[176]

Synaptic transmission at the NMJ starts when an action potential reaches the presynaptic terminal of a motor neuron, causing the neurotransmitter acetylcholine (ACh) to be released and diffuse across the synaptic cleft. ACh then binds to nicotinic acetylcholine receptors (nAChRs) on the muscle fiber's cell membrane, inducing a postsynaptic action potential. This activation triggers sarcolemmal voltage-gated dihydropyridine receptors (DHPRs) and ryanodine receptors (RYRs), leading to the release of calcium from the sarcoplasmic reticulum. Calcium binds to troponin C and induces skeletal muscle contraction.[177, 178] The motor endplates are mainly located in a characteristic "band" in the middle of the diaphragm, where they form specialized nerve-muscle contact sites that form numerous boutons.

Motor endplates are primarily located in a characteristic band in the middle of the diaphragm, where they form specialized nerve-muscle contact sites with numerous boutons. The gap between the motor neuron and the fiber, known as the synaptic basal lamina, contains a specialized extracellular matrix crucial for NMJ structural integrity, including various laminins and collagens.[178] One example is the acetylcholinesterase collagenic tail peptide

(COLQ), which anchors acetylcholinesterase (AChE) to the basal lamina, terminating synaptic transmission by breaking down acetylcholine. Schwann cells, the glial cells of the peripheral nervous system, either enwrap large nerve axons to form a myelin sheath or enwrap smaller axons without forming myelin, the so called “non-myelinating Schwann cells” or perisynaptic/terminal Schwann cells. Non-myelinating Schwann cells are found in skeletal muscles, where they cover the motor nerve endings and extend neuronal projections over the terminal branches.[179]

Important to note, without the neuronal connection, muscle fibers cannot contract and quickly atrophies. Therefore, the maintenance and function of the NMJ is of utmost importance and degeneration of these structures causes severe neuromuscular diseases, including congenital myasthenic syndrome (CMS), amyotrophic lateral sclerosis (ALS), and myasthenia gravis (MG). For example, mutations in choline acetyltransferase (ChAT) are linked with presynaptic defects and mutations in ColQ and laminin β2 (LAMB2) cause synaptic defects as seen in CMS patients. Furthermore, mutations in AChR subunits and in the pathways of activated muscle-specific receptor tyrosine kinase (MuSK), which requires the binding of the ligand agrin and the coreceptor LRP4, are also associated with the pathogenesis of CMS.[180]

Another cause of diaphragm paralysis is loss of muscle strength. For example, patients with Duchenne muscular dystrophy (DMD) suffer from progressive wasting of locomotor and respiratory muscles, leading to chronic respiratory failure, which is the leading cause of death.[61] The progressive neurodegenerative disorder amyotrophic lateral sclerosis (ALS), also known as Lou Gehrig's disease, affects motor neurons in the brain and spinal cord, leading to muscle weakness in early stages and often resulting in respiratory failure due to diaphragm and chest muscle weakness in advanced stages. So far there is no therapeutic intervention, and the disease usually leads to death within a few years. So far, the precise cause of ALS is not fully understood.[73] Notably, 90% of ALS patients have insoluble aggregates of the nuclear protein TDP43 in the cytoplasm of neurons and glial cells (**Figure 6**). The mislocalization of TDP43 disrupts RNA processing and gains toxic properties, promoting neurodegeneration.[84] This TDP43 mislocalization occurs in motor neurons of ~95% of ALS patients. It has been shown that TDP43 accumulates in intra-muscular nerves from ALS patients and the analysis of a TDP43 based ALS mouse model revealed a mislocalization of mitochondria in motor neurons.[181] In addition, the axonal and synaptic levels of nuclear-encoded mitochondrial proteins are reduced.

The ageing process also leads to a decline in NMJ function, which is very similar to the clinical signs of motor neuron diseases such as ALS. At the molecular level, reduced mitochondrial function, oxidative stress and inflammation are responsible for NMJ degeneration during aging.[177] Aged motor neurons show a reduced capacity to sprout, the boutons are smaller in size and the AChR localization is more scattered, with extended spatial uncoupling between ACh vesicle clusters and receptor clusters.[70] Therefore, a deeper understanding of the spatial architecture of the diaphragm including the NMJ will give more insights into the molecular function of the diaphragm and may help to prevent degeneration of NMJ structures in disease and during aging and neurodegenerative diseases such as ALS.

In recent years, modern mass spectrometers greatly improved in sensitivity, and nowadays small amounts of protein samples (ng range), including single skeletal and cardiac muscle fibers[121,122] from human and mice can be analyzed.

To map spatial protein patterns in the diaphragm we isolated the diaphragm from the mouse and embedded a strip of the diaphragm and prepared thin cryosections.[167] Single transversal cryotome sections were measured by short LC-MS gradients and revealed ~2500 protein profile along the longitudinal muscle fiber-tendon axis. Our profiling of known NMJ marker proteins such as ChAT and neurofilament proteins demonstrates exactly the position and morphology of the NMJ. This is the first unbiased approach to study protein patterns of the NMJ and MTJ in the diaphragm muscle and we demonstrate the high sensitivity of our workflow by detecting multiple transcription factors, neuronal signaling molecules and matrix proteins.

2.3.4. Results

2.3.4.1. Single sections profiling of the diaphragm muscle using short LC-MS gradients

We used the diaphragm muscle as a model system to identify specific protein profiles associated with the molecular function of the NMJ and MTJ. The leaf-shaped diaphragm is innervated by the phrenic nerve, with its peripheral motor neurons forming a perpendicular band to the muscle fibers in the central areas of the diaphragm. First, we tested which amount of tissue is necessary for a deep proteome analysis. We isolated the intact diaphragm and cryo-embedded muscle strips of 1-8 mm width from the lateral area (**Figure 22A, B**). To obtain longitudinal protein profiles, we generated 20 µm thick transversal sections from peripheral muscle to central tendon areas covering the NMJ and MTJ (**Figure 22C**). Each slice was transferred to 96-well microplates, where protein digestion was performed using the SP3 protocol and measured by LC-MS (**Figure 22D**). Testing short LC-MS gradients of 11 and 21 min yielded an average of 8-10K peptides, resulting in ~2,500 proteins from a single slice with a width of ~3 mm (**Figure 22E and Figure S11A-D**). As a performance and quality test, we measured HeLa cell lysates with the same LC-MS gradients (**Figure S11E-H**). Samples were measured with an ion mobility mass spectrometer (timsTOF pro 2), and RAW data were analyzed with DIA-NN. Stable MS analysis was verified by alternating injections of HeLa lysates (**Figure S12A**) and blanks (**Figure S12B**). Additionally, LC performance and peptide retention time were controlled by spike-in indexed retention time (iRT) peptides added to each sample (**Figure S12C, D**). Merging the identified protein hits of ~200 slices from peripheral to central diaphragm areas yielded more than 6000 protein hits (n=4) (**Figure 22F, Table S6**).

Next, we compared our diaphragm proteome with a previously created soleus proteome[167], and the overlap of both datasets results in a total of 9527 proteins hits. Notably, 1,898 proteins were only identified in the soleus, whereas 2,408 proteins were restricted to the diaphragm (**Figure 22G**). This discrepancy suggests a potential physiological adaptation between these two muscle groups. For the following analysis of the diaphragm, we selected 20 µm slices with a width of ~3 mm and 11 min LC-MS gradients. We then plotted the myosin heavy chain (MYH) isoform distribution of ~50 central muscle slices from diaphragm and soleus. According to previous studies, we observed mainly MYH1 and MYH2 isoforms and to a lesser extent MYH4 and MYH7 isoforms (**Figure 22H**).[175, 182] The expression of MYH1

(type IIx) and MYH2 (type IIa fibers) might reflect the adaptation to the substantially higher heart rate (600 beats/min) in small rodents compared to humans (80 beats/min). The soleus skeletal muscle expresses mainly MYH7 and MYH2 isoforms, reflecting the presence of slow type I and fast type IIa fibers (**Figure 22H**).

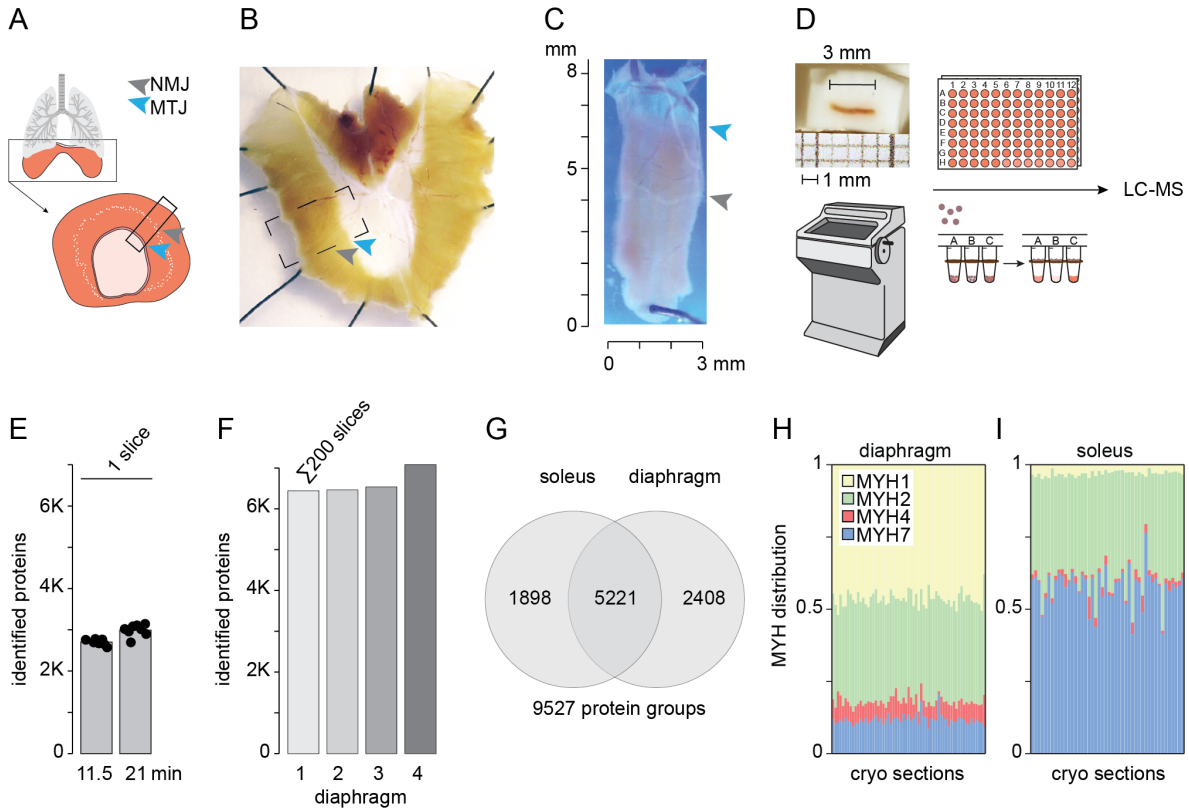

Figure 22 Overview of the spatial analysis of the mouse diaphragm muscle. A-C) Schematic (**A**) and abdominal (**B**) view of the mouse diaphragm muscle location in the body and the isolated piece for spatial analysis (**C**). Blue and grey arrow indicate the MTJ and NMJ, respectively. **D**) Short preparation worfkflow for the embedded diaphragm muscle, starting with cryotome sectioning, SP3 sample preparation, and LC-MS analysis. **E**) Identified proteins of short 11.5 and 21 min gradients. **F**) Identified proteins for the four biological replicates, including 200 slices per experiment. **G**) Venn diagram of the identified groups for this study and a previous spatial proteomics study of the mouse skeletal muscle.[167] **H, I**) MYH isoform distribution analysis of the diaphragm (**H**) and the soleus (**I**) skeletal muscle. Each bar represents the relative abundance of MYH isoforms in one cryotome section in relation to the total sum of intensities for MYH1 (yellow), MYH2 (green), MYH4 (red), and MYH7 (blue). LC-MS, liquid-chromatography mass spectrometry; MTJ, myotendinous junction; MYH, myosin heavy chain; NMJ, neuromuscular junction.

2.3.4.2. Protein profiling of the longitudinal diaphragm axis revealed the transition zone between muscle and tendon

To visualize skeletal muscle and tendon areas along the longitudinal axis of the diaphragm, we generated sagittal cryosections of the diaphragm. Immunostainings were performed with antibodies against pan-MYH for skeletal muscle tissue and tenascin-C (TNC) for the tendon area. Nuclei were stained with Hoechst dye and the MTJ was visualized with the known marker protein collagen 22 (**Figure 23A Figure S13A, B**).[41]

Expression profiles were generated as described in Schmidt et al. (**Data S3**).[167] In brief, protein intensities were normalized to the sum intensity of each slice. Using a sliding window, data was filtered for at least 70% data completeness over an area of 200 µm (10 sections) followed by a linear imputation. We then plotted the z-score normalized protein intensities of selected sarcomeric proteins along the longitudinal axis, observing a constant expression along the muscle area followed by a steep decrease in the muscle-tendon transition area (**Table S6**, **Figure 23B, and Figure S13B, C**). Conversely, ECM proteins, such as biglycan, chondroadherin, cartilage oligomeric matrix protein (COMP) and tenascin-C, showed a strong increasing profile at the start of MTJ (**Figure 23C)**. The profile plot of collagen 22 is consistent with the immunostaining and confirms the position of the MTJ (**Figure 23D**). Since we observed collagen 22 (COL22) in only ~5 slices, we assume a length of ~100 µm for the MTJ. To increase the resolution of the MTJ profile, we next generated 10 µm sections of the muscle-tendon transition area and plotted the profile plots of the known MTJ marker proteins collagen 22, FERM domain containing kindlin 2 (FERMT2, also known as kindelin 2), and sorbin and SH3 domain containing 2 (SORBS2) (**Figure 22E, Table S7, and Data S4**).

Strikingly, we observed now a clear shift between the MTJ marker proteins and the matrix proteins that form the structure of the following tendon (**Figure S13D, E**). In total, we found 104 protein profiles with high resolution. Similar, we observed collagen 22 in 10 slices and estimated again a width of 100 µm for the MTJ (**Figure 23A, D**). We also observed other collagens like collagen 6a5 and 6a6 with similar profiles compared to COL22 (**Figure 23F**). Other proteins with a maximum at the MTJ were the exocyst complex component 4 (EXOC4), Annexin 2 (ANXA2), and Ras-related Rab-8A (RAB8A). Interestingly, these proteins are associated with the targeting of exocytic vesicles to specific docking sites on the

plasma membrane (**Figure S13G**).[183, 184] We hypothesize that these candidates may have a role in cell-cell communication between muscle, matrix and tendon in the transition zone.

Similar to the mouse soleus skeletal muscle MTJ, our protein profiling revealed distinct patterns, with certain proteins showing peak expression either on the muscle or tendon side, such as collagen 22 (**Figure 23E, H**). The high resolution of 10 µm cryosections enabled us to categorize MTJ protein profiles into four distinct groups: early (**Figure 23H**), central (**Figure 23J)**, late (**Figure 23K)**, and biphasic (**Figure 23I**). For example, early proteins COL22 and XIRP2 show a maximum short before the MTJ on the muscle area. Conversely, late MTJ proteins like POSTN and LOXL1, are predominantly localized within the tendon side.

Notably, proteins with biphasic profiles, such as RAB8A, SEC31A, and AP2S1, were associated with gene ontology (GO)-terms related to vesicle transport and plasma membrane, indicating that these processes/structures seems to be important on both the muscle and tendon sides of the MTJ.[185-187] This suggests that biphasic profile proteins are localized at both the muscle and tendon sides of the membrane. For instance, AP2S1 links clathrin to vesicle membranes and plays a role in regulating extracellular calcium levels,[187] The release of calcium in response to mechanical stimuli may play a crucial role not only within the muscle itself but also at the muscle-tendon interface, where the highest forces are transmitted.[188] Overall, proteins with a maximum at the MTJ area contribute to the integrity of the muscle-tendon transition by anchoring muscle fibers and tendons to the ECM.[189]

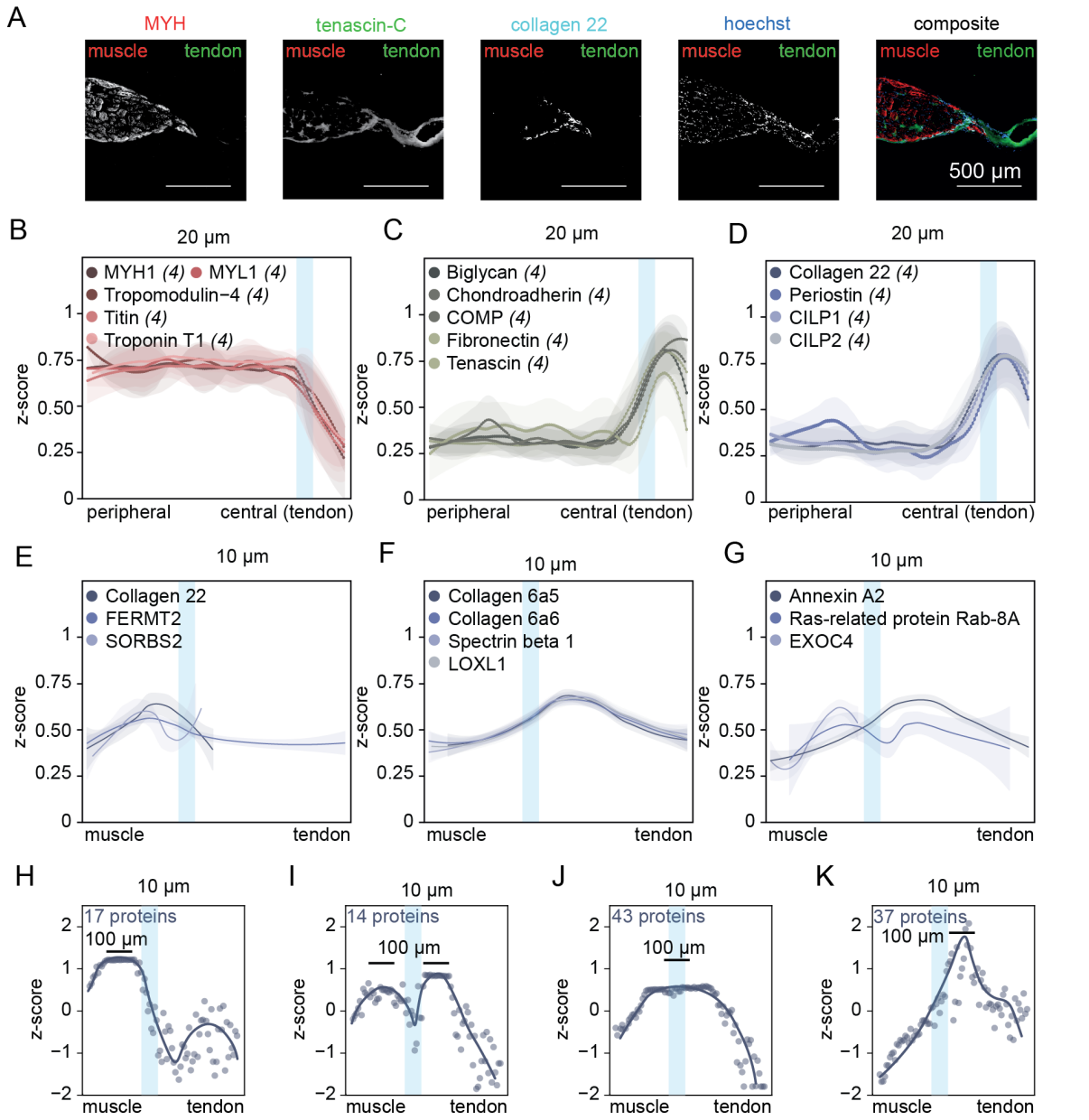

Figure 23 Protein profiling of the diaphragm MTJ reveals four different groups. A) Immunostaining for the NMJ in longitudinal mouse diaphragm sections. MYH is staining for muscle fibers, MTJ is stained with collagen 22, nuclei are stained with Hoechst, tendon is stained with tenascin-C. Scale bar = 500 µm. **B-D**) Protein expression profiles along the longitudinal peripheral muscle-central tendon axis of **B**) sarcomeric proteins, **C**) ECM proteins, **D**) MTJ proteins. **E-G**) Protein expression profiles with 10 µm thin cryotome sections along the longitudinal muscle-tendon axis of **E**) known MTJ proteins, **F**) late MTJ proteins, **G**) MTJ proteins of the interacting complex for exocytic vesicle fusion. **H-K**) MTJ protein expression profiles characterized into four groups. Blue lines indicate the overlap of muscle and tendon proteins. CILP, cartilage intermediate layer protein; EXOC1, exocyst complex component; FERMT2, FERM Domain Containing Kindlin 2; LOXL1; Lysyl oxidase homolog 1; MTJ, myotendinous junction; MYH, myosin heavy chain; MYL1, myosin light chain; SORB2, sorbin and SH3 domain containing 2.

3.2.4.3. Protein profiles with a maximum protein intensity in the NMJ reflect the complex structure of the NMJ

In leg skeletal muscles, NMJs are typically more sparsely distributed around the middle of the muscle fibers, ensuring that the action potential propagates efficiently along the skeletal muscle during contraction. Conversely, the diaphragm has a higher density of NMJs in a particular area uniformly distributed along a central ring perpendicular to the skeletal muscle fibers. This ensures a coordinated and constant contraction required for breathing. Staining with the neurotoxin a-bungarotoxin visualizes the position of the central NMJ band due to the specific binding to nAChRs on motor neurons (**Figure 21A-C, Figure 24A** and **Figure S13B, C**). Accordingly, our protein profiling revealed a protein intensity (peak) maximum for the presynaptic proteins ChAT and AChE (**Figure 23B**). These two proteins were used as a template profile to identify proteins with a similar protein profile, suggesting a function at the NMJ. In addition, we observed several known NMJ proteins with a similar profile compared to CHAT and AChE, the 2',3'-cyclic-nucleotide-3'-phosphodiesterase (CNP), the GAP junction protein gamma 3 (GJP3), and the ATPase Na^+/K^+ transporting subunit a3 (ATP1A3) (**Figure 24C**). Notably, most neurofilament proteins (NEFL, NEFM, NEFH) and myelin-related proteins showed a peak at the NMJ and additionally at the MTJ. This confirms the neuronal activity at the MTJ (**Figure 24D**). Interestingly, the myelin-associated glycoprotein (MAG) displayed a restricted signal at the NMJ (**Figure 24C**), suggesting a specific function at the NMJ. MAG is found in peri-axonal Schwann cells and oligodendrocytes within myelin sheaths, extending into the periaxonal space to facilitate interactions between glia and axons.[73] Conversely, MPZ, MBP, and proteolipid protein (PLP1) are components of the layered compact myelin in both the peripheral nervous system (PNS) and central nervous system (CNS).[190]

Other proteins with peak maxima at the NMJ and MTJ are the heat shock protein family A (HSP70, HSPA12A) which might indicate enhanced cellular stress in these junctions. The biphasic peak maxima of the neuron-specific glucose transporter type 1 (GLUT1) at the NMJ and MTJ reflect the high sensitivity and specificity of our profiling and reflects the presence of neurons in these structures (**Figure 24E**). The muscle-specific GLUT4 transporter showed a similar protein profile compared to sarcomeric proteins (**Table S6**). Another example is the expression of the muscle (CKMT1) and brain specific creatine kinase (CKB). Similar to GLUT1, the brain creatine kinase also showed a maximum at the NMJ (**Figure 25C, D** and **Figure S14B**).

In total, we identified 176 protein profiles with a restricted maximum at the NMJ, 98 with a unique maximum at the MTJ, and 24 with maxima at the NMJ and MTJ (**Figure 24F and Figure S14A**). Notably, 2146 exhibited descending protein profiles and 181 protein profiles showed an ascending pattern. This indicates the higher content of skeletal muscle proteins, including sarcomeric and mitochondrial proteins, compared to matrix proteins. A GO analysis of proteins with a maximum at the NMJ revealed enrichment in nervous system development processes, neurofilament bundle assembly, glial cell differentiation, and axonogenesis. Furthermore, GO-terms associated to ECM protein complexes like integrins, basement membrane proteins, and laminin interactions were also enriched at the NMJ (**Figure 24G**). The neuronal activity at the NMJ was further highlighted by enriched GO terms related to transport, cellular import, and Na^+ export. For example, the release of neurotransmitters like ACh into the synaptic cleft depends on vesicular transport mechanisms and enables the stimulation of muscle fiber by neuronal activity.[191] Na+/K+ ATPase pumps and other transporters maintain the electrochemical gradients across cell membranes and we have identified several ion pumps including SCNA4.[192] Overall, this is the first spatial proteomic study of the NMJ, and we find not only known marker proteins such as ChAT and AChE but also other candidates whose function in the NMJ is unknown. The detection of myelin proteins such as MAG and MPZ reflects the presence of Schwann cells which contributes to the function of the nerve-muscle junction (**Figure 24**).

To determine whether the proteins originate from muscles or neuronal cells, we isolated individual skeletal muscle fibers from the diaphragm. The sciatic nerve was isolated from the skeletal muscle by macroscopic separation of the nerve. Both fibers and nerve were analyzed by LC-MS (**Figure 25B** and **Table S8**). The top 500 proteins identified in the sciatic nerve were enriched for gene ontology cellular components (GOCC) such as the myelin sheath (q-value 2.878×10^{-116}), synapse (q-value 6.385×10^{-56}), and extracellular matrix (ECM) (q-value 2.807×10^{-23}). In contrast, the top GO terms for the diaphragm fibers were mitochondria (q-value 2.480×10^{-121}) and myofibril (q-value 4.935×10^{-44}) (**Table S8**). For example, highest intensity in the nerve was observed for the neurofilament proteins NEFM, NEFL, periaxin (PRX), and myelin basic protein (MBP); none of these myelin proteins were detected in the single muscle fibers. Conversely, tropomyosin TPM2, actin-2, and myomesin-1/3 were exclusively identified in the muscle fibers (**Figure 25A, C**).

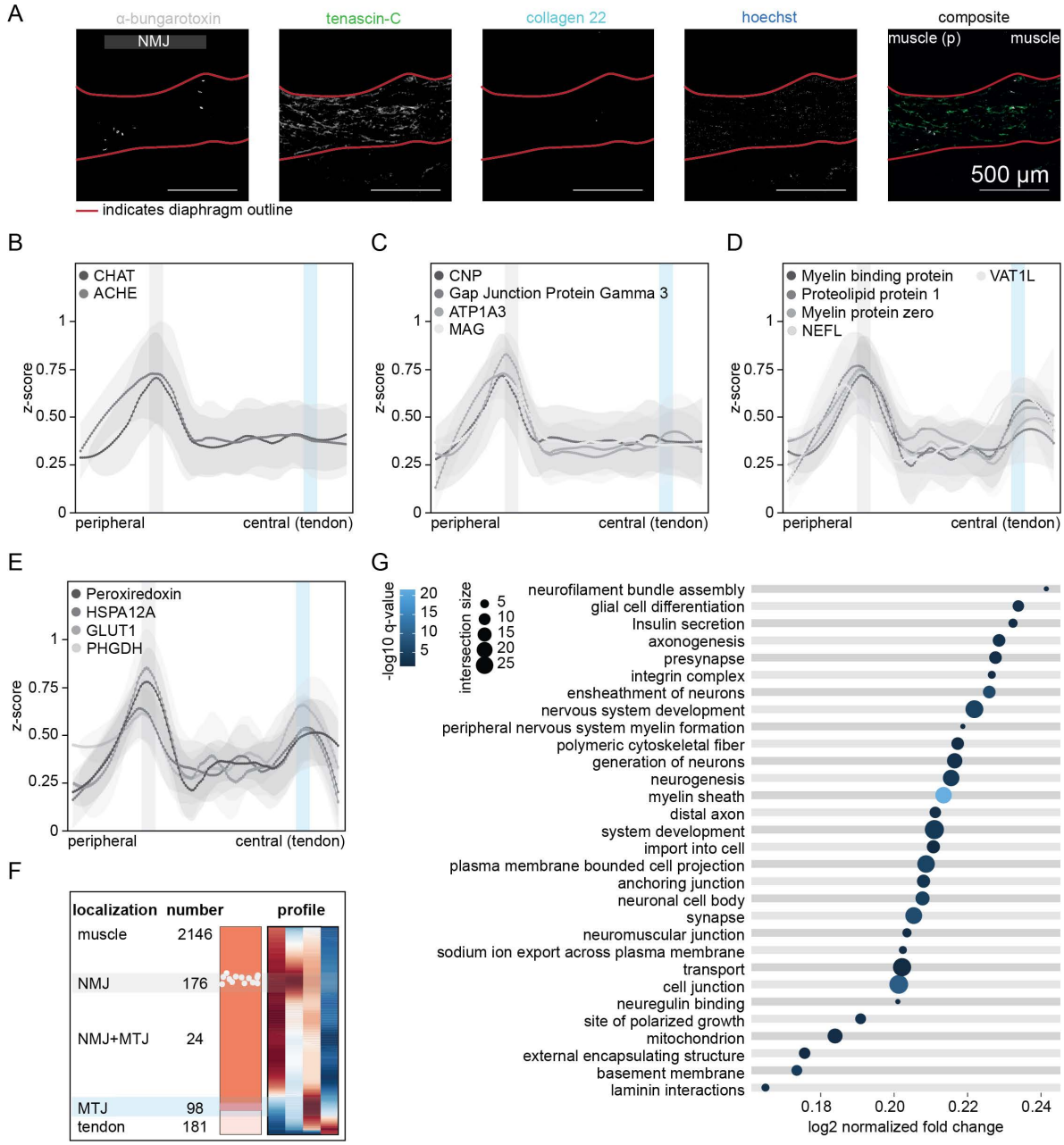

Figure 24 Resolving the NMJ structure using spatial proteomics. A) Immunostaining for the NMJ in longitudinal mouse diaphragm sections. Bungarotoxin is staining for the NMJ, nuclei are stained with Hoechst, tendon is stained with tenascin-C. Scale bar = 500 µm. Red line indicates diaphragm tissue outline. **B-E**) Protein expression profiles along the longitudinal peripheral muscle-central tendon axis of **A**) NMJ marker proteins ChAT and ACHE, **B**) proteins with a maximum at the NMJ, **C**) known NMJ marker proteins showing maxima at the NMJ and MTJ, **D**) NMJ proteins with two maxima. **E**) Summary of identified protein profiles regarding their localization, the number, and their profile along the logitudinal diaphragm axis. **F**) GO-term analysis of identified NMJ proteins. ACHE, acetylcholine esterase; ATP1A3, ATPase Na^+/K^+ transporting subunit alpha 3; CHAT, choline O-acetyltransferase; CNP, 2',3'-cyclic nucleotide 3' phosphodiesterase; GLUT1, glucose transporter type 1; HSPA12A, heat shock protein family A member 12A; MAG, myelin associated glycoprotein; MTJ, myontendinous junction; NEFL, neurofilament light; NMJ, neuromuscular junction; PHGDH, phosphoglycerate dehydrogenase; VAT1L, vesicle amine transport 1 like.

We identified 200 proteins with a maximum at the NMJ, of which 5 proteins were only detectable in skeletal muscle fibers. For 107 protein hits we found an exclusive expression in the sciatic nerve, while 32 proteins were commonly detectable in both tissues. For the remaining 57 NMJ proteins we did not observe an overlap between the protein profiling and the skeletal muscle and sciatic nerve proteome datasets (**Table S8**). Other than the known marker proteins (**Figure 25A**), the NMJ protein profiles can be characterized into mitochondrion, vesicle transport, and ECM proteins (**Figure 25D**). Even though most of the mitochondrial proteins do not show a maximum at the NMJ (**Figure S13E**), 13 mitochondrial associated proteins show a peak at the NMJ. In addition, of the identified mitochondrial proteins with a peak at the NMJ were 70% identified in both nerve and muscle fiber suggesting a general increased mitochondrial content at the NMJ. Interestingly, the mitochondrial encoded ATP synthase membrane subunit 8 (MTATP8), the transmembrane protein 14C (TMEM14C), and C8orf82, were found only in muscle fibers, suggesting a muscle specific expression and adaption of mitochondria at the NMJ (**Figure S14D**). However, due to the different dynamic range of the two tissues, we cannot exclude the possibility that some mitochondrial proteins were not detected due to "overshadowing". To address this point, isolation of mitochondrial proteins from both tissues would be necessary. Another cellular adaptation between muscle and nerve was observed for pathways associated to membrane trafficking and vesicle transport. Particularly, these processes are responsible for the maintenance of synaptic vesicles in neurons. Proper vesicle homeostasis is essential for sustained neurotransmission and overall synaptic function. Since, muscle-neuron communication is precisely controlled by motor endplates it is not surprisingly that these structures show an enrichment of proteins related to vesicle formation, transport and recycling (**Figure 23F**). For example, the vesicle transport protein clusterin (CLU) and two tetraspanins 29 and 30 (CD9, CD63) were detected with a congruent maximum at the NMJ (**Figure 24B**). Notably, these proteins were only identified in neurons. Conversely, the protein yip1 interacting factor homolog B (YIF1B) was only identified in muscle fibers. So far, YIF1B was associated with trafficking from the endoplasmic reticulum (ER) to the cell membrane and mutations lead to motor delay and myelination alterations. We suggest that YIF1B also play an important role at the NMJ to maintain the intracellular protein transport within motor neurons and the endplate.[193]

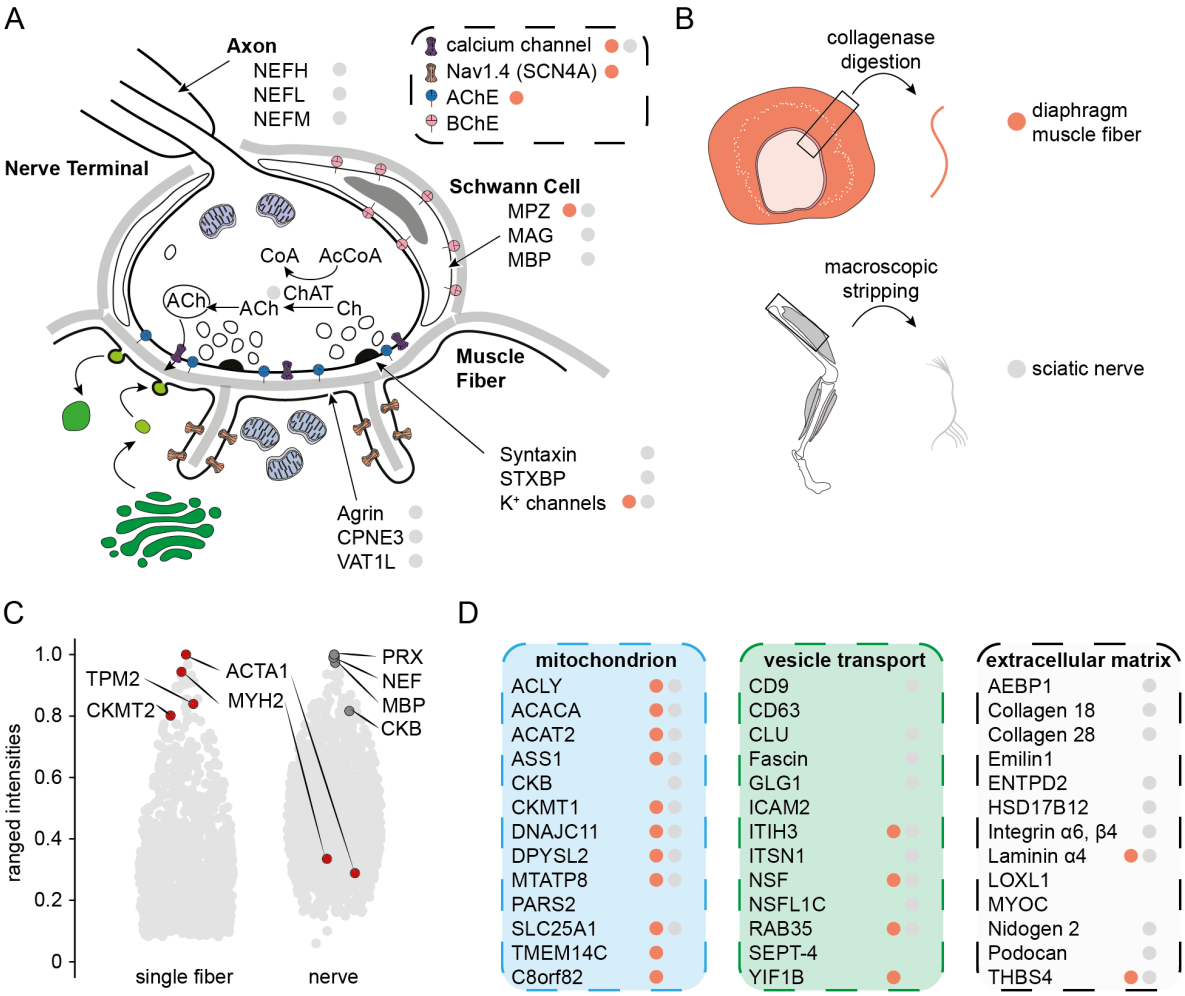

Figure 25 Identification of muscle and neuronal NMJ proteins. A, B) Schematic visualization of identified NMJ proteins **B**) into mitochondrial proteins (blue), proteins related to vesicle transport (green) or ECM (grey) and **C**) their localization in the NMJ. Orange and grey dots are proteins that were identified in single diaphragm fibers or in the sciatic nerve, respectively. C) Ranged intensity violin plot of identified protiens in single muscle fibers and sciatic nerve. **D**) Schematic overview of the isolation of single muscle fiber of the diaphragm and the sciatic nerve to identify the origin of the NMJ proteins. ACTA1, actin-1; AChE, acetylcholine esterase; ACLY, ATP citrate lyase; AEBP1, AE binding protein 1; ALDH1, aldehyde dehydrogenase 1 family member; BChE, butyryl cholinesterase; CD9, Tetraspanin-29; CD63, Tetraspanin-30; CHAT, choline O-acetyltransferase; CK, creatine kinase; CLU, Clusterin; COX20, cytochrome C oxidase assembly factor COX20; CPNE3, Copine 3; DARS2, aspartyl-tRNA synthetase 2; DNAJC11, DnaJ heat shock protein family member C11; ENTPD2, ectonucleoside triphosphate diphosphohydrolase 2; GLG1, golgi glycoprotein 1; HSD17B12, hydroxysteroid 17-beta dehydrogenase 12; ICAM2, intercellular adhesion molecule 2; ITIH3, inter-alpha-Trypsin inhibitor heavy chain 3; ITSN1, Intersectin 1; K^+, potassium ions, LOXL1, lysyl oxidase like 1; MAG, myelin associated glycoprotein; MBP, myelin binding protein; MPZ, myelin protein zero; MTATP8, mitochondrially encoded ATP synthase membrane subunit 8; MTJ, myotendinous junction; MYH, myosin heavy chain; MYOC, Myocilin; NEF(H, L, M), neurofilament (heavy, light, middle); NMJ, neuromuscular junction; NSF, N-ethylmaleimide sensitive factor; PARS2, prolyl-tRNA synthetase 2; PRX, periaxin; RAB3GAP1, RAB3 GTPase activating protein catalytic subunit 1; RAB35, Ras-related protein Rab-35; SCN4A, sodium voltage-gated channel alpha subunit 4; SEPT, Septin; SLC25A35, solute carrier family 25 member 35; STXBP, syntaxin binding protein; THBS4, Thrombospondin 4; TPM2, tropomyosin-2; VAT1L, vesicle amine transport 1 like; YIF1B, Yip1 interacting factor homolog B.

Another secreted matrix protein to be equally expressed between muscle and neurons with a NMJ maximum in the NMJ is the inter-alpha-trypsin inhibitor heavy chain 3 (ITIH3). ITIH3 is an adaptor protein between hyaluronan and other matrix proteins. A recent study described ITIH3 as a biomarker for myasthenia gravis (MG) and the protein was localized in neuromuscular endplates in diseased patients.[194] Similarly, other structural ECM proteins, such as laminin-alpha4 (LAMA4) and thrombospondin 4 (THSB4), were detected in both muscle fibers and nerves, underscoring their role in maintaining the organization of the NMJ by binding to receptors like integrins and dystroglycan (**Figure 25B**).

In summary, these data indicate that most protein maxima at the NMJ are of neuronal origin. and only a minor number of 5 skeletal muscle proteins showed a maximum at the NMJ.

2.3.4.3. Spatial analysis of aged mouse diaphragms shows a spreading of the NMJ structures

During aging the NMJ undergoes several changes, such as decreased muscle protein synthesis[195], fiber type switch[196], and reduced fiber innervation[196, 197], which negatively influence muscle function and mass.

To visualize the spatial architecture of aged NMJ structures in the diaphragm, we isolated diaphragm tissues from young controls (2-month) and aged 26-month-old mice (n=2). These ages correspond to >70 years and <20 years in humans.[198] The diaphragm lengths were measured using brightfield microscopy before embedding and sections were made. We performed approximately 50 slices (each 20 µm) prior to and posterior to the central phrenic nerve. Samples were prepared, analyzed, and protein profiles were generated as previously described (**Table S9, Data S5**). NMJ areas were determined using ChAT as a reference profile (**Figure S15A, B**). Here, we monitored an average width of the NMJ of 500 µm (**Figure S15A**).

In total, we generated 2700 protein profiles covering ~2 mm of the NMJ regions of both old and young mice. Protein profiles were correlated to the expression profile of the NMJ marker ChAT to identify NMJ proteins and FDR significance was calculated using normalized intensities of ~25 NMJ slices and 25 muscle sections on each side of NMJ (**Figure 25A, B**). Here, we identified 99 and 74 proteins with a maximum at the NMJ for aged and young animals, respectively. Of these proteins, 40 NMJ proteins were identified in both young and

aged mice, including ChAT, cell adhesion molecule 4 (CADM4), and the sodium pump subunit alpha-3 (ATP1A3)

(**Figure S15A-D**). Of the 59 exclusively regulated proteins in the aged animals, 48 are more abundant in the NMJ. Proteins that are only significantly more abundant in the young NMJ´s are for example ATP citrate synthase (ACLY), dihydropyrimidinase-like 2 (DPYSL2), and CKMT1. These proteins are related to energy metabolism and mitochondria, indicating more metabolic activity and/or mitochondria content at young compared to aged NMJs.

The 40 proteins with an equal upregulation within the NMJ between young and aged diaphragm, were further analyzed to determine the area under the curve (AUC) (**Figure S15A-D**). A Student's *t*-test revealed a significant increase in the AUC of the area between the peripheral and central NMJs in old mice, indicating a broadening of the NMJ during aging (**Figure 25C)**. Earlier studies on aged human skeletal muscle biopsy material showed an increase of the nerve terminal and postsynaptic membrane length compared to young subjects.[199] However, a detailed distribution of NMJ proteins between young and old animals is not yet known. The increased length between peripheral and central NMJ areas in aged animals is reflected by the upregulation of the GO-term for postsynapse compared to young controls (**Figure S15G**). Moreover, cell death and apoptotic processes, which correlate with increased denervation-reinnervation events, are also observed with an elevated abundance in aged animals (**Figure S15G**).[200]

As mentioned earlier, proteins associated to energy generation such as the TCA cycle and muscle contraction are downregulated in aged compared to young mice.[201] This decline in energy production leads to depleted acetate levels, potentially reducing the conversion of oxaloacetate to aspartate, which in turn leads to a reduced activation of mammalian target of rapamycin (mTOR) signaling and promotes autophagy.[201]

Among the protein profiles with significant changes between old and young animals, the sodium pump ATP1A3 showed an increased abundance, and a changed biphasic profile in aged compared to one maximum in young mice (**Figure S15C**). Other proteins with an altered protein profile in older mice are the collapsin response mediator protein DPYSL2, nidogen 1 (NID1) and caveolin 3 (CAV3), which facilitate neuron guidance, growth and polarity (**Figure 25D-F**). The glycoprotein NID1 is secreted by Schwann cells and muscle tissue, promotes neurite outgrowth and connects and stabilizes laminin and collagen layers.[202, 203] These ECM proteins are tightly linked to tissue plasticity, which declines during the aging process and might contribute to stiffer tissues with reduced regenerative capacity.[204]

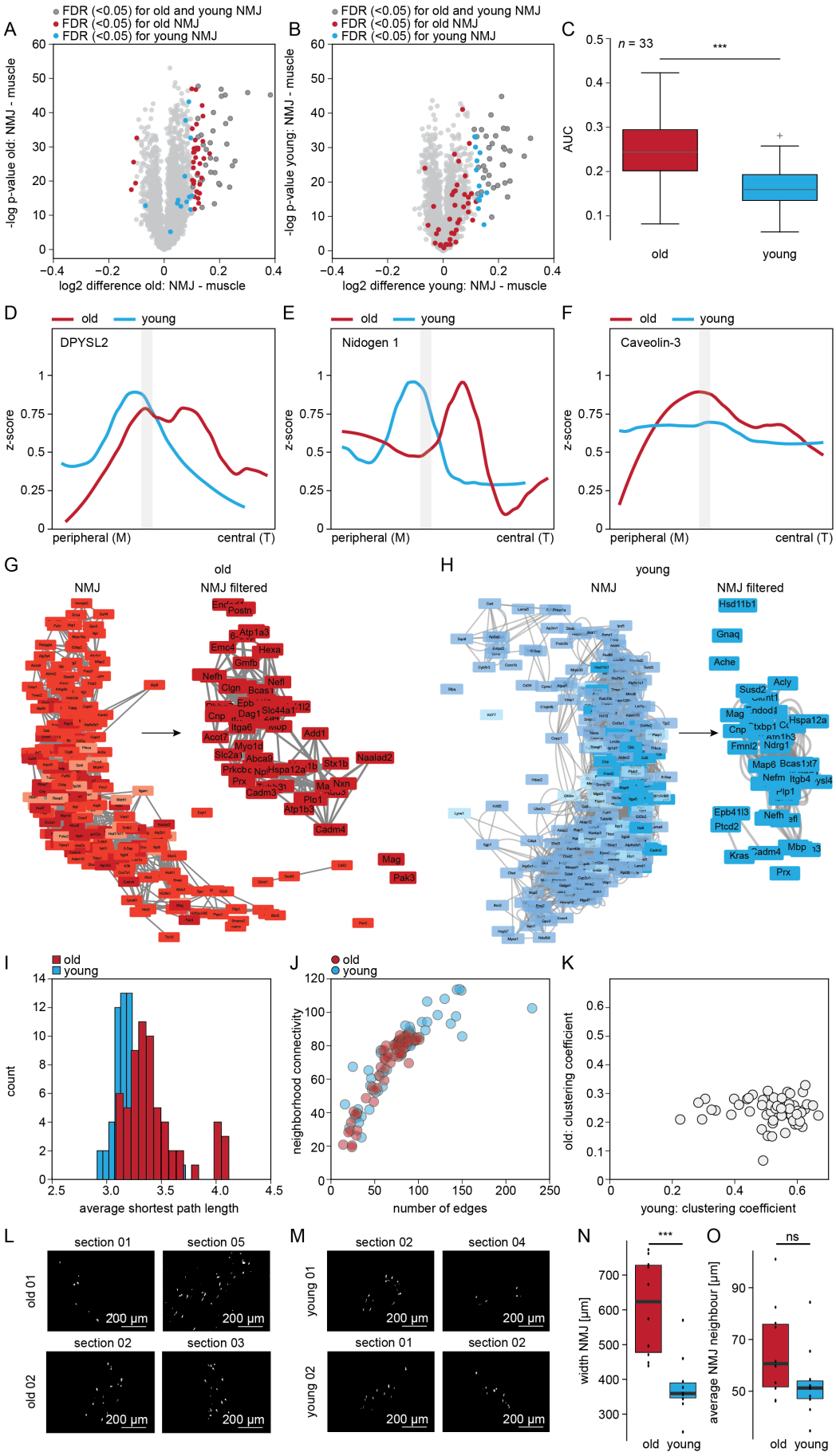
A
FDR (<0.05) for old and young NMJ
FDR (<0.05) for old NMJ
FDR (<0.05) for young NMJ
-log p-value old: NMJ - muscle
log2 difference old: NMJ - muscle
B
FDR (<0.05) for old and young NMJ
FDR (<0.05) for old NMJ
FDR (<0.05) for young NMJ
-log p-value young: NMJ - muscle
log2 difference young: NMJ - muscle
C
n = 33
***
AUC
old
young
D
old
young
DPYSL2
z-score
peripheral (M)
central (T)
E
old
young
Nidogen 1
z-score
peripheral (M)
central (T)
F
old
young
Caveolin-3
z-score
peripheral (M)
central (T)
G
old
NMJ
NMJ filtered
H
young
NMJ
NMJ filtered
I
old
young
count
average shortest path length
J
old
young
neighborhood connectivity
number of edges
K
old: clustering coefficient
young: clustering coefficient
L
section 01
section 05
section 02
section 03
old 01
old 02
200 µm
M
section 02
section 04
section 01
section 02
young 01
young 02
200 µm
N
***
width NMJ [µm]
old
young
O
ns
average NMJ neighbour [µm]
old
young

Figure 26 Spatial analysis of old and young diaphragm reveals NMJ widening in old animals. A, B) Welch's *t*-test of the normalized intensities in NMJ and muscle areas in **A**) old and **B**) young animals. FDR significant (< 0.05) proteins are marked in red, blue, or grey for old, young, or both old and young, respectively. **C**) Box plot of the average ± SEM AUC of 33 NMJ proteins identified in both young and old animals. Asterisks denote significance (*t*-test: * < 0.05, ** < 0.01, *** < 0.001). **D-F**) Protein expression profiles of the NMJ proteins significantly changed between old and young animals. **G-H**) Isolated and filtered for centered NMJ proteins of the distance-based network analysis of **G**) old and **H**) young animals. **I-K**) Characterization of the NMJ proteins with the network analysis parameters to identify the **I**) path lengths, **J**) interconnectivity, and **K**) clustering coefficients between young and old animals. **L, M)** Immunostaining for the NMJ in longitudinal mouse diaphragm sections with Bungarotoxin in old (**L**) and young (**M**) animals. Scale bar = 200 µm. **N, O**) Boxplots show the measured width (**N**) and distance to neighbours (**O**) in the stained NMJ. Data are represented as mean. Asterisks denote significance (*T*-test: * < 0.05, ** < 0.01, *** < 0.001). AUC, area under the curve; DPYSL2, dihydropyrimidinase like 2; NMJ, neuromuscular junction.

To further elucidate structural changes during aging, we performed a distance-based network analysis on protein profile datasets from both young and old animals.[167] The protein profiles were correlated based on their shape and their shift on the x-axis, representing the longitudinal axis of the diaphragm. Networks were calculated individually for old and young animals (**Figure S16**). All identified NMJ proteins (old, 99 and young, 74 proteins) were isolated in the network for parameter calculation. The 40 core NMJ proteins were the same in both age groups (**Figure 26G, H**, NMJ filtered). The average path length, indicating distances between defined NMJ proteins, was longer in older animals, supporting the observed broadening of the NMJ (**Figure 26I**). Conversely, the interconnectivity and clustering coefficient, describing the number of edges between proteins and their correlations, were higher in young compared to old animals (**Figure 26J, K**).

As a complementary approach we generated immunostainings of the NMJ with bungarotoxin on diaphragm sections (*n*=4) from both old and young animals (*n=2*) (**Figure 25L, M**). The average width of the NMJ was significantly (*p*-value 2.9×10^{-4}) greater in the old compared to the young animals (**Figure 25L**). Although there was a significant reduction of interconnectivity in the network, the change in distance between NMJ nodes was not statistically significant (**Figure 25M**).

Using spatial proteomics, distance-based network analysis and immunostainings, we identified a more widespread expression of NMJ related proteins during aging. How these structural alterations and changes in protein expression profiles influence the overall NMJ stability and aging process has to be investigated in future studies.

2.3.4.4. Spatial proteomics of TDP43 overexpressing diaphragm revealed increased protein expression of proteins associated to endocytosis dependent degradation at the NMJ.

Next, we wanted to elaborate if we can also identify changes in a severe and fast progressive neurodegenerative disease model for ALS. Here, we used an inducible TDP43 mouse model which overexpress the human TDP43 in neurons without the nuclear localization sequence (NLS).[84] Overexpression over longer time points (> 6 weeks) leads to a severe NMJ disruption and death.[205] We first isolated, paraformaldehyde-fixed diaphragms from 6-week-old mice which overexpress the human TDP43 for 4 weeks and control mice (*n*=2). As described before, samples were embedded in a cryomatrix and 20 µm sections were generated with a cryotome. Each slice was transferred to 96-well plates and prepared for LC-MS analysis.[167]

RAW data were analyzed with the software tool DIA-NN and resulting MaxLFQ intensities were used to generate protein expression profiles. To generate comparable longitudinal profiles, we used z-score normalization for each protein profile (**Table S10** and **Data S6**). The NMJ area was determined using 33 previously identified NMJ marker proteins (**Figure S17A**). Although both control and TDP43 showed protein expression of several NMJ marker proteins at the same position (**Figure S17A, B**), 26 of these NMJ markers showed a significant reduction at the center between peripheral and central NMJs in the TDP43 gain of function model compared to control diaphragm (**Figure 27A**).

Next, we calculated the distribution of four contractile myosin heavy chains (MYH1, MYH2, MYH4, MYH7) per section to detect a potential muscle fiber switch due to elevated TDP43 levels compared to wildtype control animals.[73] The plot showed neither a change in MYH abundance nor a switch from slow to fast fiber types (**Figure 27B**).

Important to note, the human and mouse TDP43 protein sequence is to 96% identical, the resulting peptides represent a mixture of both species. The detected mouse TDP43 in control animals showed constant protein levels with a slight increase towards to the MTJ. Conversely, the TDP43 transgene protein profile showed two maxima next to the central NMJ area. (**Figure 27C).** Similar to the TDP43 profile, the choline transferase ChAT and the myelin protein (MAG) showed also a biphasic profile (**Figure 27D, F** and **Figure S17B**).

Other NMJ marker proteins like the choline esterase AChE and neurofilaments (NEF) showed no profile change between control and TDP43 mice. This indicates that these

structures, including the phrenic nerve, are not yet impaired in the mutants, but a slight reduction in the overall expression of NMJ proteins was observed (**Figure 27E** and **Figure S17C**).

Another protein with a high similarity to TDP43 and MAG profile is the phosphatidylinositol binding clathrin assembly protein (PICALM) (**Figure S17D**). PICALM is involved in AP2-dependent clathrin-mediated endocytosis at the neuromuscular junction and plays an important role in synaptic vesicle fusion to the presynaptic membrane. In addition, enhanced protein expression of PICALM is linked to autophagy-mediated clearance of stress granules (SG).[206] Recent studies showed that SGs are regulated by the autophagy pathway, suggesting a connection between TDP43 and PICALM expression at the NMJ.[206]

Other proteins with an altered protein profile are the protein phosphatase 2 (PPP2RA1) and ubiquitin-specific peptidase 5 (USP5) (**Figure S17E, F**). The deubiquitinase USP5 is also involved in the assembly and disassembly of stress granules by mediating the hydrolysis of ubiquitin chains. Earlier studies from models of neurodegenerative diseases demonstrated that E3 ubiquitin ligases and DUBs are involved in regulating the degradation of toxic aggregate-prone proteins by directly modifying the ubiquitin chains of misfolded proteins. Hence it might be that USP5, which showed a similar profile compared to TDP43 in the disease model, is involved in regulating protein ubiquitination and aggregation at the NMJ.

A protein profile with two maxima next to the NMJ area was detected for the serine/threonine-protein phosphatase 2A 65 kDa regulatory subunit A α isoform **(**PPP2RA1 or PP2A). The regulatory subunit A functions as a scaffolding molecule to regulate the assembly of the catalytic subunit and a variable regulatory B subunit. Recently, an increased abundance of PPP2RA1 was observed in an ALS mouse model, which carries mutations on the DNA-/RNA-binding protein FUS.[207] Similar to TDP43, mutations in FUS induces a disruption in RNA processing and forms toxic aggregates in motor neurons.[207] Whether PPP2RA1 activity plays a role in TDP43-dependent ALS patients should be addressed in future experiments.[207]

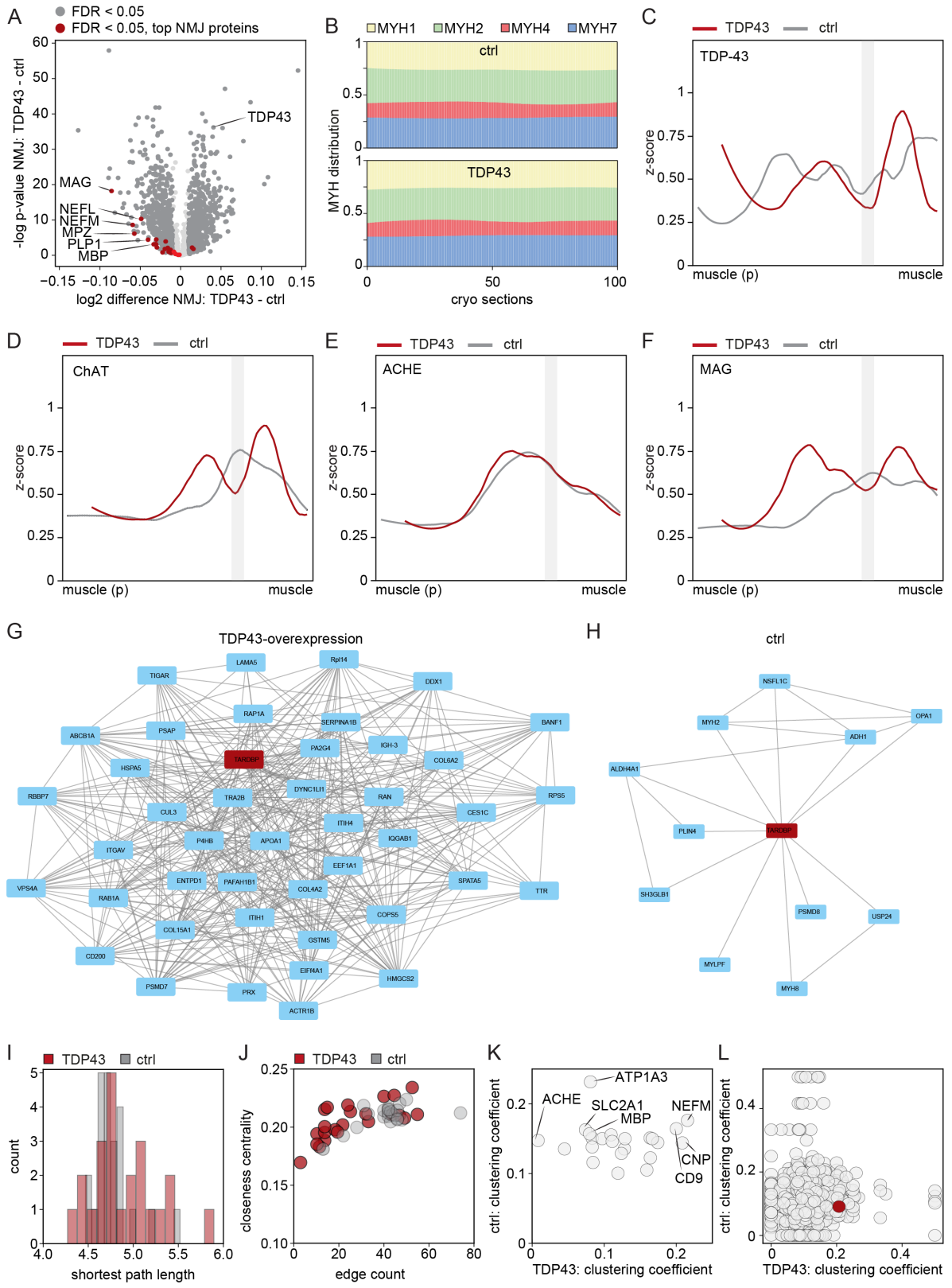

Figure 27 TDP43 dependent ALS mouse models show a slight decrease in NMJ proteins. A) Volcano plot of the NMJ area of TDP43-overexpression and control mice. Differentially abundant proteins are highlighted in dark grey (Welch's *t*-test: FDR < 0.05, s0 > 0.1) and NMJ-related proteins in red. **B**) MYH isoform distribution analysis of the diaphragm muscle in TDP43-overexpression (lower panel) and control (upper panel) mice. Each bar represents the relative abundance of MYH isoforms in one cryotome section in relation to the

total sum of intensities for MYH1 (yellow), MYH2 (green), MYH4 (red), and MYH7 (blue) **C-F**) Protein expression profiles along the longitudinal muscle-NMJ-muscle axis of TDP43, ChAT, ACHE, and MAG. Red and grey lines indicate the profile for TDP43-overexpression and control mice, respectively. **G, H**) Extracted TDP43 network of the distance-based network of TDP43-overexpression (**G**) and control (**H**) mice. **I-L**) Network parameters for the NMJ area (**I-K**) and global network (**L**). Extracted network parameters are shortest path length (**I**), closeness centrality (**J**), and clustering coefficient (**K, L**). Red and grey indicate the TDP43-overexpression and control mice, respectively. ACHE, acetylcholine esterase; ATP1A3, ATPase Na^+/K^+ transporting subunit alpha 3; ChAT, choline O-acetyltransferase; CNP, 2',3'-cyclic nucleotide 3' phosphodiesterase; MAG, myelin-associated glycoprotein; MBP, myelin binding protein; MPZ, myelin protein zero; MYH, myosin heavy chain; NEF, neurofilament; PLP1, proteolipid protein 1; SLC2A1, glucose transporter type 1; TDP43, Tar-DNA binding protein.

Similar to the MYH expression, the majority of mitochondrial proteins showed no alteration between TDP43 overexpressing and wild-type control animals. However, 16 mitochondrial-related proteins, including TP53-induced glycolysis regulatory phosphatase (TIGAR) and A-kinase anchor protein 1 (AKAP1), showed a decreased abundance in the muscle and NMJ regions in the TDP43 overexpression mice compared to control mice. TIGAR functions as a bisphosphatase that reduces fructose-2,6-bisphosphate levels, thereby inhibiting glycolysis. In models of Parkinson's disease, this inhibition has been linked to mitochondrial dysfunction and neuronal loss.[208] Although TIGAR was reported to be absent in TDP43-positive inclusions in postmortem brains of patients with motor neuron diseases[209], it might be that TIGAR contributes to ALS progression in the diaphragm by exacerbating mitochondrial dysfunction in this muscle.

2.3.4.1. Distance based network analysis of TDP43 overexpressing mice revealed changes in the NMJ connection network

Given the significant changes in the protein expression profiles of several NMJ proteins in the TDP43 transgene mouse model compared to wildtype controls, we performed a network analysis of the generated protein profiles (**Figure S18**). The connection network of TDP43 model showed clear alterations compared to control mice (**Figure 27G, H**). In addition to an increase in connections to TDP43 in the TDP43 transgenic model, the closest protein neighbors changed. Common interactors of TDP43 in the wildtype control are proteins associated with mitochondria, myonuclei, and contractile fiber parts (**Figure 27H** and **Table 13,** Myonuclei). In contrast, in the TDP43 transgenic model, interactions were significantly increased and a complete different other panel of GO-terms, including ribonucleoside triphosphate phosphatase activity (5.6×10^{-6}), response to stress (3.9×10^{-4}), and neutrophile degranulation (5.936×10^{-3}) were observed. Notably, the mRNA-binding proteins proliferation-associated protein 2G4 (PA2G4) and the eukaryotic initiation factor

4A-I (EIF4A1) were directly spatially connected to TDP43 in the ALS model. These proteins form stress-induced ribonucleoprotein granules, with PA2G4 previously linked to Alzheimer's disease and EIF4A1 is directly associated with ALS.[147, 210, 211]

As mentioned earlier, the TDP43 mouse model, overexpress the human TDP43 in neurons. The distance-based network analysis of wild-type control animals shows for the TDP43 node a close localization to skeletal muscle proteins. Conversely, the overexpression model is localized near to NMJ related proteins, indicating the overexpression of TDP43 only in neurons (**Figure S18**, red nodes). To further explore NMJ changes, we extracted significantly upregulated NMJ proteins for both ALS (32) and control mice (48) (**Figure S17H, I**). Further calculations were performed using the 28 proteins that were identified in both control and TDP43 overexpression mice. Although not all the 28 NMJ proteins show profile changes, the AUC indicates a significant decrease in abundance over the NMJ area in TDP43 overexpression mice compared to control mice (**Figure S17**G). A minor increase in path length (**Figure 27I)**, which describes how many connections are between two proteins, and decrease of the closeness centrality (**Figure 27J**) was observed for the transgenic TDP43 mice. The closeness centrality is describing how isolated nodes are. Isolated nodes are pointing against 0, suggesting less connections and higher path lengths between the proteins. Additionally, a distinct difference in the clustering coefficient of NMJ proteins was observed between TDP43-overexpression and control mice (**Figure 27K**). The clustering coefficient was higher in control mice, explained by the similar protein profiles in the control mice with one maximum at the NMJ, whereas ALS mice had differently affected proteins like ChAT and MAG, which showed a biphasic profile, but not AChE and NEFs, which showed one maximum. The overall diaphragm clustering coefficient did not change, but an increase was noted for the protein TDP43, confirming the already observed increase of connections and relocalization in the network to the side of the NMJ proteins (**Figure 27L**, red dot).

In summary, using thin cryosections for spatial muscle analysis is effective in detecting changes in an inducible TDP43 transgenic mouse model, expressing a mutant variant of TDP43 in neuronal cells. Changes in NMJ expression profiles and the TDP43 junctional network were observed, which will contribute to deciphering TDP43-dependent neurodegeneration.

2.3.5. Discussion

Our spatial protein profiling based on short LC-MS runs of single muscle sections allowed us to visualize longitudinal protein profile of the diaphragm, including the NMJ and MTJ. We were able to characterize the transition area between muscle and tendons in high resolution and identified 111 proteins with similar protein profile to the known MTJ marker protein collagen 22. To increase the resolution of our protein profiles, we reduced the section thickness from 20 µm to 10 µm to be able to classify the localization of MTJ proteins into early, central and late MTJ proteins (**Figure 23H-K**). The assessment of our protein profiles according to maxima in the area of the NMJ of the diaphragm revealed 200 proteins. To distinguish the protein profiles between skeletal muscle and neuronal proteins, we compared the proteomes of isolated single muscle fibers and the sciatic nerve with our protein profiles to unravel the cellular origin of the NMJ structure. We also compared the spatial arrangement of the NMJ between young and aged animals and observed for 40 NMJ marker proteins a broadening of the NMJ area in older animals. Accordingly, a network analysis showed decentralized NMJ proteins with reduced connectivity and clustering coefficients, suggesting structural changes associated with aging. Manual preparation methods would not have allowed such high-resolution and unbiased protein profiling of MTJ and NMJ proteins during aging and the TDP43-induced ALS model.

Next, we compared the spatial arrangement of the NMJ in old and young animals and observed for the 40 common NMJ proteins a widening of the NMJ area in older animals. Network analysis showed decentralized NMJ proteins with reduced connectivity and clustering coefficients, suggesting structural changes associated with aging. Manual dissection methods would not have allowed such high-resolution profiles of MTJ proteins or the detection of structural changes in the NMJ during aging. MTJ and NMJ proteins like collagen 22 and ChAT were used to localize the NMJ and MTJ, and correlations to these protein profiles helped further to identify further proteins localized at the MTJ and NMJ.

2.3.5.1. Protein profiles of the soleus and the diaphragm show similar structures of the muscle-tendon transition zones

A recent study analyzing the spatial protein profile of the MTJ in the soleus skeletal muscle revealed 206 MTJ proteins. The overlap to the diaphragm protein profiles revealed 33 congruent MTJ proteins, including known marker proteins such as XIRP2, CILP and POSTN.[167] (**Table 13**). Since the soleus skeletal muscle is bipennate muscle a sharp transition

between muscle and tendon was not observed. For example, the well-known MTJ marker protein COL22 showed a steady increase from muscle to tendon in the soleus and no transient maximum at the MTJ as seen in immunostaining. In contrast muscle fibers of diaphragm are parallel oriented and show a sharp transition to the tendon. Taken the number of slices and thickness into account, we observed a width of the MTJ of ~100 µm compared to 260 µm in the soleus. Thus, each skeletal muscle, dependent on its morphological structure, workload, and localization in the body might have a specific MTJ protein profile.

For eight proteins with a maximum at the MTJ in the diaphragm we found an association with cell adhesion and membrane vesicle trafficking. These proteins might be involved in the formation of the interdigitation of the muscle membrane at the MTJ. For example, cortactin (CTTN), spectrin (SPTAN), PRA1 domain family member 2 (PRAF2), and paralemmin (PALM) were observed with maximum at the MTJ. Cortactin is a binding protein which plays also a crucial role in the formation and regulation of actin skeleton by activation of the actin-related protein 2/3 complex. Additionally, it was recently shown that CTTN is involved in membrane resealing after injury by the induction of actin accumulation at the injury site in single muscle fibers in mice.[212]. Hence, cortactin might play an essential role in the dynamic organization of the plasma membrane and adherent junctions at the MTJ.

Table 13 Identified MTJ proteins in spatially analyzed soleus and diaphragm muscle.

neuronal proteins			
UniProt	**protein name**	**function**	**protein name**
P70288	HDAC2	schwann cell differentiation	Histone Deacetylase 2
Q9CZR2	NAALAD2	involved in neurotransmitter release	N-Acetylated Alpha-Linked Acidic Dipeptidase 2
O08599	STXBP1	releases neurotransmitters via regulation of syntaxin	Syntaxin Binding Protein 1
cytoskeleton			
UniProt	**gene name**	**function**	**protein name**
Q7TMB8	CYFIP1	regulates cytoskeletal dynamics and protein translation	Cytoplasmic FMR1 Interacting Protein 1
O55131	SEPT-7	involved in collective cell movement	Filament-forming cytoskeletal GTPase
Q61029	TMPO	Lamin binding, nuclear anchorage	Thymopoietin
Q4U4S6	XIRP2	enables actin filament binding activity, cell-cell junction organization	Xin Actin-Binding Repeat-Containing Protein 2

ECM

UniProt	gene name	function	protein name
Q66K08	CILP	cartilage ECM protein	Cartilage Intermediate Layer Protein 1
O88207	COL5a1	fibrillar collagen	Collagen 5a1
P28654	DCN	proteoglycan, collagen fibril assembling	Decorin
Q61576	FKBP10	collagen cross-linking	FKBP Prolyl Isomerase 10
Q62009	POSTN	tissue development and regeneration	Periostin
Q9R0M3	SRPX	ECM structural constituent, cell adhesion, contact inhibitor	Sushi Repeat Containing Protein X-Linked
Q8R054	SRPX2	identical protein binding, paralog to SRPX	Sushi Repeat Containing Protein X-Linked 2
Q8CIZ8	VWF	glycoprotein, vascular injuries	Von Willebrand Factor

cell adhesion and vesicle trafficking

UniProt	gene name	function	protein name
O70423	AOC3	cell adhesion protein, vesicle trafficking	Amine Oxidase Copper Containing 3
Q60598	CTTN	regulates and organizes interactions in adherens-type junctions	Cortactin
P08113	HSP90b1	Chaperone, functions in processing and transport of secreted proteins	Heat Shock Protein 90 Beta Family Member 1
Q6ZQI3	MLEC	regulates glycosylation in the ER	Malectin
Q9Z0P4	PALM	plasma membrane dynamics	Paralemmin
Q9JIG8	PRAF2	integral component of membrane	PRA1 Domain Family Member 2
P04919	SLC4a1	mediates electroneutral anion exchange, structural protein	Solute Carrier Family 4 Member 1
P16546	SPTAN1	scaffold proteins, stabilizes plasma membrane	Spectrin Alpha

Mitochondrion

UniProt	gene name	function	protein name
Q5SWU9	ACACA	rate-limiting step in fatty acid synthesis	Acetyl-CoA Carboxylase Alpha
Q9CZS1	ALDH1b1	oxidoreductase activity	Aldehyde Dehydrogenase 1 Family Member B1
Q8K009	ALDH1l2	distribution of one-carbon groups between the cytosolic and mitochondrial compartments	Aldehyde Dehydrogenase 1 Family Member L2
Q8JZU2	SLC25A1	citrate transporter	Tricarboxylate transport protein
Q9R112	SQOR	catalyzes conversion of sulfide to persulfide	Sulfide Quinone Oxidoreductase

Others

UniProt	gene name	function	protein name
O55028	BCKDK	PDK1 paralog, regulates valine, leucine, and isoleucine catabolic pathways	branched-chain alpha-ketoacid dehydrogenase complex
Q9QZE5	COPG1	golgi vesicle transport and localization	COPI Coat Complex Subunit Gamma 1
Q99M28	RNPS1	mRNA nuclear export and mRNA surveillance	RNA-Binding Protein with Serine-Rich Domain 1
P22437	PTGS1	FA metabolism, immune response	Prostaglandin G/H Synthase 1
Q9WV91	PTGFRN	myoblast fusion, lipid organization	Prostaglandin F2 Receptor Inhibitor

2.3.5.2. Protein profiles show an expression of proteins within the NMJ and MTJ that are associated with myelination of the Golgi tendon organ (GTO)

The Golgi tendon organ (GTO) is a proprioceptive sensory receptor organ that senses changes in muscle tension and is located at the junction between a skeletal muscle and tendon. The receptor is embedded within the collagen fibers of the tendon and monitors the amount of tension generated in a muscle during contraction. In addition, the GTO provides continuous feedback to the central nervous system (CNS) about the tension in skeletal muscles.[213]. Similarly, the NMJ also contain motor neurons, perisynaptic Schwann cells, which are also known glia cells of the peripheral nervous system (PNS). The assembly of these cells is essential for NMJ maintenance, repair, and synaptic plasticity. Accordingly, we observed for several neurofilament and myelin proteins a significant maximum at the NMJ and MTJ. This suggests the presence of neuronal innervation at both areas and the presence of sensors to modulate the activity of the skeletal muscle. Interestingly, the myelin-associated glycoprotein (MAG) that enhances axon-myelin stability, axon cytoskeleton, and axon regeneration, was only identified with a maximum at the NMJ (**Figure 24B, C**). In contrast the myelin binding protein (MBP) and the myelin protein zero (MPZ) showed a maximum at the NMJ and MTJ. MAG is enriched in membranous vesicles and selectively localized in glial membranes of myelin sheaths, distinct from compact myelin within the CNS.[214] Therefore, one of the main functions of MAG is the control of glia-axon interactions, and according to our protein profiles, this seems to be restricted to the NMJ.

A protein related to gene regulation is the histone deacetylase HDAC2, which showed a common maximum at the NMJ and MTJ (**Table 13**). HDAC2 is closely associated with the NuRD (nucleosome remodeling and deacetylase) complex and activates Schwann cell differentiation.[75] As mentioned above, Schwann cells are the glial cells of the PNS, and previous studies have shown that HDAC2 regulates gene activity in Schwann cells. The detection of HDAC2 maxima at the NMJ and MTJ indicates an enhanced expression in neuronal cells and suggests a potential role in the Golgi tendon apparatus as well as motor endplates.[215] To identify potential targets of HDAC2 which are controlled by histone de-acetylation at specific loci, one might use chromatin immunoprecipitation (CHIP) assays.

Systematic analysis of the diaphragm demonstrated 670 protein profiles associated with the GOCC-term mitochondrion. Most of these mitochondrial proteins show a constant profile with a steep decrease at the MTJ. However, around 50 mitochondrial protein profiles show

peak at the NMJ, and 20 proteins at the MTJ. This could either reflect a specific adaptation of the mitochondria, or these proteins are simultaneously localized in other cellular compartments.

For example, the citrate transporter protein (SLC25A1), which exports citrate or isocitrate from the mitochondria into the cytosol showed a maximum at the MTJ. Other proteins like ATP-citrate lyase (ACLY) and acetyl-CoA carboxylase alpha (ACACA), which are involved in lipid biosynthesis showed also a maximum at the MTJ. Recently, we proposed that enhanced expression of the SLC25A1 transporter at the MTJ increases cytosolic citrate and acetyl-CoA levels, which may be transported from the mitochondria to the nucleus. These molecules are used by histone acetyltransferases (HATs) to acetylate histones, thereby regulate fatty acid synthesis and matrix protein expression through histone acetylation at the MTJ.[167]

The protein acetyl-CoA acetyltransferase (ACAT), involved in the cholesterol pathway, was enriched at the NMJ. Cholesterol is an essential component within the myelin membrane, increases viscosity and stabilizes lipids and proteins. It might be that ACAT expression at the NMJ is responsible to stabilize synaptic membranes, including the clustering of AChRs at the postsynaptic membrane.[216, 217] In summary, elevated cholesterol biosynthesis might support the formation and maintenance of synaptic vesicles and efficient neurotransmitter release to control neuromuscular transmission.

2.3.5.3. Proteins related to ECM elasticity are changed in aged mice diaphragms

We identified 99 and 74 proteins with a maximum at the NMJ of aged and young animals.

Most strikingly, we observed an increase in the area under the curve and a broader protein profile for several NMJ marker proteins during aging (**Figure 26C, L-O**). This is consistent with previous reports in which greater dispersion, fragmentation and disorganization of NMJs during aging was observed by morphological studies.[199]

There are few data on the molecular candidates responsible for these structural changes in the NMJs. Significantly changed NMJ proteins between aged and young animals include ATP1A3, caveolin-3, DPYSL2, and NID1 (**Figure 25D-F** and **Figure S15C**). The glycoprotein NID1 is a central component of the ECM that bridges laminins, perlecan and collagens within the basement membrane. NID1 maintains ECM structures by protecting other glycoproteins from degradation and these proteins are less susceptible to proteolytic degradation.[202-204] During aging, there is an increased degradation of NID1 itself due to the

upregulation of metalloprotease. A reduced NID1 abundance at the basement membrane leads to an enhanced susceptibility of other glycoproteins to degradation. Moreover, the stabilization of the presynapse to the motor endplate can be significantly affected by reduced NID1 levels. The process of progressive loss of the connective protein NID1 may be associated with denervation and increased fragmentation, already reported in mice with ablated laminin-α4 and collagen XIII.[218]

Another protein with a restricted maximum at the NMJ is the inter-alpha-trypsin inhibitor heavy chain H3 (ITIH3) and ITIH4 (**Figure 24B**). These proteins play a role in stabilizing the extracellular matrix (ECM) and ITIH3 is primarily involved in the synthesis and degradation of hyaluronic acid (HA), a key component of the ECM. The ITIH3-HA interaction is responsible for maintaining the elasticity of the ECM and ITIH3 contributes to repair processes and shows anti-inflammatory properties.[219, 220] Recently, ITIH3 was identified as a novel myasthenia gravis (MG) biomarker to improve diseases progression identification. MG is an autoimmune disease that attacks proteins like AChR or MuSK in the postsynaptic muscle membrane, causing muscle weakness. ITIH3 abundance serves as a negative feedback mechanism, increasing in response to aberrant complement activation. In MG-affected human hindlimb muscles, ITIH3 localization at the NMJ has been observed but not in the control samples.[194] In mouse soleus muscles, an increase towards the tendon was observed, but no biphasic profile like other NMJ proteins was noted.[167] We suggest ITIH3 and ITIH4 plays a specific role at the NMJ of the diaphragm, a muscle in constant rhythmic motion and continuous contraction, with a higher density of NMJs compared to other skeletal muscles. The diaphragm NMJ likely undergoes constant repair mechanisms involving the replacement of muscle endplate proteins. As already mentioned, in aged mice more denervation and reinnervation events happen leading to a degradation of AChR, similarly to MG. An increase in ITIH3 and ITIH4 abundance in aged mice suggests similar mechanisms of muscle-nervous system connection loss (**Figure S15I, J**). Network analysis of diaphragm protein profiles showed loss of connectivity of NMJ in aged mice. In order to characterize the molecular function of ITIH3 at the NMJ in vivo, mouse models with gain and/or loss of function of ITIH3 should be generated in the future.

According to the detection of broader NMJ protein profiles during aging, our bioinformatic network analysis (**Figure S16**) showed a loss of interconnectivity and a lower clustering coefficient in aged mice compared to young controls (**Figure 25I-K**). This decrease in

interconnectivity indicates impaired communication between NMJ-associated proteins, which is likely due to the increasing distances between these proteins. This structural difference could lead to reduced motor function and muscle weakness. The loss of interconnectivity was particularly prominent among proteins such as CD9, STXBP1, and SLC2A1, which are crucial for vesicle trafficking and membrane binding. The disturbance of these pathways has been implicated in neurodegeneration and is characteristic of aging-related diseases. Conversely, proteins like MAG, MPZ, and NEFs, involved in myelination and axonal support, did not exhibit significant changes in their connectivity, suggesting that specific functional protein groups and compartments within the NMJ are differentially affected by aging. However, cellular resolution is still lacking and the isolation of individual cells and neurons by FACS or laser microdissection techniques could help to study specific cell populations in the NMJ and their changes during aging in more detail.

2.3.5.4. The NMJ of the TDP43 ALS mouse model shows similar changes compared to aged mice

Protein profiling of the TDP43-dependent ALS mouse models revealed a slight reduction with 32 protein maxima at the NMJ compared to 48 maxima in healthy control animals. The main reason for this decrease in ALS animals is an altered biphasic protein expression profile within the NMJ. For example, ChAT shows a broader and biphasic pattern in ALS animals whereas the healthy controls do show a single peak (**Figure 27D**). In total, we observed for ~50% of the NMJ protein profiles a significant alteration between the ALS model and controls.

Previous studies have shown similar changes in the NMJ in aged mice and ALS models compared to young controls. In addition to morphological changes of the NMJ, both aged and ALS mice show reduced muscle mass, less strength and increased oxidative stress probably caused by mitochondrial dysfunction.[191, 221, 222]

To detect changed proteins expression, regardless of their profile, we first selected X sections along the NMJ area and performed a quantitative analysis between the young TDP43, young control and aged mice. We observed an overlap of 104 upregulated and 43 downregulated proteins between aged and the TDP43 ALS models (**Figure 28A**). One of the most abundantly upregulated proteins in aged and TDP43 overexpression mice is calmodulin-1 (CALM1). The calcium-binding protein plays a critical role in translating calcium signals into cellular responses. Upon stimuli and elevated Ca^{2+} levels, CALM-1 binds Ca^{2+},

undergoes a conformational change, and interacts with various target proteins, such as calmodulin-dependent protein kinase II and phosphatases, influencing cellular metabolism, cell division, and gene expression. In muscle tissue, CALM-1 is essential for contraction[223], while in neurons, it regulates synaptic plasticity and neurotransmitter release[224]. CALM1 also affects neurotransmitter release from synaptic vesicles, impacting neuronal communication. Calcium dysregulation is an early and critical event in both neurodegenerative diseases and aging, leading to mitochondrial Ca^{2+} overload and disruptions in electron transport chain complexes, which increase oxidative stress.[225]

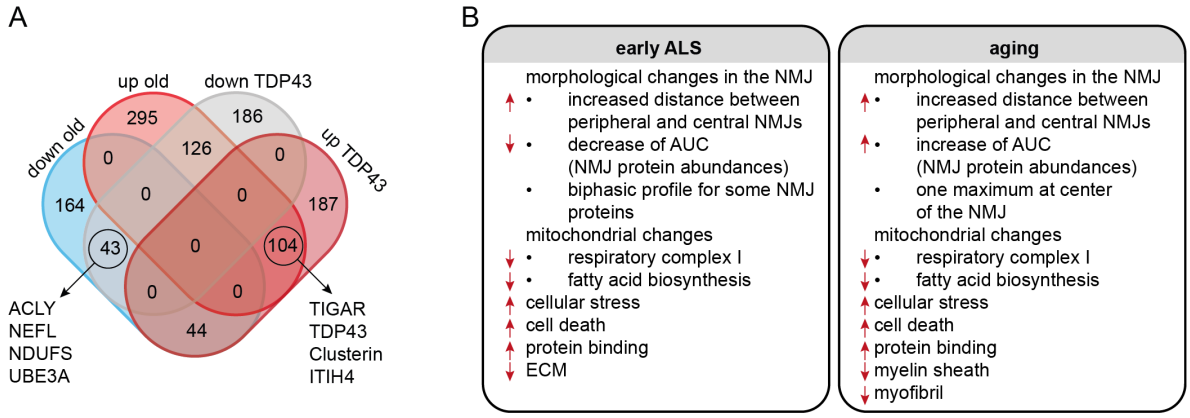

Figure 28 Shared and altered changes between TDP43 dependent ALS mice and aged mice. A) Venn diagram of up and down regulated proteins between aged and young mice, and TDP43 and control mice. **B**) Shared and altered changes between the TDP43 dependent ALS and aged mice. ACLY, ATP-citrate synthase; AUC, area under the curve; ECM, extracellular matrix; ITIH4, inter-alpha-trypsin inhibitor heavy chain 4; NDUFS, NADH-ubiquinone oxidoreductase 75 kDa subunit; NEFL, neurofilament light chain NMJ, neuromuscular junction; TIGAR, TP53-inducible glycolysis and apoptosis regulator; TDP43, TAR DNA-binding protein 43; UBE3A, ubiquitin protein ligase E3A.

Additionally, in both ALS and aging models, we observed morphological changes at the NMJ (**Figure 28B**). While both conditions show an increased distance between peripheral and central NMJ nodes (**Figure 26** and **Figure 27**), the AUC increases for aged NMJs, while it decreases for ALS mice. In aged mice, frequent denervation and reinnervation events lead to NMJ spreading and an expanded NMJ area. In the TDP43 dependent ALS mouse model, which was induced for 4 weeks, denervation may occur with reduced reinnervation, resulting in the loss of key NMJ proteins such as ChAT and MAG at the NMJ. This pattern may explain the biphasic profile observed in ALS mice, where the distance between NMJ nodes expands, but the central NMJ is already denervated.[80, 199] To shed light on the time course of degeneration and regeneration in the TDP43 model, analysis of even earlier and later time points is certainly needed. The protein profiles will help to better understand the pathobiology of neurodegeneration and loss of muscle strength in ALS animals.

Both aged mice and the ALS mouse model display similar mitochondrial alterations compared to control mice, including a reduction in respiratory complex I activity and impaired fatty acid metabolism (**Figure 28B** and **Figure S15G**). However, only the aged mice exhibited a loss of myofibrils and impaired myofiber contraction, which aligns with the known fiber-type switch and overall muscle mass loss associated with aging (**Figure S15G**). Although a shift from fast to slow muscle fibers has been observed in ALS models, we did not detect this in our study. This could be due to the early stage at which we analyzed the TDP43 mice, or it may be because many sarcomeric proteins have long half-lives, preventing noticeable changes within four weeks of TDP43 protein expression. We hypothesize that later time points would likely show an effect on MYH isoforms (**Figure 27B**).[80, 92]

In summary, this study provides more than 3000 protein profiles of the mouse diaphragm and reveals the spatial organization of the MTJ and NMJ. Similar to aged animals, the protein profile of TDP43-ALS mice showed a broadened structure of the NMJ. Whether the changes in the protein profiles of aged and ALS mice can be attributed to the same molecular mechanisms is still unclear. The analysis of further time points and disease models will provide more information about possible adaptations in the NMJ in different health conditions in the future.

2.3.6. Resource availability

2.3.6.1. Lead contact

Further information and requests for resources should be directed to and will be fulfilled by the lead contact, Marcus Krüger (marcus.krueger@uni-koeln.de).

2.3.6.2. Materials availability

- This study did not generate new unique reagents.

2.3.6.3. Data and code availability

- Proteomic data have been deposited at ProteomeXchange and are publicly available as of the date of publication (Accession number).
- All original code has been deposited at Zenodo and is publicly available as of the date of publication (DOI).
- Any additional information required to reanalyze the data reported in this paper is available from the lead contact upon request

2.3.7. Experimental model and subject participant details

Experimental model

Wildtype animal experiments were performed in accordance with national and institutional guidelines. 2-4- or 26-months old wildtype C57BL/6 mice were maintained 22 ± 2 °C, with a humidity of 55 ± 10%, and an air exchange rate of 15 times per hour on a 12:12-h light-dark cycle and had free access to standard chow diet. All mouse experiments were performed in accordance with the regulations stated in European, national, and institutional guidelines and were approved by local government authority Landesamt für Natur, Umwelt und Verbraucherschutz (LANUV) of North Rhine-Westphalia, Germany.

2.3.8. Method details

2.3.8.1. Intact tissue sample processing, protein digestion, and desalting

After sacrifice, sciatic nerves were isolated, followed by snap freezing in liquid nitrogen and storage at −80 °C. Samples were lyophilized and ground to a fine powder using a mortar and pestle. Samples were lysed in 4% SDS in PBS, heated to 95 °C and sonicated using the Bioraptor sonicator (Diagenode, Belgium) set to 14 °C water with 10 cycles of 30 on/30 off. Cell debris was pelleted by centrifugation at 18,000 g for 10 min. 25 µg of the protein extract was reduced and alkylated for 45 min at 45 °C using 5 mM TCEP and 15 mM CAA. After acetone precipitation, protein pellet was reconstituted in 3M GuHCl in 50 mM HEPES, 2.5 mM CaCl2. Proteins were digested with LysC (substrate:enzyme ratio 50:1) for 3 h at 27 °C followed by dilution of the GuHCl to 0.5 M with 50 mM HEPES, 2.5 mM CaCl2 and digestion with trypsin (substrate:enzyme ratio 100:1) for 15 h at 27 °C. Samples were acidified to 1 % formic acid (FA) and cleaned-up by using house-made SDB-RPS Tips.

2.3.8.2. Single muscle fiber isolation and digestion

Freshly dissected diaphragm muscles were placed in 0.2% Collagenase-P Dulbeccos Modified Eagle Medium (DMEM) and incubated for 20-30 min on 37 °C. Digestion was stopped by transferring the muscles in DMEM containing 5 mM EDTA, 10% FBS. Fibers were isolated by flushing the skeletal muscle several times using a glass pipette. Muscle fibers were washed 5x with 1x PBS containing 5 mM EDTA. Each single fiber was placed into a 96-well plate and lysed with 40 µl of 4% SDS in PBS containing 5 mM TCEP and 10 mM CAA. The 96-well-plates were incubated at 95 °C for 10 min followed by Bioraptor sonication at 20 °C with 10 cycles of 30 on and 30 off. Samples were digested, and peptides were purified as already described. Peptides were reconstituted in 0.1%, with iRT peptides.

2.3.8.3. Tissue slices sample preparation

Diaphragm muscles were fixed on both sides using insect needles on cork matrix, embedded in optimal cutting temperature (OCT) resin, and stored at -80 °C until further use (further details **2.2.2.1**). OCT embedded solei were cut into 10–30-µm-thick slices at -25 °C using a Reichert Jung cryostat (Leica, Nussloch, Germany) and each slice was placed individually into a well of a 96-well-plate (further details **2.2.4.1**). As controls, one column on each 96-well plate was loaded with a HEK293T protein lysate. The slices placed in the wells were mixed with 40 µL of 4% SDS in PBS containing 5 mM TCEP and 10 mM CAA. The 96-

well-plates were incubated at 95 °C for 10 min followed by Bioraptor sonication at 20 °C with 10 cycles of 30 on and 30 off. Samples were digested following the standard SP3 protocol.14 Briefly, 20 µg of washed SP3 beads were added to each well, followed by one sample volume of acetonitrile (ACN). After incubation for 8 min and a further 2 min on a magnet, the supernatant was discarded, and the magnetic beads were washed twice with 70% EtOH and once with 100% ACN. Samples were digested with 10 µL of 20 ng LysC and 40 ng trypsin in 50 mM ammonium bicarbonate buffer at 37 °C on a rotating wheel (750 rpm) overnight, acidified by addition of 100 µL 0.1% FA, followed by clean-up with house-made SDB-RPS tips. Peptides were reconstituted in 2% ACN, 5% FA, with iRT peptides (further details **2.2.4.2**).

2.3.8.4. Tissue slices quantitative proteomics analysis

Desalted peptides were loaded on EvoTips Pure. Peptide separation was performed on an EvoSep One system (both Evosep, Denmark) equipped with an in-house packed 8 cm silica emitter column (100 µm inner diameter, packed with 5 µm C18 Poroshell, Agilent) at 30 °C with the pre-programmed 60 (21 min) and 100 (11.4 min) SPD methods. Mobile phases were compromised of 0.1% FA as solvent A and 0.1% FA in ACN as solvent B. The HPLC system was coupled to a timsTOF pro 2 using a CaptiveSpray source (both Bruker). Samples were measured in dia-PASEF mode with ion mobility calibrated after every 50th sample using three ions of Agilent ESI-Low Tuning Mix following vendor specifications. The dia-PASEF window was ranging in dimension 1/k0 0.7-1.35, with 24x25 Th windows and in dimension m/z from 350 to 1250.

2.3.8.5. Bioinformatic analysis

The mass spectrometry proteomics data have been deposited to the ProteomeXchange Consortium via the PRIDE partner repository with the dataset identifier PXD054352.[161] Samples were analyzed with DIA-NN 1.8 using library free search against the UniProt mouse database (Sep. 2017) complemented with protein sequences from myosin heavy chain variants and collagens. Mass ranges were set according to the settings of the mass spectrometer; mass deviation was automatically determined from the first data file. Data was further processed using R (V 4.2.2), with the tidyverse, diann, data.table, magrittr, FactoMineR, factoextra, ggplot2, and gprofiler libraries. An in-house modified R-script based on the version by V. Demichev was used to calculate MaxLFQ values.[162, 163] To show

identified peptides we used the term “precursor”, which refers to an ion analyzed by the MS instrument. The precursor ion is fragmented into product ions and contains information about the sequence, modification status, and the charge state. Data input was filtered for unique precursor, q-value <0.01, Lib.Q.Value <0.01, PG.Q.Value < 0.01, Global.Q.Value < 0.01, Quantity.Quality > 0.7, Fragment.count >= 4; previously separated data from different compensation voltages were combined for each protein entry to the maximum value. Statistical analysis was performed with R (V 4.2.2) and Perseus (V.1.6.5.0) and visualized with Instant clue (V 0.10.10.20210315). For the analysis of sectioned tissue, files were pre-processed as described before. Further calculations were performed within R (version 4.2.2) using the diann, tidyverse, data.table, samr, vsn, ggplot2, and gprofiler libraries. All protein intensities smaller than 10^4 were replaced as missing values (further details **8**).

The protein intensities in each slice were normalized to the total protein intensity in each slice. Slices were arranged spatially, and proteins were filtered in a distance related manner; a sliding window was generated that covered an overall a distance of 200 µm, i.e., five sections back and five sections forward. Proteins with less than 70% coverage over one sliding window were excluded. For imputation, a pseudo-slice ID was established to capture sections for which measurement completely failed and to ensure that the sliding window always contained 10 sections before and 10 sections after the current slice. Sections close to the edge of the sample were truncated but required a minimum of three samples to be present for imputation. For windows that fulfilled the 70% limit, missing values in the windows were imputed with a normal linear imputation using 200 µm distances. The remaining missing values were imputed with random values 1.6 points below the mean of the lower 5% of the total expression values across all proteins.

Samples from different biological replicates had to be adjusted to obtain congruent protein profiles. We normalized each muscle section by dividing each section by the length of the whole muscle. Then, each experiment was analyzed with a bootstrap approach based on the Significance analysis of Microarrays (SAM) method [125, 165] to detect gradual increases or decreases over distance for specific proteins in a linear and non-linear relationship as local minima and maxima. The reported distribution statistics (d-statistics) were further used as readout for significantly up- or downregulated proteins. The average score across all samples was calculated and proteins with a d-statistic > 5 were selected to shift the profiles required to achieve improved matching of minima and maxima within the profiles. Z-scores were calculated row-wise, and the average protein profile was smoothed using a local regression

function, called LOESS, in which the 95% confidence intervals were calculated as representative profiles of each protein. For ease of visualization, the representative profiles were normalized to range from 0–1 for all data (further details **2.2.4.5**).

2.3.8.6. Development of a network-based representation of the muscle tendon regions

The representative profile of each protein was used as input for a time impact analysis, replacing time with distance. This comprehensive technique is used to analyze each delay event individually in chronological order to calculate its impact and to quantify each delay based on the schedule immediately before and after the delay event took place. The delay is calculated by the highest correlation of two protein profiles. Correlation was calculated by shifting two protein profiles in both directions by up to 20% of the total distance. The reported delays were filtered for correlation scores higher than 0.7 and for distances less than 100 µm. The interactions were visualized in Cytoscape and arranged using the Spring Embedded Layout of the delay, leading to a hierarchical arrangement of the proteins over distance.
Wilcoxon *t*-tests of the AUC and GO-term enrichment analysis were performed and visualized using R (V 4.2.2) using the packages gprofiler2 and ggplot2 (further details **2.2.4.6**).

2.3.8.7. Histochemistry and immunostaining

Mouse diaphragm muscles were collected, embedded as described previously, cut longitudinally in 7 µm sections, collected on glass slides (VWR) and stored at -80 °C until further use. Slides were removed from the freezer and dried at room temperature. Two biological replicates were performed for each staining. Longitudinal sections were fixed with Histofix (Histolab) for 10 min at RT. Primary antibodies against Tenascin-C (Leica Biosystems Cat# NCL-TENAS-C, RRID:AB_564026), α-Bungarotoxin-ATTO Fluor-488 (Molecular Probes Cat# T1175, RRID:AB_2313931), Collagen 22 (provided from Manuel Koch (Cologne) were diluted 1:100 in 1% BSA in TBS, except Collagen 22 was used 1:500, and applied overnight at 4 °C; the following day, secondary antibodies were diluted 1:200 and Hoechst (Invitrogen, #H1399) 1:100 in TBS and applied for 60 min at RT. As secondary antibodies were used (AF568-conjugated anti-rabbit (Molecular Probes Cat# A-11036 (also A11036), RRID:AB_10563566), AF488-conjugated anti-rabbit (Thermo Fisher Scientific Cat# A-11034 (also A11034), RRID:AB_2576217), AF568-conjugated anti-guinea pig

(Thermo Fisher Scientific Cat# A-11075, RRID:AB_2534119), AF488-conjugated anti-mouse IgG2b (Thermo Fisher Scientific Cat# A-21141, RRID:AB_2535778), AF680-conjugated anti-mouse IgG2a (Thermo Fisher Scientific Cat# A31563, RRID:AB_2536177)). Samples were washed twice for 10 min in TBS between all steps in the protocol. Finally, slides were mounted with coverslips using Prolong Gold Antifade Reagent (Thermo Fisher Scientific). For widefield fluorescence microscopy, images were captured using two different objectives (10x/0.3NA; 20x/0.5NA) on an Olympus BX51 microscope with a 0.5x camera (Olympus DP71, Olympus Deutschland GmBH, Hamburg, Germany) at the ISMC using the software Olympus cellSens Software (RRID:SCR_014551). Images were further processed using ImageJ (version 1.54d; RRID:SCR_003070) and colorblind-friendly pseudo colors were applied to the composite images.

2.3.9. Quantification and statistical analysis

All experiments were carried out in triplicates otherwise stated in the methods details. Welch's *t*-test was calculated within Perseus. The Permutation-based FDR and Number of randomizations was set to 0.05 and 500, respectively. GO-terms were compared using a *t*-test analysis and significance are indicated using asterisks (* adjusted p-value < 0.05. ** adjusted p-value < 0.01, *** adjusted p-value < 0.001). Statistical details can also be found in the according figure legends.

2.3.10. Author contributions

Isolation, preparation, sectioning, and digestion of the muscles was performed by Sina Pascher and me. I optimized the MS instrumentation and method set up as well as ensured stable data acquisition. Implementation of the bioinformatic analysis workflow and distance-based network analysis was performed by me and Philipp Antczak. Immunohistochemistry staining, imaging, and figure preparation of longitudinal muscle sections were performed by me, Christian Hoegsbjerg, and Abigail Mackey. I assembled all figures and assisted Marcus Krüger in writing the manuscript.

2.4. Prepared manuscript (IV): Single muscle fiber proteomics of pre-diabetic mice revealed increased mitochondrial fission in type IIa fibers

Luisa Schmidt[1], Katharina Neuser[1], Christiana Zollo[1], Peter Zentis[1], Ximena Hildebrandt[2], Michael Saynisch[1], Philipp Antczak[2], Bianca Collins[1], Ana Garcia[1], Nieves Peltzer[2], Marcus Krüger[1,2, $]

1 Institute for Genetics, Cologne Excellence Cluster on Cellular Stress Responses in Aging-Associated Diseases (CECAD), Cologne, Germany

2 Center for Molecular Medicine (CMMC), University of Cologne, 50931 Cologne, Germany

$ Correspondence: MK Marcus Krüger (marcus.krueger@uni-koeln.de)

This manuscript is so far not available September, 2024

2.4.1. Summary prepared manuscript IV

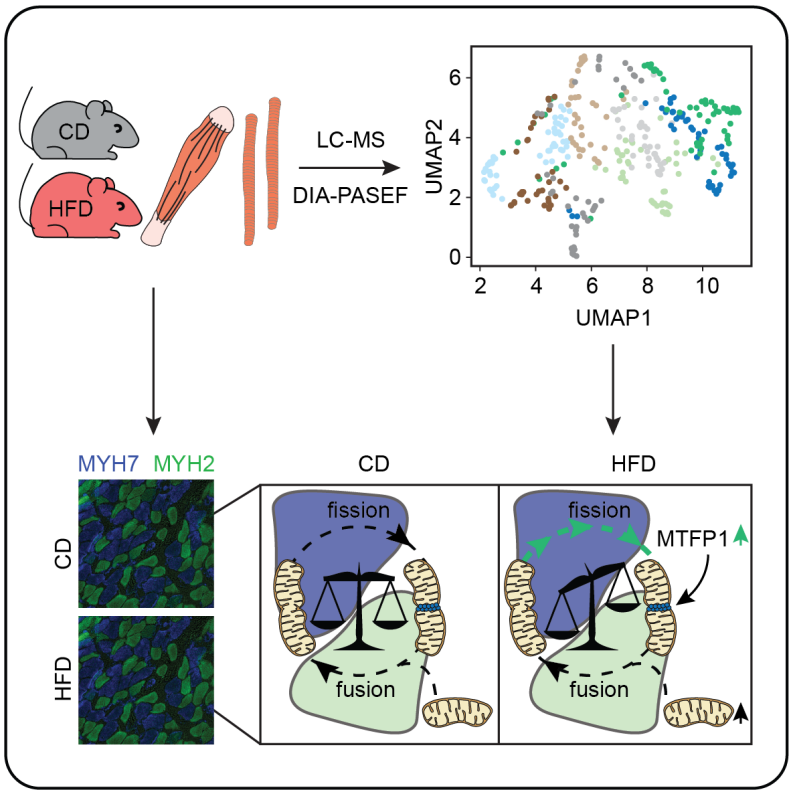

Figure 29 Graphical abstract publication IV. Mouse soleus muscles are dissected, and single muscle fibers are isolated of CD and HFD mice. Single muscle fibers are used for LC-MS analysis with following bioinformatical approaches. Intact muscles are used for IHC. Combining both approaches, we could show an increase of mitochondria after HFD and individual changes for fiber types like an increase of MTFP1 leading to the hypothesis of an imbalance of mitochondria fission and fusion in type 2a fibers after HFD.

CD, control diet; HFD, high-fat diet; LC-MS, liquid chromatography-mass spectrometry; MTFP1, mitochondrial fission protein 1; MYH, myosin heavy chain; UMAP, uniform manifold approximation and projection for dimension reduction.

Skeletal muscles consist of mixed fibers with different myosin heavy chain proteins and different metabolic activities. Due to the adjustable fiber type composition, muscles can react rapidly to different stimuli and disorders. Here, we assessed individual fibers by quantitative proteomics to dissect protein changes after administration of a high fat diet (HFD) for 16 weeks to mice (**Figure 29**). Using single fiber proteomics, we were able to quantify ~1500 proteins per single muscle fiber with short 20 min LC-MS gradients. Although myosin heavy chain profiling is currently the most reliable classifier for single skeletal muscle fibers, the challenge of comparing individual fibers becomes a concern in models with a significant change in myosin heavy chain (MYH) expression. Instead, we exploited the heterogeneity between fiber types and extended the MYH-based classifications with more than 50 fiber-specific proteins to determine the phenotype of skeletal muscle fibers independent of MYH expression with a broader panel of proteins. Mass spectrometric and bioinformatics analysis of individual fibers enabled clustering of type I, IIa, mixed I/IIa and mixed IIa/IIx fibers. Comparison of these 4 groups from control (CD) and HFD treatment revealed restricted regulation of a total of 18 proteins in response to HFD. The levels of several mitochondrial, ribosomal and signaling proteins were significantly altered, indicating rapid adaptation of metabolic processes in response to HFD. Furthermore, in HFD treated type IIa fibers a reduced abundance of peripheral mitochondria was detected and expression of the

mitochondrial fission process protein 1 (MTFP1) were increased in HFD compared to lean controls. This study provides insight into how different muscle fiber types remodel their metabolic activity and mitochondrial network during high caloric diet.

2.4.2. My contributions to publication IV

As the first author of this prepared manuscript, I was the main driver of this project. HFD and *in vivo* metabolic studies were performed by Ximena Hildebrandt and Nieves Peltzer. I was supported by Michael Saynisch and Katharina Neuser for muscle fiber isolation and preparation for LC-MSMS analysis. LC-MSMS instrument optimization was performed by me. I performed the bioinformatic analysis together with Philipp Antczak and interpreted the data. Sectioning of the soleus muscle was performed by Bianca Collins and I performed the following IHC staining. Christiana Zollo and I performed the imaging of the IHCs. Together with Peter Zentis, we analyzed the staining. I assembled all the figures and wrote the manuscript together with Marcus Krüger.

2.4.3. Introduction

The skeletal muscle, which accounts for around 40% of body mass, is responsible for almost 70% of insulin-stimulated glucose processing and therefore represents the body's largest energy reservoir. It is thus obvious that changes in food intake influence the activity of skeletal muscles. For example, skeletal muscles of individuals with severe obesity and type 2 diabetes mellitus show impaired glucose metabolism and a reduced mitochondrial activity in skeletal muscle tissue.[94]

The processing of glucose, fatty acids and lipids in the muscle is closely related to its fiber type composition, which consists of either slow (type I) or fast (type IIa, IIx, IIb) muscle fibers. Since each fiber type has unique metabolic characteristics that determine how it stores and utilizes energy during muscle contraction, a potential shift of fiber types has a significant impact for the energy homeostasis of the whole body. Previous studies have shown that the proportion of slow muscle fibers (type I) is inversely related to obesity, while the number of glycolytic type IIx fibers increases.[85] So far, the best marker proteins for fiber type identification are myosin heavy chain isoforms. Type I fibers are characterized by the expression of the myosin heavy chain 7 (MYH7) isoform and an oxidative metabolism for energy production. Conversely type II fibers mainly express MYH2 (type IIa), MYH1 (type

IIx) and MYH4 (type IIb) isoforms and display a wide range of oxidative (type IIa) and glycolytic (type IIb) activities. Further fiber subtypes are formed through mixed MYH isoform expression, thus expanding the metabolic variability of skeletal muscle tissue.[21] However, our current knowledge of the exact distribution of hybrid fibers in the muscle and in particular changes in MYH expression in obesity is quite limited.

The most abundant organelle in skeletal muscle fibers are mitochondria, which supply the contractile apparatus with energy in the form of ATP. Mitochondria are characterized by rapid biogenesis during increased physical activity and the regulation of mitochondrial activity is tightly associated with the formation of mitochondrial network through fusion and fission. At the molecular level the mitochondrial outer membrane GTPase proteins mitofusins 1 and 2 (MFN1 and MFN2) mediates mitochondrial fusion[99], while mitochondrial fission is regulated by dynamin-related protein 1 (DRP1).[100] Another fission factor is the inner membrane protein mitochondrial fission process 1 (MTFP1/MTP18). Genetic ablation of Mtfp1 reduces mitochondrial fission and leads to elongated mitochondria in cultured cells.[101] A recent MTPF1 gene ablation in mouse cardiomyocytes revealed a progressive dilated cardiomyopathy (DCM) and heart failure.[102] Although mitochondrial fission was not changed in this model, inactivation of MTFP1 leads to reduced OXPHOS efficiency caused by increased proton leak via the adenine nucleotide translocase (ANT).

Here, we used a type II diabetes mellitus mouse model to decipher how individual muscle fibers change in response to an increased food intake. Mice were fed with a high fat diet (HFD) for 16 weeks and single fiber proteomics were performed using solid-phase-enhanced sample preparation (SP3) and parallel accumulation-serial fragmentation (PASEF) on a trapped ion mobility spectrometry mass spectrometer (timsTOF). Short 20 min LC-MS gradients enabled a high-throughput approach of more than 1000 individual fibers, and we quantified ~1500 proteins per single fiber. Since the diet leads to a rapid reduction in MYH7 expression, we used 50 alternative marker proteins for the identification of type I fibers to enable a more precise comparison of the effect of the diet on type I fibers. The identification of the MTPF1 with a restricted increase in type II fibers correlates with an increased mitochondrial fission in these fibers. Slow muscle fibers showed a reduced MTPF1 abundance and change in fission in response to the HFD. Overall, the large-scale single muscle fiber analysis allowed us to compare fiber type-specific response under normal and high fat diet conditions.

2.4.4. Results

2.4.4.1. Administration of a high fat diet (HFD) for 16 weeks induces a prediabetic phenotype

Two groups of wildtype mice (n=4) were fed with a normal control diet (14% CD) or with a high fat containing diet (60% HFD) for 16 weeks (**Figure 30A**). High fat treated animals showed a significant increase of body weight and elevated glucose levels in response to glucose tolerance tests (GTT) (**Figure 30B, C**). Similarly, HFD mice became progressively more insulin resistant after 16 weeks tested by insulin tolerance tests (ITT) compared to control mice (**Figure S19**). Hematoxylin and eosin staining of liver, adipose tissue and soleus muscle sections substantiates an increased fat accumulation in both tissues (**Figure 29D** and **Figure S19B**). Overall, HFD feeding for 16 weeks leads to an obese phenotype, glucose intolerance and fat accumulation in skeletal muscle.

Next, we performed immunostaining with MYH7 (slow type I, blue) and MYH2 (fast type IIa, green) antibodies and observed a slight decrease in the cross-sectional area of MYH7 intensity in mice treated with HFD compared to controls in the soleus muscle (**Figure 30E, F**). The number of type I and type IIa fibers were not changed between control and HFD treatment (**Figure 30F**). Mass spectrometric analysis of intact soleus muscle tissue revealed significant upregulation of 23 proteins associated to the gene ontology (GO)-term of mitochondrion (**Figure 30G)** and a significant increase of all mitochondrial proteins compared to controls (**Figure 30H** and **Table S11**). This is consistent with previous reports showing that skeletal muscle exhibits an increase in its mitochondrial content in response to HFD.[226]

Next, we asked whether we could resolve the response of individual muscle fibers with distinct metabolic activities to high fat diet administration by single muscle fiber proteomics. We isolated ~ 48 single muscle fibers from the soleus of control and HFD treated mice for 16 weeks. Isolated muscles were digested with collagenase P and the single fibers were analyzed by LC-MS (*n*=4) (**Figure 30E, I**). In total, we measured 384 fibers in 96-well plate format by the SP3 protocol and trypsin digestion. Short LC-MS gradients of 20 minutes allowed us to identify ~1500 protein hits per fiber within ~6 days (**Figure S20A, B**). HeLa cell lysates and blank controls were used as quality and carry-over control every 30th sample (**Figure S20C-E**). In addition, indexed retention time peptides (11 iRT peptides) were added to each sample to control LC stability (**Figure S20D, E**). Samples were measured on an ion

mobility mass spectrometer (timsTOF pro 2) and RAW data were processed with DIA-NN.[170] Peptides with common sequences were not included in the analysis and the protein intensities were normalized by the sum intensity for each fiber (**Figure S20F** and **Table S12**). Uniform manifold approximation and projection (UMAP) for dimension reduction enabled us to visualize a separation of fiber types and changes between control and HFD conditions (**Figure 30J**).

2.4.4.2. High fat diet induces a slow to fast fiber type switch

An increase in body weight leads to slow-fast transition and has already been shown in several studies in mice and humans.[85] Although our proteomics analysis of intact soleus muscles substantiated an increase in mitochondrial content, the quantification of MYH isoforms did not reveal a significant change in response to the HFD for 16 weeks. To have a closer view on the single fiber types and their MYH isoform expression, we screened 384 fibers isolated fibers from the soleus from four independent animals under regular and HFD diet conditions (**Figure 31A, B**). Similar to earlier studies, we defined pure fibers that express at least 70 % of one MYH isoform per fiber. Of the isolated fibers from control animals, ~30% were pure type I, ~30% pure type IIa fibers and the remaining fibers were mixed type I/IIa fibers. Pure type IIx or mixed type I/IIx were not observed among the 384 selected fibers of the soleus (**Figure S20F**).

The administration of the HFD induces a shift from slow to fast fibers. We observed a reduction of type I fibers to ~19% whereas type IIa fibers increases to ~31%.

In addition, we observed an increased variability of the fiber type proportion between the 4 animals treated with HFD. The percentage of pure type I varied between 6%-33% and for pure type IIa between 10-43% (**Figure S21**).

This could be explained by biological variability of the mice and their adaptation to the HFD. Food intake and weight gain were comparable in all animals. Hence, a more detailed analysis of these variable effects on the HFD would be an interesting aspect for future experiments.

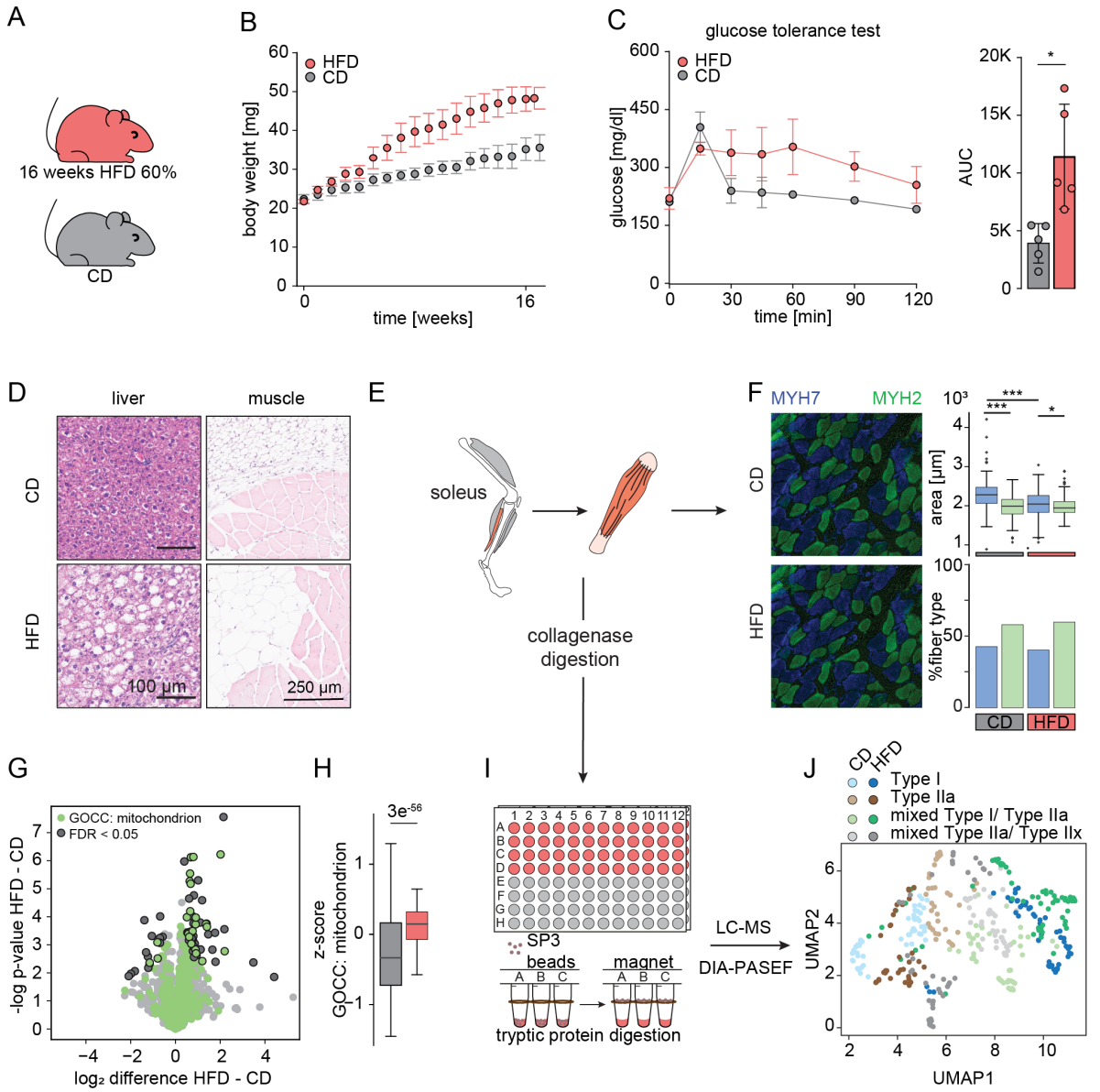

Figure 30 Animals fed for 16-weeks with a high-fat diet show a physiological change. A, B) Mice fed for 16-weeks with a high-fat diet show **B**) an increase in body weight over the weeks. **C**) HFD animals show an impaired response to the glucose tolerance test. **D**) H&E staining of liver, skeletal muscle, and white adipose tissue show an inflammatory response and an increase of fat accumulation in the liver and WAT. **E**) Schematic overview of the extraction of mouse soleus muscles to use the intact muscle for staining and bulk proteomics and collagenase digestion to isolate single muscle fibers. **F**) Staining for MYH7 (blue) and MYH2 (green) in HFD and CD mice visualize the workflow for the CSA and fiber type identification based on IHC. **G, H**) Proteomic analysis of the intact HFD and CD muscles show in **G**) a volcano plot the Welch's *t*-test differences between the HFD and CD. FDR significant (<0.05) are marked in grey. Mitochondrial associated proteins are marked in green. **H**) Student's *t*-test analysis on mitochondrial proteins shows a significant increase of mitochondrial content in HFD animals. **I**) Schematic workflow for fiber isolation of the mouse soleus muscle, followed by SP3-based preparation for LC-MS analysis. **J**) UMAP reduction identifies the grouping for followed bioinformatical analysis. AUC, area under the curve; CD, control diet; DIA-PASEF, DIA-PASEF, data independent acquisition-parallel accumulation serial fragmentation; GOCC, gene ontology term of cell components; HFD, high-fat diet; LC-MS, liquid-chromatography-mass spectrometry; MYH, myosin heavy chain; SP3, single-pot, solid-phase-enhanced sample preparation; UMAP, uniform manifold approximation and projection.

Since we found a transition from slow to fast fibers in the HFD animals based on MYH expression, the loss of type I fibers compared to control animals is a concern for statistical analysis. To provide a more accurate and unbiased classification of fiber types, we expanded the fiber type classification from only MYH to further 50 proteins that have been described as fiber type-specific proteins or that we found to be fiber type-specific in our current and previous datasets.[110, 120] For example, we selected slow and fast isoforms of troponins (TNN), tropomyosins (TPM), myosin light chains (MYL) and SERCAs (ATPase sarcoplasmic/endoplasmic reticulum Ca^{2+} transporting 2) as marker for type I or type II fibers (**Table S12**).

Next, we selected published 52 fiber-type specific proteins from earlier reports[110, 120] and performed a ClusTree approach on the CD and HFD data set.[227] First, a hard-clustering algorithm, here k-means with k = 10, was performed on the data. Each cluster is visualized as a node and the assigned number of samples to both clusters (overlap) is graphically shown as edges. Less informative edges were removed based on the ratio between the number of samples on the edge and the number of samples in the cluster it leads to. Nodes and edges are then presented in the Reingold-Tilford tree layout.[228] Four clusters were identified for both CD and HFD diet based on the stability and clearness of formed branches, and the arise of low in-proportion edges (**Figure 31C, Figure S22A**). The identified groups were filtered for more than 70% data completeness in at least one group. Log2-normalized data was imputed using a random forest approach, with an off-set of 1.6 and width of 0.5 if the 70% data-completeness was not reached.[229, 230] Validation of the clusters and specification for the fiber type was visualized using an hCluster of the normalized, log2-transformed, imputed data of the pre-selected 52 proteins (**Figure S22C**). For both CD and HFD, 4 clusters (type I, type IIa, mixed type I/IIa, mixed type IIa/IIx) were observed and show specific patterns for myosin heavy chains (MYH1, MYH2, and MYH7) and several sarcomere proteins (SERCA, tropomyosins, and troponins) (**Figure S22B**). Type I fibers show a higher expression of MYH7, TPM3, SERCA2, troponin I-1, troponin C-1, troponin T-1 compared to fast type II fiber. Conversely, type IIa fibers express more MYH2, the z-disk protein myozenin 3 (MYOZ-3) and the proline rich 33 protein (PRR33) compared to slow type I fibers. By expanding the marker proteins for the characterization of fiber types, additional properties such as metabolic and contractile activities were considered for fiber typing. This helped to generate equally sized groups for statistical analysis; in particular for the classification of mixed fibers (**Figure 31F, Figure S20H**).

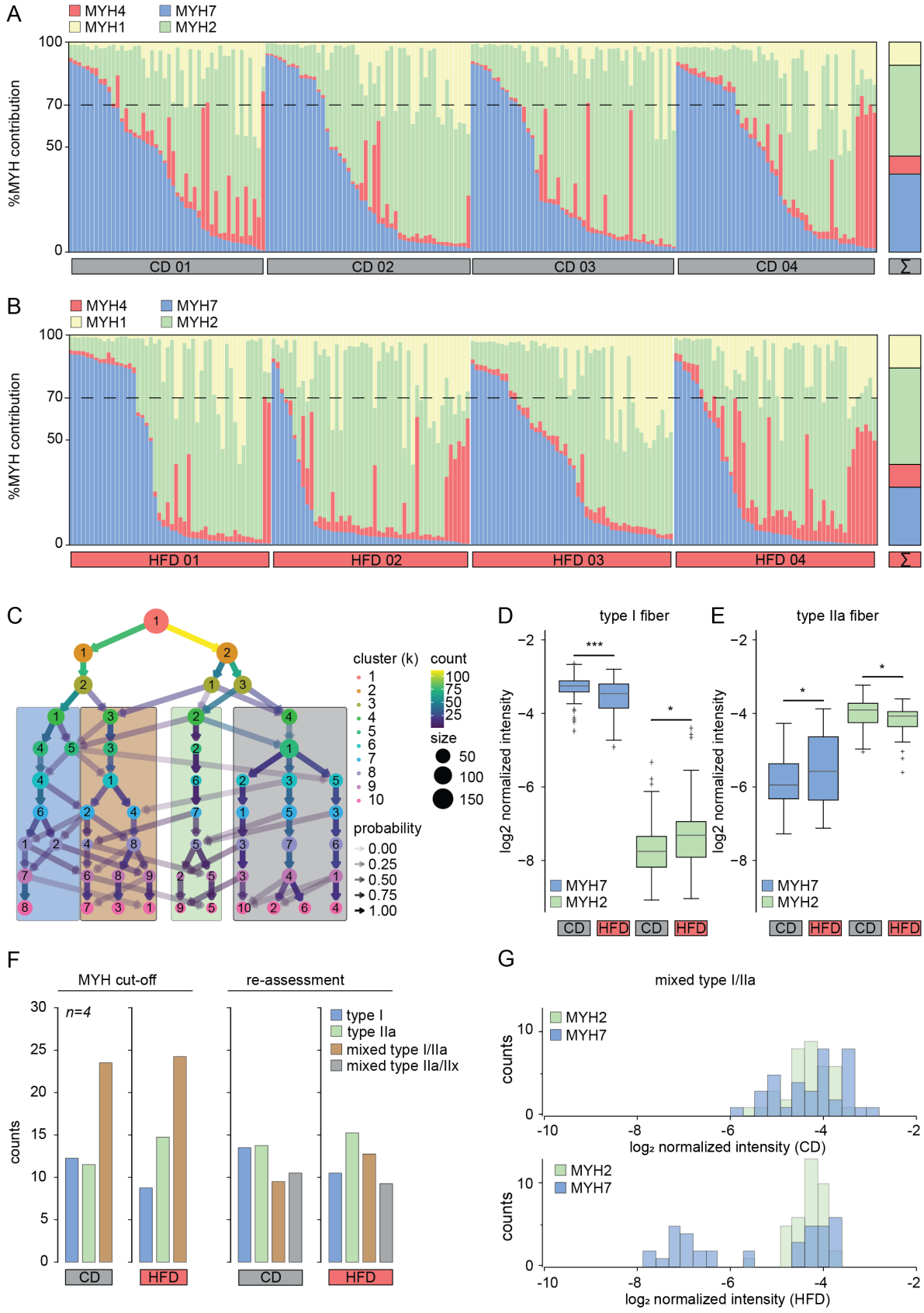

Figure 31 Fiber re-assessment using a hard clustering method identifies four fiber types. A, B) MYH isoform distribution analysis of isolated single muscle fibers from the four different animals in **A**) CD and **B**) HFD. Each bar represents the relative abundance of MYH isoforms in one fiber in relation to the total sum of

intensities for MYH1 (blue), MYH2 (red), MYH4 (purple), and MYH7 (green). Fibers from different mice are sorted and ranked from left to right of highest MYH7 abundance. On the right side the average of all fibers of all animals is represented. **C**) ClusTree of the k-means clustering using 52 proteins as input for CD. 10 clusters are presented, probability is visualized in transparency of arrows, counts of samples are represented in yellow, green, blue, and purple, size of the clusters is represented in the size of the nodes. The final grouping of fibers is visualized in boxes (type I, blue; type IIa, green; mixed type I/IIa, brown; mixed type IIa/IIx, grey). **D, E**) Box plot of the log2 normalized intensities ±SEM of MYH2 and MYH7 in **D**) type I and **E**) type IIa fibers of CD and HFD animals. Welch's *t*-test was performed to identify significant intensity changes. Asterisks indicate significance (*<0.05, **<0.01, ***<0.001). **F**) Average number of characterized fiber types in CD and HFD using the MYH cut-off and after re-assessment (type I, blue; type IIa, green; mixed type I/IIa, brown; mixed type IIa/IIx, grey). **G**) Histogramm of MYH2 and MYH7 log2 normalized intensities in CD and HFD animals. CD, control diet; HFD, high-fat diet; MYH, myosin heavy chain.

For example, mixed type I/IIa show an increased expression of MYH7 and MYH2 in response to the HFD compared to lean controls. Similarly, mixed IIa/IIx expressed more MYH2 and MYH1 upon HFD treatment (**Figure S22C**). The comparison of the MYH7 and MYH2 expression in mixed fibers revealed a reduced expression of MYH7 in response to the HFD compared to control conditions (**Figure 31G**). Overall, the ClusTree approach, using 52 marker proteins related to slow/fast contraction and metabolic activity, adjusted the classification of fiber types and improved the statistical analysis.

2.4.4.3. Individual fiber types show different metabolic adaption after HFD

The analysis of intact liver and muscle sections revealed an increased lipid content, and we also demonstrated a reduced glucose uptake in intact skeletal muscle HFD treated animals (**Figure 30**). The mass spectrometric analysis cements altered metabolic activities of all fiber types by increased expression of proteins related to fatty acid oxidation, including hypoketotic hypoglycemia factors acyl-CoA dehydrogenase very long chain (ACADVL), carnitine palmitoyl transferase 2 (CPT2) and solute carrier family 25 member 20 (SLC25A20) in HFD conditions compared to controls (**Figure 32A**). We also observed proteins associated with vesicle transport like actinin-4 (ACTN4) and EH domain-containing protein 4 (EHD4) to be equally regulated in type I and type IIa fibers (**Figure 32I**).

To further identify fiber-type specific metabolic changes, we performed a Welch's *t*-test on pure type I and IIa fiber comparing HFD with CD conditions (**Figure 32B, C**). Here, we observed for type IIa fibers 136 up and 88 down regulated proteins, compared to type I fibers which showed only 19 up and 20 down regulated proteins (**Figure S23A, B**). Notably, upregulated proteins in type I fibers were all associated to fatty acid metabolism (**Figure S23C**). A GO-term analysis of increased proteins in type IIa fibers revealed terms related to proteasome, fatty acid metabolism, and mitochondria (**Figure S23D, E)**.

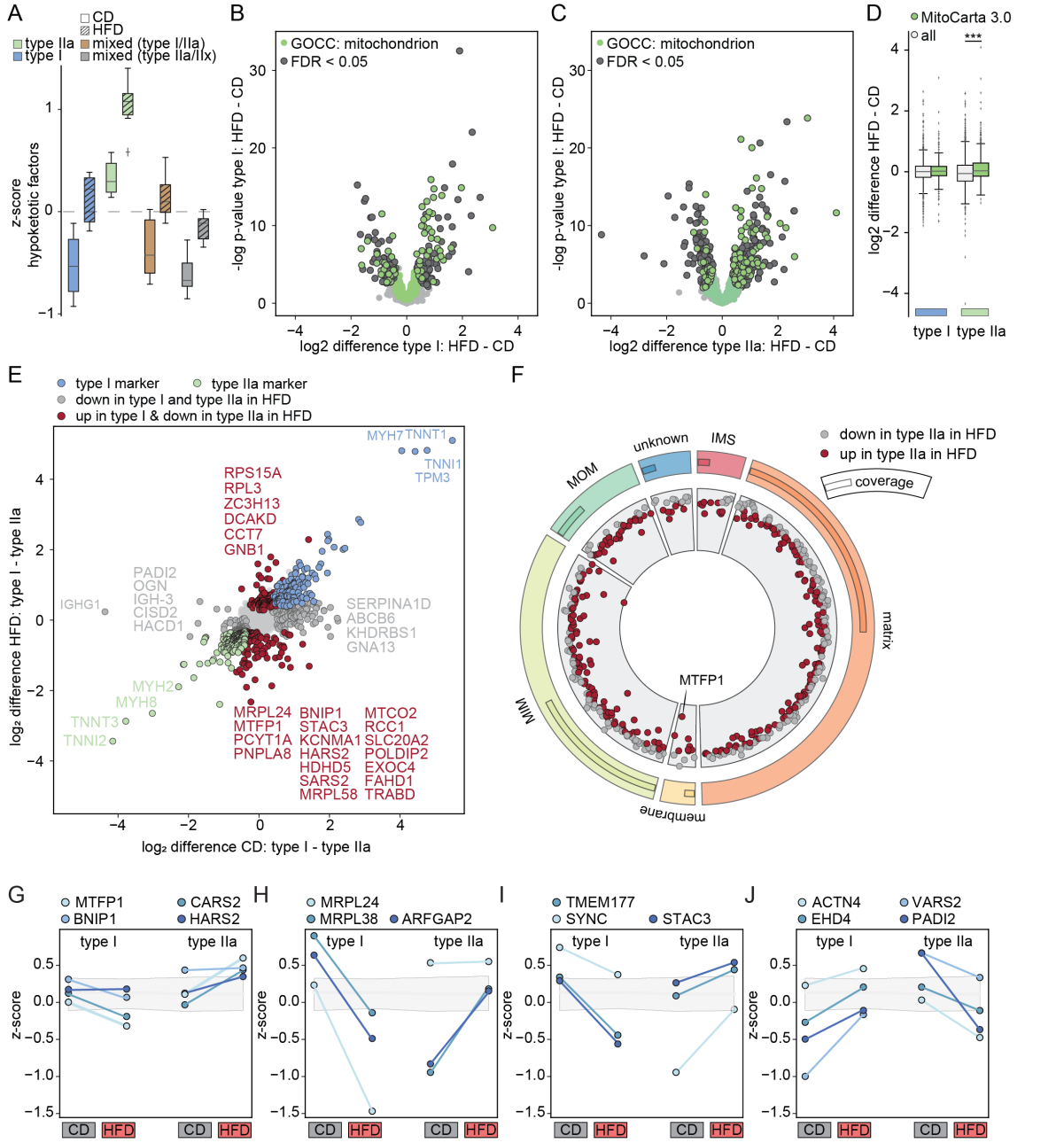

Figure 32 Fiber type specific changes after HFD. A) Boxplot of the z-scored hypoketotic factors ±SEM in for the identified fiber types in HFD and CD. **B, C)** Volcano plots show the Welch's *t*-test differences between HFD and CD in **B**) type I and **C**) type IIa fibers. FDR significant (<0.05) are marked in grey. Mitochondrial associated proteins are marked in green. **D**) Scatter plot of the differences between the fiber types in CD (*x*-axis) and HFD (*y*-axis). **E**) Solar plot of MitoCarta 3.0[231] proteins showing the differently abundant proteins in type IIa fibers in HFD compared to CD. **F-I**) Example proteins of different effects of the HFD on proteins related to **F**) mitochondria, **G**) ribosome, **H**) fiber integrity, and **I**) vesicle transport. ABCB6, ATP binding cassette subfamily B member 6; ACTN4, actinin-4; ARFGAP2, ADP ribosylation factor GTPase activating protein 2; BNIP1, BCL2 interacting protein 1; CARS, cysteinyl-tRNA synthetase 1; CCT7, chaperonin containing TCP1 subunit 7 ; CD, control diet; CISD2, CDGSH iron sulfur domain 2; DCAKD, dephospho-CoA kinase domain containing; EHD4, EH domain containing 4; EXOC4, exocyst complex component 4; FAHD1, fumarylacetoacetate hydrolase domain containing 1; GN, G Protein; HACD5, ; HARS2, histidyl-tRNA synthetase 2; HDHD5, haloacid dehalogenase like hydrolase domain containing 5; IGH, immunoglobulin heavy constant gamma; IMS, mitochondrial intermembrane space; KCNMA1, potassium calcium-activated channel subfamily M alpha 1; MIM, mitochondrial inner membrane; MOM, mitochondrial outer membrane; MYH,

myosin heavy chain, ; MRP, mitochondrial ribosomal protein; MTCO2, mitochondrially encoded cytochrome C oxidase II; MTFP1, mitochondrial fission protein 1; OGN, Osteoglycin; PADI2, peptidyl arginine deiminase 2; PCYT1A, phosphate cytidylyltransferase 1A; PNPLA8, patatin like phospholipase domain containing 8; POLDIP2, DNA polymerase delta interacting protein 2; RCC1, regulator of chromosome condensation 1; RP, ribosomal protein; SARS2, seryl-tRNA synthetase 2; SLC20A2, solute carrier family 20 member 2; STAC3, SH3 and cysteine rich domain 3; SYNC, Syncoilin; TNNI, Troponin; TPM, Tropomodulin; TRABD, TraB domain containing; VARS2, valyl-tRNA synthetase 2; ZC3H13, zinc finger CCCH-type containing 13.

Of the 30 identified proteasomal subunits we detected for 18 subunits (seven non-ATPase subunits, three ATPase subunits and eight units of the core) significant downregulated only in type IIa fibers (**Figure S23F**). This might indicate a reduced protein degradation, as shown in obesity-induced insulin resistance in the liver.[232]

Next, volcano plots were generated to visualize protein changes between CD and HFD conditions of type I and type IIa fibers (**Figure 32B-D**). To compare directly the influence of the diet and fiber type, we plotted the log2 type I/type II ratios for high fat and control diets (**Figure 32E**). Here, we detected 190 proteins that were significantly regulated in type-I fibers in response HFD and 423 proteins with a restricted regulation in type-IIa fibers (FDR < 0.05) (**Figure 32E**). For example, the mitochondrial fission protein MTFP1 were increased in type IIa fibers compared to type I fibers in response to the HFD administration. Similar to MTFP1, the phosphate cytidylyltransferase 1A (PCYT1A, also known as CCTα), shows an increased expression in type IIa fibers compared to type I fibers in response to the HFD. PCYT1A catalyzes the rate-limiting reaction in phosphatidylcholine (PC) synthesis, the most abundant phospholipid in mammalian membranes. An increased lipid concentration might further affect the metabolism and energy production.[233, 234] Other proteins with a restricted alteration in type IIa fibers were the histidyl-tRNA synthetase (HARS2) and the mitochondrially encoded cytochrome C oxidase II (MTCO2). To visualize mitochondrial changes, we generated a solar protein expression plot of mitochondrial proteins highlighting the enhanced abundance of mitochondrial proteins (30%) in type IIa fibers in response to HFD (**Figure 32F, G**).[231] Important to note type I fibers show only changes in 15% of mitochondrial proteins upon HFD treatment (**Figure S23G**). Other proteins with an increased expression in type IIa fibers are associated to protein synthesis and muscle fiber contraction and function (**Figure 32H, I**).

2.4.4.4. Increased abundance of MTFP1 alters localization of mitochondria

To visualize the changes in the mitochondria more precisely, a mitochondrial network based on MitoCarta 3.0 was created and fiber type-specific differences between HFD and CD were mapped on the network (**Figure S24**). Proteins changes resulting of fiber type differences are minimized (**Figure S24**). Most affected activities and compartments are the fatty acid oxidation, mitochondrial ribosome, and OXPHOS subunits (**Figure S23C-F**). Interestingly, the pathway mitochondrial 'trafficking' and communication contains proteins such as the mitochondrial fission protein 1 (MTFP1), fission protein 1 (FIS1), mitofusin 2 (MFN2), and dynamin 2 (DNM2) (**Figure S24**).[235]

To further investigate the changes in MTFP1 abundance, we performed immunohistochemical staining (IHC) against MTFP1 in combination with MYH2 and MYH7 under HFD and CD conditions. Here we confirmed a higher intensity of MTFP1 in type IIa compared to type I fibers following HFD (**Figure 33A**). To further elucidate mitochondrial changes, we performed immunostainings against the translocase of outer mitochondrial membrane 20 (TOM20). Fiber types were identified by co-staining's with MYH2 and MYH7 (**Figure 33B**). Here we found a slight increase of mitochondria by TOM20 staining in type IIa fibers compared to type I under HFD (**Figure 30G, H** and **Figure 32B-D**). This is in line with the observed increase in mitochondrial proteins in response to HFD. Next, we used cell pose[236] cell profiler tool[237] to define the shape and types of fibers based on MYH2 and MYH7 staining. Each fiber were fractionated into bins to distinguish between centrally localized mitochondria (also known as interfibrillar mitochondria, IFM) and peripheral mitochondria (also known as subsarcolemmal mitochondria, SSM) (**Figure 33C** and **Table S13**).[238] The central mitochondrial bins (1-3) were merged and TOM20 staining intensities revealed no change between HFD and CD in type I and a minor change in type IIa fibers (**Figure 33D, F**). In contrast, peripheral bins (8-9) showed a significant increase of TOM20 staining in type IIa fibers upon HFD treatment (**Figure 33E, F**).

Overall, we used a complementary IHC approach to substantiate an increased abundance of MTFP1 in peripheral areas of type IIa muscle fibers.

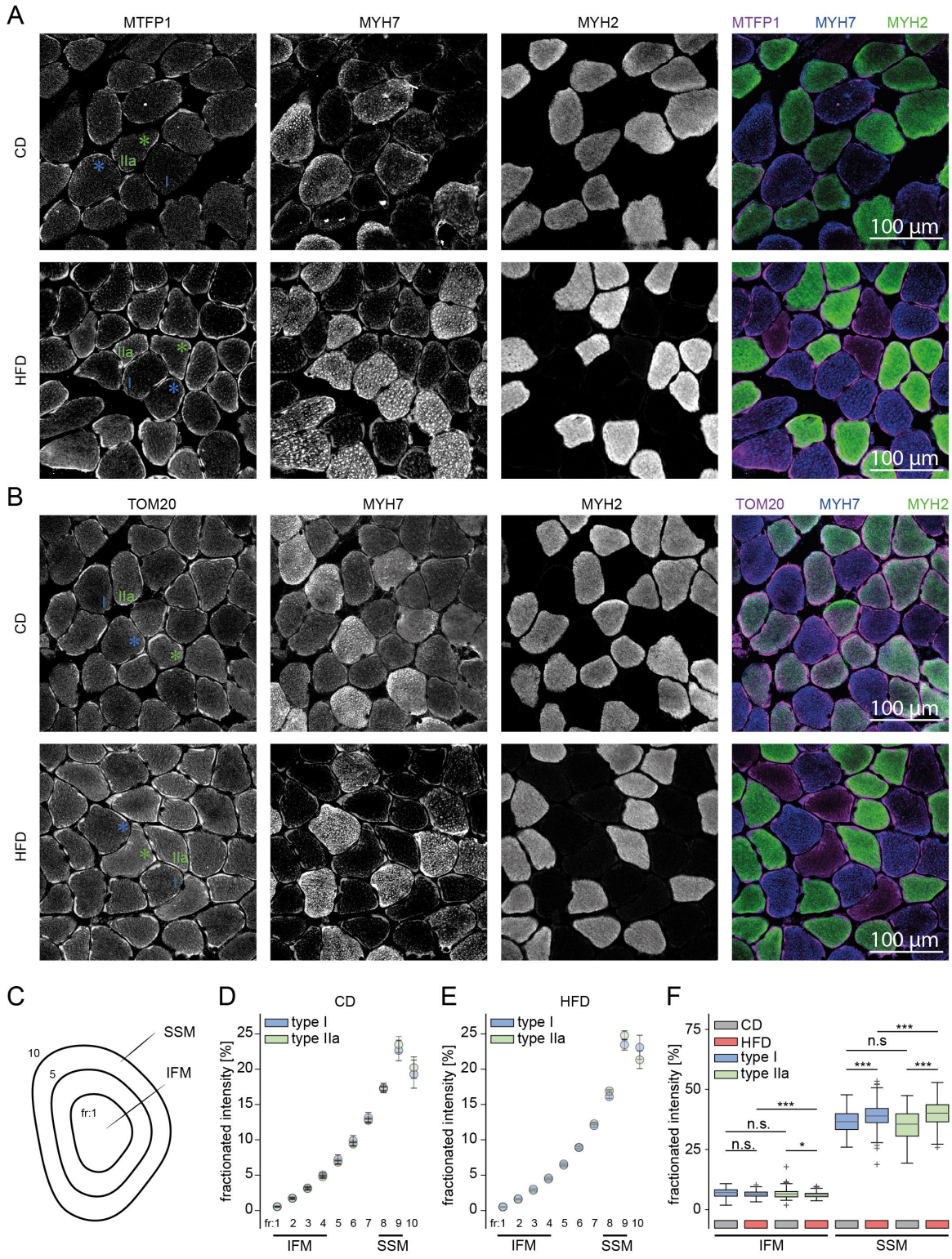

Figure 33 Altered mitochondrial localization in HFD type IIa fibers. A, B) Immunostaining of MYH2, MYH7, **A**) MTFP1, and **B**) TOM20 in mouse soleus cross sections. Type I fibers are stained with MYH7, type IIa fibers are stained with MYH2. Both MTFP1 and TOM20 are localized in the mitochondria and show an increased intensity in type IIa fibers in HFD animals. Blue and green asterixis indicating type I and type IIa fibers, respectively. **C-E**) IHC intensity is fractioned into bins to determine SSM and IFM. Two biological replicates were performed for each staining. Scale bar=100 µm. CD, control diet; fr, fraction; HFD, high fat

diet; IFM, interfibrillar mitochondria; MTFP1, mitochondrial fission protein 1; MYH, myosin heavy chain; SSM, subsarcolemmal mitochondria; TOM20, translocase of outer mitochondrial membrane 20.

2.4.5. Discussion

Feeding mice HFD for 16 weeks resulted in significant changes of several metabolic pathways related to lipid processing, fatty acid metabolism, and mitochondrial function. Detailed analysis of individual muscle fibers confirmed a reduced number of slow type I type fibers (MYH7 positive) during high fat diet administration. Although we observed a reduction of type I fibers, type IIa fibers seem to be more sensitive to the HFD, as demonstrated by their more pronounced response in metabolic pathways compared to type I fibers. Furthermore, we identified several candidate proteins, such as MTFP1, which showed differential regulation in type I and type IIa fibers. Immunostaining confirmed an increase in MTFP1 expression in peripheral areas of type IIa fibers in response to HFD. Using TOM20 as a mitochondrial marker, we observed fiber type specific changes in mitochondrial distribution in type IIa fibers, which was not detectable in type I fibers. Our findings suggest that the metabolic adaptations in type IIa fibers include alterations in long-chain fatty acid metabolism, cellular lipid metabolism, and fatty acid beta-oxidation. These adaptations might explain the heightened sensitivity of type IIa fibers to HFD-induced metabolic stress. However, it remains unclear why type I fibers, which show a lower rate of protein changes, were significantly reduced. We speculate that type I fibers may have a reduced ability to adapt to altered metabolic conditions. Notably, mixed type I/IIa fibers exhibited a more robust metabolic response compared to pure type I or type IIa fibers, which may offer a protective mechanism against the deleterious impacts of a high-fat diet. Overall, these results highlight the complex interplay between diet, muscle fiber type, and metabolic regulation, emphasizing the differential impact of a high-fat diet on type I and type IIa muscle fibers.

2.4.5.1. Loss of fiber type specificity in obese mice

Common causes of sarcopenia include aging, prolonged bed rest, and obesity, but these conditions do not exhibit identical patterns of fiber type transitions. In aging and bed rest, previous data have shown a shift towards slow-twitch muscle fibers, whereas in obesity induces a reduced number of type I fibers followed by an increased number of mixed fiber types (**Figure 31F**).[92, 239]

In aging, the fast to slow transition of muscle fibers can be attributed to a combination of reduced physical activity and enhanced neurodegeneration.[196] In particular, motor neuron degeneration gradually remodels muscle fiber composition, leading to a higher proportion of slow fibers over time.[240]

The changes in muscle fiber composition associated with obesity are not yet fully understood, and previous studies have produced contradictory results.[241] Earlier studies showed that even short-term high-fat diets reduce the synthesis of the MYH7 isoform compared to the MYH2 expression, leading to a decrease in the oxidative capacity of skeletal muscles. This reduction in oxidative potential may contribute to weight gain and obesity-related metabolic changes.[94, 242] Additionally, it has been suggested that the soleus muscle may experience changes in fiber composition due to diet-related impacts on the nervous system. Neuromuscular hyperactivity has been shown to shift fiber composition towards slower-twitch fibers.[243] However, high-fat diets can impair sensory and motor nerve function by causing damage to both myelinated and small sensory nerve fibers[244], leading to reduced neural activity in muscles like the soleus.[245] However, so far, it remains unclear whether the reduction of type I fibers after HFD administration is caused by altered neuronal innervation or activity. Moreover, hyperinsulinemia, commonly seen in obesity, has been shown to increase fast MYH1 gene expression (**Figure 31A, B**).

The shift in muscle fiber composition in obese individuals can be attributed to the excess of caloric intake and lipid accumulation. An excess of caloric intake leads to a higher availability of nutrients, citrate, acetyl-CoA and ATP. This surplus can induce metabolic changes that are less favorable for type I fibers, which are adapted to endurance and efficient energy usage.[86, 246] Moreover, an overload of FAs in the muscle tissue can lead to lipid accumulation and might negatively impact the oxidative capacity of type I fibers, promoting a shift towards type II fibers that are less reliant on oxidative metabolism.[247] In addition, increased levels and transport of citrate and acetyl-CoA from mitochondria to the nucleus has been shown increase the transfer the acetyl group to histone residues by histone acetyltransferases (HATs). An enhanced histone modification might regulate the gene activity of specific contractile proteins, including the myosin heavy chains. Hence, a high concentration of metabolites including citrate and acetyl-CoA in muscle fibers may influence the synthesis of fatty acids and alter the expression of contractile proteins via histone acetylation.

Whether specific metabolites or other small molecules directly regulate the expression of the slow MYH isoform would need to be determined by chromatin immunoprecipitation sequencing (ChIP-seq) or DNase I hypersensitivity analysis (ATAC-seq).

In addition, the decrease in type I fibers correlates with an increase in hybrid fibers, a phenomenon that has already been shown by previous studies.[241]. However, in addition to the increased number of mixed fibers, we also observed a lower MYH7 intensity in these fibers, which reflects again the down regulation of the MYH7 expression (**Figure 30G**).

We also propose that type IIa fibers also lose their specificity, as evidenced by a slight decline of the MYH2 expression in pure type IIa fibers (**Figure 30E**). This decline might influence the ATP consumption and might change muscle activity, which generally leads to a decrease in type IIa fibers.[242] Notably, this reduction is more pronounced in proteins associated with long-chain fatty acid metabolism, fatty acid metabolism, cellular lipid metabolism, and fatty acid beta-oxidation in type IIa than in type I fibers following HFD.

2.4.5.2. MTFP1 changes the mitochondrial distribution in type IIa fibers

Our study supports earlier findings showing that increased food intake and obesity induces mitochondrial biogenesis (**Figure 30G**). Under high-fat diet conditions, fatty acids become the dominant fuel source, and mitochondria are responsible for fatty acid oxidation (β-oxidation) which generates ATP and other metabolites. To handle the increased load of fatty acids needing to be oxidized, cells, particularly in tissues like muscle increase mitochondrial biogenesis. This is mainly due to the expression of the proliferator-activated receptor gamma coactivator 1-alpha (PGC-1α), transcription factor which activates the upregulation of genes related to mitochondrial biogenesis. Another important pathway related to protein synthesis and mitochondrial biogenesis is the AMP-activated protein kinase (AMPK) which is also activated under high-fat conditions, contributing to increased expression of PGC-1α. Here, we found only in type IIa an increased abundance of the AMPK subunit PRKAG1 after HFD. The increase in mitochondria upon a high-fat diet reflects the metabolic adaptation and allows the fibers to efficiently switch between carbohydrate and fat metabolism. This remodeling protects against lipotoxicity, a condition where excessive fatty acid accumulation leads to cellular damage. Since type IIa fibers have more mitochondria, it might be reasonable to assume that type IIa are more protected against lipotoxicity compared to type I fiber. However, it remains unclear why type IIa fibers show more protein changes in response to HFD than type I fibers.

Another important feature of mitochondria is the fusion and fission process, that regulate the shape, size, and metabolic activity. These processes are essential for maintaining mitochondrial health and ensuring proper cellular function. Fusion is the process by which two or more mitochondria merge to form a single, larger mitochondrion. Here, damaged components might be diluted by mixing them with healthy mitochondria, thus enhancing mitochondrial function. In contrast, mitochondrial fission is the process by which mitochondria divides into two or more smaller mitochondria. This is crucial for mitochondrial distribution, quality control, and adaptation to cellular needs. The balance between fusion and fission is therefore crucial for the maintenance of mitochondrial function, and a disruption could lead to disease.

MTFP1 is localized in the inner mitochondrial membrane (IMM), and it is thought to play a crucial role in regulating mitochondrial fission. Although the function of MTFP1 is not completely clear, it is believed that MTFP1 is involved in controlling the balance between mitochondrial fission and fusion. Previous studies showed that MTFP1 interacts with the mitochondrial fission process dynamin-related protein 1 (DRP1) and the protein regulation of mitochondrial fission (FIS1). In addition, MTFP1 might be also involved in apoptosis, where mitochondrial fission is often increased. A recent study demonstrated that MTFP1 negatively regulates inner mitochondrial membrane (IMM) fusion. Moreover, MTFP1 inhibits mitochondrial fusion to isolate and exclude damaged IMM subdomains from the remaining mitochondrial network.[235]

Immunostaining of muscle cross-sections from HFD and CD muscle cross sections for MTFP1, MYH2, any MYH7 confirmed a restricted increase in protein expression of MTFP1 in type IIa fibers in response to HFD compared to type I fibers (**Figure 33A**). In addition, TOM20 staining revealed an increased level of mitochondria in peripheral areas of type IIa fibers. Although a GO-term analysis showed no alterations for terms like fusion and fission in response to HFD compared to the administration of the control diet, we observed for several proteins like FIS1, MFN2, and BNIP1 an increased level in type IIa fibers upon HFD compared to the CD. However, other modulators of mitochondrial network including DRP1 and optic atrophy 1 (OPA1) were not changed in type IIa fibers after HFD (**Table S12**).

A recent study ablated MTFP1 specifically in cardiomyocytes and observed a reduced OXPHOS activity.[102] Since our data show increased MTFP1 expression, we hypothesize that the observed increase in OXPHOS-related proteins (Ndufs5, Ndufaf1, Ndufb9, Ndufv1,

Ndufb7, Ndufa8, Ndufb10) in type IIa fibers after HFD is caused or closely associated by MTFP1 protein abundance in the IMM.

Another regulator of mitochondrial biogenesis is sirtuin 5 (SIRT5), a member of the sirtuin family of NAD+-dependent deacetylases.[248, 249] Similar to PGC1α, the SIRT5 protein regulates mitochondrial biogenesis and activity. For example, SIRT5 induces the expression of enzymes involved in fatty acid oxidation and tricarboxylic acid (TCA) cycle, which are involved in ATP production. Related to cellular stress, SIRT5 regulates the production of ROS within mitochondria by modifying the activity of superoxide dismutase (SOD1). By controlling ROS levels, SIRT5 prevents oxidative stress, which can damage mitochondria. Whether SIRT5 directly regulates the activity of MTFP1 by desuccinylation, demalonylation, or deacetylation should be addressed in future experiments with a focus on these posttranslational modifications. In addition, it should be clarified whether MTFP1 inhibits mitochondrial fusion in obese, prediabetic mice and humans and thereby controls the mitochondrial network in skeletal muscle fibers. Alternatively, MTFP1 could also have a direct effect on OXPHOS activity and thus regulate mitochondrial density. Therefore, interaction studies for MTFP1 under different metabolic conditions would certainly be useful to characterize the function of this protein in more detail.

Another molecular pathway to regulate mitochondrial activity is their selective degradation by autophagy, also known as mitophagy. This process is vital for maintaining cellular health by removing dysfunctional mitochondria, preventing oxidative stress, and supporting metabolic efficiency.[250] Damaged mitochondria lose their membrane potential, which is a signal for the recruitment of specific proteins that mark the mitochondria for degradation. For example, the PINK1 (PTEN-induced kinase 1) and Parkin pathway is one of the most well-studied mechanisms involved in mitophagy.[251] PINK1 recruits and activates the E3 ubiquitin ligase Parkin, which ubiquitinates various outer mitochondrial membrane proteins. This ubiquitination serves as a signal for the recruitment of autophagy receptors such as p62 (also known as sequestosome-1), which binds to the autophagosome-specific Atg8-family protein (LC3, microtubule-associated protein light chain 3), a protein associated with the autophagosome membrane.[206]

Here, we observed an increased abundance of BNIP1 in type IIa skeletal muscle fibers in response to the HFD. BNIP1 is a mitochondrial outer membrane protein that can influence mitochondrial dynamics by interacting with other BCL2 family members and LC3.

Moreover, BNIP1 is involved in mitochondrial fission and fusion processes and undergoes polyubiquitination by the E3 ubiquitin ligase RNF185. Accordingly, the ubiquitination recruits p62, which links ubiquitin to LC3 thus modulating mitochondrial homeostasis.[252] Although the function of BNIP1 is not entirely clear, compared to BNIP3 or NIX, it may still contribute to mitochondrial quality control and function as a sensor for cellular stress upon increased levels of fatty acids.[235, 253]

Overall, our study shows that it is essential to achieve cellular resolution to understand the function of intact tissues and how they adapt under pathobiological situations. This is essential for metabolically active tissues such as skeletal muscle, which consists of differentially active muscle fibers. We are convinced that our method of measuring individual fibers with short LC-MS gradients can provide a comprehensive insight into disease-related protein changes.

2.4.6. Resource availability

2.4.6.1. Lead contact

Further information and requests for resources should be directed to and will be fulfilled by the lead contact, Marcus Krüger (marcus.krueger@uni-koeln.de).

2.4.6.2. Materials availability

- This study did not generate new unique reagents.

2.4.6.3. Data and code availability

- Proteomic data have been deposited at ProteomeXchange and are publicly available as of the date of publication (Accession number). Original IHC images have been deposited on Zenodo and are publicly available as of the date of publication (10.5281/zenodo.12737398).
- All original code has been deposited at Zenodo and is publicly available as of the date of publication (10.5281/zenodo.12737398 and 10.5281/zenodo.12731434).
- Any additional information required to reanalyze the data reported in this paper is available from the lead contact upon request

2.4.7. Experimental model and subject participant details

Experimental model

In all experiments, C57BL/6 6-7-week-old male mice were fed with a Control Diet (CD) DIO LS- 13% fat, 11% sucrose (Ssniff, E15748-04) or high-fat diet (HFD) DIO- 60 kJ% fat (Lard) (Ssniff, E15742-347) for 16 weeks. 3 to 5 mice were placed per cage and weight body gain was measured weekly. Normal-fed blood glucose was taken every 3 weeks with Aida Glucometer and strips (Aida 781783). At the end of the feeding protocol, mice were euthanized using Ketamine/Xylazine Cocktail (87.5 mg/kg Ketamine and 12.5 mg/kg Xylazine) with a dose of 5 µl/gr. Followed by heart puncture and cervical dislocation. All animal experiments were approved by the Federal Ministry for Nature, Environment and Consumers Protection (LANUV) of the state of North Rhine-Westphalia, Germany and were performed by the respective national, federal and institutional regulations.

2.4.8. Method details

2.4.8.1. *In vivo* metabolic studies

Glucose tolerance tests were performed on 6 h fasted animals, using glucose 2 g/kg body weight supplied by oral gavage. Insulin tolerance tests were performed on animals fasted for 6 h, using insulin lispro (Lilly) injected intraperitoneally. The dose was 0.75 U per kg body weight for HFD-fed mice and 0.5 U/Kilo for mice fed with the control diet. Blood glucose measurements were taken at 0, 15, 30, 45, 60 and 120 min after the injection and measured with Aida Glucometer and strips (Aida 781783). Data were analyzed using GraphPad Prism software (version 8.4.1) (San Diego, CA). Area under the curve (AUC) and Area over the curve (AOC) were calculated according to previous described instructions.[254] Statistical tests were used as described in Figure legends. All data are presented as mean ± SEM and were analyzed unpaired individual parametric Student's *t*-test was performed assuming same SEM between populations.

2.4.8.2. Intact tissue sample processing, protein digestion, and desalting

Isolated soleus skeletal muscles dissected (n=4) and snap-frozen in liquid nitrogen, lyophilized and ground using a mortar and pestle. Tissue was resuspended in 4% SDS in PBS, homogenized by heating for 10 min at 95 °C, and sonicated with a Bioraptor sonicator; sonication settings were 21 °C water with 10 cycles of 30 on and 30 off. Lysates were cleared by centrifugation for 10 min at 16,000 *g* and protein concentrations were determined using the Pierce Protein Assay (Thermo Scientific), then 4 µg protein extract was reduced and alkylated for 10 min at 70 °C using 5 mM TCEP and 15 mM CAA. Protein digestion was performed following the SP3 protocol.[123] In brief, 4 µg of both hydrophylic and hydrophobic beads were added to the sample and bound by adding 1:1 volume of acetonitrile (ACN). After 8-minutes incubation time, magnetic beads were immobilized and washed 2x with 70% ethanol and acetonitrile. Proteins were digested with trypsin (substrate:enzyme ratio 100:1) overnight at room temperature. Samples were acidified to 0.1% formic acid (FA) and cleaned-up using house-made SDB-RPS tips.

2.4.8.3. Single muscle fiber isolation and digestion

Freshly dissected soleus muscles were placed in 0.2% Collagenase-P Dulbeccos Modified Eagle Medium (DMEM) and incubated for 20-30 min on 37 °C. Digestion was stopped by transferring the muscles in DMEM containing 5 mM EDTA, 10% FBS. Fibers were isolated by flushing the skeletal muscle several times using a glass pipette. Muscle fibers were washed 5x with 1x PBS containing 5 mM EDTA. Each single fiber was placed into a 96-well plate and lysed with 40 µl of 4% SDS in PBS containing 5 mM TCEP and 10 mM CAA. The 96-well-plates were incubated at 95 °C for 10 min followed by Bioraptor sonication at 20 °C with 10 cycles of 30 on and 30 off. Samples were digested, and peptides were purified as already described. Peptides were reconstituted in 0.1%, with iRT peptides.

2.4.8.4. LC-MS method for intact muscles

Desalted peptide separation was performed on a nanoElute HPLC system (Bruker, Germany) equipped with 15 cm PepSep columns (EvoSep, Denmark) at 45 °C with a gradient length of 60 min. Mobile phases were compromised of 0.1% FA as solvent A and 0.1% FA in ACN as solvent B. The HPLC system was coupled to a timsTOF pro 2 using a CaptiveSpray source (both Bruker, Germany). Samples were measured in dia-PASEF mode with ion mobility calibrated using three ions of Agilent ESI-Low Tuning Mix following vendor specifications. The dia-PASEF window was ranging in dimension 1/k0 0.7-1.35, with 24x25 Th windows and in dimension m/z from 350 to 1250.

2.4.8.5. LC-MS method for single muscle fibers

Desalted peptides were loaded on EvoTips Pure. Peptide separation was performed on an EvoSep One system equipped with 4-8 cm PepSep columns (all three EvoSep, Denmark) at 30 °C with a gradient length of 21 min (60 SPD), 11 min (100 SPD), and 5 min (200 SPD). Mobile phases were compromised of 0.1% FA as solvent A and 0.1% FA in ACN as solvent B. The HPLC system was coupled to a timsTOF pro 2 using a CaptiveSpray source (both Bruker). Samples were measured in dia-PASEF mode with ion mobility calibrated using three ions of Agilent ESI-Low Tuning Mix following vendor specifications. The dia-PASEF window was ranging in dimension 1/k0 0.7-1.35, with 24x25 Th windows and in dimension m/z from 350 to 1250.

2.4.8.6. Proteomics data analysis

The mass spectrometry proteomics data have been deposited to the ProteomeXchange Consortium via the PRIDE partner repository with the dataset identifier PXD053958.[161] iRT peptides were controlled by Skyline-Daily (V 22.2.1.391) and visualized using R (V 4.3.0) with ggplot 2 package. Spectra were analyzed with DIA-NN 1.8.1 using library free search against the UniProt mouse database (Sep. 2017) complemented with protein sequences from myosin heavy chain variants and collagens. Mass ranges were set according to the settings of the mass spectrometer; mass deviation of 15 ppm for files acquired by bruker instruments. Data was further processed using R (V 4.3.0), with the tidyverse, diann, data.table, magrittr, FactoMineR, factoextra, ggplot2, and gprofiler libraries. An in-house modified R-script based on the version by V. Demichev was used to calculate MaxLFQ values.[162, 163] Data input was filtered for unique peptides, q-value <0.01, Lib.Q.Value <0.01, PG.Q.Value < 0.01, Global.Q.Value < 0.01, Quantity.Quality > 0.7, Fragment.count >= 4. Statistical analysis was performed with R (V 4.2.2) and Perseus (V.1.6.5.0) and visualized with Instant clue (V 0.10.10.20210315). The protein intensities in each muscle fiber were normalized to the total protein intensity in each muscle fiber. Fiber with less than 500 identified proteins were excluded.

2.4.8.7. Fiber type identification

MYH contribution was calculated per fiber by dividing the specific MYH by the sum of MYH1, MYH2, MYH4, and MYH7. Fibers were pre-characterized into fiber type I (>70% MYH7), fiber type IIa (>70% MYH2) and mixed fiber (<70% MYH1, <70% MYH2, <70% MYH4, <70% MYH7). Unpaired Welch's T-Test was used to identify significant (FDR < 0.001) changes between CD type I, CD type IIa, CD mixed. Identified proteins were compared with published data and resulted in 52 proteins. CD and HFD samples were first reduced to the 52 proteins followed by separately hard clustering algorithm using a k-means clustering with k=10. Each cluster was visualized as a node and the assigned number of samples to both clusters (overlap) is graphically shown as edges. Less informative edges are removed based on the ratio between the number of samples on the edge and the number of samples in the cluster it goes toward. Nodes and edges are then presented in the Reingold-Tilford tree layout.[228] Data completeness of 70% was calculated for each group. Missing values were imputed by random forest algorithm for groups with 70% data completeness, with more than 30% missing values random forest algorithm was downshifted of 0.3, width 1.5. Original

code has been deposited at Zenodo and is publicly available as of the date of publication (10.5281/zenodo.12731434). Further analysis was performed in Perseus (V 1.6.5.0) and InstantClue (V 0.10.10.20211105).

2.4.8.8. Immunostainings and image analysis

Mouse solei were collected, embedded in tragacanth, cut transversely in 7 µm sections, collected on glass slides (VWR) and stored at -20 °C until further use. Slides were removed from the freezer and dried at room temperature. Sections were permeabilized by incubation in -20 °C cold acetone for 8-min. Sections were blocked with 0.1% Triton, 5% Goat Serum, and 2% BSA for 1 h. Primary antibodies against MYH2 (Santa Cruz Biotechnology Cat# sc-53095, RRID:AB_784698), MYH7 (Santa Cruz Biotechnology Cat# sc-53089, RRID:AB_2147281), MTFP1 (Proteintech Cat# 14257-1-AP; RRID: AB_2148123), and TOM20 (Proteintech Cat# 11802-1-AP; RRID: AB_2207530) were diluted 1:100 in 1:10 blocking solution and applied overnight at 4 °C; the following day, secondary antibodies were diluted 1:200 and Hoechst (Invitrogen, #H1399) 1:100 in TBS and applied for 60 min at RT. As secondary antibodies were used anti-mouse IgG1-488 (Enzo Life Sciences Cat# ALX-211-204TD, RRID:AB_10541466), anti-mouse IgM-546 (Innovative Research Cat# A21045, RRID:AB_1500928), anti-rabbit STAR RED (Abberior Cat# STRED-1002-500UG, RRID:AB_2833015). Samples were washed 5-times for 5 min in TBS between all steps in the protocol. Finally, slides were mounted with coverslips using Aqua-Poly mount (Polysciences, Germany). Confocal imaging was performed on a TCS SP8 (Leica Microsystems) inverse confocal laser scanning microscope equipped with a PL Apo 40×/1.40 Oil CS2 objective and a tunable white light laser (470–670 nm). Fluorescence emission was detected using HyD SMD detectors. Images were further processed using ImageJ (version 1.54d; RRID:SCR_003070) and colorblind-friendly pseudo colors were applied to the composite images. Images were further processed with python (V 3.7) using the packages cellpose (V 3.0.10), matplotlib (V 3.7.5), numba (V 0.58.1), numpy (V 1.24.1), pillow (V 10.2.0), and pip (V 24.0) and cell profiler (V 4.0.7) pipeline. A detailed list of all packages can be found on Zenodo (10.5281/zenodo.12737398). Firstly, fiber shapes were identified with cellpose and masks generated for input to cell profiler. Secondly, in cell profiler the generated masks and the channels of MYH7 and MYH2 were used to distinguish between fiber types. Thirdly, the fibers were segmented into bins and TOM20 intensity was calculated and fractionated dependent on the size and bin numbers.

2.4.9. Author contributions

HFD and *in vivo* metabolic studies were performed by Ximena Hildebrandt and Nieves Peltzer. I was supported by Michael Saynisch and Katharina Neuser for muscle fiber isolation and preparation for LC-MSMS analysis. LC-MSMS instrument optimization was performed by me. I performed the bioinformatic analysis together with Philipp Antczak and interpreted the data. Sectioning of the soleus muscle was performed by Bianca Collins and I performed the following IHC staining. Me, Christiana Zollo, and Ana Garcia performed the imaging of the IHCs. Together with Peter Zentis, we analyzed the stainings. I assembled all figures and assisted Marcus Krüger in writing the manuscript.

2.5. Preprint Publication (V): Reduced ATP turnover during hibernation in relaxed skeletal muscle

Luisa Schmidt[2§], Cosimo De Napoli[1,3§], Mauro Montesel[1,3], Laura Cussonneau[1,3], Samuele Sanniti, Lorenzo Marcucci[2], Elena Germinario[3], Jonas Kindberg[4,5], Alina Lynn Evans[6], Guillemette Gauquelin-Koch[7], Marco Narici[3], Fabrice Bertile[8,9], Etienne Lefai[10], Marcus Krüger[2,*], Leonardo Nogara[1,3,11,*], Bert Blaauw[1,3,*]

1 Venetian Institute of Molecular Medicine (VIMM), Via Orus 2, 35129, Padova, Italy

2 Institute for Genetics, Cologne Excellence Cluster on Cellular Stress Responses in Aging-Associated Diseases (CECAD), University of Cologne, 50931 Cologne, Germany

3 Department of Biomedical Sciences, 35137, University of Padova, Padova, Italy

4 Norwegian Institute for Nature Research, Trondheim, Norway.

5 Department of Wildlife, Fish and Environmental Studies, Swedish University of Agricultural Sciences, Umeå, Sweden

6 Department of Forestry and Wildlife Management, Faculty of Applied Ecology and Biotechnology, Inland Norway University of Applied Sciences, Koppang, Norway

7 French Space Agency, Centre National d'Etudes Spatiales (CNES), Paris, France

8 Université de Strasbourg, CNRS, IPHC UMR 7178, 23 rue du Loess, 67037, Strasbourg Cedex 2, France

9 National Proteomics Infrastructure, ProFi, FR2048 Strasbourg, France

10 Université Clermont Auvergne, INRAE, UNH UMR 1019, CRNH Auvergne, 63000 Clermont-Ferrand, France

11 Department of Pharmaceutical Sciences, 35137, University of Padova, Padova, Italy

§ contributed equally

* Correspondence to:

Leonardo Nogara: leonardo.nogara@unipd.it

Bert Blaauw: bert.blaauw@unipd.it

Marcus Krüger: marcus.krueger@uni-koeln.de

This manuscript is in revision in Nature Communications since April, 2024

2.5.1. Summary preprint V

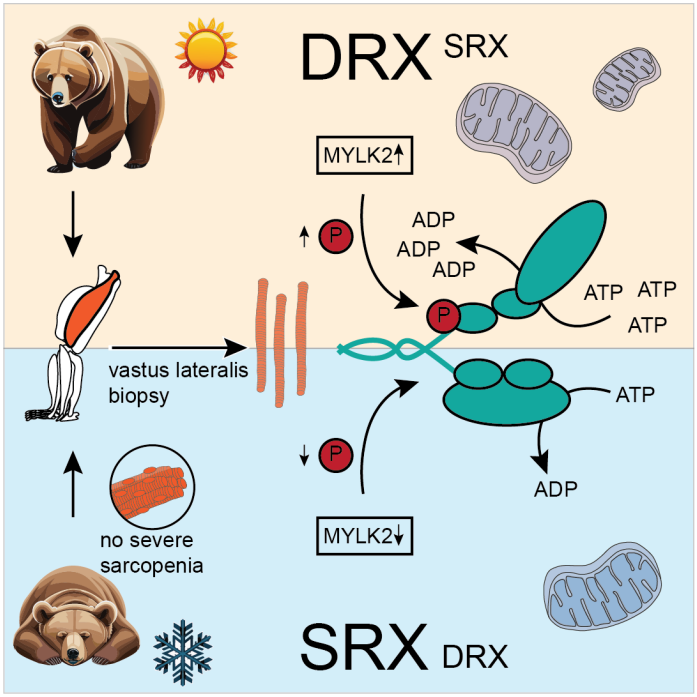

Figure 34 Graphical abstract publication V. Muscle biopsies were taken from active and hibernating bears to isolate single muscle fibers. Active bears showed an increased disordered relaxed state (DRX) and MYLK2 activity, leading to an increase phosphorylation of the myosin light chain and ATP consumption. ADP, adenosine di phosphate; ATP, adenosine tri phosphate; DRX, disordered relaxed state; MYLK2, myosin light chain kinase; P, phosphorylation; SRX, super relaxed state.

In mammals, loss of food intake and reduced mechanical loading/activity of skeletal muscles leads to a very rapid loss in mass and function. However, bears during hibernation, despite spending months without feeding and with very modest muscle activity, show only moderate muscle wasting. Part of this tissue sparing is due to a highly reduced metabolic activity in almost every tissue, including skeletal muscle. Myosin, one of the most abundant proteins in skeletal muscle, has different metabolic activities in resting muscle. To evaluate the ATPase activity of myosin in hibernating bears, we performed an analysis at the single muscle fiber level. Individual fibers were obtained from vastus lateralis muscle biopsies taken from the same bears either during hibernation or during the active phase in the summer. We confirm that muscle fibers from hibernating bears show no loss of fiber size and a mild reduction in force generating capacity. Interestingly, we find a significant reduction in ATPase activity of single muscle fibers taken from hibernating bears, which is caused by a reduced myosin ATP turnover. Single fiber proteomics analysis shows a major remodeling of their proteome, which is similar between different fiber types. Both type 2A and type 1/2A mixed fibers show a marked reduction in mitochondrial proteins during hibernation, with a decrease in proteins linked to the TCA cycle and mitochondrial translation. Western blotting, electron microscope and immunohistochemical analyses confirm mitochondrial alterations in muscles obtained in the winter season.

Using bioinformatical approaches based on the significant proteome changes, we found a decrease in Myosin Light Chain Kinase (MYLK2) targets in winter muscles compared to summer samples. This outcome was confirmed by western blotting analyses of both phosphorylated myosin light chain and MYLK2, which is a known stimulator of basal myosin ATPase activity. These results suggest that reduced myosin ATPase activity is one of the evolutionary adaptations adopted by resting skeletal muscle during hibernation to minimize energy expenditure. Interestingly, this suggests modulation of myosin ATPase activity as a new possible target to combat muscle wasting diseases, particularly those linked to altered metabolism.

2.5.2. My contribution to this publication

As shared first authors together with Cosimo De Napoli, we were the main driver from the experimental part of the project. Leonardo Nogara, Bert Blaauw, and Marcus Krüger conceived the project. Cosimo De Napoli, Mauro Montesel, Laura Cussonneau, Samuele Sanniti, Lorenzo Marcucci, Elena Germinario, Jonas Kindberg, Alina Lynn Evans, Guillemette Gauquelin-Koch, Fabrice Bertile, Etienne Lefai performed western blot analysis, mantATP chasing experiments, ATPase activity assay, tension measurement, EM analysis, and IHC staining and imaging. I performed single muscle fiber sample preparation for LC-MS analysis, stable data acquisition, and analyzed the data. All authors discussed the results and commented on the manuscript. Cosimo De Napoli and I assembled all figures and assisted Leonardo Nogara, Bert Blaauw, and Marcus Krüger in writing the manuscript and handling the revision.

2.5.3. Introduction

The regulation of muscle mass and function is affected by changes in activity levels, hormonal stimulation and mechanical stress.[255] For example, muscle disuse, as occurs when people are bed ridden for prolonged periods, or after bone fractures, are accompanied by a significant reduction in muscle mass and function within days/weeks.[256] Surprisingly, despite not eating or moving for months, hibernating bears only lose a moderate amount of muscle mass [257, 258], allowing them to look for food after arousal or to get out of the den in an emergency situation.[259] This sparing of body mass is not due to a drastic reduction in body temperature (only a few degrees), as they are able to reduce their basal metabolism independently from body temperature, in part through a very significant reduction in heart

and respiratory rate.[260, 261] With regards to skeletal muscle, the mechanisms underlying this reduction in basal metabolism and the preservation of mass and function are not completely understood. Some mechanisms have been proposed, like reduced oxidative stress [262], miRNA-dependent regulation of protein synthesis [263], or circulating factors modulating protein turnover [264], however, no clear mechanism is currently known. As a significant portion of body mass is accounted for by skeletal muscle, reductions in energy consumption by the muscle contractile apparatus can induce major alterations in whole body energy consumption. We have shown that the molecular motor of skeletal muscle, i.e. the myosin protein, can have different ATPase activity based on its conformation in relaxed muscle.[265] It can be found in a biochemical state characterized by very low ATPase activity which is known as the super relaxed state (SRX). On the other hand, if a myosin head is out of the SRX, but still in a relaxed muscle, this has been described as the disordered relaxed state (DRX). These two states have about a tenfold of magnitude difference in energy consumption, as can be measured by ATP hydrolysis rate, with the SRX having a time constant of approximately 200 s^{-1} and the DRX of 20 s^{-1}. Many different factors, ranging from changes in pH, temperature, or phosphorylation of myosin regulatory light chains, can modulate the stability of the SRX and alter basal ATPase activity of resting muscle. To understand if modulation of myosin ATPase activity in resting muscle contributes to the drastic reduction in whole body metabolic rate in hibernating bears, we analyzed summer and winter biopsies taken from the same bears. Using two different approaches we observed a significant reduction in ATPase activity in muscle fibers taken from winter biopsies. To gain mechanistic insight into the underlying processes regulating this, we performed a single fiber proteomics analysis. This revealed a significant reduction in mitochondrial proteins in winter muscle, confirming results obtained previously on snap frozen muscle.[266] We also observed a decreased myosin light chain kinase activity, possibly contributing to an increased SRX stability, as reported in other experimental systems.[267] Altogether, our results show that part of the energy saving mechanism in hibernating bears is through the reduction of ATP consumption by myosin, likely contributing to whole body energy expenditure.

2.5.4. Results

2.5.4.1. Loss in force production in permeabilized fibers from hibernating bears

Loss of muscle mass and function in hibernating bears is known to be less severe than that observed in humans or mice during muscle disuse. To determine how muscle size and function is affected at the single fiber level, we analyzed muscle biopsies taken from the same bears captured in summer or in winter, around the middle of the denning period. We collected these samples for two years in a row allowing us to analyze 11 winter and 10 summer muscle biopsies. As can be seen in **Table 15**, bear 4 and 5 were captured for two years in a row, while almost all other bears were captured in one winter and summer. Only bear 6 was not localized again in summer, as young males can migrate to find their own territory when they become young adults. The bears evaluated in this study are not yet sexually mature and have been followed from birth.

Table 14 Age, gender, and weight to the captured bears.

ID number	Year of collection	Age (year)	Gender	Summer weight [kg]	Winter weight [kg]
1	2022	3	F	57.6	49.5
2		3	F	58.2	61
3		3	F	72.6	67
4		2	F	36.8	31
5		2	F	56	35
6		2	M	NF	40
4	2023	3	F	53	52
5		3	F	76	74
7		2	F	34	38
8		2	F	34	35
9		2	M	39	37

To analyze functional properties of muscle fibers, we permeabilized muscle biopsies by placing them in a skinning solution. For this we isolated mechanically from each muscle 8-10 single fibers and determined fiber cross-sectional area. As can be seen in **Figure 35A**, there are significant differences in absolute fiber size comparing different bears, however, these can be at least in part explained by the variability in body weight of the different animals. Indeed, bear 2 and 3 (61 and 67kg) are substantially bigger than number 4 and 6 (31 and 40kg). Despite these differences in starting weight, average overall fiber size does not change when comparing summer and winter biopsies. This is in line with the relatively stable body mass between summer and winter for the same bear as shown in **Table 15**. These cross-

sectional areas are obtained on permeabilized fibers which are known to exhibit a 20-30% swelling caused by the chemical permeabilization process. Our results suggest that fiber swelling is not different between summer and winter bears as shown on the right in **Figure 35A**. Indeed, the cross-sectional areas of chemically skinned (and swollen) fibers and those measured on snap-frozen muscle sections of the corresponding bears, did not show a significant difference between summer and winter samples (**Figure S26**).

Next, we analyzed force production from isolated skinned fibers taken from each biopsy. As shown in **Figure 35B**, there was variability in the force production from fibers taken from each individual biopsy. Despite this, we were able to uncover a slight, yet significant 12±2% decrease between summer and winter biopsies, suggesting some alterations in sarcomere contractility during the hibernation period. These observations are in line with those that were reported when measuring twitch force in vivo, showing a 29% reduction after 110 days of denning.[258] It was also reported that twitch kinetics in vivo were reduced during the denning period. To address if part of these alterations in contractile kinetics in vivo can be due to changes in the core contractile apparatus, and not just a consequence of altered calcium handling, we performed a slack test on skinned fibers. This allows us to determine force re-development after a rapid shortening of 10% in an activated fiber, which is sufficient to reduce tension close to zero. In the left side of **Figure 35C** two representative force redevelopment traces are reported, showing the slower kinetics of the winter fiber compared to the summer. Force re-development kinetics, expressed as Ktr (**Figure 35C,** right), are significantly slower in hibernating muscle as compared to control tissue, in line with the observations performed previously in vivo. While it is not trivial to determine which alterations at the sarcomeric level are responsible for these changes in kinetics, it suggests that part of the alterations observed in vivo can be due to changes in the contractile apparatus.

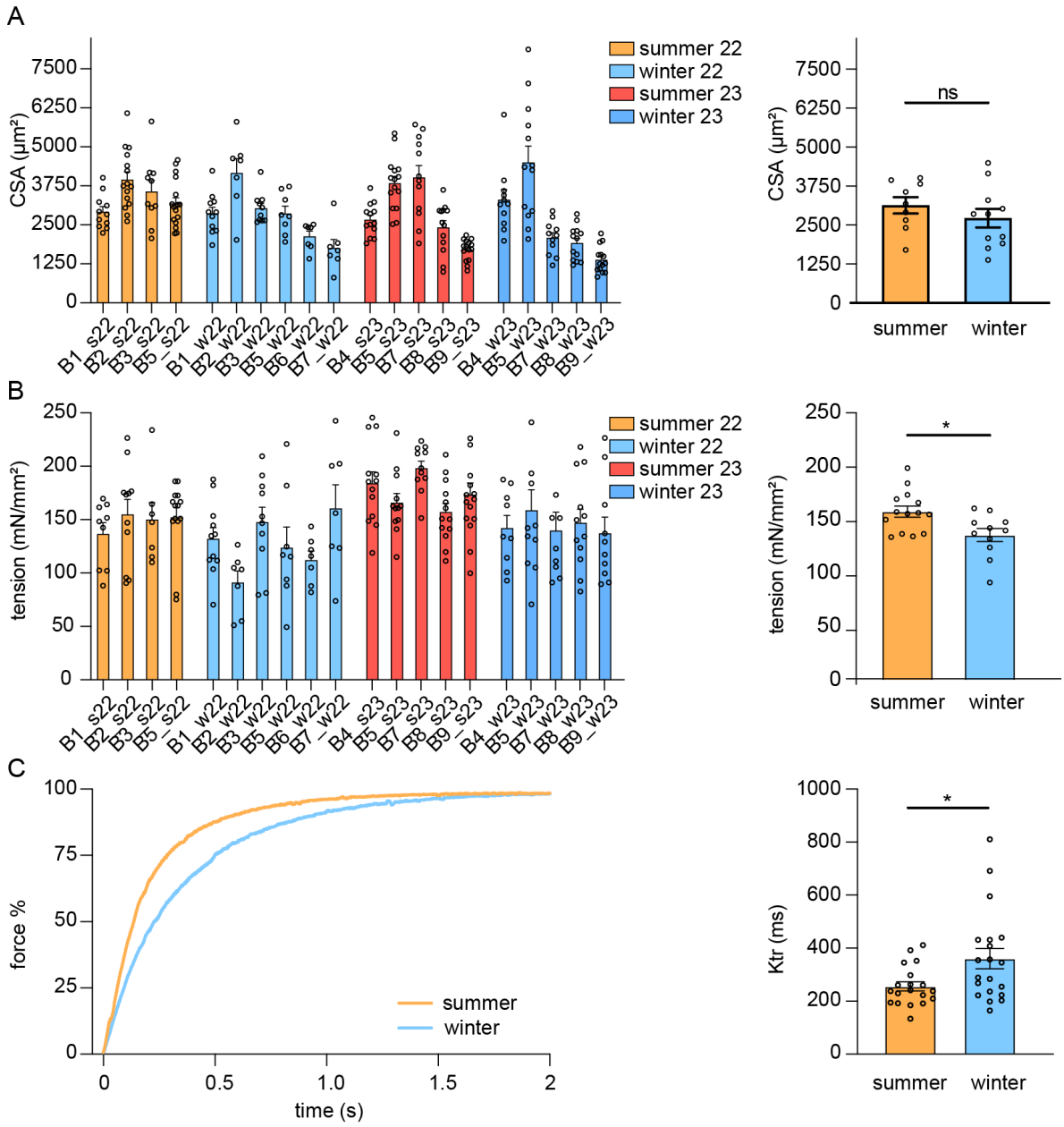

Figure 35 No changes in muscle size or force in permeabilized fibers from hibernating bears. A) Average cross-sectional area of skinned fibers taken from individual bears in winter and summer. Each dot corresponds to the CSA of a single fiber taken from that specific bear. On the right the average CSA of all bears examined divided by season (summer *n*=9, winter *n*=11). **B**) Maximal isometric tension produced from skinned fibers taken from individual bears (left) and divided by season (right), summer and winter bears show a small decrease in normalized tension in hibernating bears (summer *n*=9, winter *n*=11). **C**) Representative kTR after a 10% length shortening in a fiber from a winter biopsy compared to summer biopsy, on the right the average kTR for individual animals (summer *n*=8, winter *n*=10. Mann-Whitney test). CSA, cross sectional area; kTR, traces of force re-development.

2.5.4.2. Hibernating bears reduce ATPase activity of myosin in resting muscle fibers

The incredible capacity of bears to prevent muscle wasting, despite the lack of food intake and movement, suggests that muscles reduce energy consumption to a minimum. As was postulated more than a decade ago, muscle myosin can be found in two different resting states, the super relaxed state (SRX) and the disordered relaxed state (DRX). Estimates suggest that the SRX, has an ATPase activity which is approximately 5-10-fold lower than that observed when myosin heads are less stable and more disordered (DRX), in both cases without leading to force generation.[265] To determine if relaxed muscle fibers have a lower basal ATPase activity during the winter, we isolated single fibers and performed an ATPase activity assay. This assay is based on two enzymatic reactions that couple ADP produced by myosin spontaneous nucleotide turnover to NADH oxidation.[268] This assay reflects the activity of myosin, as the myosin inhibitor blebbistatin eliminates most ATPase activity. It is important to point out that these skinned fiber preparations have a highly permeabilized and altered plasma membrane, therefore a lot of ion pumps are no longer functioning. In **Figure 36A** on the left, each dot corresponds to the ATPase activity of one single fiber, while the histograms show the average for each bear. On the right, each dot corresponds to the average of each individual bear. As shown in **Figure 36A**, basal ATPase rate of bear muscle fibers in summer is 0.046±0,02 s-1, a range also observed in most other species, like mouse, rabbit and human.[269] Interestingly, fibers taken from the same animals during hibernation show a significant reduction in ATPase rate of 0.033±0,02 s-1. Treatment of fibers with the myosin inhibitor Blebbistatin reduces ATPase activity to 0.006 s-1 in both summer and winter muscles.

While these results clearly show that energy consumption by resting myosin is reduced in hibernating bear muscles, it does not allow us to determine the relative distributions of SRX/DRX in these fibers. To address this issue, we performed a mantATP chasing experiment, whereby we incubate fibers with a fluorescently labelled form of ATP (mantATP) and determine the decay in fluorescence after changing of the medium. The subsequent observed reduction in fluorescence can be fitted with a triple exponential decay function. The first exponential is very short since it represents the nonspecific binding of the nucleotide or that present in solution, the second exponential is associated to myosin in DRX, while the last one corresponds to myosin in SRX. Each exponential is characterized by two

parameters: the population (P) and the time constant (T). Populations are the fraction of myosin heads associated with each state, namely P1 for DRX and P2 for SRX, while time constant represents the stability of myosin in terms of nucleotide turnover rate. As can be seen in the representative traces shown on the left in **Figure 36B**, nucleotide release is slower in hibernating muscles than in summer biopsies, supporting the data presented in **Figure 36A**. The altered decay kinetic is caused by significant differences of the time constants T1 and T2, respectively that of myosin DRX and SRX (**Figure 36B**, right), being larger in winter and indicating an increased myosin stability. Relative populations of DRX and SRX are not changed in hibernating muscle, as can be observed in supplemental **Figure 36A**.

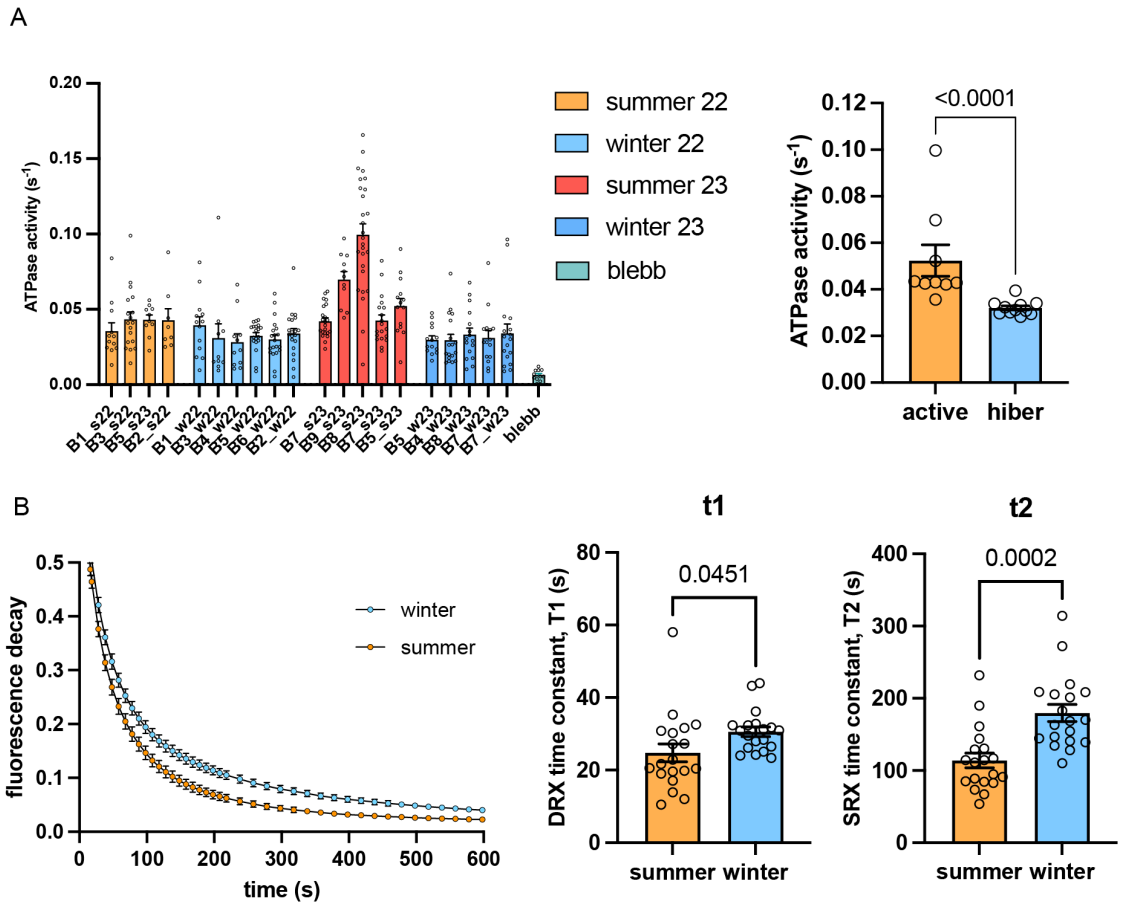

Figure 36 Hibernating bears reduce ATPase activity of myosin in resting muscle fibers. A) Average ATPase activity of skinned fibers taken from individual bears in winter and summer. Each point represents a single fiber taken from a specific biopsy. On the right the average ATPase activity divided by season, in which a decrease in ATPase activity is measured in winter compared to summer (summer *n*=9, winter *n*=11. Unpaired *t*-test). **B**) mantATP chasing experiment in skinned fibers from summer and winter bear muscle biopsies (*n*=19. Unpaired *t*-test). Winter biopsies showed a significant reduction in both DRX (T1) and SRX (T2) time constants, indicating a slower overall nucleotide release. DRX, disordered-relaxed state; SRX, super-relaxed state.

2.5.4.3. Single fiber proteomics shows drastic remodeling in hibernating muscles

How is the proteome affected in hibernating fibers, and how do these changes affect their functional properties? To address these questions, we performed a single fiber proteomics analysis on 8-10 single fibers taken from each biopsy. One of the major strengths of this single fiber approach is that one can compare the changes of the proteome within the same fiber type. We conducted our analysis on skinned fibers, which lack many soluble proteins. Consequently, our focus was on structural proteins influencing the functional shifts observed. Through this approach, we identified between 700-1200 protein per fiber (**Figure 37A** and **Table S14**). Using HEK cells for quality control, we consistently quantified over 6,000 proteins per control sample with a CV of <5%, suggesting a stable digestion and instrument performance (**Figure S28A-C**). Using unique peptides, we determined the relative proportion of MYH isoforms in each fiber. Fibers were classified based on whether they contained more than 70% of a specific MYH isoform. To prevent false-identifications, blank controls were injected every 15 samples, identifying minimal protein carry-over per sample (<50) (**Figure S28A, B**). Fiber type distribution remained stable, with Type 2a fibers being the most dominant in both summer and winter single muscle fibers (**Figure 37B**). We confirmed this finding also by an electrophoresis analysis showing how bear MYH isoforms run very similar to those taken from mouse muscles (**Figure S27B**).

While MYH isoforms showed no major changes, significant changes were observed in the proteome of type 2a fibers between hibernating and active bear muscle fibers (**Figure 37C**, **Figure S27D**). We identified 402 significantly differentially regulated proteins, with 244 upregulated proteins in summer and 158 in winter. Notable examples like the mitochondrial anion channel (VDAC1/2) are in both summer seasons more abundant while fibrillar components like Laminin-A and Desmin are more abundant in the winter months (**Figure 37D).** Fisher exact test performed on the significant changed proteins showed an enrichment of the gene ontology (GO) terms linked to mitochondrial content and function in summer muscle fibers (**Figure 37E**). A schematic representation of differentially regulated mitochondrial proteins shows how proteins linked to lipid oxidation are reduced, while glycolytic proteins are maintained, similar to previous observations (**Figure 38D**).[266] These comparisons, limited to type 2A fibers, do not reflect shifts in fiber type and concomitant change in mitochondrial content.

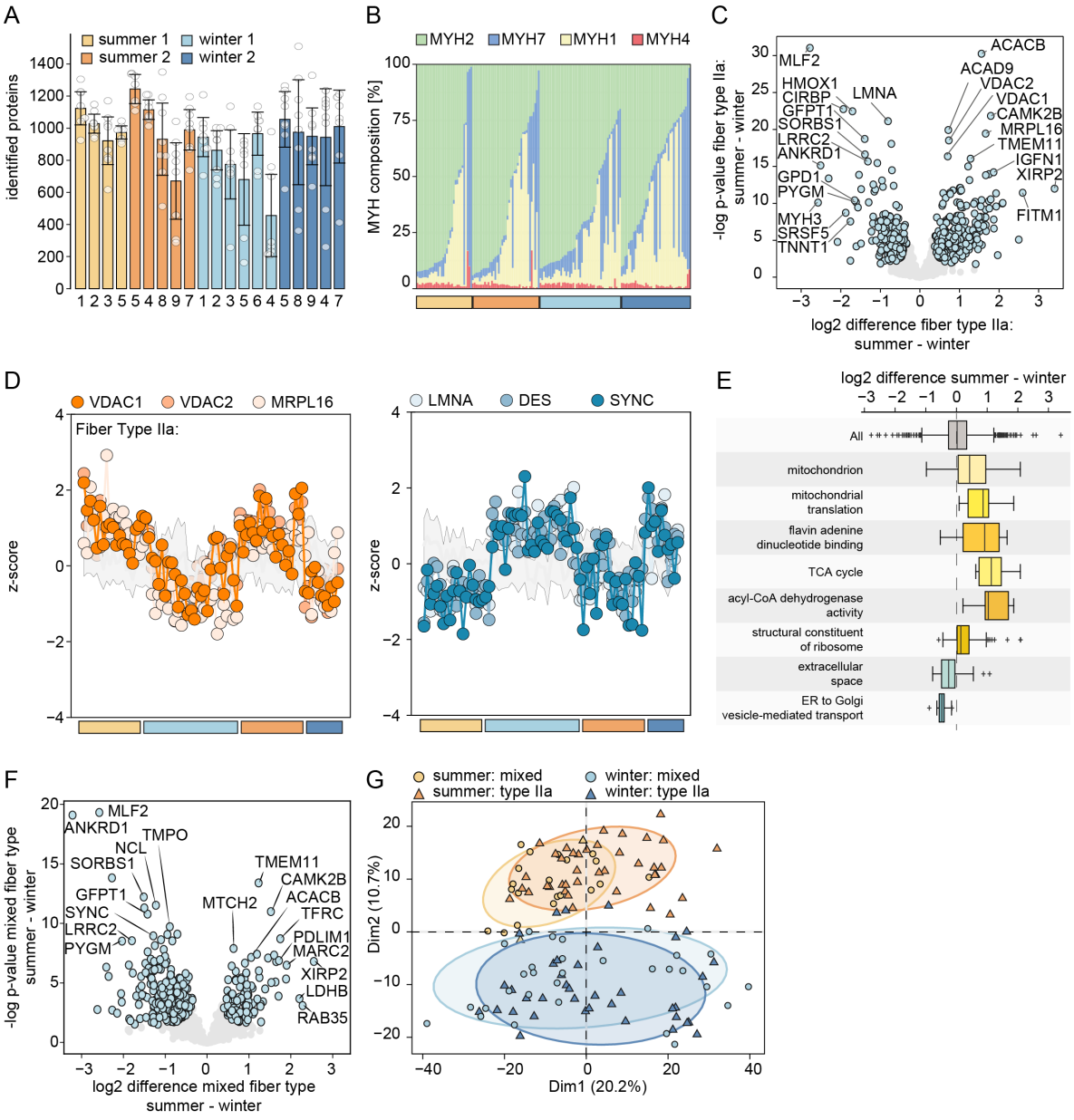

Figure 37 Single fiber proteomics shows drastic remodeling in hibernating muscles. A) identified proteins per fiber **B**) MYH isoform distribution analysis of isolated single fibers from different bears over four different seasons (orange summer, blue winter). Each bar represents the relative abundance of MYH isoforms in one fiber in relation to the total sum of intensities for MYH1 (yellow), MYH2 (green), MYH4 (red), and MYH7 (blue). Fibers from different bears are sorted into the four seasons and ranked from left to right of highest MYH2 abundance **C**) volcano plot for Type IIa Fibers summer vs winter (*n*=41-38) D) examples of proteins going up in summer (left) or winter (right) **E**) changes in GO terms comparing summer and winter type 2A fibers **F**) volcano plot for mixed (type1/2A) Fibers summer vs winter (*n*=20-30) G) Principal component analysis of protein expression patterns from isolated skinned single fibers of Type IIa (triangle) and mixed fibers (circle) collected in winter (blue) and summer (orange). ACACB, acetyl-CoA carboxylase 2; ANKRD2, ankyrin repeat domain-containing protein 2; CAMK2B, Ca^{2+}/calmodulin-dependent protein kinase type II subunit beta; DES, Desmin; ER, endoplasmatic reticulum; GFPT1, glutamine-fructose-6-phosphate aminotransferase; LMNA, Laminin; MTCH2, mitochondrial carrier homolog 2; LRRC2, leucine-rich repeat-containing protein 2; MLF2, myeloid leukemia factor 2; MRPL16, mitochondrial ribosomal protein 16; NCL, NA^{+}/Ca^{2+} exchanger NCL; PYGM, glycogen phosphorylase; SORBS1, sorbin and SH3 domain-containing protein 1; SYNC, Syncoilin; TCA, tricarboxylic acid; TFRC, transferrin receptor protein 1; TMEM11, transmembrane protein 11; TMPO, lamina-associated polypeptide 2; VDAC, voltage dependent anion channel.

To determine if these changes were specific to type 2A fibers, we also performed a single fiber proteomics analysis on mixed fibers (**Figure 37F**, **Figure S29**). Mixed fibers were defined as those expressing less than 70 % of any MYH isoform. However, they could be categorized as type 1/2a mixed fibers due to their predominant isoforms being MYH7 and MYH2. Interestingly, many proteins regulated in type 2A fibers showed similar patterns in mixed fibers, indicating a consistent muscle remodeling during hibernation regardless of fiber type (**Figure 37C, F**). Principle component analysis demonstrated clear separation between winter and summer single muscle fibers regardless of MYH content (**Figure 37G**). ANOVA analysis confirmed clustering of the fiber types based on the season rather than fiber types (**Figure S29A**). Overlapping significantly changed proteins revealed 95 upregulated and 129 down regulated in both fiber type 2A and mixed fibers (**Figure S29B-C**).

To better understand how these changes in mitochondrial GO terms reflect their organization and content within the fibers, we first performed a western blotting analysis for different proteins of the five respiratory complexes. In line with the observation in the single fiber proteomics, we observed a small, yet significant reduction in specific proteins from each complex (**Figure 38A**). Next, we performed an immunohistochemistry analysis for Tom20, a mitochondrial import receptor subunit, to determine mitochondrial distribution within the fiber. As can be seen in **Figure 38C**, summer fibers showed a more intense staining with a relatively normal distribution pattern. Electron microscope analyses of summer and winter skinned fibers showed, as expected, increased spaces between sarcomeres and swollen mitochondria in both conditions.

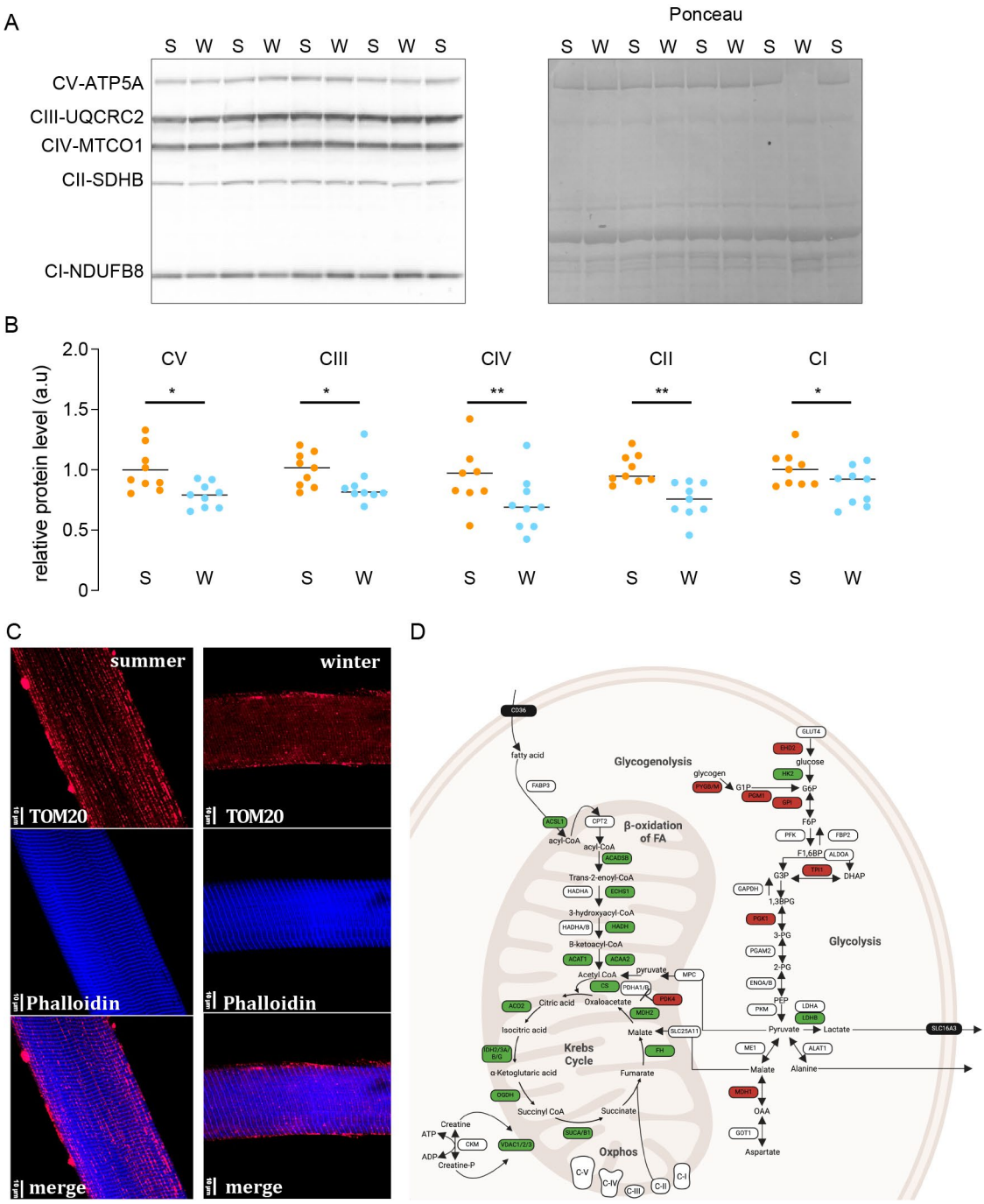

Figure 38 Alterations in mitochondrial structure and composition during hibernation. A, B) Western blotting for proteins of the different respiratory complexes shows a significant reduction in all complexes in winter (W) compared to summer (S) skinned fibers (**A**). Data are presented as individuals' values with mean bars (n=9 bears/season, the same individuals were sampled and analyzed in summer and winter) and normalized to the total protein content. Gray and black dots are for bears muscles, respectively in summer and winter (Ratio paired t-test, CV p-value=0.0145; CIII p-value=0.0202; CIV p-value=0.0095; CII p-value=0.0018; CI p-value=0.0338) (**B**). Representative western blots are shown for four couples of bears. **C**) IHC for TOM20 shows mitochondrial distribution, while Phalloidin shows actin localization in summer and winter fibers. **D**) Regulation of metabolism-related factors in skinned fibers of hibernating bear muscles. The relative abundance of skinned fibers proteins in winter (hibernating) versus summer (active) brown bears (n = X per season) is shown using the following color code: significantly (Welch t-test analysis; p-value < 0.01) up- and down-regulated proteins are shown in red and green boxes, respectively; white boxes show proteins that were unchanged between winter and summer and black boxes show proteins that we did not detect. Detailed protein

abundances and fold changes are given in Additional X. EM, electron microscopy; MTCO1, mitochondrially encoded cytochrome C oxidase I; NDUFB8, NADH:ubiquinone oxidoreductase subunit B8; SDHB, succinate dehydrogenase complex iron sulfur subunit B; TOM20, translocase of outer mitochondrial membrane 20; UQCR2, ubiquinol-cytochrome C reductase core protein 2.

2.5.4.4. Hibernating muscles shows a downregulation of myosin light chain kinase content and activity

As mentioned, there are 244 proteins with a significantly higher expression in summer muscles. To better understand what these proteins have in common, we performed an analysis using the ENRICHR software. One of the most suggestive enrichments we observed in this list is related to the so-called kinases co-expression analysis. In this analysis it is possible to determine the kinases which are co-expressed with regards to the list of proteins/genes examined. Interestingly, we observed that MYLK2 is the kinase with the strongest correlation to the enriched proteins in the summer muscles (**Figure 39A**). This captured our interest, as a reduced MYLK2 expression or activity during the winter induces a decrease in myosin regulatory light chain (RLC) phosphorylation, with subsequent stability of the SRX and a reduced ATPase activity. As skinned fibers are permeabilized, they do not allow for the determination of changes in phosphorylation levels. Therefore, we used snap frozen muscle tissue from the same bears and performed a western blotting analysis for both the total kinase levels and the phosphorylation of its main target, the myosin regulatory light chain (MLC). As shown in **Figure 39B**, **C**, we find a very consistent decrease in both MKL2 content and the phosphorylation of RLC on serine 19, the site known to be involved in the regulation of SRX stability. As it is not straightforward to find a specific protein which is unaltered during hibernation, blots were normalized for total protein content as identified by ponceau staining. Interestingly, this reduction in MYLK2 is also in line with a transcriptional reduction observed in a previous study from hibernating bears [270], or during torpor in zebrafish.[271] To understand if a similar reduction in MYLK2 levels also occurs in other models of muscle disuse, we analyzed its expression levels in a recently developed murine model of unilateral hindlimb casting.[272] As can be seen in **Figure 38D, E**, there is a significant reduction in MYLK2 after 7 and 14 days, suggesting a preserved mechanism between mice and bears during muscle unloading (**Figure S30A, B**).

taken together, our results suggest that part of the reduced ATPase activity in winter muscle is a consequence of an increased SRX stability due to reduced RLC phosphorylation.

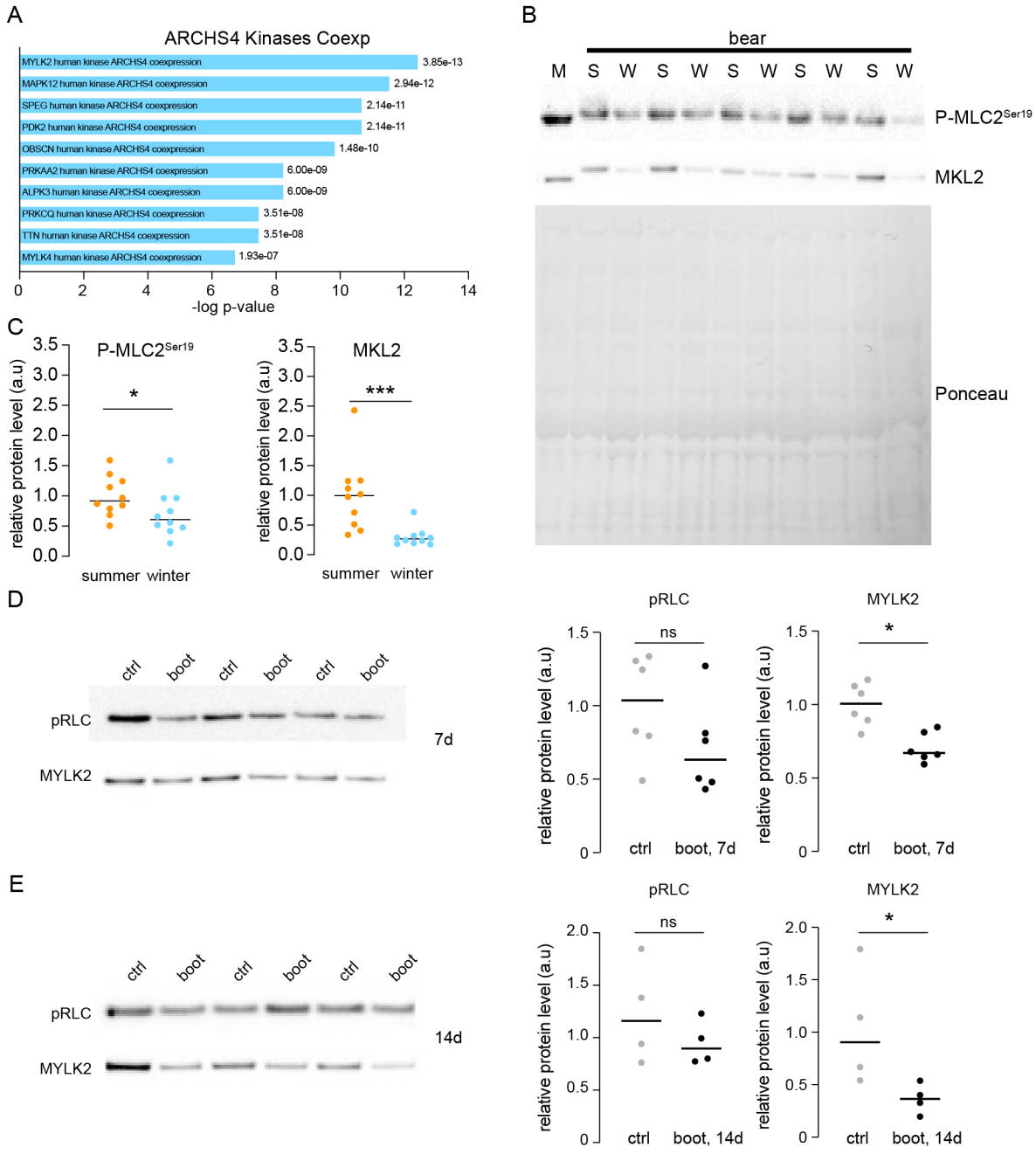

Figure 39 Hibernating muscles shows a downregulation of myosin light chain kinase content and activity. **A)** ENRICHR kinases co-expression analysis shows an increase in MYLK2 in summer bears **B**) and **C**) Western blotting analysis on frozen muscle tissue taken from the same bears as the skinned fibers shows decrease in MYLK2 and the phosphorylation of its target, P-RLC, in winter (W, blue dots) compared to summer (S, orange dots) muscles. D and E) Western blotting analysis on gastrocnemius muscle tissue from unilateral immobilized (boot d7 or d14, black dots) or the contralateral leg (ctrl, grey dots) from the same mouse show a significant decrease in MYLK2 and a tendency for the phosphorylation of its target P-MLC in immobilized leg compared to the contralateral. Data are presented as individuals' values with mean bars (n=10 bears/season, the same individuals were sampled and analyzed in summer and winter; n= 6 mice for one week, d7 and n=4 mice for 2 weeks, d14 immobilization) and normalized to the total protein content. Ratio paired t test. Representative Western blots are shown for five couples of bears, and a control of a mouse muscle (M), and 4 couples of mice. a.u., arbitrary units; ALPK3, alpha kinase 3; ARCHS4, all RNA-seq and ChIP-seq sample and signature search; MAPK12, mitogen-activated protein kinase 12; MYLK, myosin light chain kinase; MLC2, myosin regulatory light chain; OBSCN, obscurin; SPEG, Striated muscle preferentially expressed protein kinase; TTN, Titin.

2.5.5. Discussion

It is well known that muscle disuse leads to a very rapid loss in skeletal muscle mass and function in a matter of days. In this sense, hibernation represents a unique form of disuse, during which animals abstain from eating or engaging in physical activity for months, yet remarkably, experience only minimal muscle loss. For comparison, a 90-days immobilization in humans leads to a decrease in force of 54%.[273] On average, the effect of bed-rest and immobilization periods of 4-28 days showed a muscle loss in the range of 0.2-2.3 %/day, which is always exceeded by a force loss, ranging between 1.1-3.5 %/day.[256, 274] In a disuse model in rodents caused by 3d printed cast, the gastrocnemius muscle exhibits a 25% in weight loss and a 40% drop in muscle force over the course of 2 weeks.[272]

It has been reported that this remarkable tissue sparing during hibernation is achieved, among other mechanisms, by drastically reducing metabolic rate.[257, 260] Indeed heart rate and respiratory rate are reduced 3-5 fold, despite maintaining body temperatures relatively high.[260] Here, we determined if skeletal muscle myosin, one of the most abundant proteins in the body, has a reduced ATPase activity in hibernating bears. Using a single fiber ATPase assay, we find that ATPase activity in relaxed skinned fibers of hibernating muscle is significantly lower (-28%) than what is observed in muscle biopsies taken from the same bears in summer. Using a mantATP chasing approach we find that time constant for nucleotide exchange is prolonged for all myosin heads in winter samples. Performing a single fiber proteomics analysis, we find, despite no major loss in fiber size and function during hibernation, that there is a very significant remodeling of the proteome. Mitochondrial proteins are altered and show a reduction in winter muscle, independently from fiber type. Interestingly, winter fibers show a lower content and activity of MYLK2, a kinase responsible for myosin RLC phosphorylation which induces SRX destabilization, possibly explaining the different resting ATPase activity in the two seasons.

2.5.5.1. Muscles from hibernating bears show altered contractile properties and protein content

In a landmark paper published over 20 years ago, it was shown that hibernating bears only lose around 20% of muscle strength in vivo during hibernation.[275] Later, the same authors confirmed these observations and also showed that contractile kinetics of twitch tension was reduced.[276] As these measurements were performed in vivo, it is difficult to determine where muscle dysfunction or changes in kinetics occurred. Muscle disuse is known to lead to

alterations in muscle innervation, calcium dynamics and dysfunction of the contractile apparatus.[256, 277, 278] In our study, we evaluated contractile function and kinetics of single fibers, without the requirement of muscle innervation or calcium release through normal excitation-contraction coupling cycles. Interestingly, we find that most of the muscle dysfunction which occurs in hibernating bears is due to a reduced force production from the contractile apparatus. A possible explanation for a reduced normalized force in single fibers could potentially be through a different fiber swelling [279], as reduced swelling in winter fibers would lead to an underestimation of skinned fiber cross sectional area. However, as winter fibers show an increase in structural proteins like desmin and laminin A, likely reinforcing the cytoskeleton, it is unlikely winter fibers swell more. Indeed, comparisons of snap frozen and skinned CSA do not show differences between summer and winter fibers. Also, electron microscopy analysis does not show increased space between sarcomere in parallel or the presence of damaged sarcomeres. This suggests that reduced force is most likely due to alterations in the force generating capacity of the contractile proteins in the fiber. One of the few modifications known to affect functional properties of skinned fibers is oxidation, leading to reduced contractile force and kinetics.[280] Indeed, incubation of permeabilized fibers with a nitric oxide donor, is sufficient to reduce contractile force and kinetics, but even resting ATPase activity, suggesting this oxidative stress acts on the myosin head and not on the actin-myosin interaction. It has been reported that antioxidant defense and general oxidative stress in hibernating muscles is reduced, even though overall nitrosylation is increased.[262] However, it is possible that proteins with a very high half-life, like structural muscle proteins [278], can accumulate these relatively stable oxidative modifications over time, leading to the observed functional decrease. This issue is likely to be particularly pronounced during hibernation, as it has been reported that general protein turnover is strongly reduced.[258] While we were not able to link the functional deficit to changes in a specific protein, the proteomics analyses performed on single fibers show a major remodeling of the proteome in both fast and slow fibers. The most obvious alteration is observed in the mitochondrial proteome, with many proteins showing a significant reduction. Similar results have been reported in many hibernating species [281], and could contribute to some redox-dependent modifications of contractile proteins. While many proteins show a decrease in winter muscle, there are also interesting proteins which strongly increase during hibernation that can potentially explain some of the protective processes that occur under these extreme

conditions. One interesting example is Cold-inducible RNA binding protein (CIRBP), an mRNA binding protein, which can stabilize specific transcripts to improve survival under prolonged cold conditions. Indeed, loss of CIRBP reduces hypothermic cardio protection [282], a critical issue for heart transplant. Interestingly, this protective effect of CIRBP appears to be mediated by its inhibitory effect on ferroptosis [283], a specific type of cell death accompanied by iron accumulation and lipid peroxidation.[284] While the regulation of ferroptosis as a protective mechanism during hibernation has been suggested [285], it is interesting to note that similar changes might also occur in hibernators which do not lower their body temperature that much, like the bears.

2.5.5.2. Hibernating muscles reduce myosin ATP consumption

The major finding in this study is that relaxed skeletal muscle myosin consumes less ATP during hibernation. Both an ATPase activity measurement (NADH-oxidation) and a mantATP chasing approach clearly showed that myosin in single muscle fibers taken from hibernating bears consumes less ATP. While summer fibers showed some variability, winter fibers had a consistently reduced ATPase activity in all biopsies examined. Some of this variability observed in the ATPase activity in the summer group can be due to the high variability in activity patterns and daily energy expenditure reported in bears.[286] In non-denning adult polar bears daily energy expenditure can vary 5-10-fold, while activity patterns can show an even wider range. The more homogeneous values obtained in winter muscles are most likely due to the more uniform conditions at the moment all bears are captured. Changes in ATPase activity and ATP/ADP levels are also known to affect contractile kinetics, linking metabolic changes directly to contractile characteristics. Indeed, using an in vitro motility assay it was shown that sliding velocity of myosin is strongly affected by ADP dissociation from actomyosin and decreased in dystrophic muscle, a condition known to have an increased oxidative stress.[287, 288] A reduction in ATPase activity of myosin is also comforted by findings from snap frozen biopsies that support the reduction in both the production and use of ATP in the muscles of hibernating bears.[266] Proteomics studies suggest that this is accompanied by a preferred use of lipids, albeit with a lower rate of oxidation, while sparing glycogen stores.[266]

MYLK2 activity through RLC phosphorylation is a well-known mechanism that causes an increased calcium sensitivity and an altered thick filament conformation, with more disordered myosin heads arrays.[289] In response to this phosphorylation, an increase in resting

myosin ATP consumption has been reported for cardiac myofibrils [290], while its energetic contribution in skeletal muscle is controversial, with some literature stating little-to-no effect [291] and others suggesting an increase only at low calcium levels.[292] It must be stated that divergent outcomes may be due to an undetermined initial sample phosphorylation level, as well as the marginal modulation of nucleotide turnover in a resting muscle compared to active contraction. In fact, myosin light chain phosphorylation does not alter the stability of the SRX in a linear fashion and does not abolish it completely.[265] MYLK2 is rapidly activated by the calmodulin-calcium complex in a contracting muscle, while it is slowly deactivated by its autoinhibitory alpha helix in absence of free cytosolic calcium. In skeletal muscle, the phosphatase kinetics are quite slow [293], leaving myosin RLC phosphorylation as a molecular memory of muscle activation, and inducing post tetanic potentiation.[294] As muscles are highly inactive during hibernation, it is reasonable to assume that the lack of calcium release from the SR is one of the major reasons for the reduced MYLK2 activity, even though changes in phosphatase activity cannot be excluded either for the reduced RLC phosphorylation.

According to our data, the decrease in ATP consumption from myosin during hibernation is caused by a prolongation of myosin DRX and SRX time constants, as shown by the mantATP chasing experiments. Even in the absence of a change in DRX and SRX populations, an increased time constant reflects a different myosin heavy chain heads stability. In fact, in skinned fibers from winter biopsies the DRX constant (T1) is increased by about 25% while the SRX constant (T2) is almost double. The corresponding difference in nucleotide exchange rate causes the increased stability of myosin in the DRX population to contribute in a stronger manner to the decrease in ATP hydrolysis, followed by the increased stability of myosin in the SRX population. These data support the idea that an energy preservation mechanism is acting on the biochemical equilibrium of the thick filament. It has been reported that age could affect myosin SRX in the same fashion we showed here [295], by altering time constant rather than myosin populations. It is known that, upon oxidation, myosin produces less force, but its effect on nucleotide exchange and possibly on myosin heads dragging on the thin filament in a lightly attached configuration is not well established. Temperature is unlikely to have a major impact on the seasonal differences reported in this work. Indeed, bears during hibernation do not experience a massive drop in body temperature, not enough to induce a structural destabilization and the appearance of myosin

heads in the refractory state.[296] Also, it is known that with the lowering of the temperature myosin heads undergo an order-to-disorder transition [297], increasing DRX and consequentially futile ATP hydrolysis. To give an estimation of the contribution of the SRX/DRX balance to whole body energy consumption, we performed a rough calculation based on the energy consumption of resting muscle myosin (**Figure S30**). These suggest that energy sparing in muscle tissue is around 30% in hibernating muscle compared to summer muscle.

Taken together, we find that in large, hibernating mammals, like the brown bear, skeletal muscle myosin reduces ATPase activity, highlighting a new energy saving mechanism during extreme situations. Interestingly, also a murine model of muscle disuse showed a similar reduction in MYLK2 levels, suggesting that myosin ATPase activity might also play a role in other conditions of muscle wasting, particularly those affected by major modulations of muscle metabolism.

2.5.6. Materials and methods

2.5.6.1. Bear Sample Collection

Biopsies from the vastus lateralis muscle were collected from 9 free-ranging brown bears, 2–3 years old (Ursus arctos), from Dalarna and Gävleborg counties, Sweden, from 2022 to 2023 (**Table 15**). The samples were immediately frozen on dry ice until storage at −80 °C or processed to obtain a chemically skinned sample. Each year, the same bears were captured during winter hibernation (February) and recaptured during their active period by helicopter darting (June).[298] Two bears were captured in two consecutive years. The study was conducted according to the guidelines of the Declaration of Helsinki and of the European Directive 2010/63/EU and approved by the Institutional Review Board (or Ethics Committee) of (1) the Swedish Ethical Committee on Animal Experiment (applications Dnr C3/2016 and Dnr C18/2015), the Swedish Environmental Protection Agency (NV-0741-18), and the Swedish Board of Agriculture (Dnr 5.2.18–3060/17). All procedures complied with Swedish laws and regulations. Capture, anesthesia, and sampling were carried out according to an established biomedical protocol (Arnemo, J.M.; Evans, A.L. Biomedical Protocols for Free-Ranging Brown Bears, Wolves, Wolverines and Lynx; Inland Norway University of Applied Sciences: Elverum, Norway, 201). For skinned fibers, bundles of bear muscle were harvested and stored at 4 °C in a skinning solution (150mM potassium propionate, 5mM potassium dihydrogen phosphate, 5mM magnesium acetate, 5mM EGTA, 2mM DTT, 2.9mM ATP, 0.5mM sodium azide,s proteases and phosphatases inhibitors, pH 7.0) for 24 hours and then transferred to a storage solution (same as skinning but 50% glycerol) at -20°C.[268]

2.5.6.2. Mouse Sample Collection

Biopsies from the gastrocnemius muscle were collected at different time points: after 1 (D7, n=6 mice) and 2 weeks (D14, n=4 mice) of unilateral immobilization using custom-made 3D-printed boot as previsouly described.[272] Gastrocnemius muscles of the contralateral leg were collected at the same time and all the muscles were snap-frozen in liquid nitrogen for subsequent analyses.

The study was conducted according to the Guide for the Care and Use of Laboratory Animals (NIH; National Academies Press, 2011), as well as the Italian law for the welfare of animals.

The Italian Ministero della Salute approved all animal experiments, Ufficio VI (Rome, Italy; authorization number 448/2021 PR)

2.5.6.3. Western Blot

Vastus lateralis muscles or skinned fibers from 9 bears (paired samples collected in summer and winter in a given year for the same individual; **Table 15**) and gastrocnemius muscles from mice after 1 week (D7, n=6) or 2 weeks (D14, n=4) of unilateral immobilization or the controlateral leg (Ctrl), were used. Samples were homogenized using metallic beads in 100 µL of an ice-cold buffer (50 mM Tris pH 7.5, 150 mM NaCl, 1 mM EDTA, 10 mM MgCl2, 0.5 mM DTT, 10% Glycerol, 2% SDS) containing inhibitors of proteases (complete Tablets EDTA-free, Roche) and phosphatases (phosphoSTOP, Roche, Monza, Italy). The homogenates were lysated for 3 minutes at 30 Hz in TissueLyser II (Qiagen, Milan, Italy) and then centrifuged at 10,000 g for 15 min at 4 ◦C. The resulting supernatants were then stored at −80 °C until further use. The concentration of proteins was determined using the PierceTM BCA Protein Assay (Thermo Fisher Scientific, Parma, Italy). Proteins were then diluted in Laemmli buffer and stored at −80 °C until further use. Protein extracts were subjected to SDS-PAGE (sodium dodecyl sulfate-polyacrylamide gel electrophoresis) using BoltTM 4 to 12%, Bis-Tris Plus WedgeWellTM gels (Thermo Fisher Scientific, Parme, Italy) and transferred onto a nitrocellulose membrane. Blots were blocked for 1 h at room temperature with 5% bovine serum albumin in TBS buffer with 0.1% Tween-20 (TBS-T, pH 7.8), then washed thrice in TBS-T and incubated (stirring overnight at 4 °C) with appropriate primary antibodies against Phospho-Myosin Light Chain 2 (Ser19)(Rabbit, 1:1000 5%BSA, CST#3671, Cell Signaling Technology, Milan, Italy), MYLK2 (Rabbit, 1:1000 5%BSA, HPA059704, Atlas antibodies, Rome, Italy) and OXPHOS (Mouse, 1:2000 5%BSA, #ab110413, Abcam, Milan, Italy). Blots were washed and incubated for 1 h with an appropriate secondary horseradish peroxidase-conjugated antibody at room temperature Goat Anti-Mouse IgG-HRP Conjugate (1:5000) and Goat Anti-Rabbit IgG-HRP Conjugate (1:4000), respectively #1706516 and #1706515, Biorad, Segrate MI, Italy. Signals were detected after incubation with Luminata Classico Western HRP substrate (Millipore, Burlington, MA, USA) and visualized using iBright750 imaging system (Thermo Fisher Scientific, Parme, Italy). Signals were quantified using the ImageJ software 1.53f51[299] and normalized against the total amount of proteins determined by Ponceau signals to correct for uneven loading. Protein data were presented as individual values. The bilateral ratio paired

Student's t-test was used to compare the muscles of bears during summer and winter (S and W, respectively). Statistical analysis was performed using Prism 8 (GraphPad Prism 9, San Diego, CA, USA).

Muscle samples for protein electrophoresis were solubilized in the SDS-PAGE sample buffer (62.5 mM Tris pH 6.8, 2.3% SDS, 5% Beta-mercaptoethanol,10% glycerol) containing the Complete Protease Inhibitor Cocktail (Roche, Basel, Swiss) and analyzed by SDS-PAGE on 8% polyacrylamide gels according to the method described by Talmadge and Roy [300]. MyHC protein bands were revealed by Coomassie Blue (EZBlue Gel Staining Reagent, Sigma Aldrich) and isoform percentage composition was evaluated by densitometry using ImageJ.

2.5.6.4. mantATP chasing

Single fibers were dissected from biopsies and then mounted on aluminum T-clips on a 3D printed setup (**Figure S26B**). The setup was then placed on the stage of a Nikon Eclipse inverted fluorescence microscope equipped with a Hamamatsu ORCA Flash-4.0 camera. The sarcomere length was adjusted between 2.4-2.5µm using a micromanipulator. The experiment was performed at room temperature. The fiber was incubated in a rigor buffer solution (potassium acetate 120mM, MOPS 50mM, EGTA 4 mM, potassium dihydrogen phosphate 5mM, magnesium acetate 5mM, DTT 1mM, pH 6.8) for 5 minutes. Then, the fiber was moved to another chamber containing rigor buffer plus 250µM mantATP (NU-202L, Jena Bioscience, Germany) and incubated for 10 minutes. At the beginning of the recording, the fiber was moved to a new chamber containing a fresh relaxing buffer (rigor buffer with the addition of 4mM ATP). Pictures were taken using the DAPI filters set through a 10X magnification objective (PLAN FLUOR 10X/0.30 WD 16.0), plus additional 1.5X magnification of the Nikon Eclipse stage. The recording protocol was the following: 10 frames were taken every 2 seconds, then 20 frames every 10 seconds, and 20 additional frames every 20 seconds, for a total measurement time of 620 seconds. Every frame exposure was 400ms with the camera set to binning 4x4. The recording protocol and camera setting has been optimized to reduce photobleaching during the total illumination time of about 50s. The decrease in fluorescence intensity was fitted with the following three exponential decay function:

$$Y=1- P0*(1-\exp(-X/T0))-P1*(1-\exp(-X/T1))-P2*(1-\exp(-X/T2)).$$

Initial fitting values are set to P0=0.25, T0=2, P1=0.375, T1=20, P2=0.375, T2=200 and fitting is run for 1000 iterations using GraphPad Prism (V 10.0.2 for Mac, GraphPad Software, Boston, Massachusetts USA). P1 and P2 are expressed as a percentage of P1 + P2, thus the total fitted populations, excluding the non-specific P0.

2.5.6.5. NADH coupled reaction ATPase activity assay

Single fibers were dissected and pipetted into a 384-well plate in relaxing buffer (Potassium propionate 100 mM, MOPS 50 mM, EGTA 12 mM, magnesium acetate 6 mM, potassium dihydrogen phosphate 6 mM, ATP 4 mM, DTT 2 mM, Triton X-100 0.025%, protease inhibitor, pH 7.4) plus the coupled reaction buffer (NADH 1.6mM, PEP 5 mM, pyruvate kinase 40 U/ml and lactate dehydrogenase 40 U/mL) to a final volume of 30 µL. The plate was covered with an optically clear seal and placed in a temperature controlled multiplate reader set to 27 °C (Multiskan SkyHigh, ThermoFisher Scientific). The coupled reaction act as the following: myosin hydrolyses ATP to ADP and inorganic phosphate, ADP and phosphoenolpyruvate are converted by pyruvate kinase to ATP and pyruvate, pyruvate and NADH are converted to lactate and NAD+ by Lactate dehydrogenase.[268, 301, 302] The oxidation rate of NADH was measured every 2 min as the decreasing absorbance at 340 nm, total run time 25 min. The linear decrease was estimated using NADH absorbance epsilon of 6300 mol-1 cm-1 and using a calibration curve obtained by the addition of a growing concentration of ADP. A concentrated KCl solution was added to each well at the end of the assay to reach the final concentration of 0.4 M and extract myosin from the bear fiber, the protein amount was measured using PierceTM 660 nm Protein Assay Reagent (ThermoFisher nr. 22660) for normalization purposes.

2.5.6.6. Single fibers tension measurement

Single skeletal muscle fibers were dissected in cold storage solution, clipped with aluminum T-clips at each end and mounted on an Aurora Scientific Permeabilized Fibers 802D setup (Aurora Scientific, Ontario, Canada). A thin flow of 5% toluidine blue and 8% glutaraldehyde[303] was used to crosslink each end of the fiber. After an extensive wash with relaxing solution, the diameter was measured, and sarcomere length was adjusted to 2.5 µm using a camera mounted on an inverted microscope. The maximal tension of the fibers has been measured at 21°C. For single fiber shortening the sarcomere length was adjusted at 2.9 µm, so during the activation of the fiber a steady shortening of 10% L0 was imposed at the

plateau. Relaxing, pre-activating and activating buffers, as well as calcium sensitivity buffers are derived from Fusi et al.[297]. Force is normalized to cross sectional area using the measured diameter and assuming circular geometry. The time constant of the force redevelopment after a slack test has been obtained through a single exponential fitting. The tension-time trace has been analyzed between the time of the initial rise in tension just above the zero level, reached after a shortening of 10% of the SL, to the time when the plateau was fully reached. The build-in MATLAB® function fit has been used with the custom function

$$T = a(1 - e^{-\frac{t}{t_c}})$$

being T the tension, t the time, a the tension at the plateau and t_c the time constant. R2 were higher than 0.9 for all the traces. Ktr is described as the rate of force redevelopment following a rapid shortening of the fiber after reaching maximal isometric tension. The rapid shortening allows the tension to be redeveloped from zero in a saturating calcium condition so that the kinetic is not affected by Ca^{2+} diffusion, the thin filament is activated, and the force increases proportionally to the thick filament activation and myosin recruitment. The experimental traces are fitted using a single exponential function as reported extensively in the literature.[304]

2.5.6.7. Single fiber proteomics

Bear fibers were placed in a 96-well plate. On each plate, one column was used for the quality standard based on 20k HEK cells to process sample preparation and the performance of the LC-MS instrumentation. 40 µl of 4% SDS in PBS containing 5 mM TCEP and 10 mM CAA were added to each well. Next, 96 well plates were placed on 95 °C for 10 min followed by sonication in a Bioraptor sonicator set to 20 °C water temperature with 10 cycles of 30 on/30 off. Samples were digested following the standard SP3 protocol.[123] Briefly, 20 µg of each washed SP3 beads were added to each well followed by immediately adding one sample volume of acetonitrile (ACN). After the incubation period of 8 min and 2 min on a magnet, supernatant was discarded and magnetic beads were washed 2x with 70% EtOH, 1x with 100% ACN. Samples were digested with 10 µl of 20 ng LysC and 40 ng trypsin dissolved in 50 mM ammonium bicarbonate at 37 °C, 750 rpm overnight. Samples were acidified by using 100 µl 0.1% FA followed by a clean-up with house-made SDB-RPS tips. Purified peptides were loaded with indexed retention time peptides (iRT) on EvoTips Pure and applied a 60 SPD method on an EvoSep One system (both Evosep, Denmark) with an 8 cm PepSep Column. Mobile phases were compromised of 0.1% FA as solvent A and 0.1% FA in ACN

as solvent B. The HPLC system was coupled to a timsTOF pro 2 using a CaptiveSpray source (both Bruker). Samples were measured in dia-PASEF mode with daily ion mobility calibration using three ions of Agilent ESI-Low Tuning Mix following vendor specifications. The DIA-PASEF window was ranging in dimension 1/k0 0.7-1.35, with 24x25 Th windows and in dimension m/z from 350 to 1250. The mass spectrometry proteomics data have been deposited to the ProteomeXchange Consortium via the PRIDE partner repository with the dataset identifier PXD050980.[161] Files were processed with DIA-NN 1.8.1 using library free search against UniProt Ursus Arctos database (2019) complemented with protein sequences from myosin heavy chain variants. Database was blasted against existing GO-terms with GOblast. Mass ranges were set according to the settings of the mass spectrometer, mass deviation was automatically determined from the first data file for thermos files and set to a mass deviation of 15 ppm for files acquired by Bruker instruments. Further calculations were performed within R (version 4.2.2) using the following libraries: diann, tidyverse, data.table, samr, vsn, and ggplot2, gprofiler, missForest. Data was further processed using an in house modified R-script based on the version by V. Demichev (Github page, cit MaxLFQ). Data input was filtered for unique peptides, q-Value <0.01, Lib.Q.Value <0.01, PG.Q.Value < 0.01, Global.Q.Value < 0.01, Quantity.Quality > 0.7, Fragment.count >= 4. Fiber with less than 500 identified proteins were excluded. Protein intensities of each fiber were normalized to the total fiber intensity. Fibers were characterized into fiber type I (>70% MYH7), fiber type IIa (>70% MYH2), fiber type IIx (>70% MYH1), and mixed fiber (<70% MYH1, <70% MYH2, <70% MYH4, <70% MYH7). Data completeness of 70% was calculated for each group. One group is specified by season and fiber type. Missing values were imputed by random forest algorithm for groups with 70% data completeness, with more than 30% missing values random forest algorithm was downshifted of 0.3, width 1.5. Further analysis was performed in Perseus (V 1.6.5.0) and InstantClue (V 0.10.10.20211105). ANOVA analysis and Welch's T-test analysis was performed with an FDR with less than 0.05 and 500 randomizations, Quality control of iRT peptides were performed in Skyline-Daily (V 22.21.391).

2.5.6.8. Electron microscopy

Small bundles (about 15-20 myofibers) were dissected from each skinned bear biopsies and pinned, slightly stretched, over a silicone support (SYLGARD 184 Silicone; GMID 01673921). The pinned bundles were then washed with relaxing buffer (potassium

propionate 100 mM, MOPS 50 mM, EGTA 12 mM, magnesium acetate 6 mM, potassium dihydrogen phosphate 6 mM, ATP 4 mM, DTT 2 mM, protease inhibitor, pH 7.4) to remove the storage solution while avoiding spontaneous fiber contraction. Still stretched, the samples were fixed overnight at 4 °C with 2.5% glutaraldehyde (EMS; Cat. N°16220) in 0.1 M sodium cacodylate buffer (pH 7.4). Subsequently the samples ware post fixed with 1% in 0.1 M sodium cacodylate buffer for 1 hour at 4°C. After three water washes, samples were dehydrated in a graded ethanol series and embedded in an epoxy resin (Sigma-Aldrich 46345). Ultrathin sections (60-70 nm) were obtained with Leica Ultracut EM UC7 ultramicrotome, counterstained with uranyl acetate and lead citrate and viewed with a Tecnai G2 (FEI) transmission electron microscope operating at 100 kV. Images were captured with a Veleta (Olympus Soft Imaging System) digital camera.

2.5.6.9. Immunohistochemistry

Each fiber was dissected from the bear biopsies and pinned over a silicone support (SYLGARD 184 Silicone; GMID 01673921) and washed with relaxing buffer (Potassium propionate 100 mM, MOPS 50 mM, EGTA 12 mM, magnesium acetate 6 mM, potassium dihydrogen phosphate 6 mM, ATP 4 mM, DTT 2 mM, protease inhibitor, pH 7.4) and slightly stretched. The fibers were then fixed in paraformaldehyde 2% for 5 minutes and permeabilized with PBS Triton X-100 1% for 3 minutes. The samples were blocked with mouse-on-mouse blocking reagent (Vector laboratory MKB-2213) for 1 hour at room temperature. TOM20 primary antibody (Proteintech, Nr 11802-1-AP) (dilution rate 1:50) was incubated as a cocktail solution of PBS (Sigma-Aldrich, Life science, P4417) 0.5% BSA (Sigma-Aldrich, Life science, A3912) and 2% goat serum (Sigma-Aldrich, Life science, G9023) overnight at 4 °C. Alexa Fluor® 647 conjugated Anti-Rabbit IgG (Alexa Fluor® 647 AffiniPure™ Goat Anti-Rabbit IgG H+L, Jackson ImmunoResearch, 111-605-144; 1:100 dilution) secondary antibody was subsequentially incubated together with a cocktail solution of Phalloidin (Alexa Fluor 568 phalloidin, Invitrogen, Life Technologies corporation, A1238; 1:1000 dilution), BSA 0.5% and 4% goat serum for 1 hour at 37 °C. After each step the fibers were washed three times in PBS. Lastly, each fiber was carefully placed on microscope slides (series 3 adhesive, Trajan, T7611) and mounted with Elvanol (0.01 g/vol polyvinyl alcohol, 30% glycerol, PBS). Images were acquired with a confocal scanning laser microscope (Zeiss LSM900 upright confocal).

2.5.6.10. Statistical analysis

Statistical analysis has been carried out using GraphPad Prism software (V 10.0.2 for Mac, GraphPad Software, Boston, Massachusetts USA). Individual datasets were tested for outliers using the ROUT method Q=1%, then tested for normal distribution using D'Agostino & Pearson test before proceeding to parametric or nonparametric unpaired Student t-test. Statistical significance is reported for p-value <0.05. Data are presented as means ± standard error of the mean (SEM), and individual data points are shown to visualize distribution. In **Figure 44A, B** and **Figure 45A** the histograms on the right report a single value for each bear which was obtained as the mean of the multiple single fiber analysis represented in the histograms on the left. In **Figure 44C** and **Figure 45B** each dot represents a single fiber belonging to all the subjects analyzed within the corresponding season (n=2±5 fibers per subject per season).

2.5.7. Acknowledgements

This work was supported by grants from Association Française contre les Myopathies (AFMTéléthon to B.B., no. 24357), Associazione Italiana per la Ricerca sul Cancro (AIRC)-27007 to B.B. This work is supported by the European Union – NextGenerationEU, by the 2021 STARS Grants@Unipd programme and Association Française contre les Myopathies (AFMTéléthon, no. 24328) granted to L. N., This work was supported by the European Union EU-NMJ-Chip (JPND2019-466-146), EU-NMJ-Chip (FKZ:01ED2006), and the Deutsche Forschungsgemeinschaft DFG FOR2722/2 (DFG 384170921) to MK. French Space Agency (CNES, #7906 and #8072) to F.B., and Agence Nationale de la Recherche (ANR-22-CE14-0018) to F.B. and E.L. The authors thank the field capture team of the Scandinavian Brown Bear Research Project (SBBRP). The long-term funding of SBBRP has come primarily from the Swedish Environmental Protection Agency, the Norwegian Environment Agency, the Austrian Science Fund, and the Swedish Association for Hunting and Wildlife Management.

2.5.8. Author contributions

L.N., B.B., M.K. conceived the project and wrote the manuscript. C.DN., L.S., M.M., L.C., S.S., L.M., E.G., J.K., AL.E., G. GK., M.N. F.B., and E.L. performed experiments and analyzed data. All authors discussed the results and commented on the manuscript.

2.5.9. Conflict of interest

Cosimo De Napoli, Luisa Schmidt, Mauro Montesel, Laura Cussonneau, Samuele Sanniti, Lorenzo Marcucci, Elena Germinario, Jonas Kindberg, Alina Lynn Evans, Guillemette Gauquelin-Koch, Marco Narici, Fabrice Bertile, Etienne Lefai, Marcus Krüger, Leonardo Nogara, and Bert Blaauw declare that they have no conflict of interest.

3. Discussion

Skeletal muscle is the largest organ in the human body and plays an important role in many diseases that are based on metabolic impairments.[2] Here we have provided several approaches to skeletal muscle analysis that focus on intact skeletal muscle, the spatial distribution of proteins in skeletal muscle, and individual skeletal muscle fibers. We were able to perform deep proteomic analysis using thin cryotome sections and generated protein profiles across the longitudinal axis in mouse soleus and diaphragm skeletal muscle. We identified a number of proteins that are restricted to specialized matrix regions such as the MTJ and NMJ. Furthermore, we were able to perform a distance-based network analysis to validate the biological idea of a highly connected MTJ.

To test our protein profiling, we examined different aging conditions and found a loss of connectivity and a broadening of the NMJ in aged mice. In addition, this work focused on individual mouse soleus fibers in a prediabetic state to characterize the effects of increased food intake on the different mouse skeletal muscle fiber types. We observed altered mitochondrial localization in peripheral areas of skeletal muscle fibers, which was restricted to type IIa fibers. One marker protein we investigated was MTFP1, which may regulate mitochondrial activity in type IIa muscle fibers. Metabolic syndromes and reduced activity often lead to a significant loss of muscle mass. This often leads to a pathological loss of muscle mass in older people, which is also described as sarcopenia. An exception is hibernating animals, whose muscles show only minor effects even after 6 months of hibernation. To investigate this protective mechanism in more detail, bear muscle fibers were examined under normal and hibernating conditions using proteomic analysis. Reduced myosin ATPase activity was observed, suggesting a new mechanism for energy conservation in extreme situations.

3.1. Spatial proteomics using thin cryosections allows to deconvolute the data to cellular populations

The mammalian skeletal muscle is a heterogenous tissue, comprising different skeletal muscle fiber types, multiple cell populations and specialized ECM areas (**Figure 2**). Usually, skeletal muscle tissue has been studied either as a complete mixture or by isolating specific cell types via FACS to focus on individual cell populations. However, spatial analysis along the longitudinal or transversal axis of the skeletal muscle has been lacking.

Our approach involves profiling of skeletal muscle tissue using thin cryosections, allowing us to generate protein profiles from different intra- and extra-cellular proteins in an unbiased manner. With over 3,500 identified protein profiles from the diaphragm and soleus muscles, we are paving the way for future spatial proteomics studies. Although our method does not achieve cellular resolution, we identified several marker proteins for each cell type, enabling us to track their abundance across the muscle (**Table 15**).

For example, FAPs include subpopulations such as myocyte-like FAPs, transitional FAPs, and CD142-like FAPs. The latter can be further classified into CD9+, CYP1B1+, and MYOC+ cells. Our studies show a clear increase of MYOC in the tendon, while CD9 is enriched at NMJ and MTJ.[305] Myocilin (MYOC) is an uncharacterized protein predicted to function as a SNARE protein, while CD9 is a tetraspanin primarily surrounding nerves and muscle spindles, known to be a marker for extracellular vesicles in muscles, potentially originating from FAPs. CD9+ CD142-FAPs might play an important role at highly communicative areas such as NMJ and MTJ.[306]

MuSCs are crucial for the growth, repair, and regeneration of skeletal muscle tissue. However, the stem cell population is compared to the whole skeletal muscle mass rather low and the identification of MuSC marker proteins, including transcription factors (for example PAX7) is challenging. Moreover, the detection of low abundant proteins in differentiated tissues like body fluids and skeletal muscles is the high concentration of sarcomere and matrix proteins, leading to a high dynamic range within the sample. For example, the myogenic transcription factor MyoD was identified in several central muscle slices, but complete profiling was hindered by an excessive number of missing values. Nevertheless, other proteins such as desmin[307], filamin-C , and glutathione peroxidase 3[308] can be used to validated the presence of MuSCs if they are all identified together with a higher intensity (**Figure S6**).

Similarly, detecting the basic-loop-helix transcription factor scleraxis, a specific tenocyte marker, was not possible using the slice approach or comprehensive tenocyte proteome analysis, despite identifying 8,000 proteins (**Figure 14**). However, other tenocyte-specific markers like tenomodulin and tenascin C showed increasing expression profiles from muscle to tendon, consistent with previous studies.

Proteins associated with glial cells are more abundant in NMJ and MTJ areas, while crystallin alpha-B (CRYAB) and diazepam binding inhibitor (DBI), which were both reported to be

highly abundant in glial cells[309, 310], display constant expression across the muscle, decreasing towards the tendon. DBI has been recently identified as part of a peripheral neuron-glia communication mechanism modulating pain signaling, which may be distributed throughout the muscle, not just at NMJ.[310]

Marker proteins for pericytes or smooth muscle myosin cells (SMMCs) in the diaphragm exhibit multiphasic profiles with four maxima, often decreasing after the MTJ, whereas in the soleus muscle, these proteins are more abundant within the muscle. These cell types are essential for maintaining the structural integrity of blood vessels.[282, 311] The arterial anatomy influences this distribution, with large blood vessels running parallel to muscle fibers in the soleus and branching from the tendon center in the diaphragm, similar to the phrenic nerve's path between the central tendon and peripheral muscle.

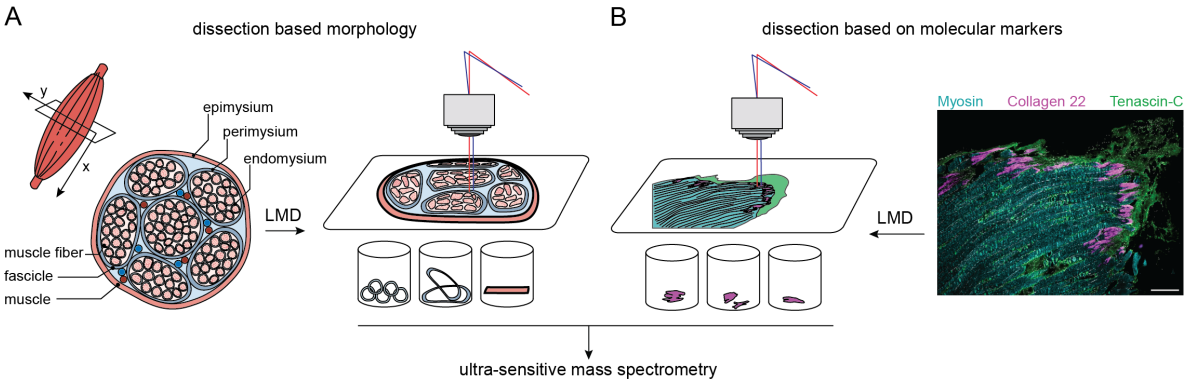

Figure 40 Improvement for the spatial proteomics workflow of muscle. A, B) Workflow for laser capture microdissection of **A**) morphological structures and **B**) molecular markers to isolate single cells from longitudinal skeletal muscle sections.

To achieve cellular resolution, a complementary approach such as laser capture microdissection (LMD) can be employed. In this technique, tissue sections are mounted on special slides, and a laser is used to precisely dissect specific cell types and structures within the section for subsequent proteomics experiments (**Figure 40A**). This method allows for the generation of a 3D representation by isolating different cell populations not only within a single section but also across several consecutive sections. This approach will enhance our understanding of muscle tissue, enabling us to observe spatial differences within a single cell population.

In summary, we generated over 3,500 protein profiles from the soleus and diaphragm muscles, providing a deeper understanding of muscle structure. While our approach does not achieve cellular resolution, we identified and localized several marker proteins for each cell type in specific muscle areas, offering valuable insights for future studies.

Table 15 Protein marker for the cell types FAPs, endothelial cells, MuSCs, inflammatory cells, myonuclei, glial cells, myotenocytes, activated fibroblasts, pericytes, and SMMCs.

FAPs

UniProt	gene name	protein name	max. intensity, soleus	max. intensity, diaphragm
P01027	C3	Acylation stimulating protein	tendon	constant
P40240	CD9	Tetraspanin CD9	tendon	NMJ, MTJ
P08121	COL3A1	Collagen 3	tendon	tendon
P12804	FGL2	Fibroleukin	no profile, tendon	no profile, tendon
P13020	GSN	Gelsolin	multiphased	tendon
Q61647	HAS1	Hyaluronan synthase 1	constant	muscle
P51885	LUM	Lumican	tendon	Down with maxima at MTJ and NMJ
Q9QZJ6	MFAP5	Microfibrillar-associated protein 5	to less data points	-
O70624	MYOC	Myocilin	tendon	tendon
Q9ET66	PI16	Peptidase inhibitor 16	to less data points	to less data points
Q05769	PTGS2	Prostaglandin G/H synthase 2	-	no profile, muscle
P48759	PTX3	Pentraxin-related protein PTX3	-	no profile, muscle
P97290	SERPING1	Plasma protease C1 inhibitor	-	muscle, multiphased
O70475	UGDH	UDP-glucose 6-dehydrogenase	-	to less data points

Endothelial cells

UniProt	gene name	protein name	Max. intensity, soleus	Max. intensity, diaphragm
Q9WTQ5	AKAP12	A-kinase anchor protein 12	MTJ	MTJ, tendon
Q08857	CD36	Platelet glycoprotein 4	muscle	muscle
P55284	CDH5	Cadherin-5	muscle	muscle, NMJ
P04117	FABP4	Fatty acid-binding protein, adipocyte	muscle	muscle
P35969	FLT1	Vascular endothelial growth factor receptor 1	to less data points	no profile, tendon
P01901	H2-K1	H-2 class I histocompatibility antigen, K-B alpha chain	No profile	NMJ, multiphased
Q9Z0E6	GBP2	Interferon-induced guanylate-binding protein 2	MTJ	muscle
Q64282	IFIT1	Interferon-induced protein with tetratricopeptide repeats 1	-	to less data points
Q9QZ85	IIGP1	Interferon-inducible GTPase 1	MTJ	no profile, MTJ
Q64339	ISG15	Ubiquitin-like protein ISG15	no profile, tendon	no profile, tendon

Tenocytes

UniProt	gene name	protein name	Max. intensity, soleus	Max. intensity, diaphragm
O55226	CHAD	Chondroadherin	tendon	tendon

D3Z7H8	CILP2	Cartilage intermediate layer protein 1	tendon	MTJ
Q60847	COL12A1	Collagen 12a1	tendon	tendon
P11087	COL1A1	Collagen 1a1	tendon	tendon
Q01149	COL1A2	Collagen 1a2	tendon	tendon
Q9R0G6	COMP	Cartilage oligomeric matrix protein	tendon	tendon
Q9D2L5	CPXM2	Inactive carboxypeptidase-like protein X2	-	no profile, tendon
P29268	CTGF	Connective tissue growth factor	MTJ	MTJ
P50608	FMOD	Fibromodulin	tendon	MTJ
O35367	KERA	Keratocan	tendon	tendon
P28301	LOX	Protein-lysine 6-oxidase	tendon	tendon
Q9D1H9	MFAP4	Microfibril-associated glycoprotein 4	MTJ	MTJ
P97298	SERPINF1	Pigment epithelium-derived factor	tendon	tendon
Q9Z1T2	THBS4	Thrombospondin-4	tendon	tendon
Q9EP64	TNMD	Tenomodulin	Tendon	MTJ

MuSCs

UniProt	gene name	protein name	Max. intensity, soleus	Max. intensity, diaphragm
Q9D1A4	ASB5	Ankyrin repeat and SOCS box protein 5	constant	-
P41731	CD63		-	NMJ
P31001	DES	DES	muscle	muscle
Q8VHX6	FLNC	Filamin-C	muscle	muscle
P46412	GPX3	Glutathione peroxidase 3	muscle	muscle
O88940	MSC	Musculin	-	no profile, NMJ
P10085	MYOD1	Myoblast determination protein 1	no profile, muscle	-
P00860	ODC1	Ornithine decarboxylase	-	no profile, muscle
Q9CWP8	POLD4	DNA polymerase delta subunit 4	-	no profile, muscle
Q9D708	S100A16	-	to less data points	-
P29533	VCAM1	vascular cell adhesion molecule 1	no profile, muscle	no profile, muscle

Inflammatory cells

UniProt	gene name	protein name	Max. intensity, soleus	Max. intensity, diaphragm
P08226	APOE	Apolipoprotein E	tendon	Constant
P04441	CD74	H-2 class II histocompatibility antigen gamma chain	to less data points	-
O70370	CTSS	Cathepsin S	-	No profile, MTJ
P20491	FCER1G	High affinity immunoglobulin epsilon receptor subunit gamma	to less data points	-
P14483	H2-AB1	H-2 class II histocompatibility antigen, A beta chain	increases in direction of MTJ	-

P18468	H2-EB1	H-2 class II histocompatibility antigen, I-A beta chain	-	to less data points
P16110	LGALS3	Galectin-3	to less data points	to less data points
Q9Z126	PF4	Platelet factor 4	-	to less data points
O54885	TYROBP	TYRO protein tyrosine kinase-binding protein	to less data points	-

Myonuclei

UniProt	gene name	protein name	Max. intensity, soleus	Max. intensity, diaphragm
P68134	ACTA1	Actin, alpha skeletal muscle	muscle	muscle
O88990	ACTN3	Alpha-actinin-3	muscle	muscle
P05064	ALDOA	Fructose-bisphosphate aldolase A	muscle	muscle
Q8R429	ATP2A1	Sarcoplasmic/endoplasmic reticulum calcium ATPase 1	muscle	muscle
P07310	CKM	Creatine kinase M-type	muscle	muscle
P21550	ENO3	Beta-enolase	muscle	muscle
P16858	GAPDH	Glyceraldehyde-3-phosphate dehydrogenase	muscle	muscle
Q5SX39	MYH4	Myosin-4	muscle	muscle
P05977	MYL1	Myosin light chain 1/3, skeletal muscle isoform	muscle	muscle
P97457	MYLPF	Myosin regulatory light chain 2, skeletal muscle isoform	muscle	muscle
Q9JK37	MYOZ1	Myozenin-1	muscle	muscle
O70250	PGAM2	Phosphoglycerate mutase 2	muscle	Muscle, increases in direction of MTJ
Q9D119	PPP1R27	Protein phosphatase 1 regulatory subunit 27	muscle	-
P32848	PVALB	Parvalbumin alpha	muscle	muscle, multiphased
P48962	SLC25A4	ADP/ATP translocase 1	muscle	muscle
O70548	TCAP	Telethonin	muscle	muscle, increases in direction of MTJ
P20801	TNNC2	Troponin C, skeletal muscle	muscle	muscle, increases in direction of MTJ
P13412	TNNI2	Troponin I, fast skeletal muscle	muscle	muscle
Q9QZ47	TNNT3	Troponin T, fast skeletal muscle	muscle	muscle
P58771	TPM1	Tropomyosin alpha-1 chain	muscle	muscle, increases in direction of MTJ

Glial cells

UniProt	gene name	protein name	Max. intensity, soleus	Max. intensity, diaphragm
P39061	COL18A1	Collagen 18	muscle	NMJ, MTJ
Q00493	CPE	Carboxypeptidase E	to less data points	to less data points
P23927	CRYAB	Alpha-crystallin B chain	muscle	muscle
P31786	DBI	Acyl-CoA-binding protein	to less data points	muscle
Q9D964	GATM	Glycine amidinotransferase, mitochondrial	-	No profile, NMJ

P16110	LGALS3	Galectin-3	to less data points	to less data points
P27573	MPZ	Myelin protein P0	Biphasic, MTJ	Biphasic, NMJ, MTJ
P60202	PLP1	Myelin proteolipid protein	to less data points	Biphasic, NMJ, MTJ
Q6F5E0	TMEM158	Transmembrane protein 158	-	to less data points
Q80YX1	TNC	Tenascin	tendon	tendon
Q9CWF2	TUBB2B	Tubulin beta-2B chain	tendon	to less data points
P20152	VIM	Vimentin	tendon	MTJ
P68510	YWHAH	14-3-3 protein eta	muscle	constant

Myotenocytes

UniProt	gene name	protein name	Max. intensity, soleus	Max. intensity, diaphragm
P68134	ACTA1	Actin, alpha skeletal muscle	muscle	muscle
P05064	ALDOA	Fructose-bisphosphate aldolase A	muscle	muscle
P56383	ATP5G1	ATP synthase F(0) complex subunit C1	constant	-
P07310	CKM	Creatine kinase M-type	muscle	muscle
P43023	COX6A2	Cytochrome c oxidase subunit 6A2, mitochondrial	muscle	muscle, biphasic
P50462	CSRP3	Cysteine and glycine-rich protein 3	muscle	muscle
P31001	DES	DES	muscle	muscle
P97447	FHL1	Four and a half LIM domains protein 1	muscle	muscle
Q5EBG6	HSPB6	Heat shock protein beta-6	muscle	muscle, increases in direction of MTJ
P04247	MB	Myoglobin	muscle	muscle
P05977	MYL1	Myosin light chain 1/3, skeletal muscle isoform	muscle	muscle
P97457	MYLPF	Myosin regulatory light chain 2, skeletal muscle isoform	muscle	muscle
P48962	SLC25A4	ADP/ATP translocase 1	muscle	muscle
O70548	TCAP	Telethonin	muscle	muscle, increases in direction of MTJ
P20801	TNNC2	Troponin C, skeletal muscle	muscle	muscle, increases in direction of MTJ
P13412	TNNI2	Troponin I, fast skeletal muscle	muscle	muscle
Q9QZ47	TNNT3	Troponin T, fast skeletal muscle	muscle	muscle
P58771	TPM1	Tropomyosin alpha-1 chain	muscle	muscle, increases in direction of MTJ
P58774	TPM2	Tropomyosin alpha-2 chain	muscle	muscle

Activated fibroblasts

UniProt	gene name	protein name	Max. intensity, soleus	Max. intensity, diaphragm
P51910	APOD	Apolipoprotein D	-	no profile, NMJ
O35903	CCL2	C-C motif chemokine 25	to less data points	-
Q61147	CP	Ceruloplasmin	constant	MTJ
Q8CFZ4	GPC3	Glypican-3	-	to less data points

Q04998	INHBA	Inhibin beta A chain	to less data points	to less data points
P51885	LUM	Lumican	tendon	muscle, MTJ and NMJ
P13516	SCD1	acyl-CoA desaturase 1	tendon	-
P82198	TGFBI	transforming growth factor-beta-induced protein ig-h3	tendon	tendon

Pericytes

UniProt	gene name	protein name	Max. intensity, soleus	Max. intensity, diaphragm
P70170	ABCC9	ATP-binding cassette sub-family C member 9	muscle	muscle, multiphased
Q8R2G4	ART3	Ecto-ADP-ribosyltransferase 3	muscle	muscle, multiphased
Q8K353	CYSTM1	Cysteine-rich and transmembrane domain-containing protein 1	-	no profile, muscle
Q07802	EBF1	transcription factor COE1	-	to less data points
P22339	GADD45B	growth arrest and DNA damage-inducible protein GADD45 beta	-	to less data points
P17879	HSPA1A	heat shock 70 kDa protein 1A	-	muscle, multiphased
Q61696	HSPA1B	heat shock 70 kDa protein 1B	-	muscle, multiphased
P97794	KCNJ8	ATP-sensitive inward rectifier potassium channel 8	-	no profile, muscle
Q4FZG9	NDUFA4L2	NADH dehydrogenase [ubiquinone] 1 alpha subcomplex subunit 4-like 2	-	no profile, muscle
Q64695	PROCR	endothelial protein C receptor	-	no profile, tendon
O08850	RGS5	regulator of G-protein signaling 5	-	no profile, muscle
Q923B6	STEAP4	metalloreductase STEAP4	tendon	muscle, multiphased
P29788	VTN	Vitronectin	tendon	muscle

SMMCs

UniProt	gene name	protein name	Max. intensity, soleus	Max. intensity, diaphragm
P27699	CREM	cAMP-responsive element modulator	-	no profile, muscle
P63254	CRIP1	cysteine-rich protein 1	constant	to less data points
P97315	CSRP1	cysteine and glycine-rich protein 1	MTJ	multiphased
Q9R0P5	DSTN	Destrin	constant	multiphased
O08579	EMD	Emerin	muscle	no profile, muscle
Q8BTM8	FLNA	Filamin-A	muscle	multiphased
Q99JI1	MUSTN1	musculoskeletal embryonic nuclear protein 1	-	no profile, muscle
O08638	MYH11	myosin-11	muscle, increases in direction of MTJ	multiphased
Q60605	MYL6	myosin light polypeptide 6	constant	muscle

Q9CQ19	MYL9	myosin light polypeptide 9	-	muscle, multiphased
Q6PDN3	MYLK	myosin light chain kinase, smooth muscle	muscle, increases in direction of MTJ	MTJ, multiphased
Q9D1G2	PMVK	phosphomevalonate kinase	-	no profile, muscle
P37804	TAGLN	Transgelin	muscle, increases in direction of MTJ	muscle, multiphased
P58774	TPM2	tropomyosin beta chain	muscle	muscle
P62500	TSC22D1	TSC22 domain family protein 1	constant	-

3.2. Spatial proteomics of the diaphragm and soleus muscle enables us to characterize the muscle-tendon interface

Previous transcriptomics and proteomics experiments of MTJ in humans, mice and horses show very little overlap, most likely due to manual isolation based on morphological characteristics. The only candidate identified as MTJ protein in all studies is the FACIT collagen 22.[43, 118, 130]

Here, we identified 175 and 206 MTJ proteins by spatial proteomics based on thin cryosections of the diaphragm and soleus skeletal muscle. However, the overlap between earlier studies and our analysis was limited; we only detected an overlap for 4 proteins in diaphragm, soleus, and published data and an overlap of 6 or 5 for the soleus and diaphragm with published data, respectively (**Figure 41A**). One reason for the low extent of overlap between these datasets could be that the correlation between mRNA and protein expression is poor due to variation in the half-lives of proteins and post-transcriptional regulation. Moreover, the isolation of different skeletal muscles from different species could be another possible explanation for the high variation in the MTJ candidates identified to date.

In our studies we were able to show an overlap of 34 MTJ proteins between the soleus and diaphragm which are associated to GO terms of vesicle transport, cell adhesion, mitochondrion, cytoskeleteon, and neuronal marker proteins (**Figure 41A** and **Table 13**). This allowed us to further characterize the molecular network the MTJ as shown in **Figure 41B**. In all the studies, CILP, Periostin, XIRP2, and the solute carrier family 4 member 1 (SLC4A1) were identified. CILP and Periostin are both described as ECM proteins involved in tissue remodeling and repair. Both ECM proteins are also connected with the TGFβ signaling and subsequent tissue fibrosis.[312, 313]

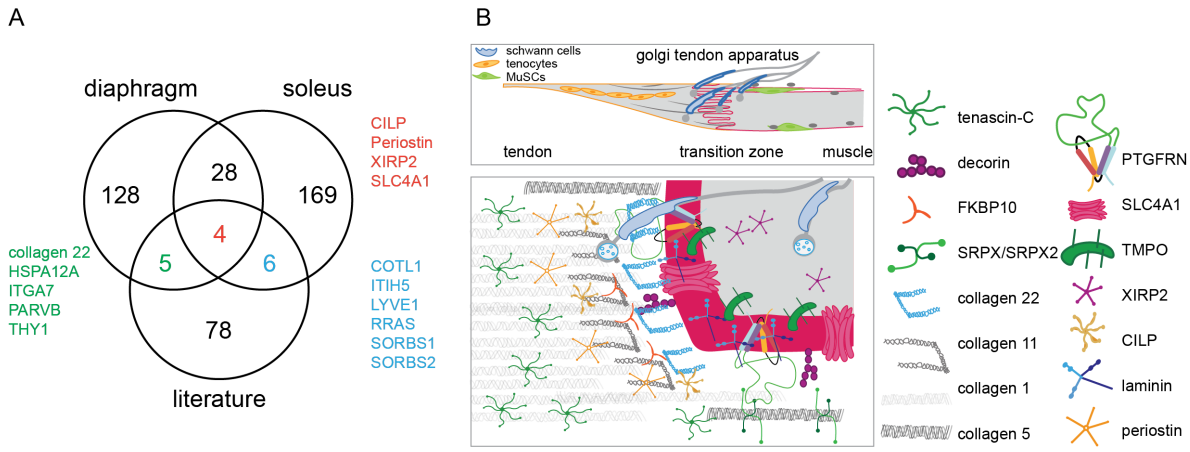

Figure 41 Schematic overview of the identified MTJ proteins. A) Venn diagram of the identified MTJ proteins in the diaphragm (**2.3.3.2**) and soleus (**2.1.1**) from this study and published MTJ proteins. **B**) Schematic overview of the muscle fiber- tendon transition zone with a zoom-in to the most abundant proteins in the MTJ.

Additionally, we identified the metabolic pathway closely linked to blood pressure regulation is the renin-angiotensin system (RAS). The angiotensin converting enzyme (ACE) cleaves the inactive peptide angiotensin I to produce the active peptide angiotensin II. For associated enzymes to RAS, we identified an increase in protein profiles towards the tendon, suggesting enhanced levels of angiotensin in the MTJ and tendon. This pathway is closely linked to the activation of transforming growth factor beta (TGFβ) and SMAD2/3 signaling, which also play critical roles in the regulation of ECM gene expression and fibrosis.[156] We were able to show a decreased ECM expression after blocking the RAS pathway using a blood pressure medication. In previous studies, a direct correlation between Achilles tendon rupture was identified which might be associated to altered ECM components in the MTJ and tendon.[157] Interestingly, the plasma membrane glycoprotein SLC4A1 is important in hypertension is affected by blood medication drugs. Thereby, it is conversely effected to Periostin and CILP by TGFβ and an overactive pathway is downregulating SLC4A1 and also Nidogen and SRPX.[314] Mainly SLC4A1 functions as a transporter mediating electroneutral anion exchange of HCO_3^- for Cl^- and the transport of glucose and water but also it interacts with other structural proteins like ankyrin, cytoskeletal proteins, and glycolytic enzymes.[315-317] So far, the transporter was associated to erythrocytes and kidney tubes but it might be possible that SLC4A1 play also a function in different cel population within the MTJ.[314] To further improve our understanding of MTJ, future experiments could be performed with the laser dissection microscope. Here, not only individual structures can be cut out, but also individual cells. This would then allow the spatial analysis to be extended to the single cell (population) (**Figure 40B**).

3.3. Spatial proteomics of the NMJ improves the understanding of the NMJ

3.3.1. Correlation of identified NMJ proteins shows a poor overlap with other NMJ proteomics datasets

The function of motor neurons and their innervation to the skeletal muscle within the NMJ has been extensively investigated using immunostaining and genetic gain and loss of function experiments. Using our spatial proteomics approach based on thin cryotome sections, we identified 200 NMJ proteins, with 176 showing one significant maximum at the NMJ and the other 24 proteins at the NMJ and MTJ (**Figure 24F**).

So far most studies have manually dissected the NMJ to investigate the molecular composition of this structure in human and mouse diaphragm.[318] While our dataset identified only MPZ and NEFH as species-overlapping NMJ proteins, other proteins such as NEFL, NEFH, SNCG, and peripherin (PRPH, also known as NEF4) were found in our and Jones et al. published mouse datasets (**Figure 42**). Peripherin, together with other NEF proteins, forms a filamentous network to stabilize neurons and was already identified as a neuronal NMJ component.

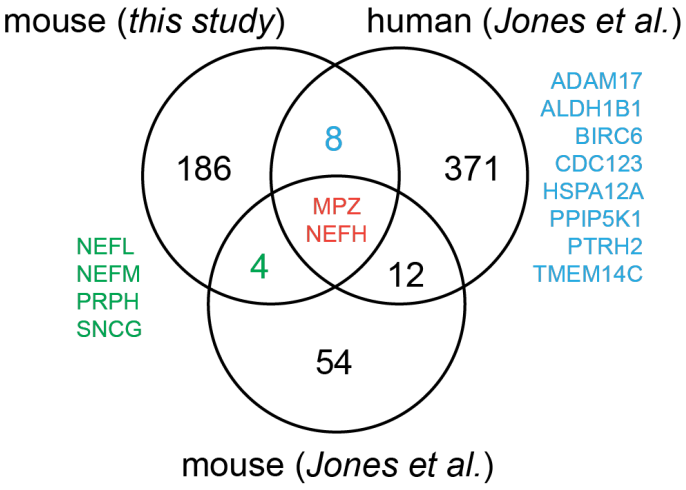

Figure 42 Poor overlap with NMJ proteins identified with proteomics. Venn Diagram of identified NMJ proteins compared to a human and mouse proteomics study of the NMJ. ADAM17, ADAM metallopeptidase domain 17; ALDH1B1, aldehyde dehydrogenase 1 family member B1; BIRC6, baculoviral IAP repeat containing 6; CDC123, cell division cycle 123; HSPA12A, heat shock protein family A member 12A; NEF, neurofilament; PPIP5k1, diphosphoinositol pentakisphosphate kinase 1; PRPH, Peripherin; PTRH2, peptidyl-tRNA hydrolase 2; SNCG, synuclein gamma; TMEM14C, transmembrane protein 14C.

An intriguing candidate identified which was identified in a human study and presented in our mouse study is the ADAM metallopeptidase domain 17 (ADAM17), also known as TNF-α converting enzyme (TACE). This transmembrane enzyme cleaves cell surface proteins,

including Notch receptors, which leads to the activated notch intracellular domain (NICD).[319] Notch signaling plays a crucial role in stem cells and has also been shown to be active in synaptic plasticity in Drosophila and the worm C. elegans.[320, 321] In the worm, the LIN-12-Notch receptor pathway activates the expression of proteins that stimulate muscle arm formation, guidance of neurons at the NMJ, and regulates synaptic function via GABA signaling.[321, 322] An increased abundance of the Notch receptor cleavage protein ADAM17 might suggest a similar mechanism in the mouse NMJ. Another substrate of ADAM17 is neuregulin-1 (NRG1), a protein involved in the development and maintenance of the NMJ.[323] ADAM17 cleaved NRG1 at several positions and is crucial for myelin formation. Myelin is required for the correct transmission of electrical impulses along axons and the genetic ablation of ADAM17 leads to increased levels of myelin on axons and Schwann cells.[324] It has been demonstrated that ADAM17 ensures the correct timing and myelination levels of axons in the PNS.[325]

The local maximum of ADAM17 reflects the presence of neuronal and Schwan cells at the NMJ. Motor neurons are wrapped with Schwan cells and myelin and the enhanced expression of ADAM17 might indicate its function to myelin maintenance. The therapeutic potential of ADAM17 was shown by the development of several small molecules that modulate the activity of ADAM17 and have already been tested in clinical trials for rheumatoid arthritis. Thus, modulating ADAM17 activity at the NMJ may be a useful approach to promote myelination in dysmyelinating peripheral neuropathies.

3.3.2. Identification of the origin of the NMJ proteins

While high-resolution protein profiles can be generated from the NMJ, determining the cellular origin of these proteins remains challenging. To address this, we performed analyses on isolated single muscle fibers and sciatic nerve tissue, using the latter as a representative neuronal source. We identified 200 proteins from the NMJ and compared these to the proteins detected in muscle fibers and sciatic nerve. Our tissue-specific analysis revealed that 32 of these proteins were expressed in both muscle and nerve, while five proteins were uniquely expressed in muscle, and 107 proteins were exclusively found in nerve cells (**Figure 24**). Three of the skeletal muscle specific NMJ proteins are the mitochondrially encoded ATP synthase membrane subunit 8 (MTATP8), transmembrane protein 14C (TMEM14C), and C8orf82 (**Figure S14D**).

Also, yip1 interacting factor homolog B (YIF1B) was exclusively detected in single muscle fibers with a maximum at the NMJ. YIF1B has been previously associated with trafficking between the endoplasmic reticulum (ER) and the cell membrane, and mutations in this gene have been linked to myelination defects. This suggests that YIF1B may play a critical role at the NMJ, particularly in maintaining intracellular protein transport at the motor endplate.[193]
A recent study described the NMJ in hindlimb muscles using single-nucleus RNA sequencing (snRNAseq) and identified several new genes to be localized at the NMJ. To identify the cellular origin of the identified transcripts, they used various animal models, including neuronal denervation, treatment with botulinum toxin (BoTX) and a genetic MuSK knockout mouse model. Overall, the study showed 472 genes to be expressed in the NMJ.[326]
A future comparison of these mRNA studies with our spatial proteomics data could further clarify from which cell types the detected proteins originate.

3.4. Distance based network analysis improves the interpretation of generated expression profiles

3.4.1. High betweenness centrality score of identified MTJ proteins identifies prospective MTJ candidates

Generated protein profiles in spatial proteomics studies served as input for delay network analysis, a bioinformatic methodology that operates without prior knowledge of established tissue relationships. Consequently, it is essential to comprehensively investigate all relationships between proteins to ensure robust and complete results. Delay-based analysis aims to determine whether two proteins are associated across spatial organization, whereas time-based analysis suggests that proteins separated by temporal units may exhibit co-regulatory, reciprocal, or functional interdependencies.[140] Spatial associations, however, indicate more pronounced functional reliance, as the physical proximity of proteins within a specific tissue or cellular environment often reflects direct interactions or coordinated roles in biological processes. When proteins are spatially co-localized, they are more likely to participate in the same molecular pathways, form complexes, or engage in sequential biochemical reactions. This spatial proximity can indicate that these proteins rely on one another for stability, activation, or function, highlighting the importance of their co-existence in maintaining cellular structure or function.

The mechanisms underlying the spatial co-expression of proteins are complex and can be based on a variety of factors, such as metabolic pathways, cellular compartments, and protein signaling pathways. Therefore, it is mandatory to narrow down the spatial distance within which two proteins can be associated, as the likelihood of direct effects diminishes with increasing distance. Proteins in close spatial proximity are more likely to share common features requiring their expression profiles to align for specific functions. For example, collagen 1a1 (COL1A1) was used as a starting point to identify neighboring proteins in the network. Proteins such as biglycan (BGN), CILP2, thrombospondin-4 (THBS4), and elastin were predicted to be direct or indirect interaction partners of COL1A1. However, disentangling these complex factors, including potential co-regulation through environmental stimuli, remains challenging using our proteomic approach alone. Co-immunoprecipitation is, for example, a complementary approach to verify the interaction between proteins.

Parameters such as betweenness and connectivity scores, clustering coefficient, and path length are helpful in interpreting these networks. Our network analysis revealed significantly higher betweenness centrality at the MTJ compared to other skeletal muscle or tendon sections, suggesting more cellular connections at the junction between muscle fiber tips and matrix proteins than within centrally located muscle fibers (**Figure 15**). Betweenness centrality is often used to identify nodes in a network that serve as bridges between different parts of the graph. Proteins within the MTJ with increased betweenness centrality indicate a greater likelihood of traversing from a muscle protein to a tendon protein through the MTJ, supporting our understanding of MTJ biology and reinforcing the biological insights gathered by our bioinformatic approach.

From a biological significance perspective, such analyses enable the detection of pivotal MTJ proteins with high centrality scores, indicating their crucial role in bridging adjacent tissues. These findings provide a hierarchical ranking of prospective targets for further studies. For example, GLI pathogenesis related 2 (GLIPR2) is one of the proteins with the highest betweenness centrality score (>17, with a median of ~0.7). Further investigation revealed GLIPR2 as a downstream target of the lysine methyltransferase SMYD2, which methylates chaperones outside the nucleus and interacts with myosin heavy chains and titin.[133] Both GLIPR2 and SMYD2 were identified with a maximum at the MTJ and are related to protein secretion and fibrosis in lung and kidney tissues.[327] Whether the increased expression of

SMYD2 and its downstream target GLIPR2 at the MTJ also contributes to the stability of the protein by methylating chaperones and/or sarcomere-associated proteins remains unclear and requires future investigation.

3.4.2. Network analysis to identify possible structural changes in the NMJ of the diaphragm in different animal models

To further determine if network analysis can effectively identify structural changes between different animal models, we compared the NMJ network of the diaphragm from young and aged mice. Although all skeletal muscles are innervated by motor neurons, in most muscles in the leg or arm the NMJs are distributed throughout the entire muscle. The diaphragm is an exception. Here, the NMJ is arranged in a circle and the NMJ structures are localized on a line (**Figure S16**). The overall network of nodes and edges remained consistent, confirming reproducibility across the same tissues in different animal models.

When calculating different parameters, such as path length, neighborhood connectivity, and clustering coefficient, for the extracted NMJ proteins in young and aged mice, we observed a loss of interconnectivity, particularly among proteins like tetraspanin-29 (CD9), syntaxin-binding protein 1 (STXBP1), and the glucose transporter GLUT1 (SLC2A1), which are involved in trafficking and binding of vesicles. Other proteins, such as the myelin proteins MAG, MPZ, and neurofilament isoforms (NEF), did not show significant changes in connectivity. Disruption of the control of vesicle transport and trafficking is associated with neurodegeneration and disease.[328] Similar endothelial cells in brain of aged mice show a dysregulation of vesicle transport and several genes associated to endocytosis, exocytosis, and vesicle mediated transport were changed. For example, key proteins with an altered expression were clathrin, dynamin, and small G-proteins of the Rab family which are involved in fusion of vesicles, cellular communication, and nutrient support. In our studies we identified significantly changed expression protein profiles for clathrin interactor 1, dynamin-2, and eleven of the small G-proteins of the Rab family (**Table S10**, Overlap_Aging_TDP43). This can potentially affect the delivery of nutrients and the removal of protein aggregates as well as influence the integrity of the neuronal cells.[329] This indicates that the unbiased network analysis supports the identification of proteins which are most affected and potentially involved in structural changes.

In a follow-up study, we used an ALS model based on the overexpression of the TAR binding protein TDP43. In this model, the overexpression of human TDP43 lacking the nuclear

localization sequence (NLS) is induced through doxycycline administration. At later stages, this overexpression led to NMJ disruption and death of the animals. Initially, mitochondria-related protein synthesis is affected and contributes to local energy deficiencies that ultimately drive NMJ degeneration.[84] Notably, at early stages of induction (four weeks), no obvious morphological of the skeletal muscle architecture was detectable. However, protein expression profiles revealed significant alterations in 50% of NMJ proteins compared to control mice. Key affected proteins included MAG, MBP, and NEFs. TDP43 itself was also detected at the NMJ with increased abundance, displaying a biphasic expression pattern. The expression profiles of ChAT and MAG shifted to a biphasic profile similar to the TDP43 profile. In contrast wild-type controls show single-peak TDP43, ChAT and MAG at the NMJ. Given the significant changes in the protein expression profiles of TDP43 and NMJ proteins, we performed a network analysis of the generated profiles. Network analysis of TDP43-overexpressed animals showed a significant increase in connection partners compared to healthy control animals. In addition, the new interaction partners indicate an increased stress response and neutrophil degranulation. It is suggested that neutrophils may contribute to the disease progression of ALS specifically at the NMJ. Their increased presence could worsen NMJ degeneration, either by direct interactions with motor neurons or by influencing the local inflammatory environment.[330] Notably, the mRNA-binding proteins PA2G4 and EIF4A1 were directly spatially connected to TDP43 in the ALS model.

PA2G4, also known as ErbB3 binding protein 1 (Ebp1), plays several roles in neurons. For example, it serves as a substrate for the E3 ubiquitin ligase PARKIN, which is one of the main drivers for mitophagy, a mechanism to degrade damaged mitochondria. This process is crucial for protecting neurons by maintaining a healthy mitochondrial population and preventing the accumulation of reactive oxygen species (ROS), which can lead to neuronal damage and disease progression. In ALS, mitophagy is often impaired, leading to the accumulation of damaged mitochondria and promoting neurodegeneration.[251, 331]

Increased levels of PA2G4 in the ALS model suggest a still functioning mitophagy pathway. However, this may also indicate an accumulation of damaged mitochondria, which the cell attempts to manage through elevated PA2G4 levels. PA2G4 role in modulating translation initiation through the inhibition of eIF2α phosphorylation is also significant. In ALS, the formation of protein aggregates, often triggered by the phosphorylation of eIF2α, disrupts the translational process. The phosphorylation of eIF2α is a critical control point in the stress

response. In ALS, phosphorylation of eIF2α reduces general protein synthesis but allows the translation of specific stress response proteins.[147] Chronic phosphorylation, however, can lead to detrimental effects, including impaired protein synthesis and increased formation of stress granules, which are associated with neurodegeneration. Therefore, the increased abundance of PA2G4, associated with translational inhibition, presents a complex picture that requires further investigation.[332]

Similarly, EIF4A1 is another mRNA-binding protein that was found to be directly connected to TDP43 in the ALS model. EIF4A1 plays a role in translation initiation and is known to be involved in the formation of stress granules, which are linked to the cellular response to stress. In ALS, the dysregulation of proteins like EIF4A1 contributes to the pathology through impaired RNA metabolism and protein aggregation.[147]

The interplay between PA2G4, EIF4A1, and eIF2α phosphorylation highlights the complex regulatory networks involved in ALS. The increased abundance and altered localization of PA2G4 suggests a potential compensatory mechanism in response to mitochondrial dysfunction and stress. Understanding these mechanisms could lead to new therapeutic targets that enhance mitophagy or modulate the stress response to protect neurons.

Our spatial analysis using thin cryosections has proven to be a valuable tool for tracking protein profiles across muscle tissue and conducting unbiased network analyses. This technique can identify cell marker proteins, enabling the localization of different cell types within tissues and helping to characterize transition states and junctions. It is effective not only as a repository of protein expression profiles but also for comparing animal models, such as aging and early stages of ALS. This will facilitate future studies investigating the localization of newly identified connected proteins and therapeutic targets. Further experiments, particularly those involving phosphorylated peptide analysis, are necessary to elucidate the precise role of PA2G4 in ALS progression.

3.5. HFD induces in muscle metabolic adaptations

A short-term high-fat diet for several weeks leads to weight gain and reduced insulin sensitivity due to impaired glucose transport. In addition, a high-fat diet leads to an accumulation of lipids in skeletal muscle cells, which results in increased oxidative stress. Here we observed that feeding mice a HFD for 16 weeks led to significant protein changes in both intact muscle and isolated single muscle fibers. These changes included increased activity in metabolic pathways related to lipid processing, fatty acid metabolism, and

mitochondrial function. A detailed analysis revealed a decrease in MYH7 expression in type I fibers, with a notable loss of these fibers. Type IIa fibers, however, showed a more pronounced response to the HFD, particularly in metabolic pathways.

Several candidate proteins, including BNIP1 and MTFP1, exhibited differential regulation between type I and type IIa fibers. IHC substantiates and visualizes an increase in MTFP1 expression in type IIa fibers, suggesting potential imbalances in mitochondrial fission and fusion processes. Moreover, the mitochondrial outer membrane marker TOM20 showed changes in mitochondrial distribution specifically in type IIa fibers.

3.5.1. Fiber type shift as protection against negative impacts of HFD

Obesity, along with aging and prolonged inactivity, affects muscle fiber composition. While aging and bed rest often shift muscle composition towards slow fibers[93], obesity leads to a loss of type I fibers[241] and an increase in type IIa and mixed type I/IIa fibers (**Figure 31F**). Early research highlighted the critical role of nerve innervation in muscle fiber type switching.[333]

Type I and type II muscle fibers differ significantly in their function and metabolic properties. Type I fibers are highly efficient in energy utilization, relying predominantly on oxidative metabolism to support sustained, endurance-based activities, which makes them more resistant to fatigue and better suited for long-duration, low-intensity tasks. In contrast, type II fibers are adapted for short, powerful bursts of activity, relying less on oxidative metabolism and more on glycolytic pathways, leading to quicker ATP consumption and a higher susceptibility to fatigue.[21] The susceptibility of these fiber types to atrophy and metabolic changes is linked to different signaling pathways. For example, PGC1α helps protect type I fibers from atrophy by enhancing their oxidative capacity, while the TGFβ family and nuclear factor kappaB (NF-κB) primarily impact fast fibers, making them more vulnerable to degradation. While aging and obesity share some similarities in how they affect skeletal muscle health, a notable difference is seen in aged individuals, where there is a pronounced shift from fast to slow fibers. This shift is closely associated with changes in motor unit composition and neuromuscular activity, as motor neurons die during aging and reinnervation occurs, which increases the number of type I fibers.[334]

The effects of obesity on the composition of muscle fibers are still not fully understood, and previous studies contradict each other. It remains unclear whether the changes in muscle fiber

distribution seen in obese humans and mice are a direct consequence of obesity or if the loss of type I fiber contribute to its development.[94] Some evidence suggests that high-fat diets can decrease the synthesis of the MYH7 isoform, but not affect the expression of MYH2. This could lead to a reduction in the oxidative capacity of skeletal muscles, potentially contributing to weight gain and other obesity-related metabolic changes.[242] Additionally, high-fat diets impair sensory and motor nerve function, damaging both myelinated and small sensory nerve fibers.[244] Which could lead to a shift towards slow fiber types.[243]. However, why we and other studies see fewer type I fibers in obesity remains to be elucidated.

Interestingly, some human studies suggest that genetic predisposition plays a significant role in determining muscle fiber composition even before birth. In these cases, a reduced proportion of type I fibers could be a contributing factor to obesity, rather than a consequence.[94]

We hypothesize that in obesity, excess caloric intake and lipid accumulation negatively affect the oxidative capacity of type I fibers, promoting a shift towards type II fibers. This shift could reduce overall muscle endurance and efficiency, further exacerbating metabolic imbalances.

In our study, the administration of a high fat diet induces significant metabolic adaptations in type IIa muscle fibers, particularly affecting long-chain fatty acid metabolism, cellular lipid metabolism, and fatty acid beta-oxidation. Similar changes are observed to a lesser extent in type I fibers, except in long-chain fatty acid metabolism, where no significant alterations are detected. These adaptations suggest that type IIa fibers are more sensitive to HFD-induced metabolic stress and might represent a compensatory mechanism to handle excess fat. However, these changes can lead to increased ROS production, contributing to metabolic stress and inflammation. Additionally, type IIa fibers lose their specificity, as evidenced by a decline in MYH2 expression, which could potentially affect the ATP consumption and muscle activity (**Figure 31E**).

Interestingly, mixed type I/IIa fibers exhibit a more robust metabolic response to HFD indicated by less dominant changes in the fatty acid related GO-terms than pure type I or type IIa fibers (**Figure S25**), suggesting that mixed fibers might offer some protection against the negative impacts of a HFD. Mixed fibers function as intermediates during the fiber-type switches associated with skeletal muscle development, adaptation to exercise, and aging. They achieve a greater range of contractile functions and fiber phenotypes. Notably, in this study we observed shifts in MYH expression in type I and type IIa fibers after HFD but did

not see changes in other proteins related to their metabolic capacity. To accurately classify fiber types, 50 additional marker proteins were used, allowing for the separation of mixed fibers from pure fibers. In future, these 52 markers should be used to categorize fiber types to separate fiber type shifts and decrease of MYH.[335]

3.5.2. Changes in mitochondrial dynamics induced by an increase of MTFP1 after HFD

Several mitochondrial proteins are changed with an increased abundance only in type IIa fibers after HFD, for example hyaluronan synthase 2 (HAS2), BNIP1, SIRT5, and MTFP1. BNIP1 is involved in regulating mitochondrial homeostasis via mitochondrial fission and mitochondrial autophagic degradation. MTFP1 inhibits mitochondrial fusion to isolate altered IMM subdomains and serves as a quality control to maintain mitochondrial DNA levels.[235] Similar to BNIP1, MTFP1-rich fragmented mitochondria interact with LC3 and p62 to promote autophagic degradation.[235] Using TOM20 immunostaining, changes in mitochondrial distribution were observed (**Figure 33B**, **F**). In contrast, no change in the abundance of other fusion and fission factors such as FIS1, MFN2, DRP1 and OPA1 could be observed. Other studies suggest MTFP1 maintains IMM integrity and regulates the activity of OXPHOS complexes. Increased MTFP1 abundance may lead to a general increase in OXPHOS-related proteins in type IIa fibers after HFD, enhancing the capacity for fatty acid oxidation. Additionally, an increase in mitochondria can be observed in the type IIa fibers which also corresponds to the increased SIRT5 abundance (**Figure 32D**). If an increase of MTFP1 and OXPHOS complexes leads now to more mitochondria or if there are more mitochondria and consequently more MTFP1 and OXPHOS is unclear and should be further investigated.

Another mitochondrial protein with increased abundance in response to HFD was the is the NAD-dependent protein deacetylase SIRT5, which can influence mitochondrial dynamic by post-translational modify other mitochondrial proteins and regulates their activity. Overexpression of SIRT5 is associated to an increase of MFN2 and OPA1 both regulating the mitochondrial morphology, fusion and fission processes, and mitophagy.[250]

However, enhanced complex I activity can lead to increased ROS production. In obese mice, who already experience higher oxidative stress, this can exacerbate oxidative damage, contributing to muscle inflammation, insulin resistance, and further metabolic dysregulation.

Understanding the differential impact of obesity on muscle fiber composition is crucial for developing targeted interventions, like early diet control, weight reduction, and exercise, to maintain muscle health and metabolic function.

3.6. Mechanisms of muscle preservation in hibernating bears

While we observed an expected fiber type shift to a decrease of type I fibers in mice after HFD, other muscle wasting conditions like bed rest normally come along with a decrease of fast fibers. Even short periods of inactivity can lead to rapid muscle deterioration in humans, contributing to increased frailty and decreased physical function. Understanding the underlying mechanisms of muscle preservation in states of disuse can provide insights into preventing and managing sarcopenia.[260] Despite the absence of major changes in muscle fiber size, function, and fiber type (**Figure 34** and **Figure 36B**), hibernating bears experience a reduction in muscle strength and contractile kinetics, albeit to a lesser extent than expected given the prolonged inactivity.[275] This reduction in force production is partly attributed to changes in the contractile apparatus of the muscle fibers (**Figure 34C**). Despite these changes, there is no significant increase in fiber cross-sectional area or damage to sarcomeres, suggesting that the observed dysfunction is due to alterations in the force-generating capacity of the contractile proteins.

Additionally, the bear can significantly minimize energy expenditure and conserves vital body functions. Central to this adaptation is the reduction in skeletal muscle myosin ATPase activity (**Figure 35A**). Myosin plays a crucial role in muscle contraction through its ATPase activity, which hydrolyzes ATP to produce energy. In hibernating bears, myosin ATPase activity in relaxed muscle fibers is significantly lower compared to the active summer months. This reduction in ATPase activity is linked to a slower rate of nucleotide exchange on the myosin heads, contributing to decreased energy consumption during hibernation (**Figure 35B**). Additionally, changes in kinase activity, particularly MYLK2, influence myosin regulation and ATPase activity, further supporting the reduced energy expenditure observed during hibernation (**Figure 38C**). A reduced oxidative stress level in hibernating bear muscle may contributes to the observed decrease in myosin ATPase activity and force production [262], indicating a complex interplay between metabolic adaptation and muscle preservation.

We suggest here a novel energy conservation mechanism involving prolonged time constants for nucleotide exchange on myosin heads, which stabilizes the muscle protein structure and

decreases ATP hydrolysis. In conditions of muscle wasting, such as bed rest-related sarcopenia, modulations in myosin ATPase activity may play a crucial role. The reduced ATPase activity observed in hibernating bears highlights the potential for targeting myosin regulation as a therapeutic approach to mitigate muscle loss in humans. By understanding the biochemical equilibrium of the thick filament and the role of myosin ATPase activity, new interventions can be developed to preserve muscle mass and function during periods of inactivity. Additionally, understanding the role of oxidative stress and antioxidant defenses in muscle preservation can inform the development of antioxidant therapies to protect muscle function.

Further research is needed to explore the specific molecular pathways involved in myosin ATPase regulation and proteomic remodeling during hibernation. Investigating the role of MYLK2 activity and calcium sensitivity in muscle preservation can provide deeper insights into the mechanisms underlying reduced energy expenditure. Additionally, studying the impact of temperature and other environmental factors on muscle function during hibernation can help refine our understanding of these processes.

3.7. Conclusion and outlook

In recent years, the role of muscles in overall body health has gained significant attention. Muscles are no longer seen as mere locomotor tissues; they are now recognized as crucial regulators for metabolic and inflammatory activities for the whole body. Consequently, advanced techniques for studying muscle biology have become increasingly important. Established methods often involve extracting individual cell populations for LC-MS/MS analysis, which allows for precise molecular profiling of different muscle cell types. However, this approach disrupts the ECM and removes cells from their native spatial context, making it difficult to draw conclusions about the spatial organization of proteins and cells within muscle tissue.

To address this limitation, we have developed a novel approach to muscle tissue analysis that preserves the spatial organization of the tissue. Generating thin cryosections prior to LC-MS/MS analysis enables spatial protein mapping across the longitudinal axis. This method allowed us to achieve new insights into the molecular architecture of key muscle structures, including the MTJ and NMJ. In particular, our work on the soleus and diaphragm muscles led to the discovery of several novel marker proteins for both transition areas. Moreover, we identified the critical role of the RAS in the muscle-tendon transition zone, a finding that has potential implications for therapeutic interventions, particularly since the RAS can be influenced by common blood pressure medications.

In addition to the MTJ, we applied this spatial proteomics approach to the NMJ, a critical site of communication between motor neurons and muscle fibers. We identified new marker proteins specific to the NMJ and were able to map their spatial distribution. This level of spatial detail is particularly valuable when studying age-related changes in muscle or neurodegenerative diseases such as ALS. By applying this method to aged mice and TDP43-dependent ALS mouse models, we uncovered spatial structural changes that would have been challenging to detect with tissue separation methods. These findings underscore the benefit of our slicing approach, which reveals detailed insights into the architecture of both the NMJ and MTJ that are essential for understanding muscle function and disease progression.

However, despite the advantages of thin cryosections and LC-MS analysis, limitations remain in achieving cellular resolution. Muscle tissue is highly heterogeneous, and precise analysis at the single-cell level is often required to capture the functional differences between various muscle fiber types. To address this, we also conducted single skeletal muscle fiber analysis. This is particularly important for understanding how metabolic diseases affect

muscle fibers with different metabolic profiles, such as the oxidative type I fibers versus the glycolytic type II fibers. Single-cell analysis requires processing a large number of samples, but it is crucial for detecting the distinct effects on different cell types that may be masked in whole-tissue analysis, which represents a complex mixture of cell types.

To enhance the analysis of individual cell populations, we have adopted the use of shorter chromatographic gradients, which increases throughput. In future, sample throughput of 500 samples per day (SPD) and a gradient time of 2.2 minutes, might enable us to analyze 1,000 fibers within two days. While this approach has so far been applied mainly to low-dynamic tissues like HeLa cell lysates or blood samples, it shows great promise for high-throughput applications in muscle fibers and cardiomyocytes, particularly when focusing on high-abundance proteins rather than full proteome coverage.

Looking ahead, reducing the dynamic range of muscle tissue remains a key challenge in deepening our understanding of the muscle proteome. One promising strategy involves leveraging the unique nano-bio interaction properties of magnetic nanoparticles. This technique has already shown success in plasma proteomics, where it enabled the identification of up to 2,000 proteins; compared to 300-500 with regular proteomics. The application of this technique to intact skeletal muscle tissue and single muscle fibers could greatly enhance our ability to detect low-abundance proteins. Another promising approach is to use StageTips for prefractionation, employing materials such as C18-silica, poly(styrene-divinylbenzene) copolymer (SDB), or ion exchange. With the sensitivity of modern mass spectrometers, which require less than 200 ng of peptide input, even a modest three-step fractionation could substantially reduce the dynamic range and increase identification of protein hits.

Another critical aspect of muscle research is the study of post-translational modifications (PTMs), particularly phosphorylation, which plays a central role in regulating muscle function and signaling pathways. Recent advancements have significantly reduced the required sample input for phosphoproteome analysis, with less than 30 µg now sufficient for deep insights. Even in single cells, more than 300 phosphosites can be identified without the need for enrichment methods. This advancement makes phosphoproteomics increasingly feasible for single muscle fiber studies, allowing for detailed investigations of cellular signaling events. Enriching phosphorylated peptides (5%) from single muscle fibers (approximately 1 µg of input) using magnetic beads with chelating ligands should provide a

sufficient amount of peptide input. Given that a single HeLa cell (~250 pg of protein) can yield 300 phosphosites without enrichment, analyzing the phosphoproteome of a single muscle fiber should be achievable with the latest highly ultra-sensitive mass spectrometers.

Future studies are expected to increasingly leverage spatial proteomics to study skeletal muscle tissue. Laser microdissection (LMD) is emerging as a powerful tool for isolating specific cells while preserving spatial context. This technique allows for the precise excision of areas as small as 5,000 μm^2 (with a slice thickness of 7 µm), corresponding to the volume of a single HeLa cell. Although isolating small muscle stem (MuSC) or immune cell populations, such as T cells or macrophages, remains challenging, LMD can successfully target areas enriched with these cell types, providing valuable insights into the cellular composition of tissues, spatial cell orientation, and potentially cell-to-cell communication. When combined with thin cryosections, LMD has the potential to generate 3D proteome models, offering an even more comprehensive understanding of muscle architecture and biology. This is particularly important for studying muscle diseases, where spatial organization and cell-cell interactions play a critical role in disease progression.

These advancements in spatial proteomics and single-cell analysis will pave the way for novel therapeutic strategies aimed at improving muscle function and combating muscle-wasting diseases such as sarcopenia, muscular dystrophy, and ALS. As spatial proteomics continues to evolve, it will enhance our ability to precisely map and understand the complex interplay of proteins within muscle tissues, ultimately leading to better health outcomes for individuals with muscle-related diseases.

4. Supplementary Material

4.1. List of supplementary figures

Figure S1

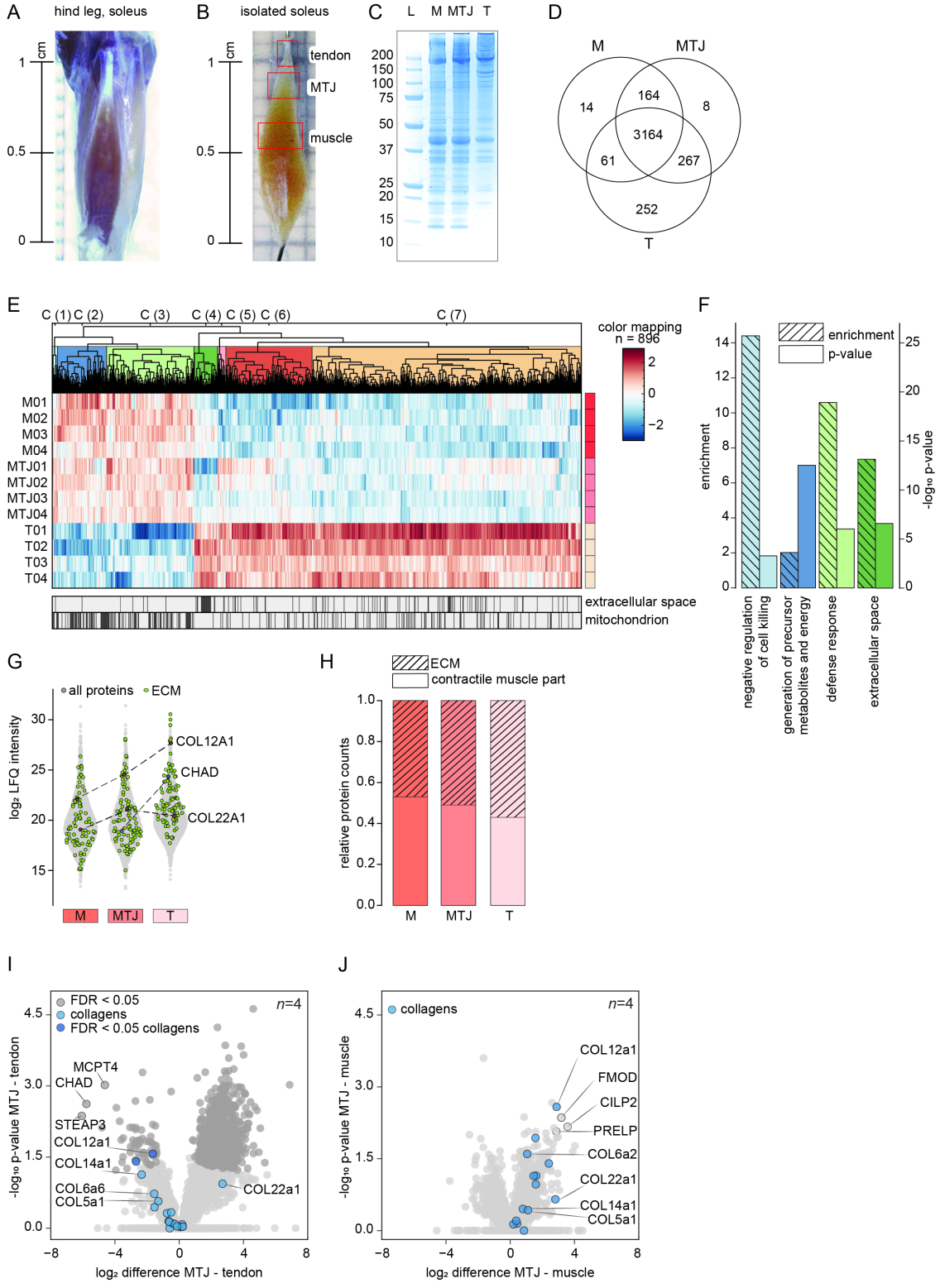

Figure S1 Proteomics analysis of manually dissected skeletal muscle areas of the soleus muscle. **A, B**) Position of the soleus muscle in the mouse hindleg and isolated soleus muscle. **C**) Coomassie stained SDS-PAGE of muscle, MTJ, and tendon samples. **D**) Venn diagram of proteins identified from muscle, MTJ, and tendon samples ($n = 4$). **E**) Hierarchical clustering of muscle, MTJ, and tendon samples. **F**) GO term enrichment analysis of cluster 1-3 and cluster 4-7. **G**) Intensity plots of all detected proteins (grey) and selected ECM proteins (green) identified in muscle, MTJ, and tendon areas. **H**) Relative protein counts of matrix and

contractile proteins in muscle, MTJ, and tendon samples. **I, J**) Volcano plots showing significantly regulated proteins (log_2 differences) between MTJ/tendon and MTJ/M. Proteins with FDR < 0.05 are marked in dark grey and blue. ECM: extracellular matrix, GO: gene ontology, M: muscle; MTJ: myotendinous junction; T: tendon, SDS-PAGE: Sodium Dodecyl Sulfate–PolyAcrylamide Gel Electrophoresis.

Figure S2

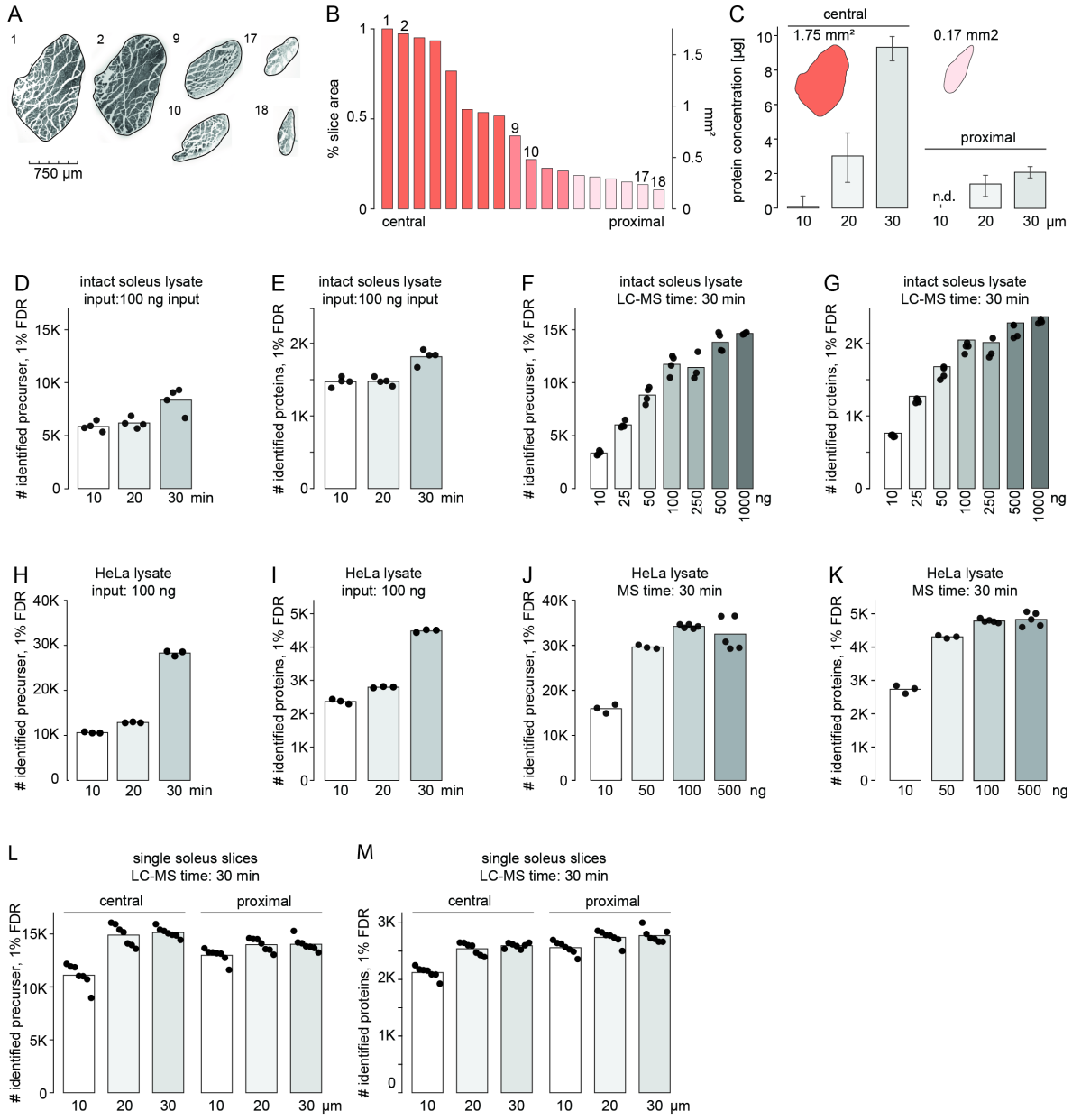

Figure S2 LC-MS method optimization. A) Hematoxylin and eosin-stained muscle sections of central muscle (1-2), MTJ (9-10), and tendon (17-18) areas. **B)** Surface area (in mm^2) of sections from the central and distal areas. **C)** Protein concentrations of single cryo-sections with thicknesses of 10–30 µm from central muscle and proximal tendon areas. **D, E)** Precursor and proteins identified in intact soleus muscle lysates using LC-MS gradients of 10–30 min; input protein concentration, 100 ng. **F, G)** Precursor and proteins identified in intact soleus muscle lysates ranging from 10–1000 ng input material using constant 30 min LC-MS gradients. **H, I**) Control HeLa cell lysates; precursor and proteins identified with 100 ng input material and 10–30 min LC-MS gradients. **J, K)** Precursor and proteins identified in 10–500 ng HeLa cell lysates using constant 30 min LC-MS gradients. **L, M)** Precursor and proteins identified in 10-30 µm sections of central soleus muscle slices and proximal soleus tendon slices using 30 min LC-MS gradients. LC-MS: liquid chromatography-mass spectrometry, MTJ: myotendinous junction.

Figure S3

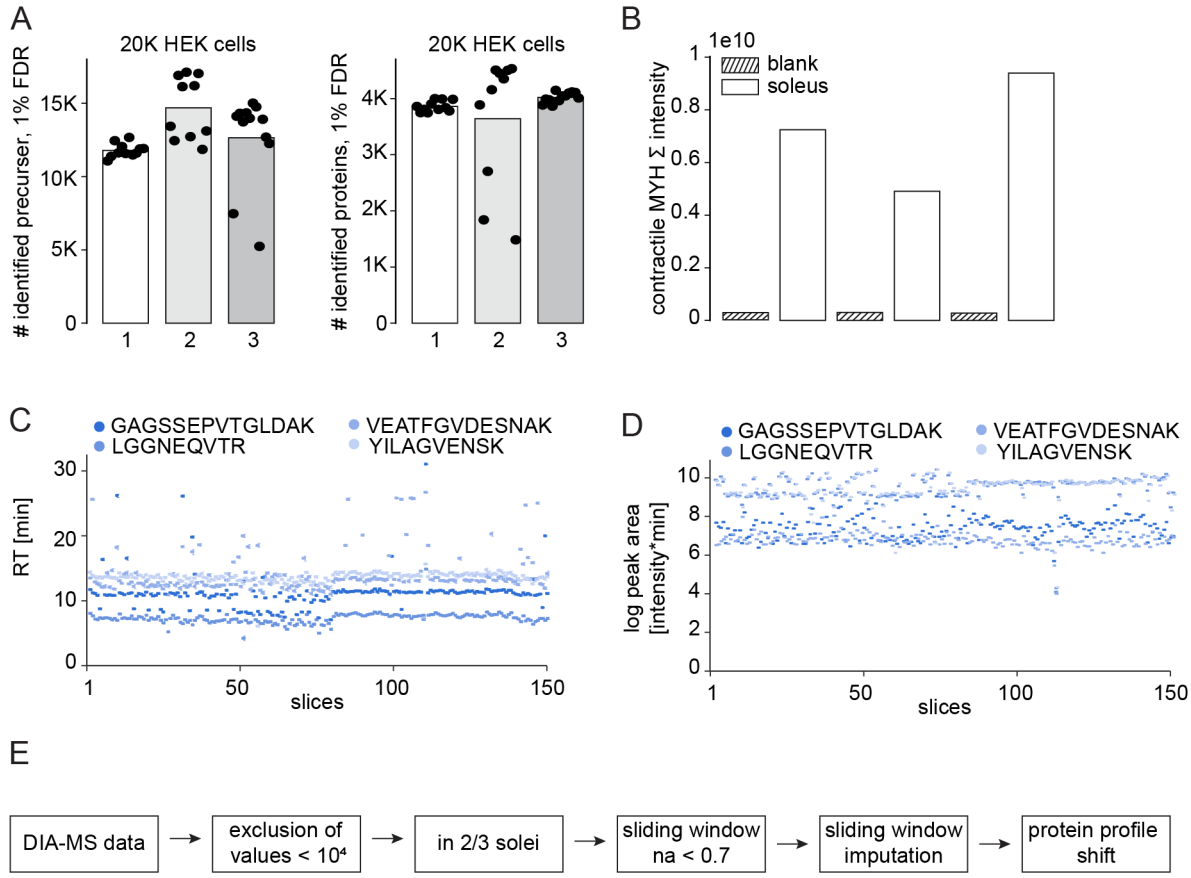

Figure S3 Quality control based on spike-in peptides and blank runs. **A**) Precursors and proteins identified in HEK cell lysates from ~20K cells. Samples were randomly measured during the soleus profiling experiments (Exp. 1-3). **B**) Sum intensities of contractile myosin heavy chain isoforms in central muscle slices and blank samples to control sample carryover. **C, D**) Retention times and peak areas for 4 of 11 indexed retention time peptides (iRT peptides). **E**) Summarized workflow for data filtering and analysis.

Figure S4

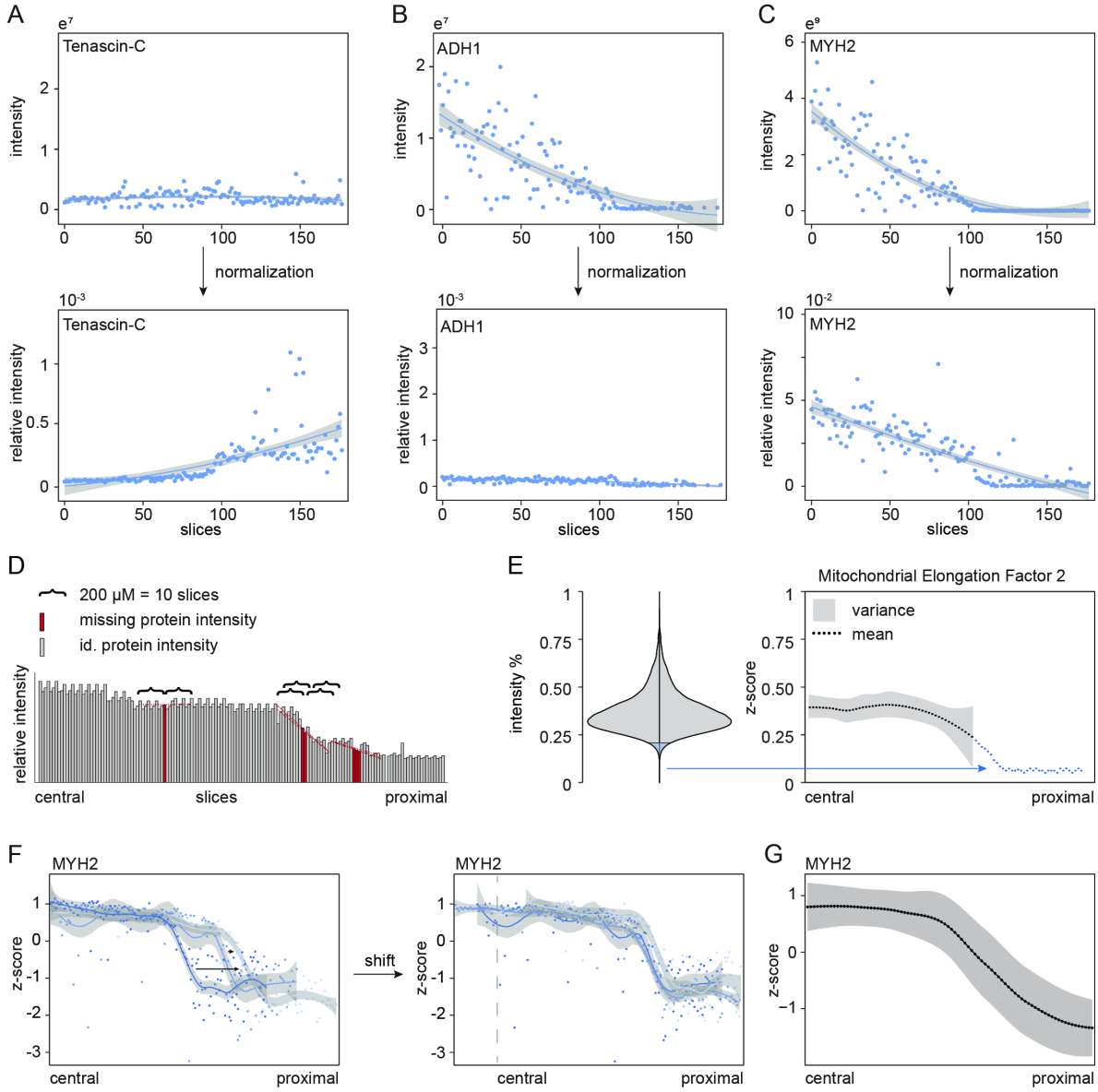

Figure S4 Bioinformatic analysis and protein normalization for generation of protein profiles. A-C) Examples of the normalization procedure; tenascin-C (TNC), alcohol-dehydrogenase 1 (ADH1), and myosin heavy chain 2 (MYH2). **D)** Linear data imputation using a sliding window approach. **E)** Missing values were replaced with random values by the mean of the lower 5% of the total expression values of all proteins. **F-G)** Protein profile of MYH2 and shifting the three independent replicates to achieve a congruent profile.

Figure S5

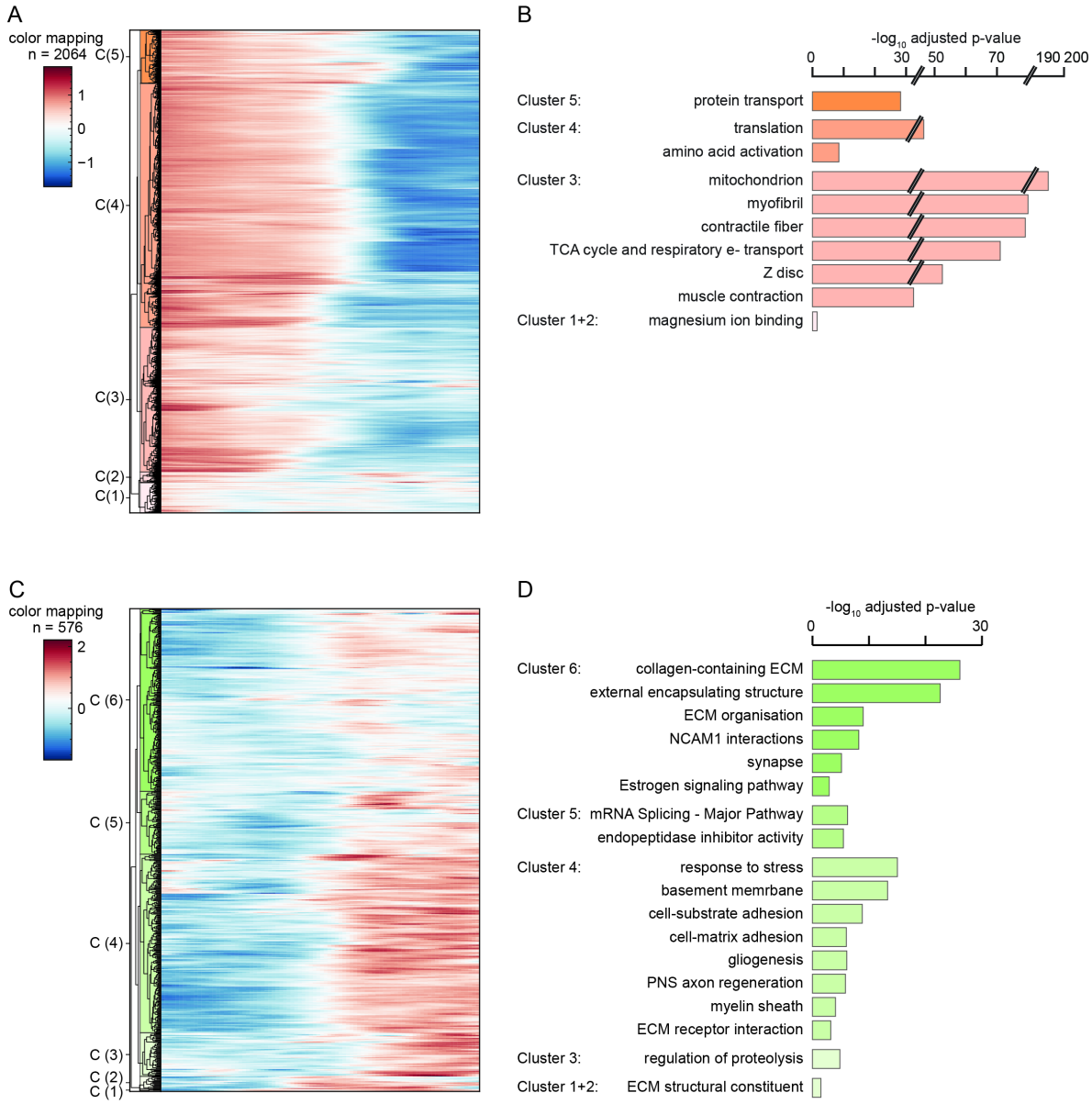

Figure S5 Hierarchical clustering of protein profiles. A) Hierarchical cluster analysis of descending and **C**) ascending protein profiles. **B, D**) Gene ontology term enrichment of different clusters with **B**) descending and **D**) ascending profiles along the longitudinal muscle-tendon axis.

Figure S6

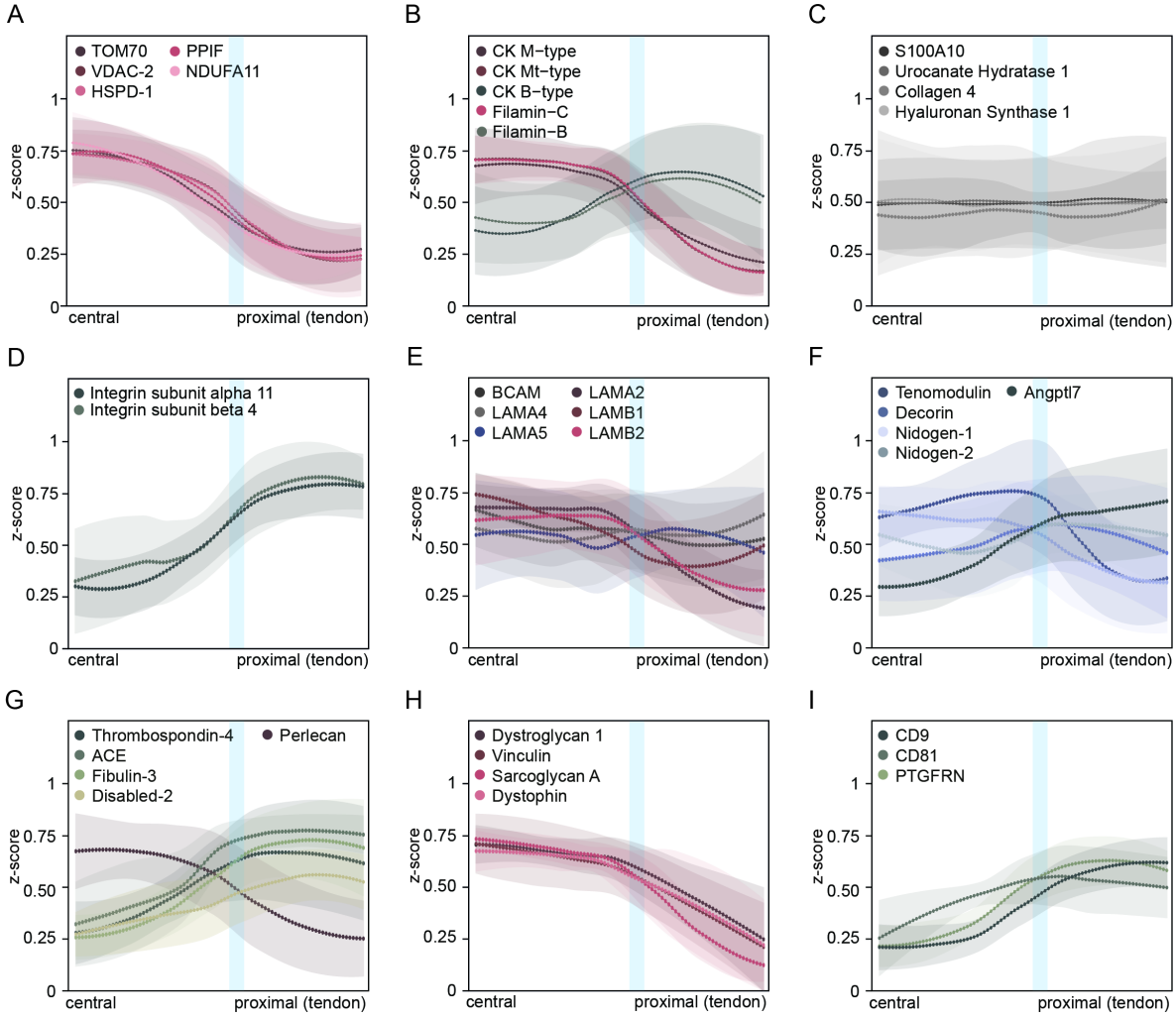

Figure S6 Expression profiles of skeletal muscle and matrix proteins of the soleus. **A**) Protein expression profiles of mitochondrial proteins. **B**) Profiles of creatine kinase (CK) isoforms and filamins. **C**) Selected profiles with a constant profile along the muscle-tendon axis. **D, E**) Selected members of the integrin family. **F**) Selected members of the laminin family and the basal cell adhesion molecule (BCAM). **G, H**) Additional protein profiles of selected matrix and secreted proteins. **I**) Selected protein profiles of the sarcoglycan complex.

Figure S7

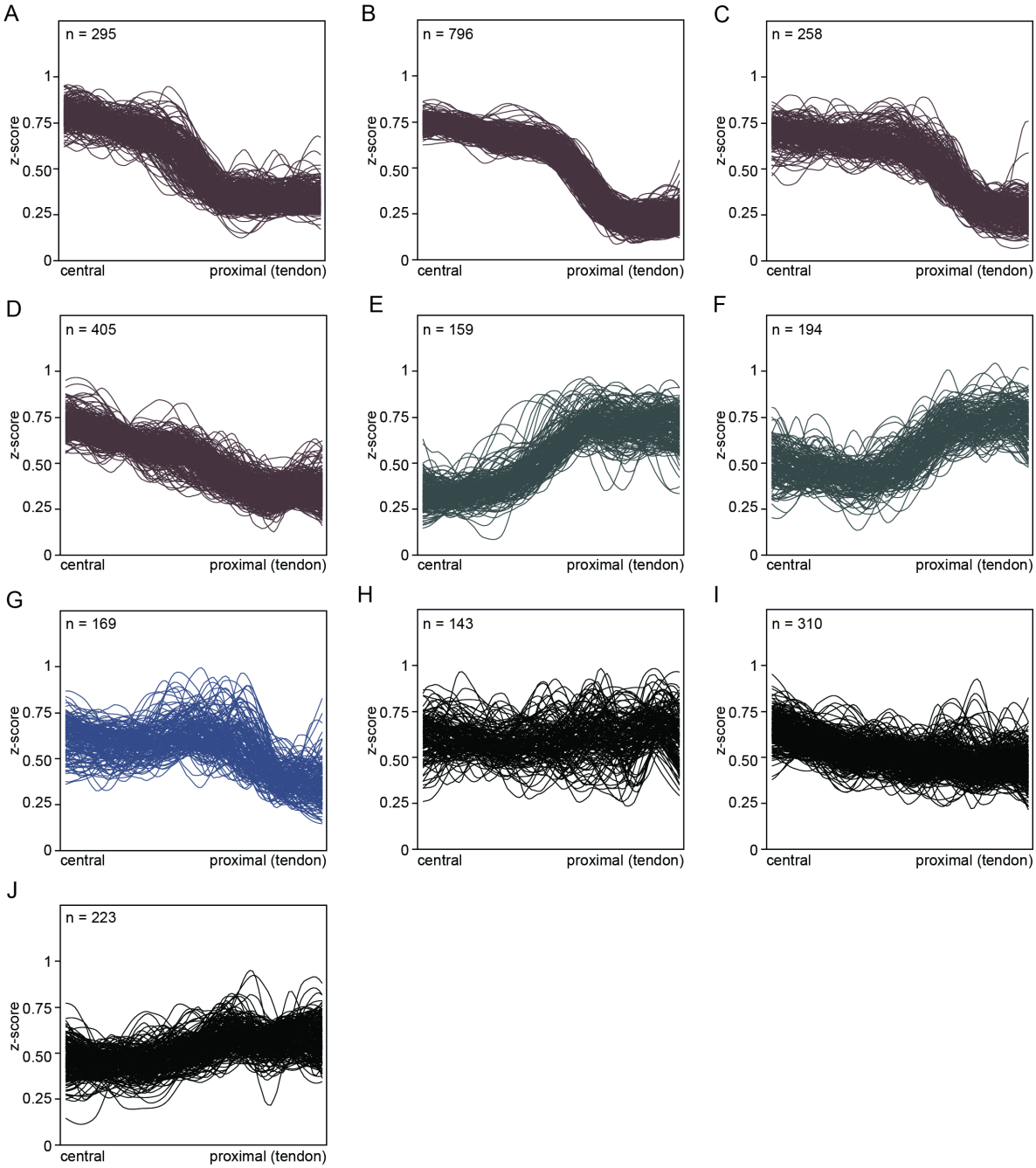

Figure S7 K-means analysis reveals 10 clusters with different ascending and descending profiles. A-D) Four clusters showing descending profiles. **E, F**) Two clusters with ascending profiles. **G**) Cluster showing a transient maximum in the center of the muscle-tendon axis. **H-J**) Three clusters with constant profiles from central to distal areas.

Figure S8

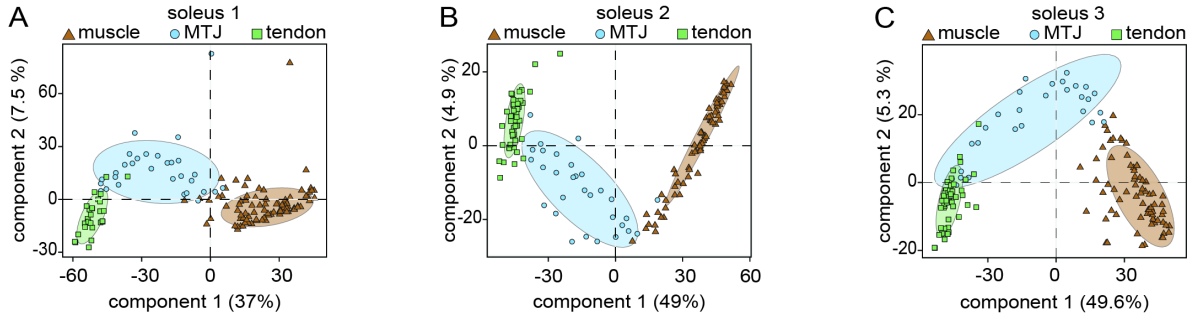

Figure S8 Principal component analysis of the three sliced soleus muscles show a clear separation of the muscle, MTJ, and tendon area. Principal component analysis of the sliced soleus muscle 1 (**A**), 2 (**B**), and 3 (**C**). Muscle slices are marked in brown, MTJ slices in blue and tendon slices in green.

Figure S9

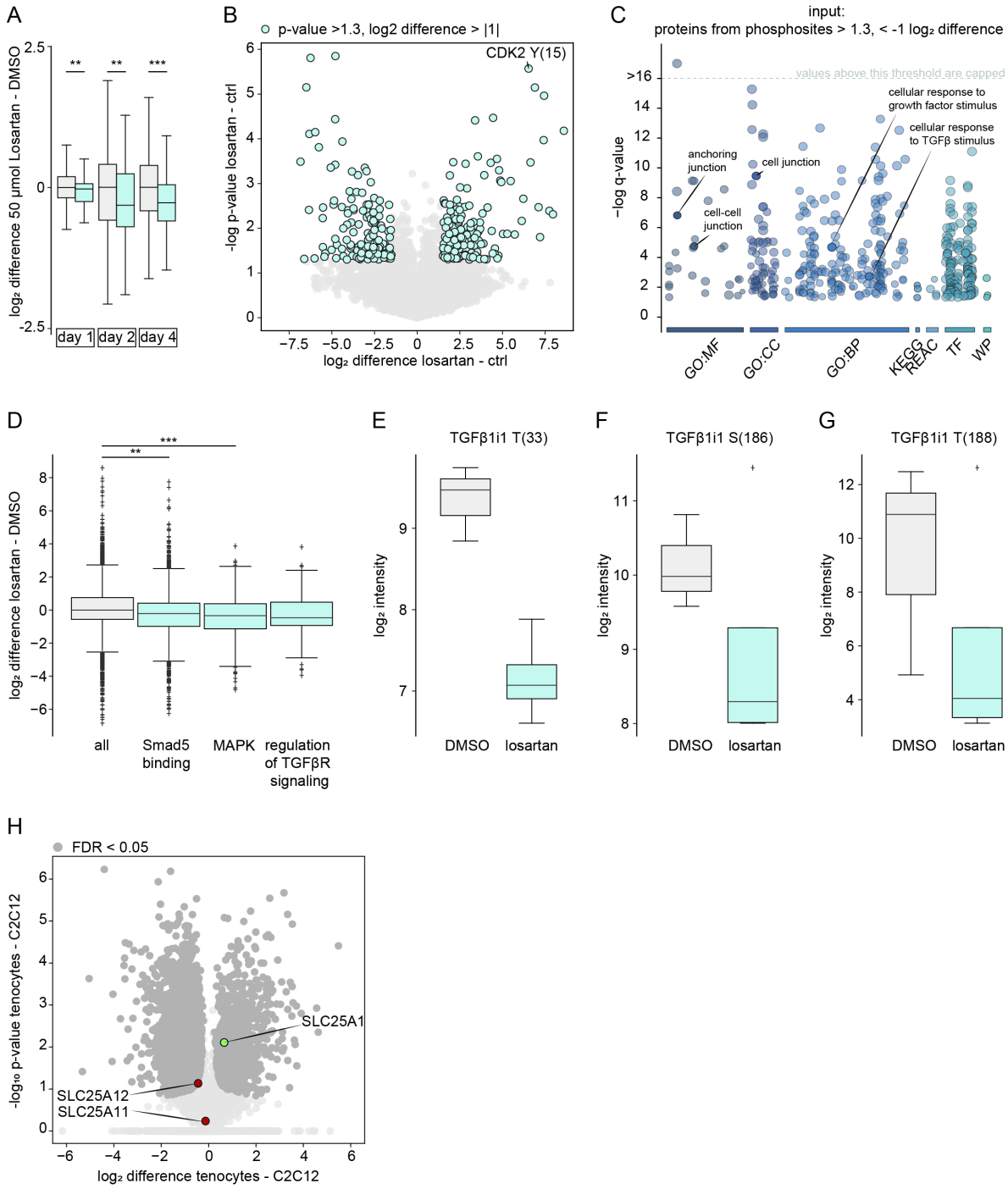

Figure S9 Tenocytes show higher expression of the SLC25A1 transporter. A) Tenocytes treated with 50 µm losartan over 1–4 days showed a decrease in proteins related to matrix formation. **B**) Volcano plot of Welch's t-test between tenocytes treated with 10 µm losartan over for 4h showed an increased phosphorylation on Cyclin D kinase 2 at pY15. **C**) GO-term enrichment of proteins with significantly downregulated phosphosites. **D**) Significantly decreased phosphorylation on proteins related to Smad5 binding, MAPK, and regulation of TGFβR signaling. **E-G**) Regulated phosphosites on TGFβ1i1. **H**) Volcano plot of Student's *t*-test between tenocytes and myoblasts showing significantly higher expression of the SLC25A1 transporter in tenocytes. DMSO, dimethyl sulfoxide; GO(:CC, :MF, :BP), gene ontology (:cell component, :metabolic factor, biological process); KEGG, kyoto encyclopedia of genes and genomes; MAPK, mitogen-activated protein kinase 2; REAC, reactome; SLC, solute carrier family; SMAD5, mothers against decapentaplegic homolog 5; TF, Transfac; TGFβ(R), transforming growth factor (receptor); WP, WikiPathway.

Figure S10

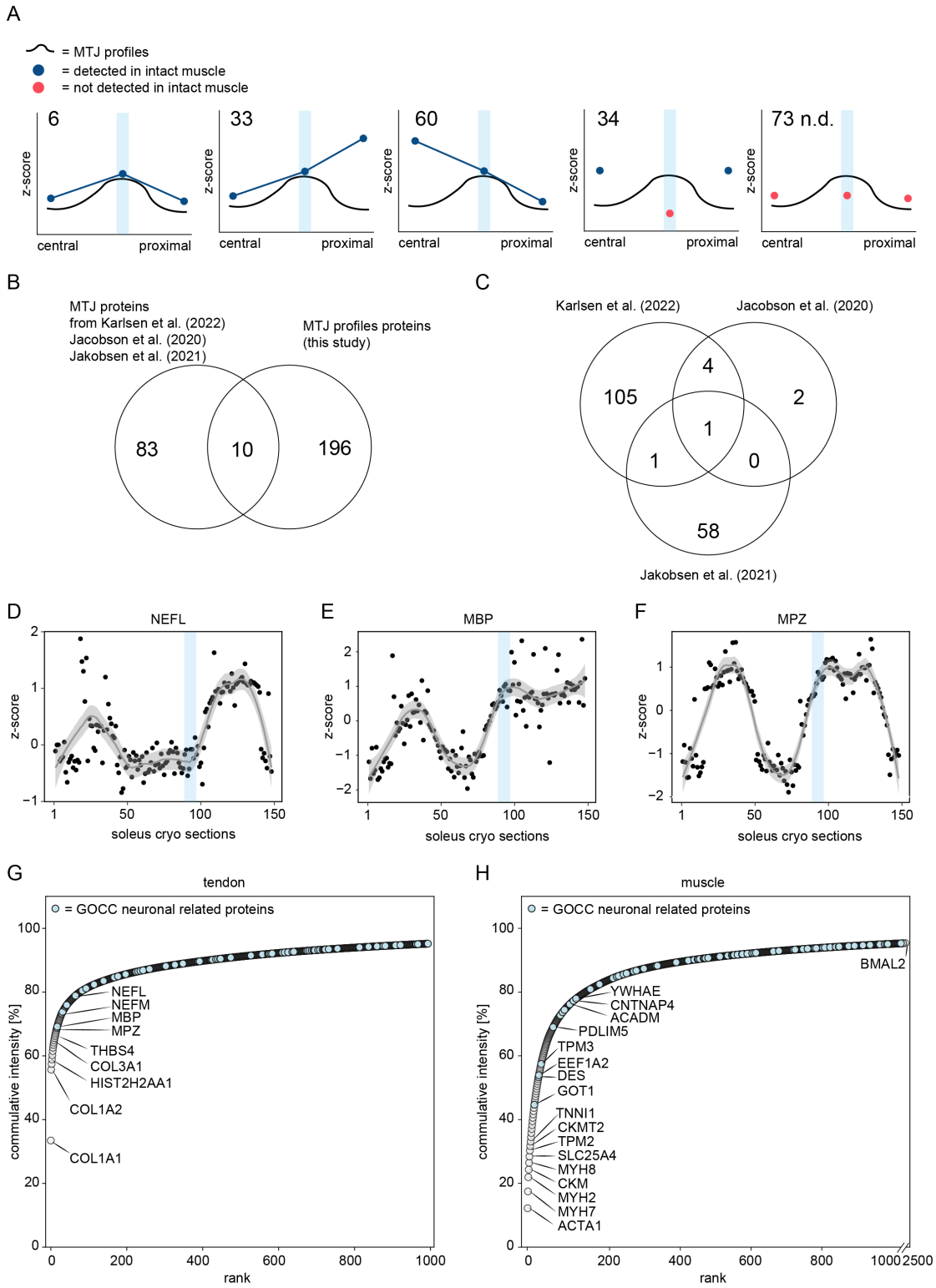

Figure S10 Protein ranking reveals the most abundant proteins in muscle and tendon areas. A) Comparison of enriched MTJ proteins based on the analysis of intact muscle samples and protein profiling. **B-C)** Ranking of protein abundance for the first 1000 proteins based on the average of 10 sections in the tendon (**B**) and muscle (**C**). **D-F)** Biphasic protein expression profile of the nuclear factors NEFL (**D**), MBP (**E**), and MPZ (**F**). **G)** Overlap of 10 MTJ proteins identified in three other studies and our study. **H)** Comparison of three independent studies from mouse, horse, and humans.

Figure S11

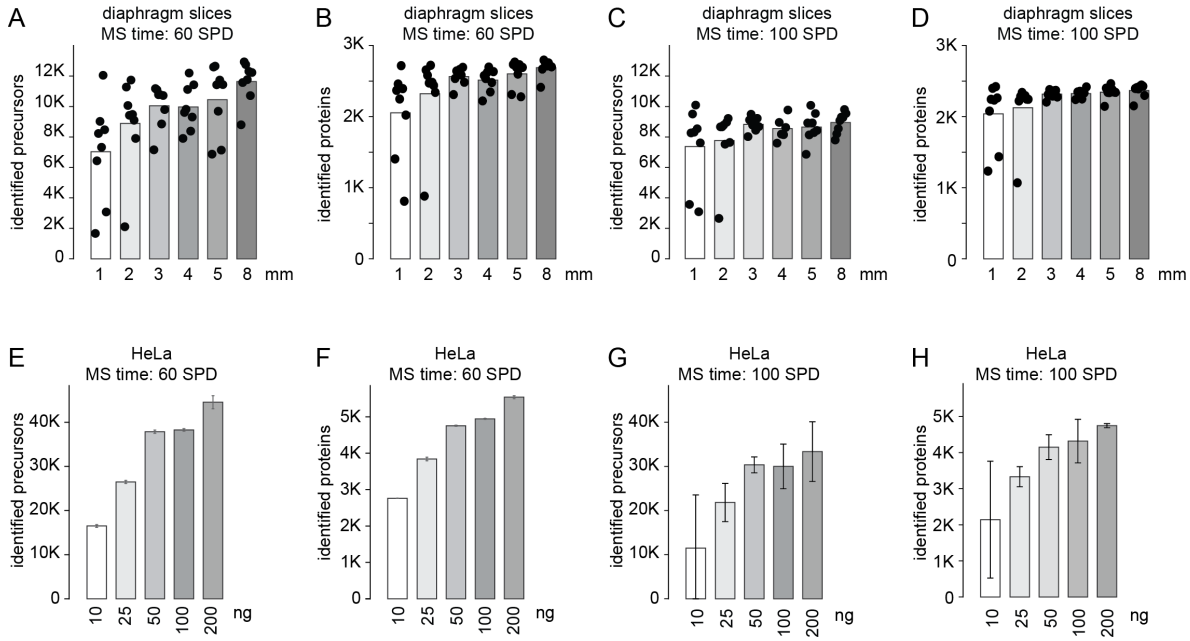

Figure S11 Input and gradient length optimization of diaphragm cryotome sections for LC-MS analysis. Identified precursors (**A, C, E, G**) and proteins (**B, D, F, H**) for diaphragm slices ranging 1-8 mm width and HeLa lysates ranging 10-200 ng using short LC-gradients of 60 and 100 SPD, respectively.

Figure S12

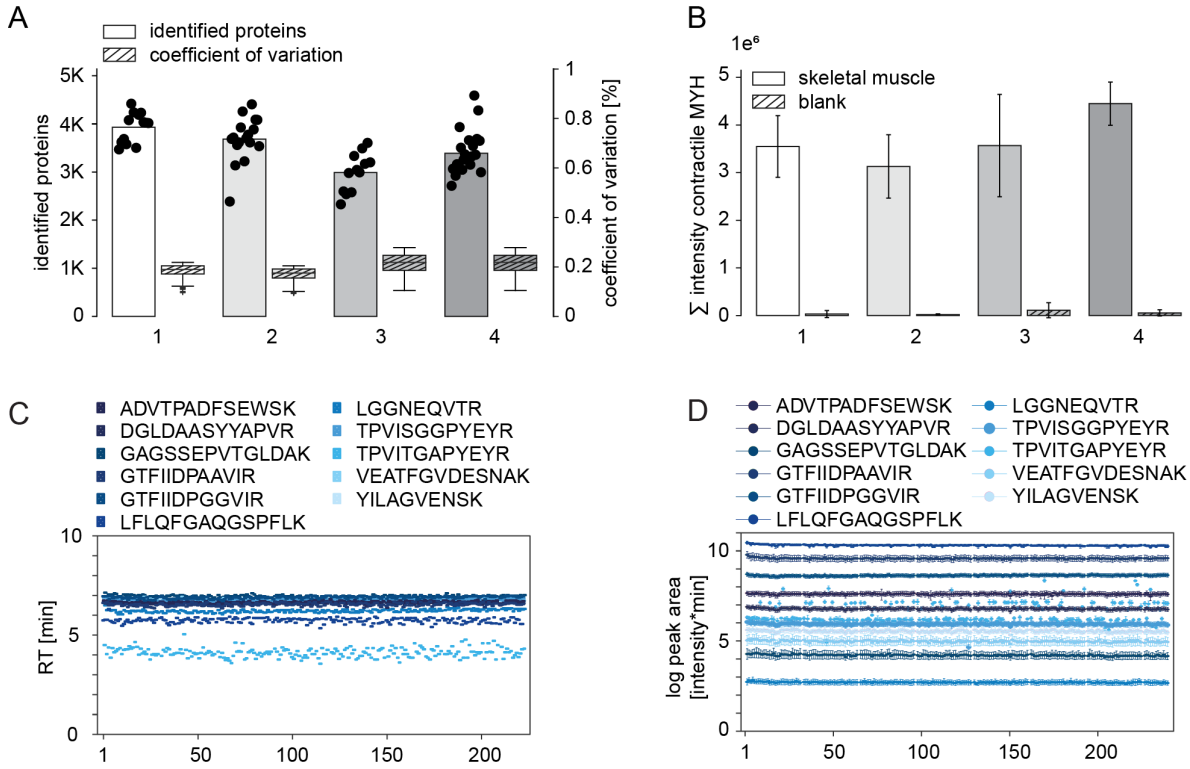

Figure S12 Quality control of the stable diaphragm slices analysis. A) Identified proteins and coefficient of variation of 200 ng HeLa lysates controlled over all 4 experiments. **B**) Boxplot of the sum intensity of contractile MYH ±SEM of skeletal muscle and blank samples represent a minimal carryover. **C, D**) RT (**C**) and log peak area (**D**) of spike-in indexed retention time peptides analyzed over all runs from one experiment.

Figure S13

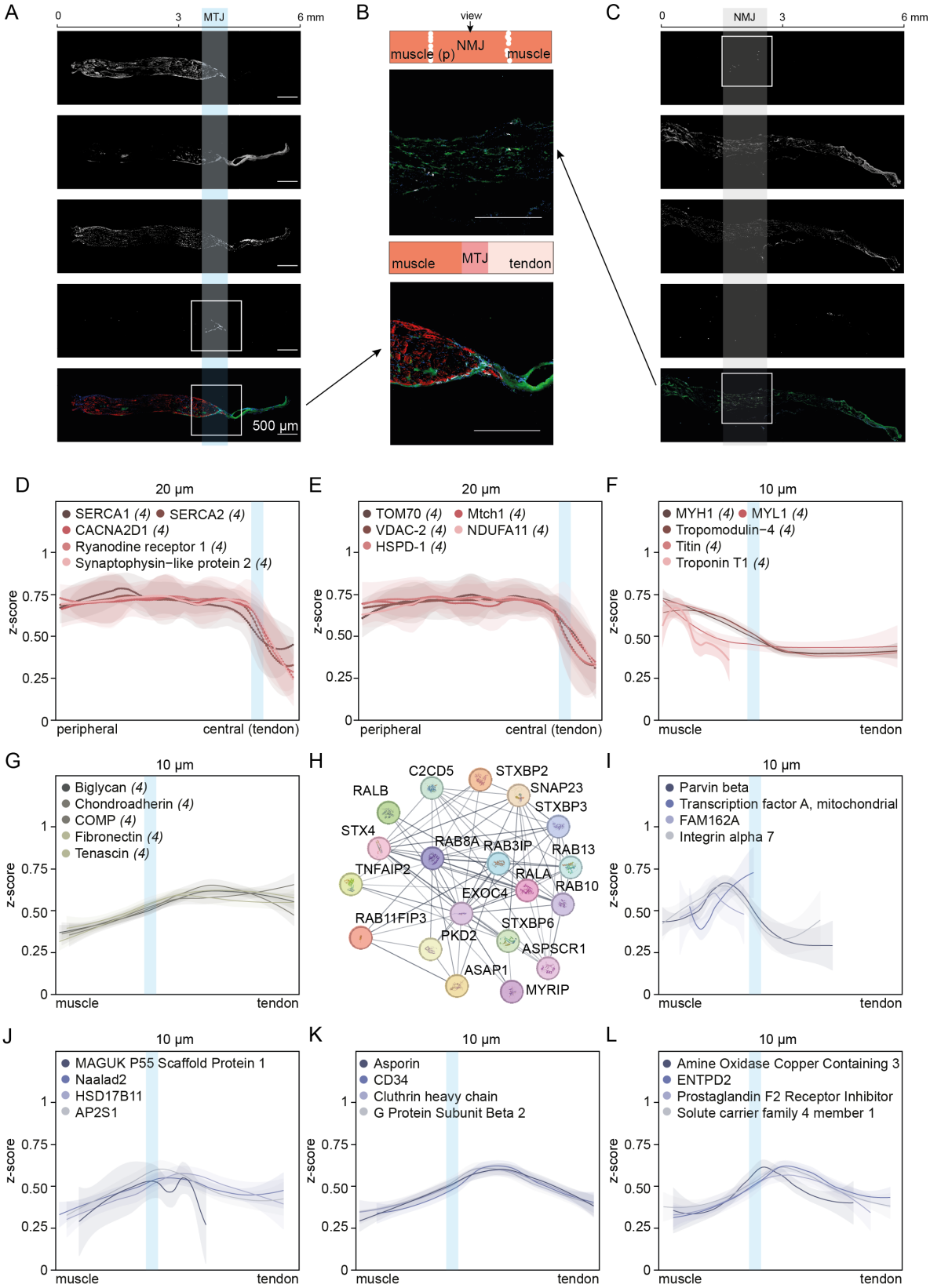

Figure S13 Protein expression of diaphragm MTJ proteins. A) Immunostaining for the NMJ in longitudinal mouse diaphragm sections with Bungarotoxin, MTJ is stained with collagen 22, nuclei are stained with Hoechst, tendon is stained with tenascin-C. Scale bar = 500 µm. **B, C**) Protein expression profiles along the longitudinal

peripheral muscle-central tendon axis of **B**) selected calcium housekeeping proteins, **C**) mitochondrial proteins. **D, E**) Protein expression profiles with 10 µm thin cryotome sections along the longitudinal muscle-tendon axis of **D**) selected sarcomeric proteins, **E**) selected ECM proteins. **F**) STRING interaction network of EXOC4. **G-J**) Protein expression profiles with 10 µm thin cryotome sections along the longitudinal muscle-tendon axis of **G**) selected MTJ proteins of the MTJ group 1, **H**) selected MTJ proteins of the MTJ group 2, **I**) selected MTJ proteins of the MTJ group 3, **J**) selected MTJ proteins of the MTJ group 4. Blue lines indicate the overlap of muscle and tendon proteins. AP2S1, AP-2 complex subunit sigma; CACNA2D1, calcium voltage-gated channel auxiliary subunit alpha 2 delta 1; ENTPD2, ectonucleoside triphosphate di phosphohydrolase 2; HSD17B11, hydroxysteroid 17-beta dehydrogenase 11; MTCH1, mitochondrial carrier 1; MTJ, myotendinous junction; MYH, myosin heavy chain; MYL1, myosin light chain; NAALAD2, N-acetylated-alpha-linked acidic dipeptidase 2; NMJ, neuromuscular junction; SERCA, sarcoplasmic/endoplasmic reticulum Ca^{2+}-ATPase.

Figure S14

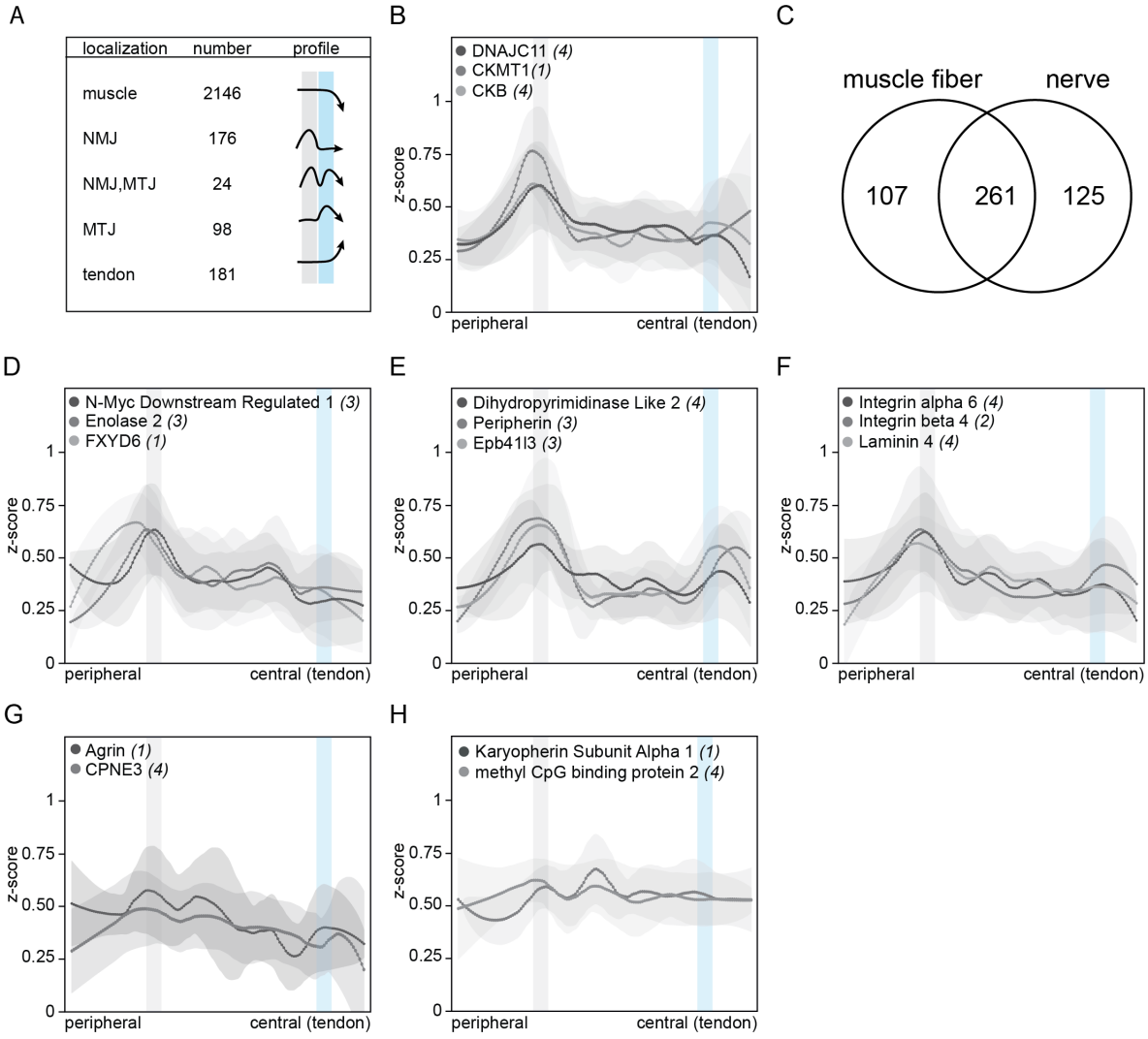

Figure S14 Expression profiles for NMJ proteins. A) Summary table of identified protein profiles regarding their localization, the number, and their profile along the logitudinal diaphragm axis. **B, D-H)** Protein expression profiles along the longitudinal peripheral muscle-central tendon axis of proteins **B, D)** with a global maximum at the NMJ, **E, F**) with maxima at the NMJ and MTJ, **G, H**) with maxima before and after the NMJ. **C**) Venn diagram of identified mitochondrial proteins in diaphragm muscle fibers and sciatic nerve. CK, creatine kinase; CPNE3, Copine 3; DNAJC11, DnaJ Heat Shock Protein Family Member C11; EPB41L3, Erythrocyte Membrane Protein Band 4.1 Like 3; MTJ, myotendinous junction; NMJ, neuromuscular junction.

Figure S15

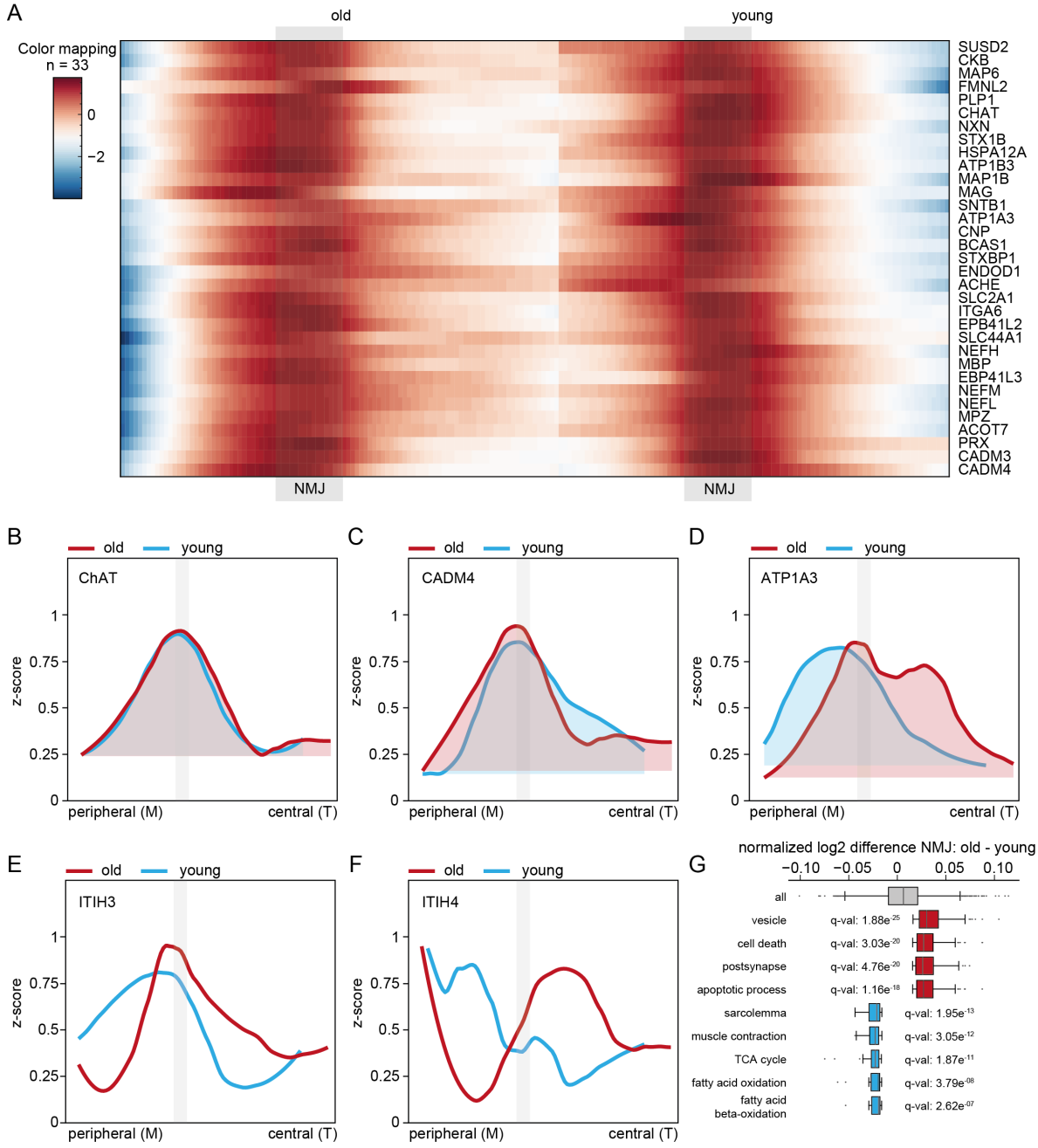

Figure S15 Widening of the NMJ in old animals. A) Heatmap of the z-score profiles of the 33 NMJ proteins in old and young mice. **B-D**) Protein expression profiles of **B**) CHAT, **C**) CADM4, **D**) ATP1A3. In red and blue are the old and young animals, respectively. Area under the curve is filled in the corresponding colour. **E, F**) Protein expression profiles of ITIH3 (**E**) and ITIH4 (**F**). **G**) Boxplot shows the significant changed GO-terms in old against young NMJ proteins. Data are represented as mean ±SEM. ACHE, acetyl choline esterase; ACTO7, acyl-CoA thioesterase 7; ATP1A3, ATPase Na^+/K^+ transporting subunit alpha 3; BCAS1, brain enriched myelin associated protein 1; CADM, cell adhesion molecule; CHAT, O-choline acetyl transferas; CK, creatine kinase; CNP, 2',3'-cyclic nucleotide 3' phosphodiesterase; ENDOD1, endonuclease domain containing 1; FMNL2, Formin like 2; HSPA12A, heat shock protein family A member 12A; ITIH4, inter-alpha-trypsin inhibitor heavy chain 4; ITGA6, integrin alpha-6; MAG, myelin associated glycoprotein; MAP, microtubule associated protein; MBP, myelin binding protein; NEF, neurofilament; MPZ, myelin protein zero; NXN, Nucleoredoxin; PLP1, proteolipid protein 1; PRX, periaxin; SLC2A1, glucose transporter type 1; SLC44A1,

solute carrier family 44 member 1; SNTB1, syntrophin beta 1; STXBP1, syntaxin binding protein 1; SUSD2, sushi domain containing 2.

Figure S16

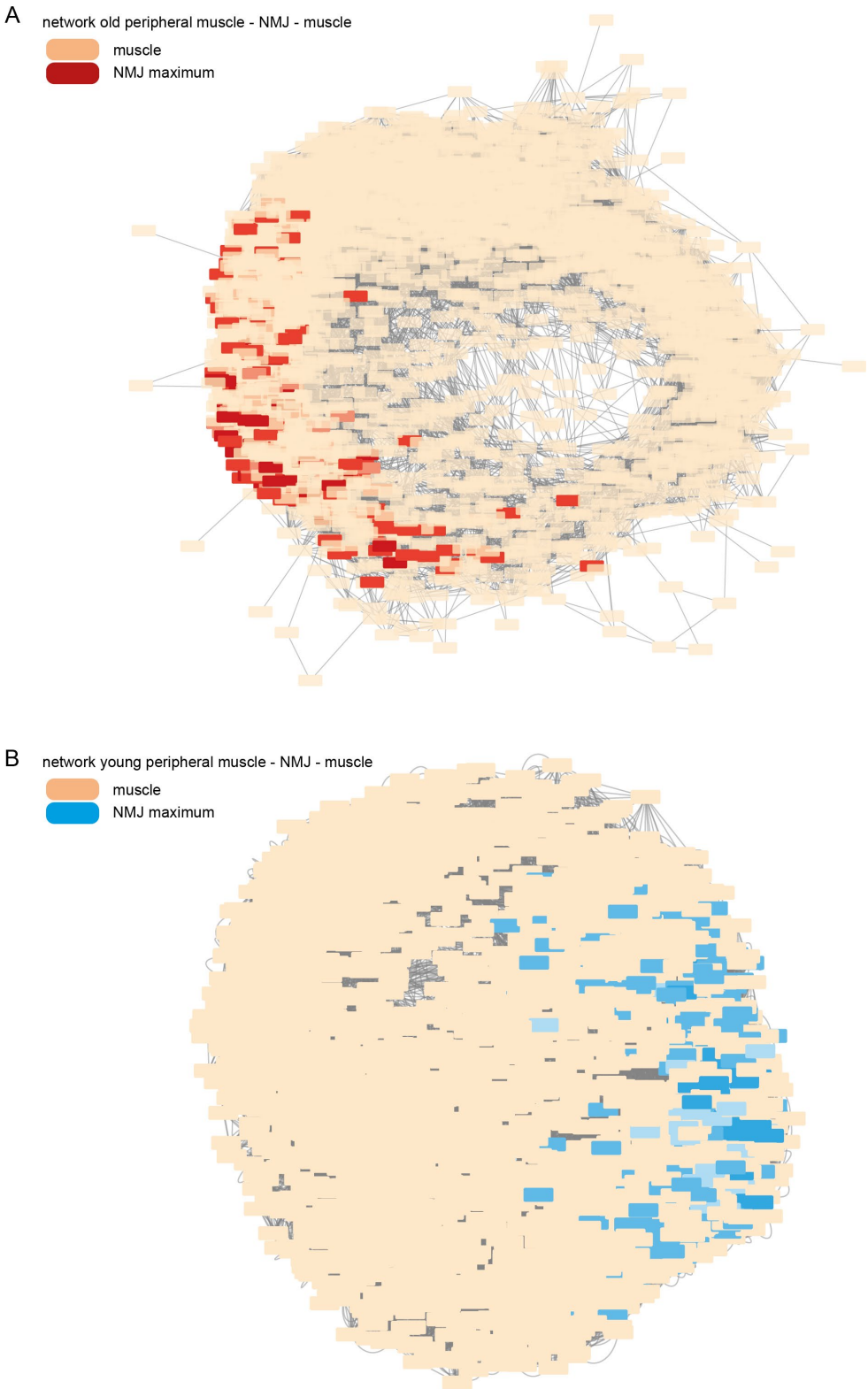

Figure S16 Network analysis of the old and young diaphragm. A, B) Distance-based network analysis of the **A**) old and **B**) young animals. Orange edges are muscle related proteins, red and blue edges are NMJ enriched proteins in old and young animals, respectively**.** NMJ, neuromuscular junction.

Figure S17

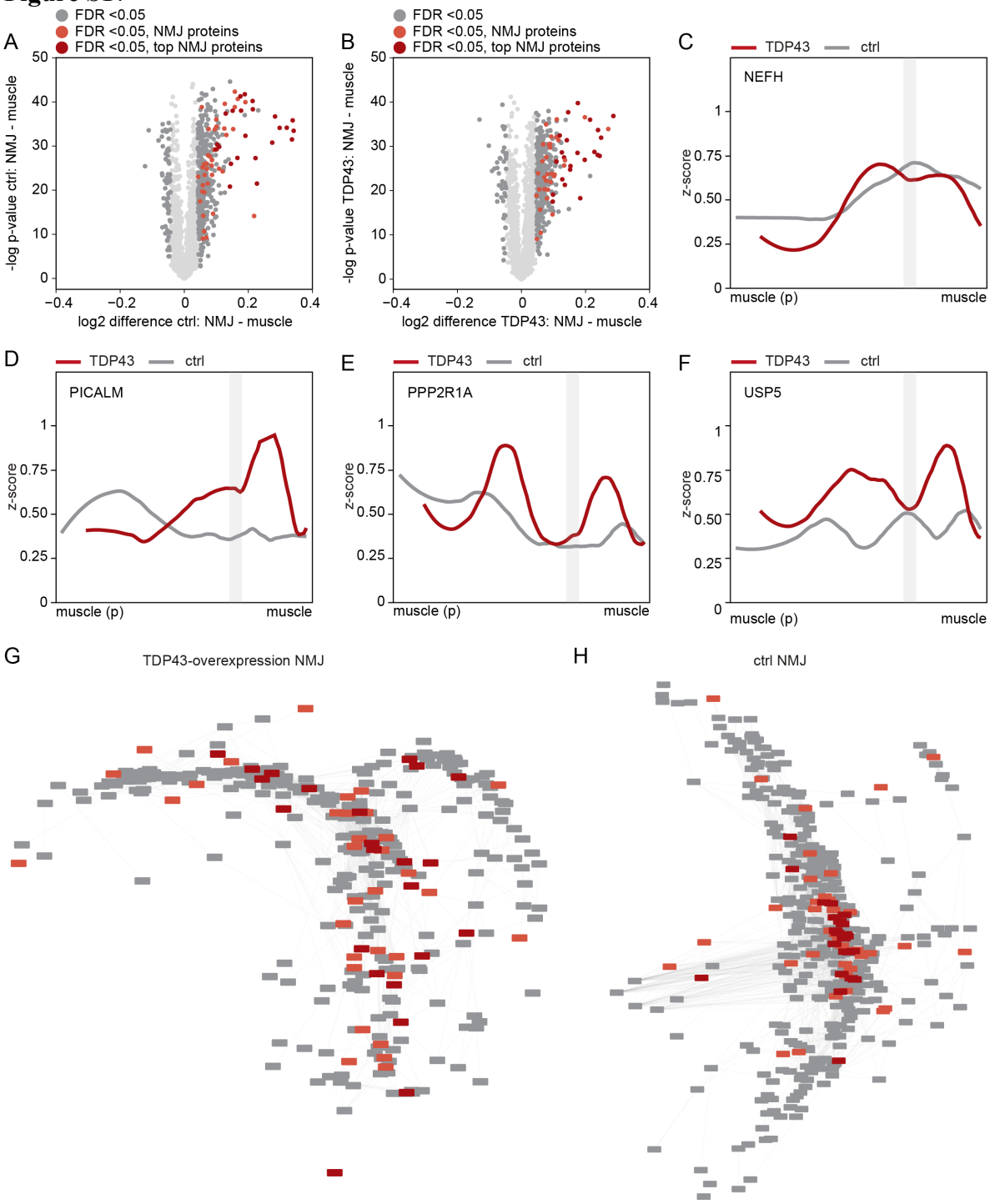

Figure S17 TDP43 dependent ALS mouse models show a slight decrease in NMJ proteins. A, B) Volcano plot of the NMJ and muscle area of TDP43-overexpression (**A**) and control mice (**B**). Differentially abundant proteins are highlighted in dark grey (Welch's *t*-test: FDR < 0.05, s0 > 0.1) and NMJ-related proteins in red. **C-F**) Protein expression profiles along the longitudinal muscle-NMJ-muscle axis of NEFH, PICALM, PPP2R1A, and USP5. Red and grey lines indicate the profile for TDP43-overexpression and control mice, respectively. **G, H**) Extracted NMJ network of the distance-based network of TDP43-overexpression (**G**) and control (**H**) mice. ctrl, control; NEFH, neurofilament heavy; PPP2R1A, protein phosphatase 2 scaffold subunit A α; PICALM, phosphatidylinositol binding clathrin assembly protein; TDP43, TAR DNA-binding protein 43; USP5, ubiquitin specific peptidase 5.

Figure S18

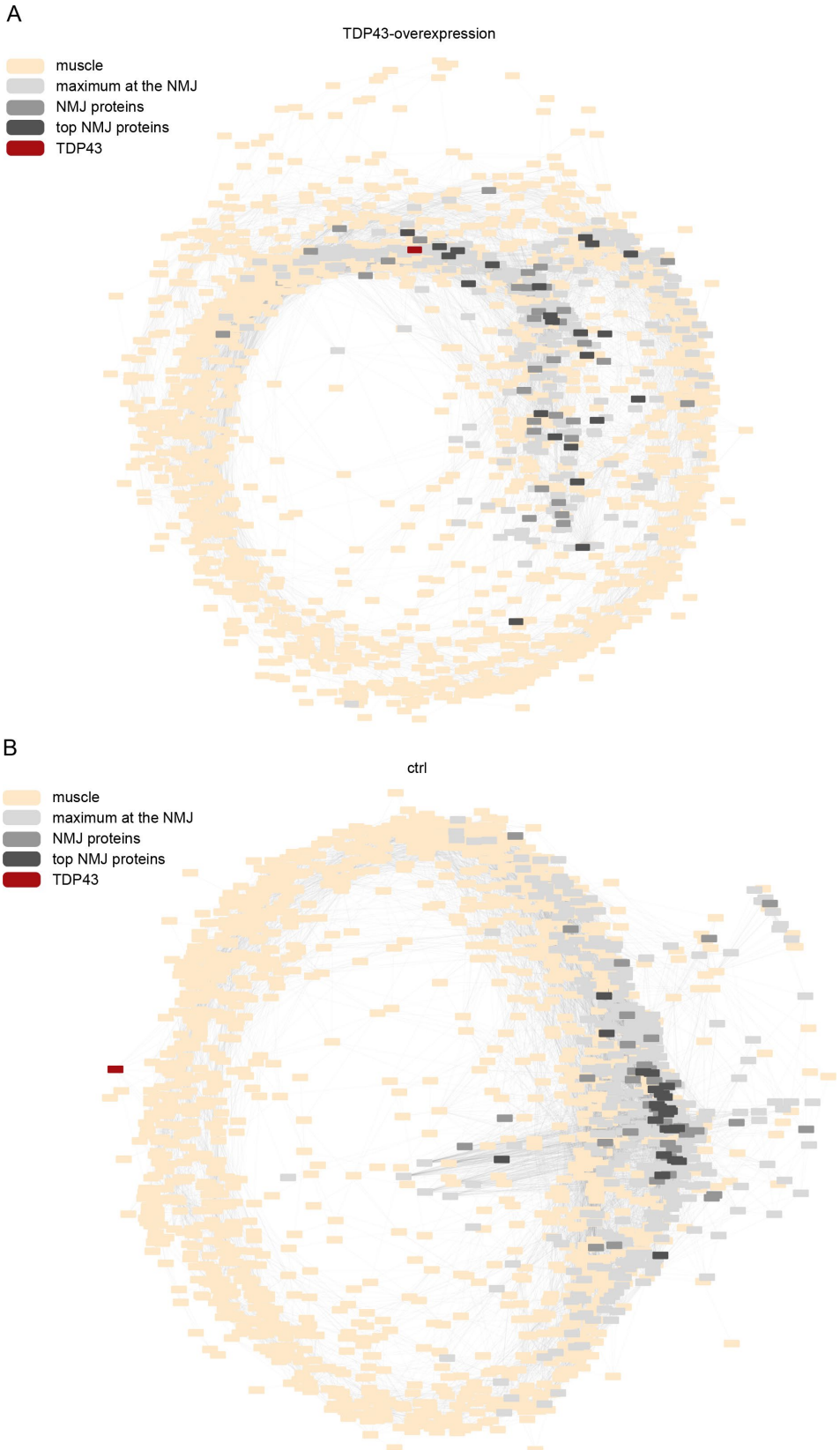

Figure S18 Network analysis of the old and young diaphragm. A, B) Distance-based network analysis of the **A**) TDP43-overexpression and **B**) control mice. Orange edges are muscle related proteins, grey and red edges are NMJ enriched proteins and TDP43, respectively**.** NMJ, neuromuscular junction.

Figure S19

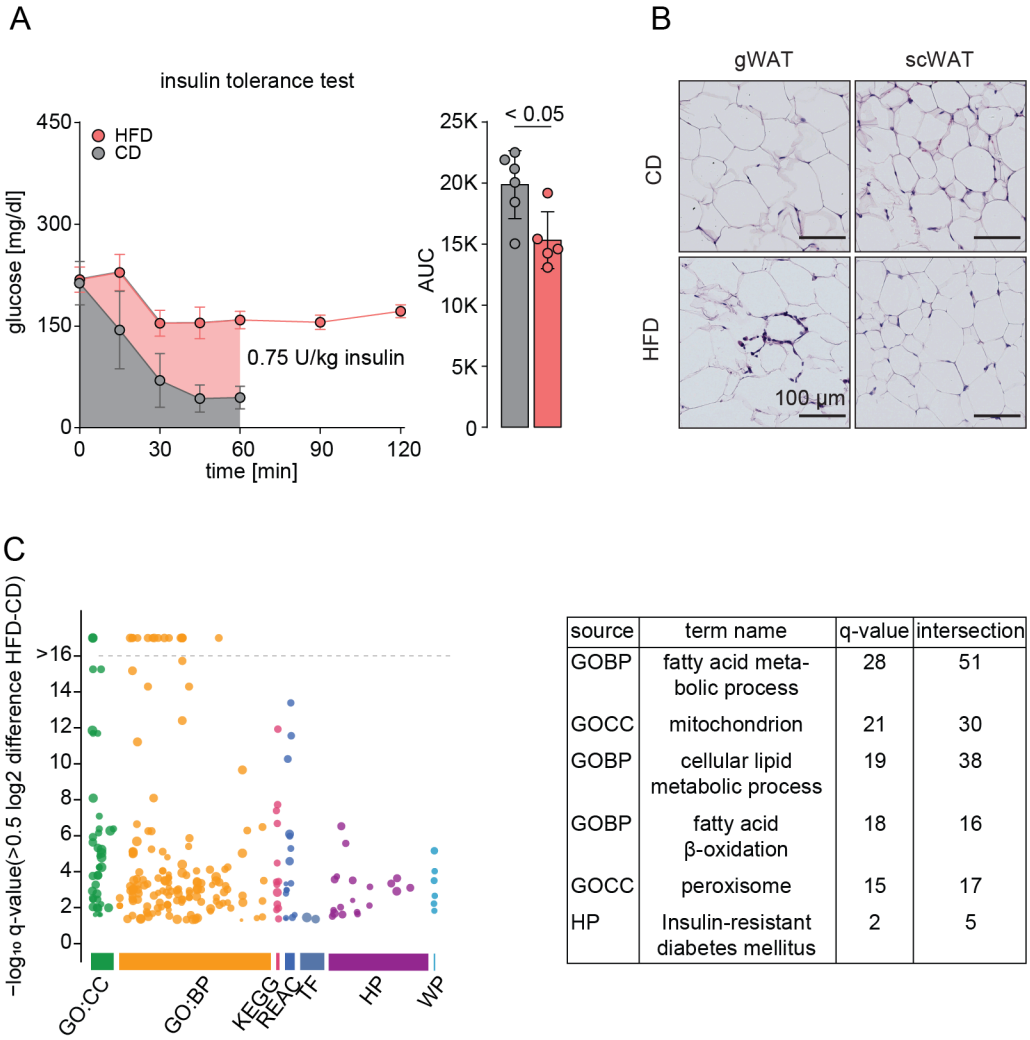

source	term name	q-value	intersection
GOBP	fatty acid meta-bolic process	28	51
GOCC	mitochondrion	21	30
GOBP	cellular lipid metabolic process	19	38
GOBP	fatty acid β-oxidation	18	16
GOCC	peroxisome	15	17
HP	Insulin-resistant diabetes mellitus	2	5

Figure S19 HFD animals physiology. A) HFD animals show an impaired response to the glucose tolerance test. Barplot of the AUC±SEM for the insulin tolerance test in HFD and CD **B)** H&E staining of gonadal and subcutaneous white adipose tissues show an inflammatory response. **C**) GO-term analysis of 1.5 times more abundant (log2 0.5) in HFD animals compared to the CD. Most abundant terms are listed on the right side. AUC, area under the curve; BP, biological processes; CC, cell component; CD, control diet; GO, gene ontology; gWAT, gonadial white adipose tissue; HFD, high-fat diet; HP, human proteome; REAC, reactome; scWAT, sub cutane white adipose tissue; TF, Transfac; WP, WikiPathways.

Figure S20

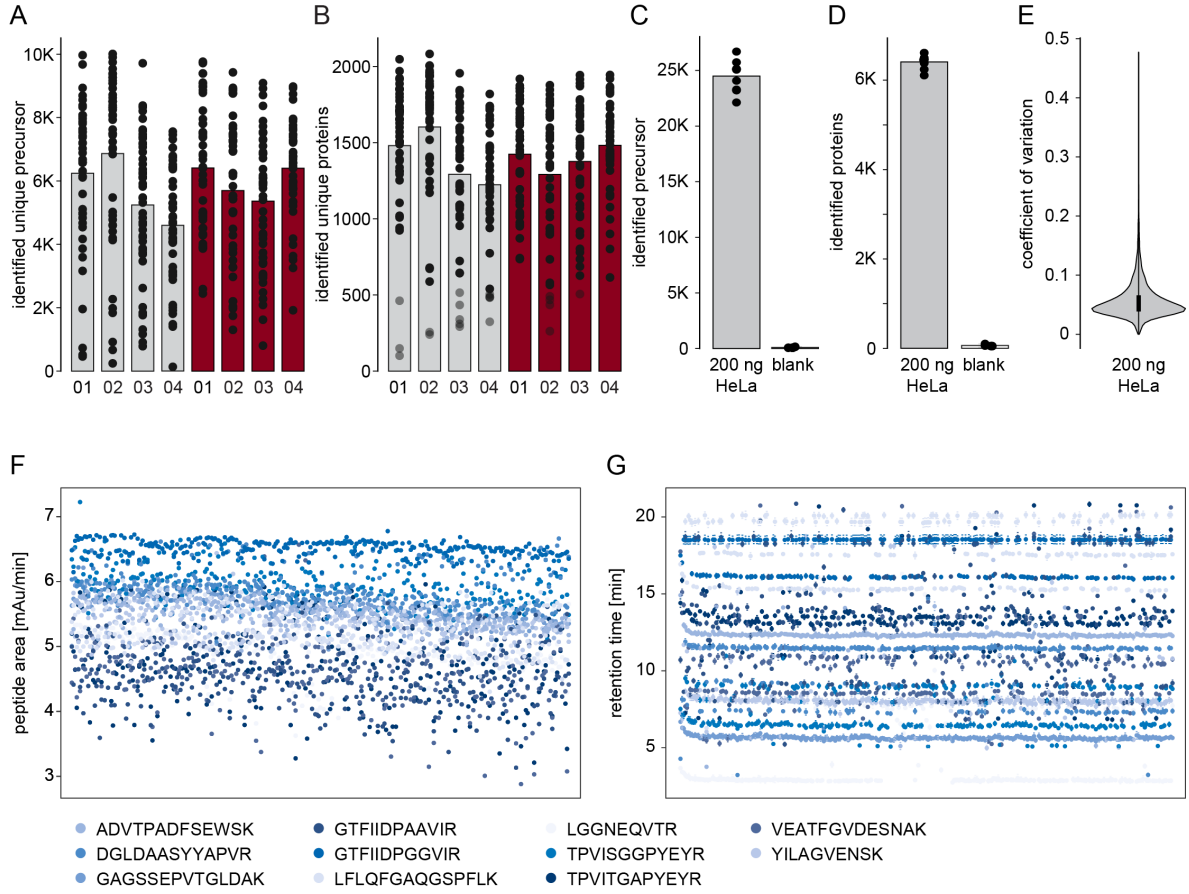

H

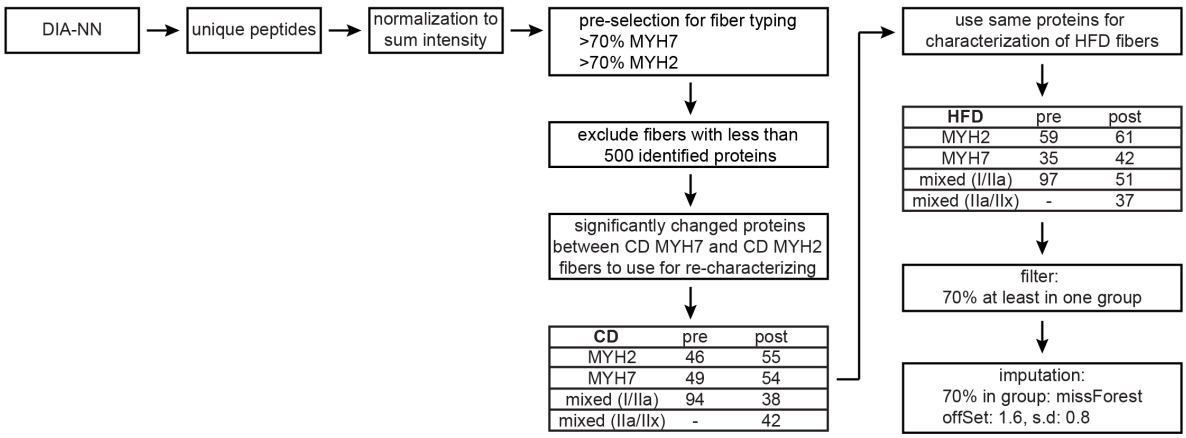

CD	pre	post
MYH2	46	55
MYH7	49	54
mixed (I/IIa)	94	38
mixed (IIa/IIx)	-	42

HFD	pre	post
MYH2	59	61
MYH7	35	42
mixed (I/IIa)	97	51
mixed (IIa/IIx)	-	37

Figure S20 Quality control for stable data acquisition over single muscle fiber analysis. A, B) Identified **A**) unique precursors and **B**) unique proteins per single fiber in CD (*n*=4) and HFD (*n*=4) animals. C-E) Identified C) precursors and D) proteins in 200 ng HeLa cell lysates and blank controls and E) coefficient of variation of the HeLa cell lysates, showing a stable protein identification over the measurements and minimal carry-over. **F, G**) Spike-in iRT peptides over all runs showing a stable LC performance. **H**) Bioinformatical workflow. CD, control diet; DIA-NN, data-independent-neural networks; HFD, high-fat diet; MYH, myosin heavy chain.

Figure S21

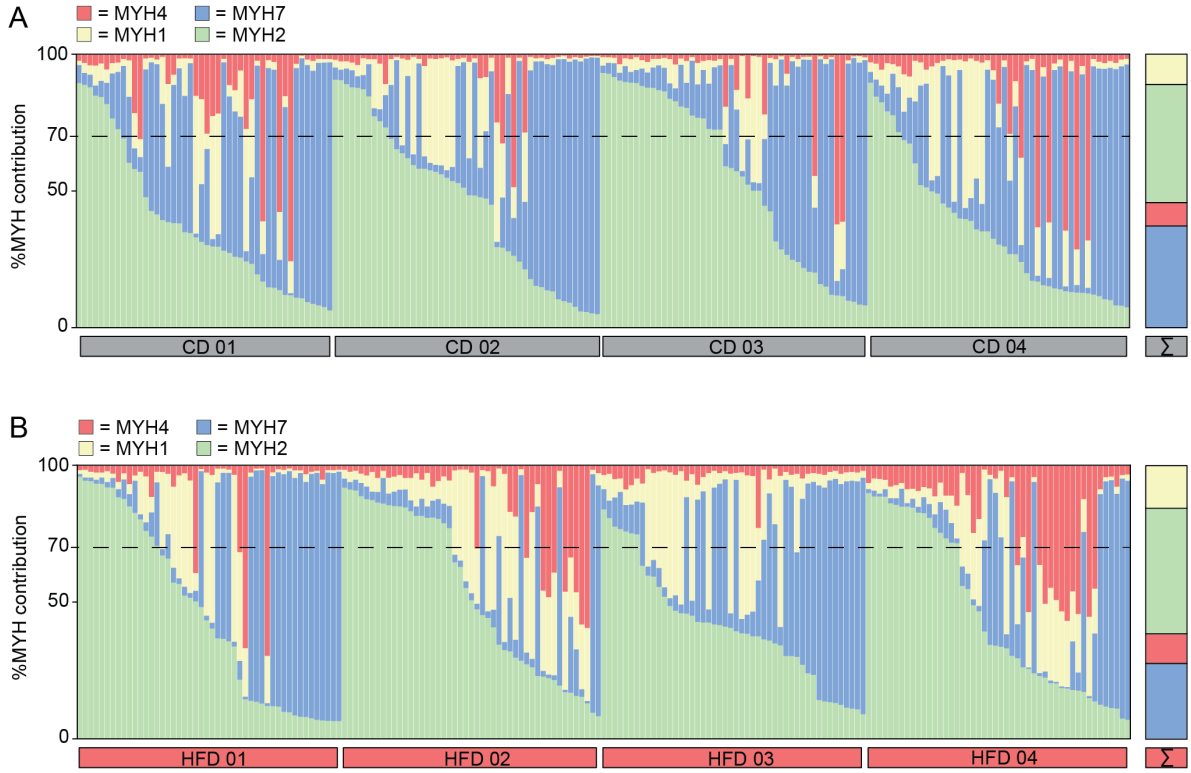

Figure S21 MYH distribution in CD and HFD. A, B) MYH isoform distribution analysis of isolated single muscle fibers from the four different animals in **A)** CD and **B)** HFD. Each bar represents the relative abundance of MYH isoforms in one fiber in relation to the total sum of intensities for MYH1 (blue), MYH2 (red), MYH4 (purple), and MYH7 (green). Fibers from different mice are sorted and ranked from left to right of highest MYH2 abundance. On the right side the average of all fibers of all animals is represented. CD, control diet; HFD, high-fat diet.

Figure S22

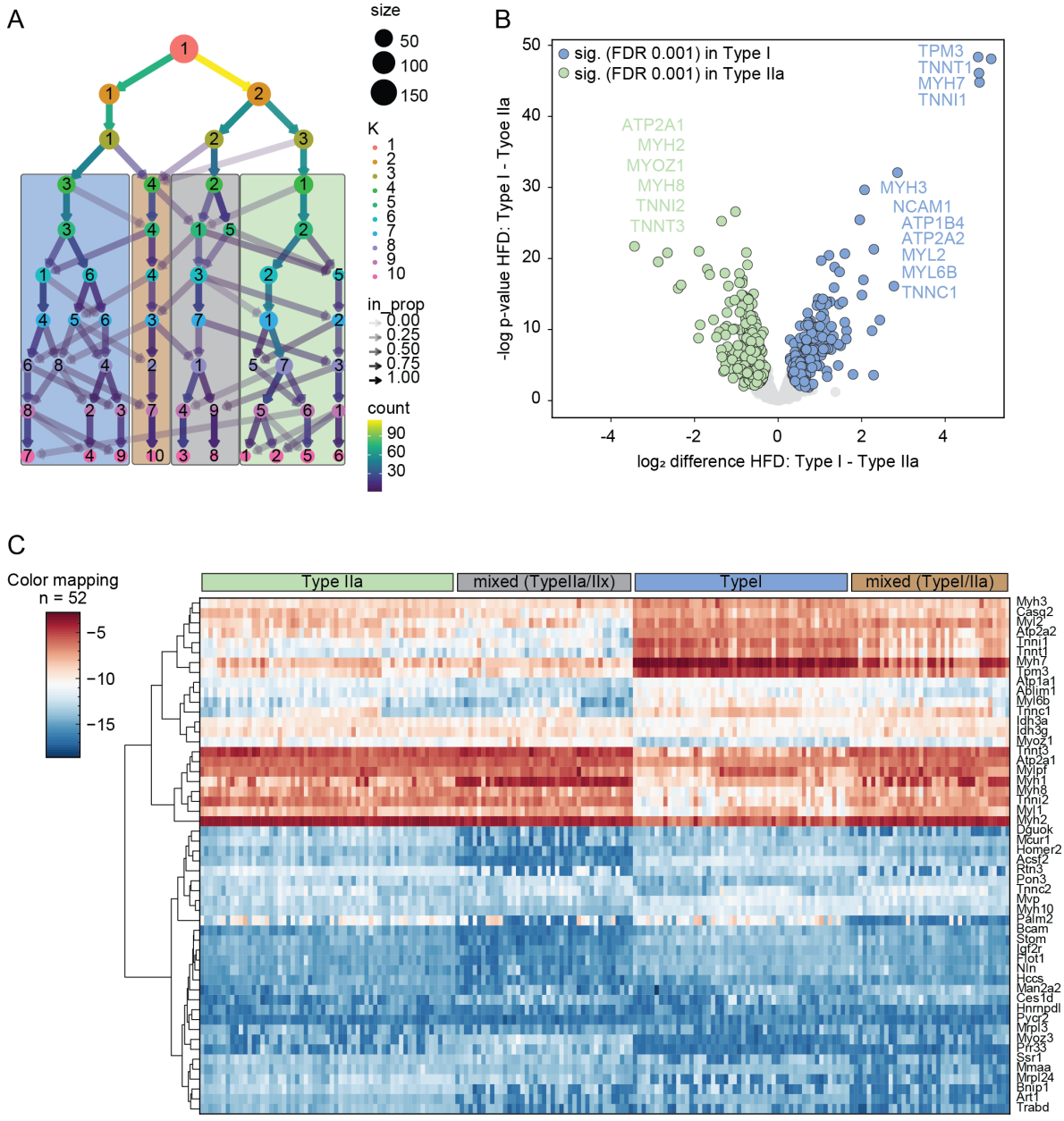

Figure S22 ClusTree analysis of HFD single fibers. A) ClusTree of the k-means clustering using 52 proteins as input for CD. 10 clusters are presented, probability is visualized in transparency of arrows, counts of samples are represented in yellow, green, blue, and purple, size of the clusters is represented in the size of the nodes. The final grouping of fibers is visualized in boxes (type I, blue; type IIa, green; mixed type I/IIa, brown; mixed type IIa/IIx, grey). **B**) Volcano plot shows the Welch's *t*-test differences between HFD type I and type IIa fibers. FDR significant (<0.001) proteins more abundant in type I and type IIa are marked in blue and green, respectively. **C**) Heatmap of the 52 proteins used for the ClusTree approach. ATP1B4, ATPase Na^+/K^+ transporting family member beta 4; ATP2, SERCA; MYH, myosin heavy chain; MYL, myosin light chain; MYOZ, myozenin; NCAM, neural cell adhesion molecule; TPM, tropomodulin; TNN, troponin.

Figure S23

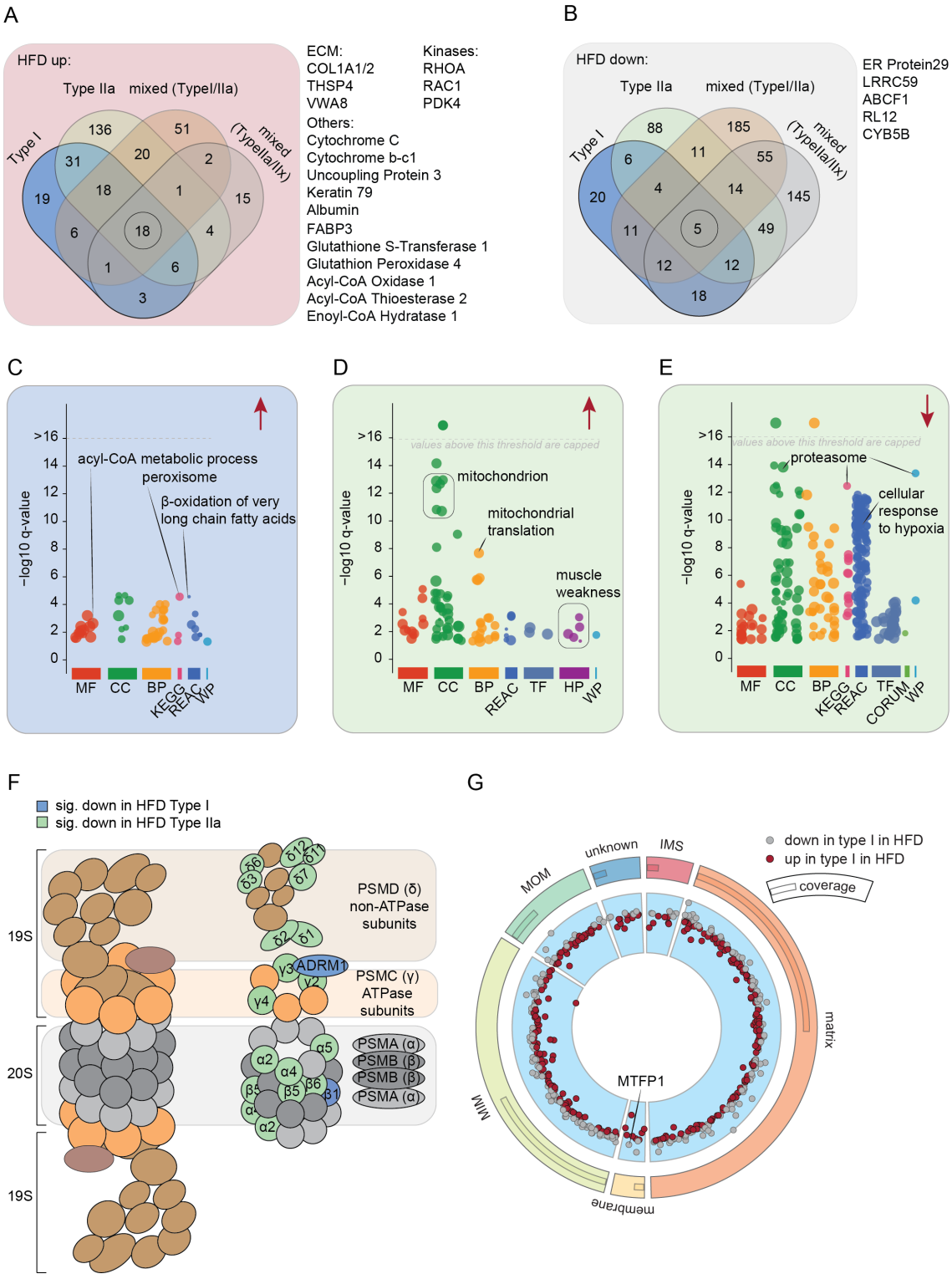

Figure S23 Different effects of the HFD on the fiber types. A, B) Venn Diagram of the proteins that are more abundant **A**) after HFD **B**) in CD in the different fiber types. **C-E**) GO-term analysis of proteins **C**) more abundant after HFD in type I fiber, **D**) more abundant after HFD in type IIa fiber, and **E**) less abundant after HFD in type IIa fiber. **F**) Proteasome subunits showing the different effects of HFD between type I and type IIa fibers. **G**) Solar plot of MitoCarta 3.0[231] proteins showing the differently abundant proteins in type I fibers in HFD compared to CD. ABCF1, ATP binding cassette subfamily F member 1; CD, control diet; COL1A1,

collagen 1a1; CYB5B, cytochrome B5 type B; FABP3, fatty ccid binding protein 3; HFD, high-fat diet; IMS, mitochondrial intermembrane space; LRRC59, leucine rich repeat containing 59; MIM, mitochondrial inner membrane; MOM, mitochondrial outer membrane; PDK4, pyruvate dehydrogenase kinase 4; PSM, proteasome subunit; RAC1, rac family small GTPase 1; RHOA, ras homolog family member A; RL12, ribosomal protein L12; THSP4, Thrombospondin-4; VWA8, von Willibrandt factor 8.

Figure S24

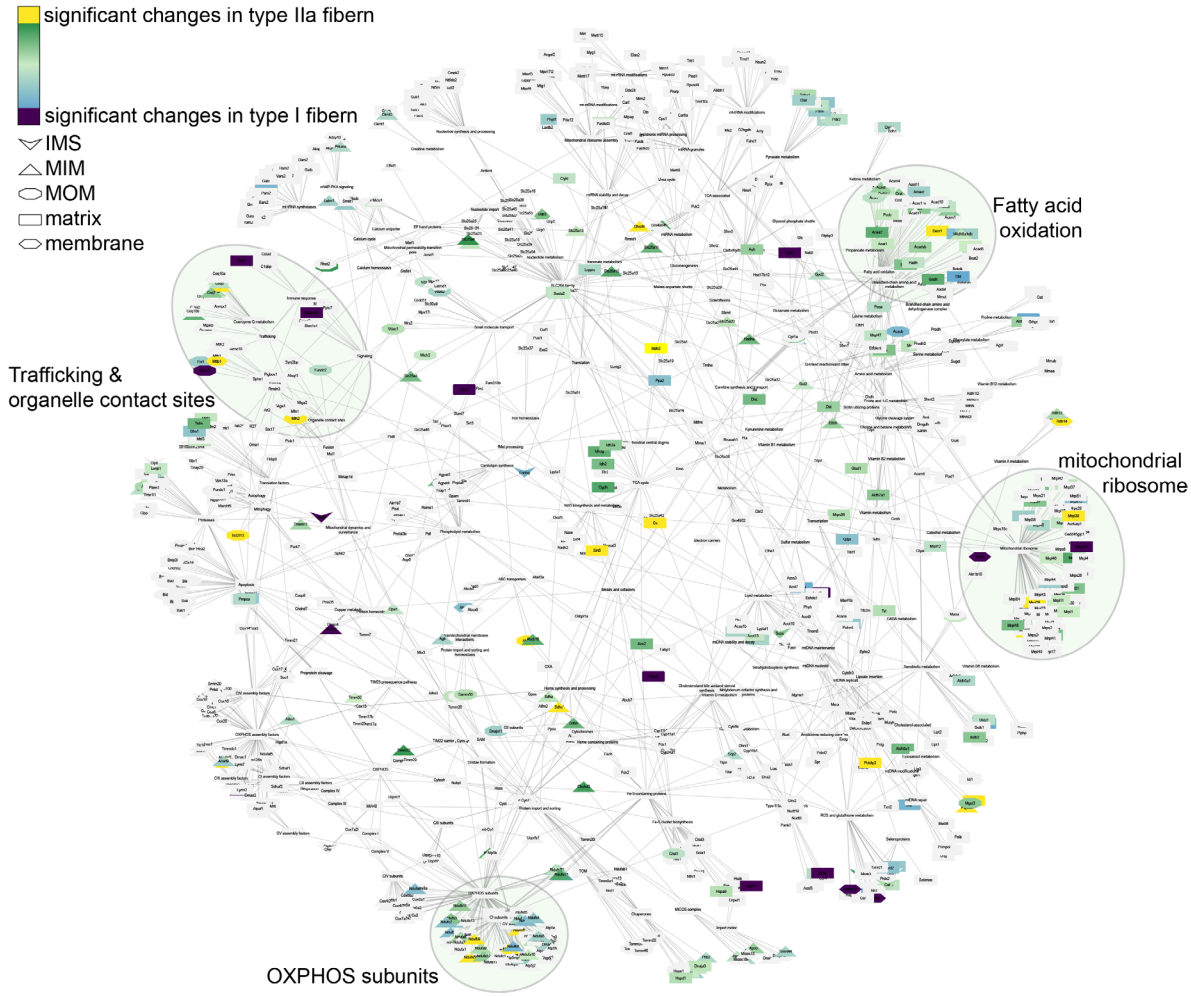

Figure S24 Mitochondrial pathways visualized in a network. Each node represents one protein or one pathway term of the MitoCarta 3.0.[231] Green (yellow) and blue (purple) marked proteins show a tendency to an increased abundance of type IIa or type I fiber (significant). Shapes are visualizing the localization of the protein in the mitochondrion (V-shaped, IMS; triangle, MIM; octagon, MOM; rectangle, matrix; hexagon, membrane).

Figure S25

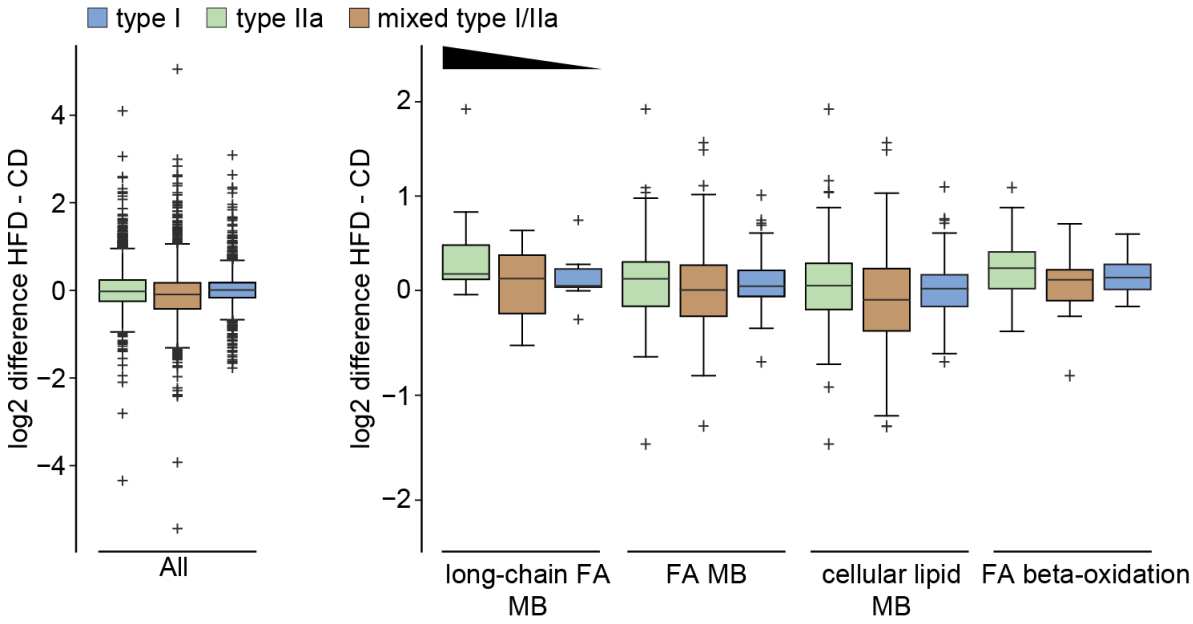

Figure S25 GO-term changes in type IIa, mixed type I/IIa, and type IIa fibers. Boxplot of the log2 fold change between HFD and CD±SEM for the identified proteins related to the GO-terms of long-chain fatty acid metabolism, fatty acid metabolism, cellular lipid metabolism, and fatty acid beta-oxidation. Blue, green, and brown bars represent type I, type IIa, and mixed type I/IIa fibers, respectively. FA, fatty acid; MB, metabolic process.

Figure S26

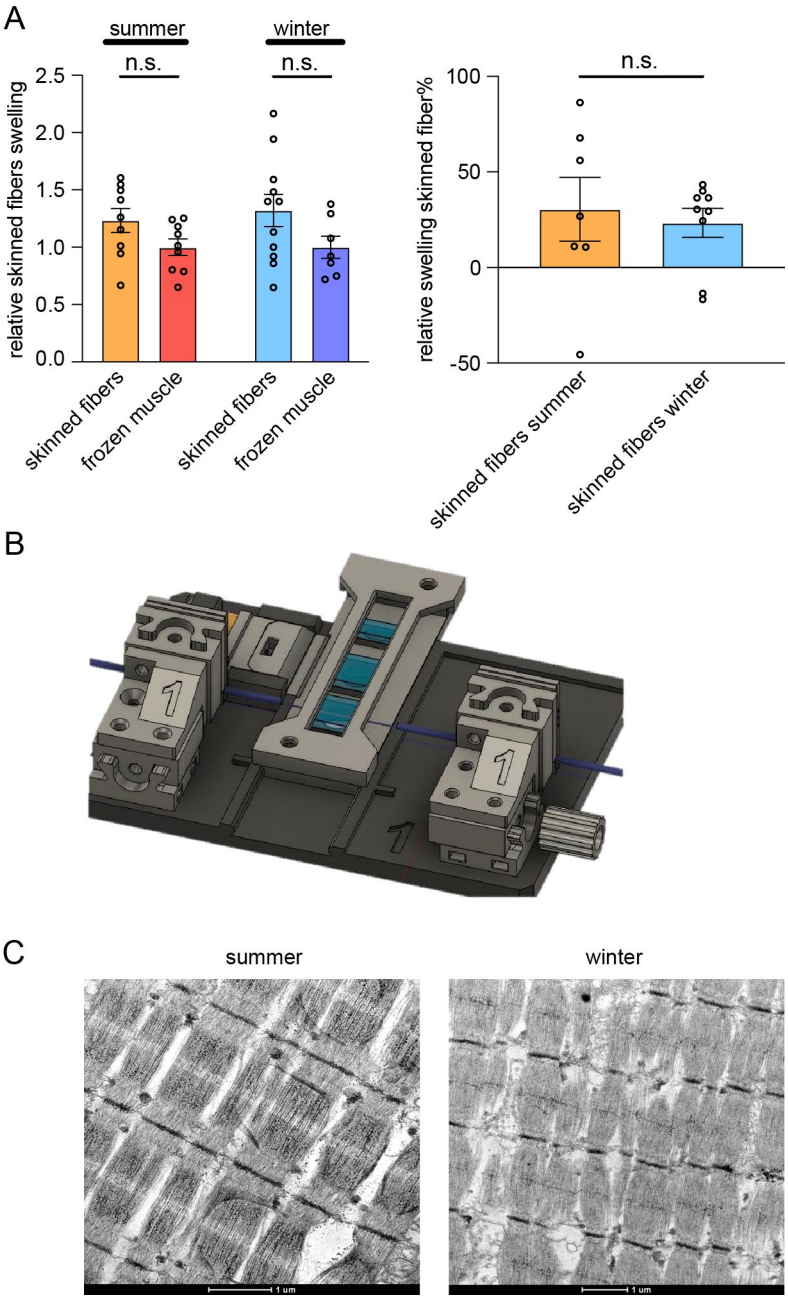

Figure S26 Swelling of skinned fibers. Swelling of skinned fibers is determined by comparing average cross-sectional area on frozen sections to the cross-sectional area determined for individual skinned fibers placed at optimal length. Swelling is clear for winter and summer fibers, without any difference between groups (n=2÷15; Unpaired t-test skinned fibers and frozen muscle. Mann-Whitney test skinned fibers summer and skinned fibers winter). **C**) Electron microscope images of skinned fibers from winter and summer fibers. Spaces are observed between sarcomeres in both cases, which are due to swelling. The yellow arrows denote relatively intact mitochondria, while red arrows show completely swollen mitochondria in the winter muscle.

Figure S27

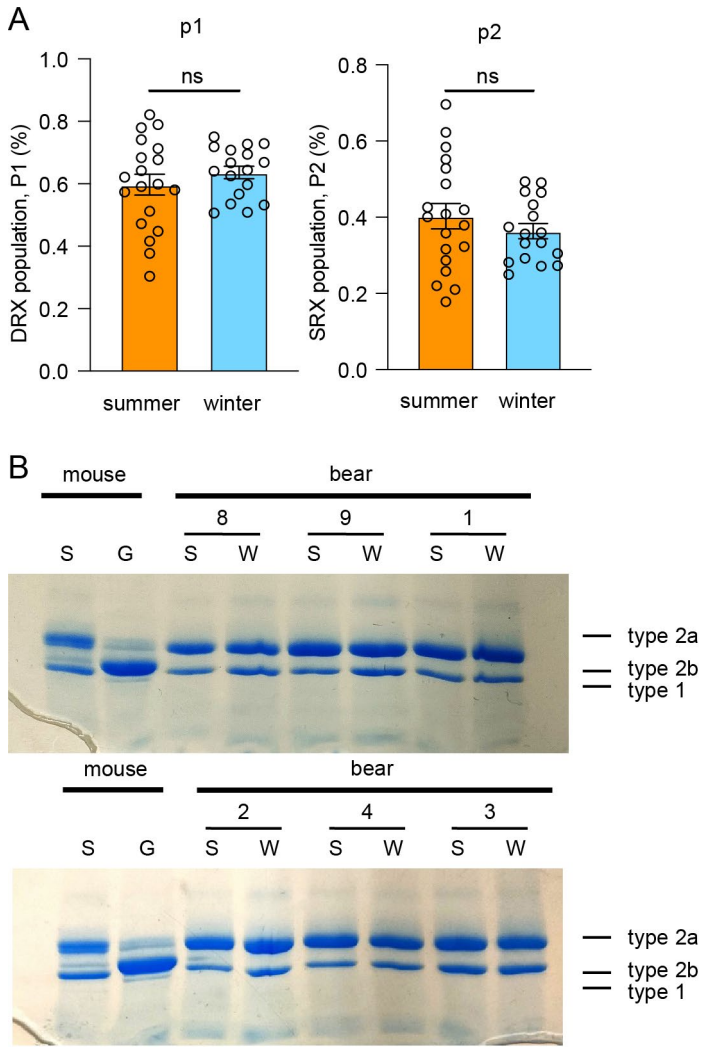

Figure S27 Identification of MYH in single bear fibers. A) Relative population of myosin heads in DRX (P1) or SRX (P2) in summer and winter biopsies show no differences **B**) Overall, no major shift in myosin heavy chain isoform in winter and summer bear muscle. On the left two mouse samples were loaded, with a slow (soleus, S) and fast (gastrocnemius, G) mouse muscle lysate to indicate the weight of the different isoforms. DRX, disordered relaxed state; SRX, super relaxed state; S, summer; W, winter.

Figure S28

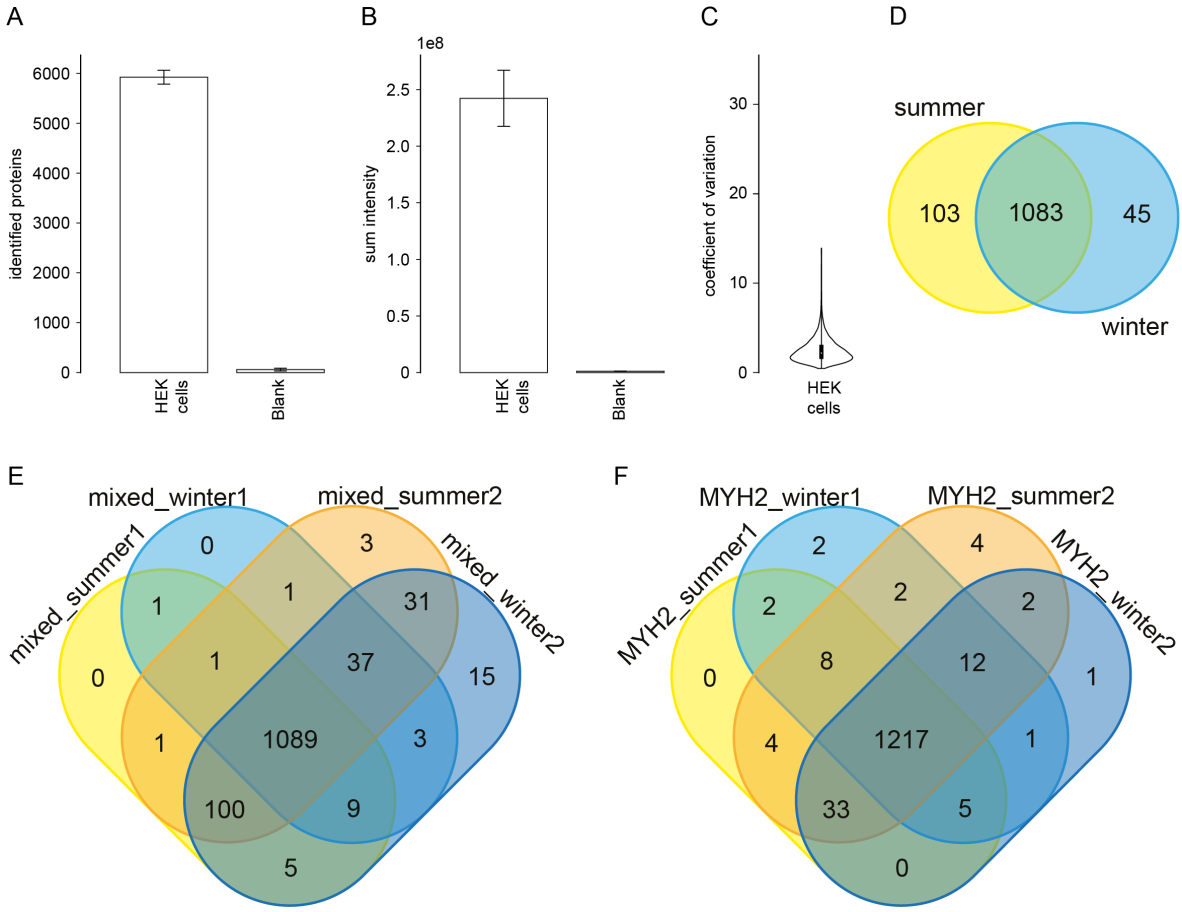

Figure S28 VennDiagram. Venn diagram showing the presence of specific proteins in the different groups. Most proteins are found in both winter and summer muscles. MYH, myosin heavy chain.

Figure S29

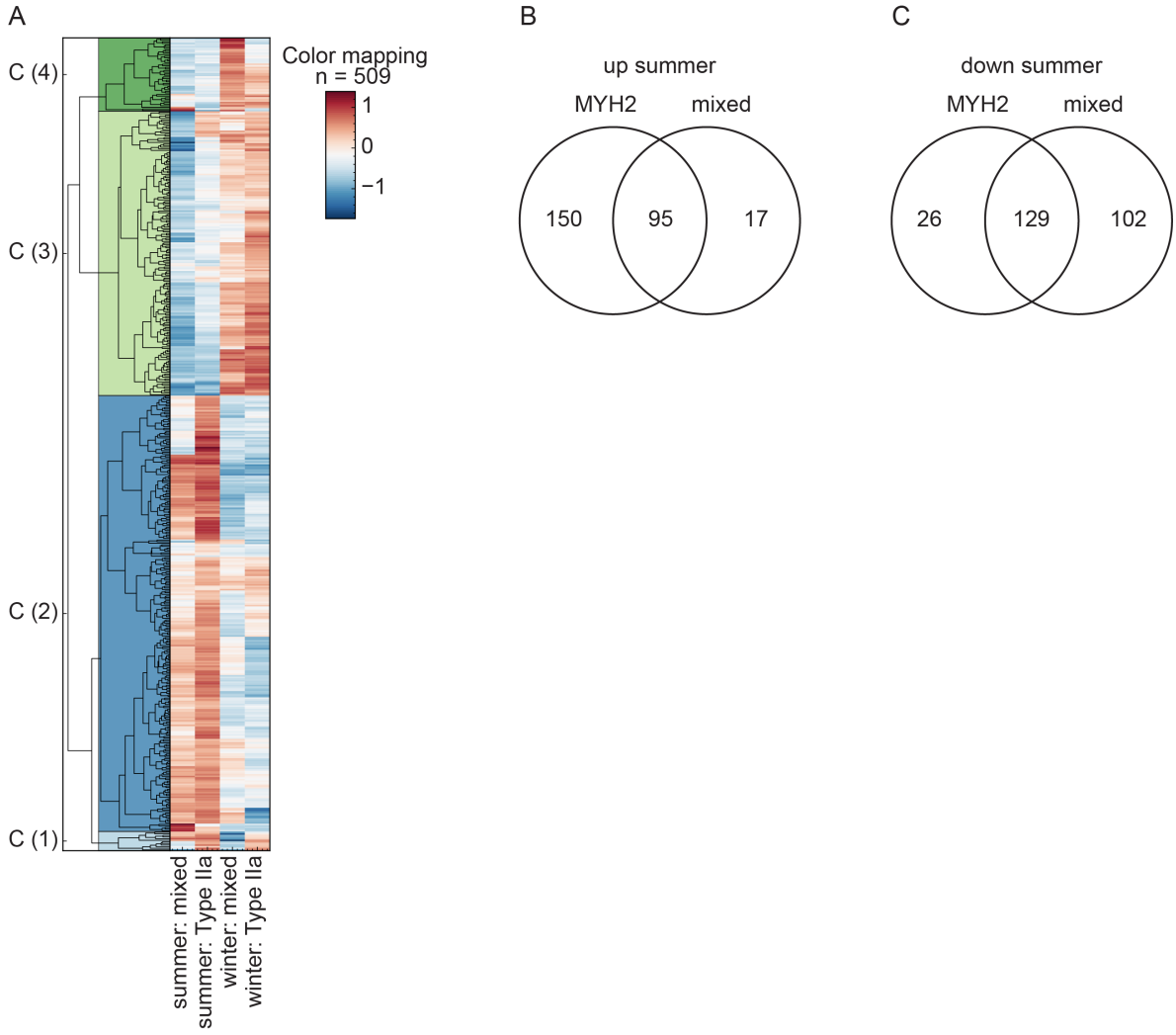

Figure S29 Heatmap. Heat map showing hierarchical clustering of median normalized Z-scores for mixed fibers in both summers and winters. As can be seen, protein regulation is similar between the two different years. MYH, myosin heavy chain.

Figure S30

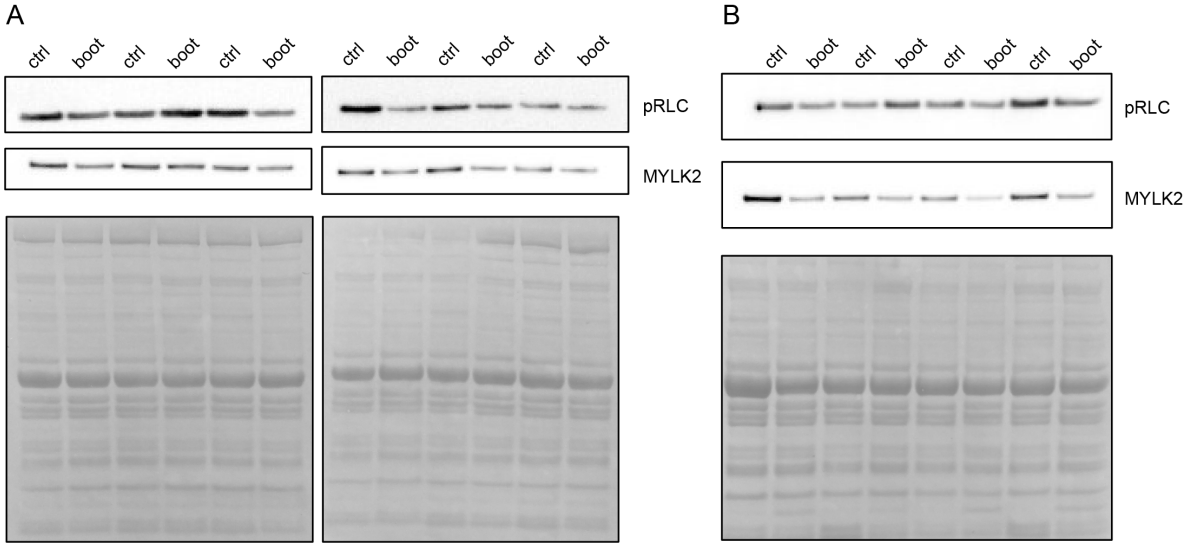

Figure S30 Western blot analysis of immobilized mice muscles. A, B) Western blotting analysis on gastrocnemius muscle tissue from unilateral immobilized for 7 (**A**) and 14 (**B**) days from the same mouse show a significant decrease in MYLK2 and a tendency for the phosphorylation of its target P-MLC. *n*= 6 mice for 7 days and *n*=4 mice for 14 days.

4.2. List of supplementary tables

Table S1: Data for manually dissected muscle, MTJ, and tendon areas from intact muscles, related to Figure 9. Protein group output data of muscle, MTJ, and tendon lysates from isolated wild-type mouse solei (n = 4). Unpaired two-sided Welch's t-test, FDR < 0.05, s0 = 0.1, ANOVA, s0 = 0.1.

Table S2: Data for protein profiling from sectioned muscles, related to Figure 10 and 13. (Representative profiles) Z-score normalized and summarized data of sectioned muscles (n = 3). (Profile completeness) Identification scores for each experiment over distances of 200 µm in the muscle. (MTJ) MTJ proteins identified in this study, along with their spatial categorization as early, central, or late MTJ proteins. (Overlap known MTJ proteins) MTJ proteins identified in previous studies overlapped with data from the protein profiles identified in this study. (Identified marker proteins) Published marker proteins for specific cell types identified in this study.

Table S3: Data for the proteome of losartan-treated immortalized tenocytes, related to Figure 13. (Tenocytes losartan treatment) MaxLFQ values of tenocytes treated with DMSO or 10 µM or 50 µM losartan for 4 days (n = 3). Unpaired two-sided Student's t-test, s0 = 0.1. (Tenocytes - C2C12) MaxLFQ values of tenocytes and myoblasts (C2C12 cells; n = 3). Unpaired two-sided Student's t-test, FDR < 0.05, s0 = 0.1.

Table S4: Data for the phosphoproteom of losartan-treated immortalized tenocytes, related to Figure 13. (Phosphosites) MaxLFQ values of enriched phosphosites in tenocytes treated with DMSO or 10 µM losartan for 4 h (n=3 DMSO, n=4 losartan). Unpaired two-sided Welch's t-test, s0 = 0.1. (Proteome) MaxLFQ values of tenocytes treated with DMSO or 10 µM losartan for 4 h (n=3 DMSO, n=4 losartan). Unpaired two-sided Welch's t-test, s0 = 0.1.

Table S5: Instrument methods and iRT peptide concentrations. (Method overview) Overview of window size, gradient length, MS length, MSMS length, and number of windows. (iRT peptides) Overview of iRT peptide sequences and concentrations.

Table S6: Data for protein profiling from sectioned diaphragm, related to Figure 21-24. (Representative profiles) Z-score normalized and summarized data of sectioned diaphragm muscles ($n = 4$). Unpaired two-sided Welch's *t*-test, FDR < 0.05, s0 = 0.1. (Profile completeness) Identification scores for each experiment over distances of 200 µm in the muscle.

Table S7: Data for protein profiling from sectioned MTJ area of diaphragm, related to Figure 22. (Representative profiles_10 µm) Z-score normalized and summarized data of 10 µm sectioned diaphragm muscles ($n = 1$). (MTJ_20 µm) Identified MTJ proteins of the diaphragm sectioned with 20 µm. (MTJ_10 µm) Identified MTJ proteins of the diaphragm sectioned with 10 µm. (Literature) MTJ proteins identified in previous studies overlapped with data from the protein profiles identified in this study.

Table S8: Data for identifying the origin of NMJ proteins, related to Figure 24. (Diaphragm fiber) Normalized intensities to the sum intensities of isolated diaphragm fiber ($n = 15$) (Sciatic nerve) Max LFQ intensities of isolated sciatic nerve ($n = 4$) (Overlap) Representative profiles, diaphragm fiber proteome, sciatic nerve proteome overlapped. Unpaired two-sided Welch's *t*-test, FDR < 0.05, s0 = 0.1. (NMJ) Overlap of identified NMJ, diaphragm fiber, and sciatic nerve proteins. (Localization) Overlap of NMJ, MTJ_10 µm, and MTJ_20 µm proteins. (Literature) NMJ proteins identified in previous studies overlapped with data from the protein profiles identified in this study.

Table S9: Data for protein profiling from sectioned diaphragm muscles for young and old animals, related to Figure 26. (Representative profiles) Z-score normalized and summarized data of sectioned muscles ($n = 2$). (Overlap) Overlap of NMJ proteins identified in young and old animals and previously identified NMJ proteins. Unpaired two-sided Welch's *t*-test, FDR < 0.05, s0 = 0.1. (Network_analysis) Parameters for the network analysis. (Overlap_Aging_TDP43) Significantly changed proteins (FDR < 0.01) in the NMJ between aged and young mice, and TDP43 and control mice.

Table S10: Data for protein profiling from sectioned diaphragm muscles TDP43-overexpression mouse model and ctrl, related to Figure 27. (Representative profiles) Z-score normalized and summarized data of sectioned muscles (n = 2). Unpaired two-sided Welch's t-test, FDR < 0.05, s0 = 0.1. (Network_analysis) Parameters for the network analysis.

Table S11: Data for proteome analysis of intact muscles from HFD and CD, related to Figure 29. Protein group output data of soleus muscle protein lysates from HFD (n = 9) and CD (n = 4) mice. Unpaired two-sided Welch's t-test, FDR < 0.05, s0 = 0.1.

Table S12: Data for proteome analysis of isolated muscle fibers from HFD and CD, related to Figure 30, 31. (Analysis) Normalized intensities to the sum intensities data of single soleus muscle fiber (n = 48) from HFD (n = 4) and CD (n = 4) mice. Unpaired two-sided Welch's t-test, FDR < 0.05, s0 = 0.1. (Fiber Types_52) Published marker proteins to characterized fiber types in this study.

Table S13: Data for image analysis of mitochondrial distribution in type I and IIa fibers for HFD and CD, related to Figure 32. (EXP1_DilatedFibers) Radial distribution of TOM20 IHC intensities in single muscle fibers accounted to their fiber type and CD (n = 10) and HFD (n = 10). (EXP2_DilatedFibers) Radial distribution of TOM20 IHC intensities in single muscle fibers accounted to their fiber type and CD (n = 10) and HFD (n = 10). (Fractions) Summarized data of experiment 1 and 2.

Table S14: Data for proteome analysis of isolated muscle fibers from hibernating and active bears, related to Figure 36. (type IIa fiber) Normalized intensities to the sum intensities data of type IIa single bear muscle fibers from active (n = 8) and hibernating (n = 8) bears. Unpaired two-sided Welch's t-test, FDR < 0.05, s0 = 0.1, ANOVA, s0 = 0.1. (mixed fiber) Normalized intensities to the sum intensities data of mixed single bear muscle fibers from active (n = 8) and hibernating (n = 8) bears. Unpaired two-sided Welch's t-test, FDR < 0.05, s0 = 0.1, ANOVA, s0 = 0.1.

4.3. List of supplementary data

Data S1: Profile plots: Protein profiles of ~3000 proteins from the mouse soleus muscle

Data S2: Spatial network of the soleus muscle. Distance-based network generated in cytoscape using the protein expression profiles. Known muscle (orange), tendon (green), and potential MTJ (blue) proteins are marked.

Data S3: Profile plots: Protein profiles of ~2500 proteins from the mouse diaphragm muscle

Data S4: Profile plots: Protein profiles of ~1200 proteins from the MTJ area of the 10 µm sectioned mouse diaphragm muscle

Data S5: Profile plots: Protein profiles of ~2800 proteins from the NMJ area of young and old sectioned mouse diaphragm muscle

Data S6: Profile plots: Protein profiles of ~1900 proteins from the NMJ area of TDP43-overexpressing and ctrl sectioned mouse diaphragm muscle

5. References

1. Frontera, W. R.; Ochala, J., Skeletal Muscle: A Brief Review of Structure and Function. *Calcified Tissue International* **2015,** *96* (3), 183-195.

2. Tipton, K. D.; Hamilton, D. L.; Gallagher, I. J., Assessing the Role of Muscle Protein Breakdown in Response to Nutrition and Exercise in Humans. *Sports Medicine* **2018,** *48* (1), 53-64.

3. Noto, R. E.; Leavitt, L.; Edens, M. A., Physiology, Muscle. In *StatPearls*, StatPearls Publishing

Copyright © 2024, StatPearls Publishing LLC.: Treasure Island (FL) ineligible companies. Disclosure: Logan Leavitt declares no relevant financial relationships with ineligible companies. Disclosure: Mary Ann Edens declares no relevant financial relationships with ineligible companies., 2024.

4. McCuller, C.; Jessu, R.; Callahan, A. L., Physiology, Skeletal Muscle. In *StatPearls*, Treasure Island (FL) with ineligible companies. Disclosure: Rishita Jessu declares no relevant financial relationships with ineligible companies. Disclosure: Avery Callahan declares no relevant financial relationships with ineligible companies., 2024.

5. Lieber, R. L., Muscle fiber length and moment arm coordination during dorsi- and plantarflexion in the mouse hindlimb. *Acta Anat (Basel)* **1997,** *159* (2-3), 84-9.

6. Moo, E. K.; Fortuna, R.; Sibole, S. C.; Abusara, Z.; Herzog, W., In vivo Sarcomere Lengths and Sarcomere Elongations Are Not Uniform across an Intact Muscle. *Front Physiol* **2016,** *7*, 187.

7. Schweitzer, R.; Zelzer, E.; Volk, T., Connecting muscles to tendons: tendons and musculoskeletal development in flies and vertebrates. *Development* **2010,** *137* (17), 2807-17.

8. Hall, Z. W.; Sanes, J. R., Synaptic structure and development: the neuromuscular junction. *Cell* **1993,** *72 Suppl*, 99-121.

9. Yin, H.; Price, F.; Rudnicki, M. A., Satellite cells and the muscle stem cell niche. *Physiol Rev* **2013,** *93* (1), 23-67.

10. Joe, A. W.; Yi, L.; Natarajan, A.; Le Grand, F.; So, L.; Wang, J.; Rudnicki, M. A.; Rossi, F. M., Muscle injury activates resident fibro/adipogenic progenitors that facilitate myogenesis. *Nat Cell Biol* **2010,** *12* (2), 153-63.

11. Arnold, L.; Henry, A.; Poron, F.; Baba-Amer, Y.; van Rooijen, N.; Plonquet, A.; Gherardi, R. K.; Chazaud, B., Inflammatory monocytes recruited after skeletal muscle injury switch into antiinflammatory macrophages to support myogenesis. *J Exp Med* **2007,** *204* (5), 1057-69.

12. Latroche, C.; Weiss-Gayet, M.; Muller, L.; Gitiaux, C.; Leblanc, P.; Liot, S.; Ben-Larbi, S.; Abou-Khalil, R.; Verger, N.; Bardot, P.; Magnan, M.; Chrétien, F.; Mounier, R.; Germain, S.; Chazaud, B., Coupling between Myogenesis and Angiogenesis during Skeletal Muscle Regeneration Is Stimulated by Restorative Macrophages. *Stem Cell Reports* **2017,** *9* (6), 2018-2033.

13. Subramanian, A.; Schilling, T. F., Tendon development and musculoskeletal assembly: emerging roles for the extracellular matrix. *Development* **2015,** *142* (24), 4191-204.

14. Giordani, L.; He, G. J.; Negroni, E.; Sakai, H.; Law, J. Y. C.; Siu, M. M.; Wan, R.; Corneau, A.; Tajbakhsh, S.; Cheung, T. H.; Le Grand, F., High-Dimensional Single-Cell Cartography Reveals Novel Skeletal Muscle-Resident Cell Populations. *Mol Cell* **2019,** *74* (3), 609-621.e6.

15. Hynes, T. R.; Block, S. M.; White, B. T.; Spudich, J. A., Movement of myosin fragments in vitro: domains involved in force production. *Cell* **1987,** *48* (6), 953-63.

16. Spudich, J. A., The myosin swinging cross-bridge model. *Nature Reviews Molecular Cell Biology* **2001,** *2* (5), 387-392.

17. Gautel, M.; Djinović-Carugo, K., The sarcomeric cytoskeleton: from molecules to motion. *Journal of Experimental Biology* **2016,** *219* (2), 135-145.

18. Buonfiglio, V.; Pertici, I.; Marcello, M.; Morotti, I.; Caremani, M.; Reconditi, M.; Linari, M.; Fanelli, D.; Lombardi, V.; Bianco, P., Force and kinetics of fast and slow muscle myosin determined with a synthetic sarcomere-like nanomachine. *Commun Biol* **2024,** *7* (1), 361.

19. Gong, H. M.; Ma, W.; Regnier, M.; Irving, T. C., Thick filament activation is different in fast- and slow-twitch skeletal muscle. *J Physiol* **2022,** *600* (24), 5247-5266.

20. Dong, H.; Tsai, S. Y., Mitochondrial Properties in Skeletal Muscle Fiber. *Cells* **2023,** *12* (17).

21. Schiaffino, S.; Reggiani, C., Fiber types in mammalian skeletal muscles. *Physiol Rev* **2011,** *91* (4), 1447-531.

22. Feige, P.; Brun, C. E.; Ritso, M.; Rudnicki, M. A., Orienting Muscle Stem Cells for Regeneration in Homeostasis, Aging, and Disease. *Cell Stem Cell* **2018,** *23* (5), 653-664.

23. Gioftsidi, S.; Relaix, F.; Mourikis, P., The Notch signaling network in muscle stem cells during development, homeostasis, and disease. *Skeletal Muscle* **2022,** *12* (1), 9.

24. Péault, B.; Rudnicki, M.; Torrente, Y.; Cossu, G.; Tremblay, J. P.; Partridge, T.; Gussoni, E.; Kunkel, L. M.; Huard, J., Stem and Progenitor Cells in Skeletal Muscle Development, Maintenance, and Therapy. *Molecular Therapy* **2007,** *15* (5), 867-877.

25. Choo, H. J.; Canner, J. P.; Vest, K. E.; Thompson, Z.; Pavlath, G. K., A tale of two niches: differential functions for VCAM-1 in satellite cells under basal and injured conditions. *Am J Physiol Cell Physiol* **2017,** *313* (4), C392-c404.

26. Song, W. K.; Wang, W.; Foster, R. F.; Bielser, D. A.; Kaufman, S. J., H36-alpha 7 is a novel integrin alpha chain that is developmentally regulated during skeletal myogenesis. *J Cell Biol* **1992,** *117* (3), 643-57.

27. Liu, J.; Burkin, D. J.; Kaufman, S. J., Increasing alpha 7 beta 1-integrin promotes muscle cell proliferation, adhesion, and resistance to apoptosis without changing gene expression. *Am J Physiol Cell Physiol* **2008,** *294* (2), C627-40.

28. Contreras, O.; Brandan, E., Fibro/adipogenic progenitors safeguard themselves: a novel mechanism to reduce fibrosis is discovered. *J Cell Commun Signal* **2017,** *11* (1), 77-78.

29. Loomis, T.; Hu, L.-Y.; Wohlgemuth, R. P.; Chellakudam, R. R.; Muralidharan, P. D.; Smith, L. R., Matrix stiffness and architecture drive fibro-adipogenic progenitors' activation into myofibroblasts. *Sci Rep-Uk* **2022,** *12* (1), 13582.

30. Sastourné-Arrey, Q.; Mathieu, M.; Contreras, X.; Monferran, S.; Bourlier, V.; Gil-Ortega, M.; Murphy, E.; Laurens, C.; Varin, A.; Guissard, C.; Barreau, C.; André, M.; Juin, N.; Marquès, M.; Chaput, B.; Moro, C.; O'Gorman, D.; Casteilla, L.; Girousse, A.; Sengenès, C., Adipose tissue is a source of regenerative cells that augment the repair of skeletal muscle after injury. *Nat Commun* **2023,** *14* (1), 80.

31. Oreff, G. L.; Maurer, B.; Elkhamary, A. N.; Gerner, I.; Sexl, V.; Jenner, F., Immortalized murine tenocyte cells: a novel and innovative tool for tendon research. *Sci Rep-Uk* **2023,** *13* (1), 1566.

32. Kääriäinen, M.; Järvinen, T.; Järvinen, M.; Rantanen, J.; Kalimo, H., Relation between myofibers and connective tissue during muscle injury repair. *Scand J Med Sci Sports* **2000,** *10* (6), 332-7.

33. Tong, S.; Sun, Y.; Kuang, B.; Wang, M.; Chen, Z.; Zhang, W.; Chen, J., A Comprehensive Review of Muscle–Tendon Junction: Structure, Function, Injury and Repair. *Biomedicines* **2024,** *12* (2), 423.

34. Yucel, N.; Chang, A. C.; Day, J. W.; Rosenthal, N.; Blau, H. M., Humanizing the mdx mouse model of DMD: the long and the short of it. *NPJ Regen Med* **2018,** *3*, 4.

35. Wang, H. V.; Chang, L. W.; Brixius, K.; Wickström, S. A.; Montanez, E.; Thievessen, I.; Schwander, M.; Müller, U.; Bloch, W.; Mayer, U.; Fässler, R., Integrin-linked kinase stabilizes myotendinous junctions and protects muscle from stress-induced damage. *J Cell Biol* **2008,** *180* (5), 1037-49.

36. Boppart, M. D.; Mahmassani, Z. S., Integrin signaling: linking mechanical stimulation to skeletal muscle hypertrophy. *Am J Physiol Cell Physiol* **2019,** *317* (4), C629-c641.

37. Mayer, U.; Saher, G.; Fässler, R.; Bornemann, A.; Echtermeyer, F.; von der Mark, H.; Miosge, N.; Pöschl, E.; von der Mark, K., Absence of integrin alpha 7 causes a novel form of muscular dystrophy. *Nat Genet* **1997,** *17* (3), 318-23.

38. Miosge, N.; Klenczar, C.; Herken, R.; Willem, M.; Mayer, U., Organization of the myotendinous junction is dependent on the presence of alpha7beta1 integrin. *Lab Invest* **1999,** *79* (12), 1591-9.

39. Yoshida, M.; Ozawa, E., Glycoprotein complex anchoring dystrophin to sarcolemma. *J Biochem* **1990,** *108* (5), 748-52.

40. Law, D. J.; Tidball, J. G., Dystrophin deficiency is associated with myotendinous junction defects in prenecrotic and fully regenerated skeletal muscle. *Am J Pathol* **1993,** *142* (5), 1513-23.

41. Koch, M.; Schulze, J.; Hansen, U.; Ashwodt, T.; Keene, D. R.; Brunken, W. J.; Burgeson, R. E.; Bruckner, P.; Bruckner-Tuderman, L., A novel marker of tissue junctions, collagen XXII. *J Biol Chem* **2004,** *279* (21), 22514-21.

42. Karlsen, A.; Yeung, C. C.; Schjerling, P.; Denz, L.; Hoegsbjerg, C.; Jakobsen, J. R.; Krogsgaard, M. R.; Koch, M.; Schiaffino, S.; Kjaer, M.; Mackey, A. L., Distinct myofibre domains of the human myotendinous junction revealed by single-nucleus RNA sequencing. *J Cell Sci* **2023,** *136* (8).

43. Karlsen, A.; Gonzalez-Franquesa, A.; Jakobsen, J. R.; Krogsgaard, M. R.; Koch, M.; Kjaer, M.; Schiaffino, S.; Mackey, A. L.; Deshmukh, A. S., The proteomic profile of the human myotendinous junction. *iScience* **2022,** *25* (2), 103836.

44. Charvet, B.; Ruggiero, F.; Le Guellec, D., The development of the myotendinous junction. A review. *Muscles, ligaments and tendons journal* **2012,** *2 2*, 53-63.

45. Pratt, J.; De Vito, G.; Narici, M.; Boreham, C., Neuromuscular Junction Aging: A Role for Biomarkers and Exercise. *The Journals of Gerontology Series A Biological Sciences and Medical Sciences* **2020**.

46. Bugiardini, E.; Nunes, A. M.; Oliveira-Santos, A.; Dagda, M.; Fontelonga, T. M.; Barraza-Flores, P.; Pittman, A. M.; Morrow, J. M.; Parton, M.; Houlden, H.; Elliott, P. M.; Syrris, P.; Maas, R. P.; Akhtar, M. M.; Küsters, B.; Raaphorst, J.; Schouten, M.; Kamsteeg, E. J.; van Engelen, B.; Hanna, M. G.; Phadke, R.; Lopes, L. R.; Matthews, E.; Burkin, D. J., Integrin α7 Mutations Are Associated With Adult-Onset Cardiac Dysfunction in Humans and Mice. *J Am Heart Assoc* **2022,** *11* (23), e026494.

47. Oliver, K. M.; Florez-Paz, D. M.; Badea, T. C.; Mentis, G. Z.; Menon, V.; de Nooij, J. C., Molecular correlates of muscle spindle and Golgi tendon organ afferents. *Nat Commun* **2021,** *12* (1), 1451.

48. Jozsa, L.; Kannus, P.; Järvinen, T. A.; Balint, J.; Järvinen, M., Number and morphology of mechanoreceptors in the myotendinous junction of paralysed human muscle. *J Pathol* **1996,** *178* (2), 195-200.

49. Davis, L. A.; Fogarty, M. J.; Brown, A.; Sieck, G. C., Structure and Function of the Mammalian Neuromuscular Junction. *Compr Physiol* **2022,** *12* (4), 3731-3766.

50. Tejero, R.; Lopez-Manzaneda, M.; Arumugam, S.; Tabares, L., Synaptotagmin-2, and -1, linked to neurotransmission impairment and vulnerability in Spinal Muscular Atrophy. *Hum Mol Genet* **2016,** *25* (21), 4703-4716.

51. Wu, Y. J.; Tejero, R.; Arancillo, M.; Vardar, G.; Korotkova, T.; Kintscher, M.; Schmitz, D.; Ponomarenko, A.; Tabares, L.; Rosenmund, C., Syntaxin 1B is important for mouse postnatal survival and proper synaptic function at the mouse neuromuscular junctions. *J Neurophysiol* **2015,** *114* (4), 2404-17.

52. Ohkawara, B.; Ito, M.; Ohno, K., Secreted Signaling Molecules at the Neuromuscular Junction in Physiology and Pathology. *Int J Mol Sci* **2021,** *22* (5).

53. Skaper, S. D., Neurotrophic Factors: An Overview. In *Neurotrophic Factors: Methods and Protocols*, Skaper, S. D., Ed. Springer New York: New York, NY, 2018; pp 1-17.

54. Meeker, R. B.; Williams, K. S., The p75 neurotrophin receptor: at the crossroad of neural repair and death. *Neural Regen Res* **2015,** *10* (5), 721-5.

55. Garcia, N.; Tomàs, M.; Santafé, M. M.; Besalduch, N.; Lanuza, M. A.; Tomàs, J., The interaction between tropomyosin-related kinase B receptors and presynaptic muscarinic receptors modulates transmitter release in adult rodent motor nerve terminals. *J Neurosci* **2010,** *30* (49), 16514-22.

56. Kim, N.; Stiegler, A. L.; Cameron, T. O.; Hallock, P. T.; Gomez, A. M.; Huang, J. H.; Hubbard, S. R.; Dustin, M. L.; Burden, S. J., Lrp4 is a receptor for Agrin and forms a complex with MuSK. *Cell* **2008,** *135* (2), 334-42.

57. Glass, D. J.; Bowen, D. C.; Stitt, T. N.; Radziejewski, C.; Bruno, J.; Ryan, T. E.; Gies, D. R.; Shah, S.; Mattsson, K.; Burden, S. J.; DiStefano, P. S.; Valenzuela, D. M.; DeChiara, T. M.; Yancopoulos, G. D., Agrin acts via a MuSK receptor complex. *Cell* **1996,** *85* (4), 513-23.

58. Forsgren, S.; Alfredson, H.; Andersson, G., Further proof of the existence of a non-neuronal cholinergic system in the human Achilles tendon: Presence of the AChRα7 receptor in tendon cells and cells in the peritendinous tissue. *International Immunopharmacology* **2015,** *29* (1), 195-200.

59. Fong, G.; Backman, L. J.; Andersson, G.; Scott, A.; Danielson, P., Human tenocytes are stimulated to proliferate by acetylcholine through an EGFR signalling pathway. *Cell Tissue Res* **2013,** *351* (3), 465-75.

60. Finsterer, J.; Löscher, W. N.; Wanschitz, J.; Quasthoff, S.; Grisold, W., Secondary myopathy due to systemic diseases. *Acta Neurol Scand* **2016,** *134* (6), 388-402.

61. Ling, C.; Dai, Y.; Geng, C.; Pan, S.; Quan, W.; Ding, Q.; Yang, X.; Shen, D.; Tao, Q.; Li, J.; Li, J.; Wang, Y.; Jiang, S.; Wang, Y.; Chen, L.; Cui, L.; Wang, D., Uncovering the true features of dystrophin gene rearrangement and improving the molecular diagnosis of Duchenne and Becker muscular dystrophies. *iScience* **2023,** *26* (12), 108365.

62. Aartsma-Rus, A.; Van Deutekom, J. C.; Fokkema, I. F.; Van Ommen, G. J.; Den Dunnen, J. T., Entries in the Leiden Duchenne muscular dystrophy mutation database: an overview of mutation types and paradoxical cases that confirm the reading-frame rule. *Muscle Nerve* **2006,** *34* (2), 135-44.

63. Ramaswamy, K. S.; Palmer, M. L.; van der Meulen, J. H.; Renoux, A.; Kostrominova, T. Y.; Michele, D. E.; Faulkner, J. A., Lateral transmission of force is impaired in skeletal muscles of dystrophic mice and very old rats. *J Physiol* **2011,** *589* (Pt 5), 1195-208.

64. Yang, S.; Plotnikov, S. V., Mechanosensitive Regulation of Fibrosis. *Cells* **2021,** *10* (5).

65. Stedman, H. H.; Sweeney, H. L.; Shrager, J. B.; Maguire, H. C.; Panettieri, R. A.; Petrof, B.; Narusawa, M.; Leferovich, J. M.; Sladky, J. T.; Kelly, A. M., The mdx mouse diaphragm reproduces the degenerative changes of Duchenne muscular dystrophy. *Nature* **1991,** *352* (6335), 536-9.

66. Karpati, G.; Carpenter, S.; Prescott, S., Small-caliber skeletal muscle fibers do not suffer necrosis in mdx mouse dystrophy. *Muscle Nerve* **1988,** *11* (8), 795-803.

67. Andrysiak, K.; Ferdek, P.; Sanetra, A.; Machaj, G.; Schmidt, L.; Kraszewska, I.; Sarad, K.; Palus-Chramiec, K.; Lis, O.; Targosz-Korecka, M.; Krüger, M.; Lewandowski, M.; Ylla Bou, G.; Stępniewski, J.; Dulak, J., Upregulation of utrophin improves the phenotype of Duchenne muscular dystrophy hiPSC-derived cardiomyocytes. *Molecular Therapy - Nucleic Acids 35* (3).

68. Barton-Davis, E. R.; Cordier, L.; Shoturma, D. I.; Leland, S. E.; Sweeney, H. L., Aminoglycoside antibiotics restore dystrophin function to skeletal muscles of mdx mice. *J Clin Invest* **1999,** *104* (4), 375-81.

69. Elangkovan, N.; Dickson, G., Gene Therapy for Duchenne Muscular Dystrophy. *J Neuromuscul Dis* **2021,** *8* (s2), S303-s316.

70. Deschenes, M. R.; Roby, M. A.; Eason, M. K.; Harris, M. B., Remodeling of the neuromuscular junction precedes sarcopenia related alterations in myofibers. *Exp Gerontol* **2010,** *45* (5), 389-93.

71. Bonaldo, P.; Sandri, M., Cellular and molecular mechanisms of muscle atrophy. *Dis Model Mech* **2013,** *6* (1), 25-39.

72. Gao, Y.; Arfat, Y.; Wang, H.; Goswami, N., Muscle Atrophy Induced by Mechanical Unloading: Mechanisms and Potential Countermeasures. *Front Physiol* **2018,** *9*, 235.

73. Rosen, D. R.; Siddique, T.; Patterson, D.; Figlewicz, D. A.; Sapp, P.; Hentati, A.; Donaldson, D.; Goto, J.; O'Regan, J. P.; Deng, H. X.; et al., Mutations in Cu/Zn superoxide dismutase gene are associated with familial amyotrophic lateral sclerosis. *Nature* **1993,** *362* (6415), 59-62.

74. Cunha-Oliveira, T.; Montezinho, L.; Mendes, C.; Firuzi, O.; Saso, L.; Oliveira, P. J.; Silva, F. S. G., Oxidative Stress in Amyotrophic Lateral Sclerosis: Pathophysiology and Opportunities for Pharmacological Intervention. *Oxid Med Cell Longev* **2020,** *2020*, 5021694.

75. Kausar, S.; Wang, F.; Cui, H., The Role of Mitochondria in Reactive Oxygen Species Generation and Its Implications for Neurodegenerative Diseases. *Cells* **2018,** *7* (12).

76. Berdyński, M.; Miszta, P.; Safranow, K.; Andersen, P. M.; Morita, M.; Filipek, S.; Żekanowski, C.; Kuźma-Kozakiewicz, M., SOD1 mutations associated with amyotrophic lateral sclerosis analysis of variant severity. *Sci Rep-Uk* **2022,** *12* (1), 103.

77. Chiu, A. Y.; Zhai, P.; Dal Canto, M. C.; Peters, T. M.; Kwon, Y. W.; Prattis, S. M.; Gurney, M. E., Age-dependent penetrance of disease in a transgenic mouse model of familial amyotrophic lateral sclerosis. *Mol Cell Neurosci* **1995,** *6* (4), 349-62.

78. Barber, S. C.; Shaw, P. J., Oxidative stress in ALS: Key role in motor neuron injury and therapeutic target. *Free Radical Biology and Medicine* **2010,** *48* (5), 629-641.

79. Dal Canto, M. C.; Gurney, M. E., Development of central nervous system pathology in a murine transgenic model of human amyotrophic lateral sclerosis. *Am J Pathol* **1994,** *145* (6), 1271-9.

80. Nilaver, B. I.; Urbanski, H. F., Mechanisms underlying TDP-43 pathology and neurodegeneration: An updated Mini-Review. *Front Aging Neurosci* **2023,** *15*, 1142617.

81. Belov Kirdajova, D.; Kriska, J.; Tureckova, J.; Anderova, M., Ischemia-Triggered Glutamate Excitotoxicity From the Perspective of Glial Cells. *Front Cell Neurosci* **2020,** *14*, 51.

82. Gwon, Y.; Maxwell, B. A.; Kolaitis, R. M.; Zhang, P.; Kim, H. J.; Taylor, J. P., Ubiquitination of G3BP1 mediates stress granule disassembly in a context-specific manner. *Science* **2021,** *372* (6549), eabf6548.

83. Ionescu, A.; Altman, T.; Perlson, E., Looking for answers far away from the soma—the (un)known axonal functions of TDP-43, and their contribution to early NMJ disruption in ALS. *Molecular Neurodegeneration* **2023,** *18* (1), 35.

84. Altman, T.; Ionescu, A.; Ibraheem, A.; Priesmann, D.; Gradus-Pery, T.; Farberov, L.; Alexandra, G.; Shelestovich, N.; Dafinca, R.; Shomron, N.; Rage, F.; Talbot, K.; Ward, M. E.; Dori, A.; Krüger, M.; Perlson, E., Axonal TDP-43 condensates drive neuromuscular junction disruption through inhibition of local synthesis of nuclear encoded mitochondrial proteins. *Nature Communications* **2021,** *12* (1), 6914.

85. Damer, A.; El Meniawy, S.; McPherson, R.; Wells, G.; Harper, M. E.; Dent, R., Association of muscle fiber type with measures of obesity: A systematic review. *Obes Rev* **2022,** *23* (7), e13444.

86. Civitarese, A. E.; Carling, S.; Heilbronn, L. K.; Hulver, M. H.; Ukropcova, B.; Deutsch, W. A.; Smith, S. R.; Ravussin, E., Calorie restriction increases muscle mitochondrial biogenesis in healthy humans. *PLoS Med* **2007,** *4* (3), e76.

87. Sandri, M.; Barberi, L.; Bijlsma, A. Y.; Blaauw, B.; Dyar, K. A.; Milan, G.; Mammucari, C.; Meskers, C. G.; Pallafacchina, G.; Paoli, A.; Pion, D.; Roceri, M.; Romanello, V.; Serrano, A. L.; Toniolo, L.; Larsson, L.; Maier, A. B.; Muñoz-Cánoves, P.; Musarò, A.; Pende, M.; Reggiani, C.; Rizzuto, R.; Schiaffino, S., Signalling pathways regulating muscle mass in ageing skeletal muscle: the role of the IGF1-Akt-mTOR-FoxO pathway. *Biogerontology* **2013,** *14* (3), 303-23.

88. Ham, D. J.; Börsch, A.; Chojnowska, K.; Lin, S.; Leuchtmann, A. B.; Ham, A. S.; Thürkauf, M.; Delezie, J.; Furrer, R.; Burri, D.; Sinnreich, M.; Handschin, C.; Tintignac, L. A.; Zavolan, M.; Mittal, N.; Rüegg, M. A., Distinct and additive effects of calorie restriction and rapamycin in aging skeletal muscle. *Nature Communications* **2022,** *13* (1), 2025.

89. Gomes, M. D.; Lecker, S. H.; Jagoe, R. T.; Navon, A.; Goldberg, A. L., Atrogin-1, a muscle-specific F-box protein highly expressed during muscle atrophy. *Proc Natl Acad Sci U S A* **2001,** *98* (25), 14440-5.

90. Bodine, S. C.; Latres, E.; Baumhueter, S.; Lai, V. K.; Nunez, L.; Clarke, B. A.; Poueymirou, W. T.; Panaro, F. J.; Na, E.; Dharmarajan, K.; Pan, Z. Q.; Valenzuela, D. M.; DeChiara, T. M.; Stitt, T. N.; Yancopoulos, G. D.; Glass, D. J., Identification of ubiquitin ligases required for skeletal muscle atrophy. *Science* **2001,** *294* (5547), 1704-8.

91. Skinner, S. K.; Fenton, A. I.; Konokhova, Y.; Hepple, R. T., Variation in muscle and neuromuscular junction morphology between atrophy-resistant and atrophy-prone muscles supports failed re-innervation in aging muscle atrophy. *Experimental Gerontology* **2021,** *156*, 111613.

92. Lee, W. S.; Cheung, W. H.; Qin, L.; Tang, N.; Leung, K. S., Age-associated decrease of type IIA/B human skeletal muscle fibers. *Clin Orthop Relat Res* **2006,** *450*, 231-7.

93. Nilwik, R.; Snijders, T.; Leenders, M.; Groen, B. B.; van Kranenburg, J.; Verdijk, L. B.; van Loon, L. J., The decline in skeletal muscle mass with aging is mainly attributed to a reduction in type II muscle fiber size. *Exp Gerontol* **2013,** *48* (5), 492-8.

94. Serrano, N.; Hyatt, J. K.; Houmard, J. A.; Murgia, M.; Katsanos, C. S., Muscle fiber phenotype: a culprit of abnormal metabolism and function in skeletal muscle of humans with obesity. *Am J Physiol Endocrinol Metab* **2023,** *325* (6), E723-E733.

95. Garvey, W. T.; Maianu, L.; Zhu, J. H.; Hancock, J. A.; Golichowski, A. M., Multiple defects in the adipocyte glucose transport system cause cellular insulin resistance in gestational diabetes. Heterogeneity in the number and a novel abnormality in subcellular localization of GLUT4 glucose transporters. *Diabetes* **1993,** *42* (12), 1773-85.

96. Huang, X.; Liu, G.; Guo, J.; Su, Z., The PI3K/AKT pathway in obesity and type 2 diabetes. *Int J Biol Sci* **2018,** *14* (11), 1483-1496.

97. Sylow, L.; Tokarz, V. L.; Richter, E. A.; Klip, A., The many actions of insulin in skeletal muscle, the paramount tissue determining glycemia. *Cell Metabolism* **2021,** *33* (4), 758-780.

98. Pennathur, S.; Heinecke, J. W., Mechanisms of oxidative stress in diabetes: implications for the pathogenesis of vascular disease and antioxidant therapy. *Front Biosci* **2004,** *9*, 565-74.

99. Koshiba, T.; Detmer, S. A.; Kaiser, J. T.; Chen, H.; McCaffery, J. M.; Chan, D. C., Structural basis of mitochondrial tethering by mitofusin complexes. *Science* **2004,** *305* (5685), 858-62.

100. Chang, C. R.; Manlandro, C. M.; Arnoult, D.; Stadler, J.; Posey, A. E.; Hill, R. B.; Blackstone, C., A lethal de novo mutation in the middle domain of the dynamin-related GTPase Drp1 impairs higher order assembly and mitochondrial division. *J Biol Chem* **2010,** *285* (42), 32494-503.

101. Tondera, D.; Czauderna, F.; Paulick, K.; Schwarzer, R.; Kaufmann, J.; Santel, A., The mitochondrial protein MTP18 contributes to mitochondrial fission in mammalian cells. *J Cell Sci* **2005,** *118* (Pt 14), 3049-59.

102. Donnarumma, E.; Kohlhaas, M.; Vimont, E.; Kornobis, E.; Chaze, T.; Gianetto, Q. G.; Matondo, M.; Moya-Nilges, M.; Maack, C.; Wai, T., Mitochondrial Fission Process 1 controls inner membrane integrity and protects against heart failure. *Nat Commun* **2022,** *13* (1), 6634.

103. Chen, C.; Wang, J.; Pan, D.; Wang, X.; Xu, Y.; Yan, J.; Wang, L.; Yang, X.; Yang, M.; Liu, G. P., Applications of multi-omics analysis in human diseases. *MedComm (2020)* **2023,** *4* (4), e315.

104. Meier, F.; Beck, S.; Grassl, N.; Lubeck, M.; Park, M. A.; Raether, O.; Mann, M., Parallel Accumulation–Serial Fragmentation (PASEF): Multiplying Sequencing Speed and Sensitivity by Synchronized Scans in a Trapped Ion Mobility Device. *Journal of Proteome Research* **2015,** *14* (12), 5378-5387.

105. Giebelstein, J.; Poschmann, G.; Højlund, K.; Schechinger, W.; Dietrich, J. W.; Levin, K.; Beck-Nielsen, H.; Podwojski, K.; Stühler, K.; Meyer, H. E.; Klein, H. H., The proteomic signature of insulin-resistant human skeletal muscle reveals increased glycolytic and decreased mitochondrial enzymes. *Diabetologia* **2012,** *55* (4), 1114-27.

106. Kleinert, M.; Parker, B. L.; Jensen, T. E.; Raun, S. H.; Pham, P.; Han, X.; James, D. E.; Richter, E. A.; Sylow, L., Quantitative proteomic characterization of cellular pathways associated with altered insulin sensitivity in skeletal muscle following high-fat diet feeding and exercise training. *Sci Rep-Uk* **2018,** *8* (1), 10723.

107. Schönke, M.; Björnholm, M.; Chibalin, A. V.; Zierath, J. R.; Deshmukh, A. S., Proteomics Analysis of Skeletal Muscle from Leptin-Deficient ob/ob Mice Reveals Adaptive Remodeling of Metabolic Characteristics and Fiber Type Composition. *Proteomics* **2018,** *18* (5-6), e1700375.

108. Deshmukh, A. S.; Steenberg, D. E.; Hostrup, M.; Birk, J. B.; Larsen, J. K.; Santos, A.; Kjøbsted, R.; Hingst, J. R.; Schéele, C. C.; Murgia, M.; Kiens, B.; Richter, E. A.; Mann, M.; Wojtaszewski, J. F. P., Deep muscle-proteomic analysis of freeze-dried human muscle biopsies reveals fiber type-specific adaptations to exercise training. *Nature Communications* **2021,** *12* (1), 304.

109. Roberts, M. D.; Ruple, B. A.; Godwin, J. S.; McIntosh, M. C.; Chen, S. Y.; Kontos, N. J.; Agyin-Birikorang, A.; Max Michel, J.; Plotkin, D. L.; Mattingly, M. L.; Brooks Mobley, C.; Ziegenfuss, T. N.; Fruge, A. D.; Kavazis, A. N., A novel deep proteomic approach in human skeletal muscle unveils distinct molecular signatures affected by aging and resistance training. *bioRxiv* **2023**.

110. Kallabis, S.; Abraham, L.; Muller, S.; Dzialas, V.; Turk, C.; Wiederstein, J. L.; Bock, T.; Nolte, H.; Nogara, L.; Blaauw, B.; Braun, T.; Kruger, M., High-throughput proteomics fiber typing (ProFiT) for comprehensive characterization of single skeletal muscle fibers. *Skelet Muscle* **2020,** *10* (1), 7.

111. Dowling, P.; Trollet, C.; Muraine, L.; Negroni, E.; Swandulla, D.; Ohlendieck, K., The potential of proteomics for in-depth bioanalytical investigations of satellite cell function in applied myology. *Expert Review of Proteomics*, 1-7.

112. Reggio, A.; Rosina, M.; Krahmer, N.; Palma, A.; Petrilli, L. L.; Maiolatesi, G.; Massacci, G.; Salvatori, I.; Valle, C.; Testa, S.; Gargioli, C.; Fuoco, C.; Castagnoli, L.; Cesareni, G.; Sacco, F., Metabolic reprogramming of fibro/adipogenic progenitors facilitates muscle regeneration. *Life Sci Alliance* **2020,** *3* (3).

113. Hynes, R. O.; Naba, A., Overview of the matrisome--an inventory of extracellular matrix constituents and functions. *Cold Spring Harb Perspect Biol* **2012,** *4* (1), a004903.

114. Csapo, R.; Gumpenberger, M.; Wessner, B., Skeletal Muscle Extracellular Matrix - What Do We Know About Its Composition, Regulation, and Physiological Roles? A Narrative Review. *Front Physiol* **2020,** *11*, 253.

115. Kjaer, M., Role of extracellular matrix in adaptation of tendon and skeletal muscle to mechanical loading. *Physiol Rev* **2004,** *84* (2), 649-98.

116. Jozsa, L.; Balint, J.; Kannus, P.; Jarvinen, M.; Lehto, M., Mechanoreceptors in human myotendinous junction. *Muscle Nerve* **1993,** *16* (5), 453-7.

117. Jarvinen, T. A.; Jozsa, L.; Kannus, P.; Jarvinen, T. L.; Hurme, T.; Kvist, M.; Pelto-Huikko, M.; Kalimo, H.; Jarvinen, M., Mechanical loading regulates the expression of tenascin-C in the myotendinous junction and tendon but does not induce de novo synthesis in the skeletal muscle. *J Cell Sci* **2003,** *116* (Pt 5), 857-66.

118. Jacobson, K. R.; Lipp, S.; Acuna, A.; Leng, Y.; Bu, Y.; Calve, S., Comparative Analysis of the Extracellular Matrix Proteome across the Myotendinous Junction. *J Proteome Res* **2020,** *19* (10), 3955-3967.

119. Peffers, M. J.; Thorpe, C. T.; Collins, J. A.; Eong, R.; Wei, T. K.; Screen, H. R.; Clegg, P. D., Proteomic analysis reveals age-related changes in tendon matrix composition, with age- and injury-specific matrix fragmentation. *J Biol Chem* **2014,** *289* (37), 25867-78.

120. Murgia, M.; Nogara, L.; Baraldo, M.; Reggiani, C.; Mann, M.; Schiaffino, S., Protein profile of fiber types in human skeletal muscle: a single-fiber proteomics study. *Skelet Muscle* **2021,** *11* (1), 24.

121. Lang, F.; Aravamudhan, S.; Nolte, H.; Turk, C.; Holper, S.; Muller, S.; Gunther, S.; Blaauw, B.; Braun, T.; Kruger, M., Dynamic changes in the mouse skeletal muscle proteome during denervation-induced atrophy. *Dis Model Mech* **2017,** *10* (7), 881-896.

122. Kreimer, S.; Binek, A.; Chazarin, B.; Cho, J. H.; Haghani, A.; Hutton, A.; Marban, E.; Mastali, M.; Meyer, J. G.; Mesquita, T.; Song, Y.; Van Eyk, J.; Parker, S., High-Throughput Single-Cell Proteomic Analysis of Organ-Derived Heterogeneous Cell Populations by Nanoflow Dual-Trap Single-Column Liquid Chromatography. *Anal Chem* **2023,** *95* (24), 9145-9150.

123. Hughes, C. S.; Moggridge, S.; Muller, T.; Sorensen, P. H.; Morin, G. B.; Krijgsveld, J., Single-pot, solid-phase-enhanced sample preparation for proteomics experiments. *Nat Protoc* **2019,** *14* (1), 68-85.

124. Escher, C.; Reiter, L.; MacLean, B.; Ossola, R.; Herzog, F.; Chilton, J.; MacCoss, M. J.; Rinner, O., Using iRT, a normalized retention time for more targeted measurement of peptides. *Proteomics* **2012,** *12* (8), 1111-21.

125. Tusher, V. G.; Tibshirani, R.; Chu, G., Significance analysis of microarrays applied to the ionizing radiation response. *Proc Natl Acad Sci U S A* **2001,** *98* (9), 5116-21.

126. Li, Y.; Wu, T.; Liu, S., Identification and Distinction of Tenocytes and Tendon-Derived Stem Cells. *Front Cell Dev Biol* **2021,** *9*, 629515.

127. Schlattner, U.; Tokarska-Schlattner, M.; Wallimann, T., Mitochondrial creatine kinase in human health and disease. *Biochim Biophys Acta* **2006,** *1762* (2), 164-80.

128. Glancy, B.; Balaban, R. S., Energy metabolism design of the striated muscle cell. *Physiol Rev* **2021,** *101* (4), 1561-1607.

129. Zhou, X.; Tian, F.; Sandzen, J.; Cao, R.; Flaberg, E.; Szekely, L.; Cao, Y.; Ohlsson, C.; Bergo, M. O.; Boren, J.; Akyurek, L. M., Filamin B deficiency in mice results in skeletal malformations and impaired microvascular development. *Proc Natl Acad Sci U S A* **2007,** *104* (10), 3919-24.

130. Jakobsen, J. R.; Schjerling, P.; Svensson, R. B.; Buhl, R.; Carstensen, H.; Koch, M.; Krogsgaard, M. R.; Kjaer, M.; Mackey, A. L., RNA sequencing and immunofluorescence of the myotendinous junction of mature horses and humans. *Am J Physiol Cell Physiol* **2021,** *321* (3), C453-C470.

131. Ubaida-Mohien, C.; Lyashkov, A.; Gonzalez-Freire, M.; Tharakan, R.; Shardell, M.; Moaddel, R.; Semba, R. D.; Chia, C. W.; Gorospe, M.; Sen, R.; Ferrucci, L., Discovery proteomics in aging human skeletal muscle finds change in spliceosome, immunity, proteostasis and mitochondria. *Elife* **2019,** *8*.

132. Just, S.; Meder, B.; Berger, I. M.; Etard, C.; Trano, N.; Patzel, E.; Hassel, D.; Marquart, S.; Dahme, T.; Vogel, B.; Fishman, M. C.; Katus, H. A.; Strähle, U.; Rottbauer, W., The myosin-interacting protein SMYD1 is essential for sarcomere organization. *J Cell Sci* **2011,** *124* (Pt 18), 3127-36.

133. Donlin, L. T.; Andresen, C.; Just, S.; Rudensky, E.; Pappas, C. T.; Kruger, M.; Jacobs, E. Y.; Unger, A.; Zieseniss, A.; Dobenecker, M. W.; Voelkel, T.; Chait, B. T.; Gregorio, C. C.; Rottbauer, W.; Tarakhovsky, A.; Linke, W. A., Smyd2 controls cytoplasmic lysine methylation of Hsp90 and myofilament organization. *Genes Dev* **2012,** *26* (2), 114-9.

134. Kivela, R.; Kyrolainen, H.; Selanne, H.; Komi, P. V.; Kainulainen, H.; Vihko, V., A single bout of exercise with high mechanical loading induces the expression of Cyr61/CCN1 and CTGF/CCN2 in human skeletal muscle. *J Appl Physiol (1985)* **2007,** *103* (4), 1395-401.

135. Paracchini, S.; Thomas, A.; Castro, S.; Lai, C.; Paramasivam, M.; Wang, Y.; Keating, B. J.; Taylor, J. M.; Hacking, D. F.; Scerri, T.; Francks, C.; Richardson, A. J.; Wade-Martins, R.; Stein, J. F.; Knight, J. C.; Copp, A. J.; Loturco, J.; Monaco, A. P., The chromosome 6p22 haplotype associated with dyslexia reduces the expression of KIAA0319, a novel gene involved in neuronal migration. *Hum Mol Genet* **2006,** *15* (10), 1659-66.

136. Platt, M. P.; Adler, W. T.; Mehlhorn, A. J.; Johnson, G. C.; Wright, K. A.; Choi, R. T.; Tsang, W. H.; Poon, M. W.; Yeung, S. Y.; Waye, M. M.; Galaburda, A. M.; Rosen, G. D., Embryonic disruption of the candidate dyslexia susceptibility gene homolog Kiaa0319-like results in neuronal migration disorders. *Neuroscience* **2013,** *248*, 585-93.

137. Gyimesi, G.; Hediger, M. A., Sequence Features of Mitochondrial Transporter Protein Families. *Biomolecules* **2020,** *10* (12).

138. Naba, A.; Clauser, K. R.; Hoersch, S.; Liu, H.; Carr, S. A.; Hynes, R. O., The Matrisome: In Silico Definition and In Vivo Characterization by Proteomics of Normal and Tumor Extracellular Matrices*. *Molecular & Cellular Proteomics* **2012,** *11* (4), M111.014647.

139. Zoppoli, P.; Morganella, S.; Ceccarelli, M., TimeDelay-ARACNE: Reverse engineering of gene networks from time-course data by an information theoretic approach. *BMC Bioinformatics* **2010,** *11*, 154.

140. Basili, D.; Zhang, J. L.; Herbert, J.; Kroll, K.; Denslow, N. D.; Martyniuk, C. J.; Falciani, F.; Antczak, P., In Silico Computational Transcriptomics Reveals Novel Endocrine Disruptors in Largemouth Bass (Micropterus salmoides). *Environ Sci Technol* **2018,** *52* (13), 7553-7565.

141. Sun, M.; Luo, E. Y.; Adams, S. M.; Adams, T.; Ye, Y.; Shetye, S. S.; Soslowsky, L. J.; Birk, D. E., Collagen XI regulates the acquisition of collagen fibril structure, organization and functional properties in tendon. *Matrix Biol* **2020,** *94*, 77-94.

142. Sherratt, M. J.; Baldock, C.; Louise Haston, J.; Holmes, D. F.; Jones, C. J. P.; Adrian Shuttleworth, C.; Wess, T. J.; Kielty, C. M., Fibrillin Microfibrils are Stiff Reinforcing Fibres in Compliant Tissues. *Journal of Molecular Biology* **2003,** *332* (1), 183-193.

143. Tsuda, T., Extracellular Interactions between Fibulins and Transforming Growth Factor (TGF)-beta in Physiological and Pathological Conditions. *Int J Mol Sci* **2018,** *19* (9).

144. Jakobsen, J. R.; Jakobsen, N. R.; Mackey, A. L.; Koch, M.; Kjaer, M.; Krogsgaard, M. R., Remodeling of muscle fibers approaching the human myotendinous junction. *Scand J Med Sci Sports* **2018,** *28* (8), 1859-1865.

145. Petrany, M. J.; Swoboda, C. O.; Sun, C.; Chetal, K.; Chen, X.; Weirauch, M. T.; Salomonis, N.; Millay, D. P., Single-nucleus RNA-seq identifies transcriptional heterogeneity in multinucleated skeletal myofibers. *Nat Commun* **2020,** *11* (1), 6374.

146. Black, S.; Phillips, D.; Hickey, J. W.; Kennedy-Darling, J.; Venkataraaman, V. G.; Samusik, N.; Goltsev, Y.; Schürch, C. M.; Nolan, G. P., CODEX multiplexed tissue imaging with DNA-conjugated antibodies. *Nat Protoc* **2021,** *16* (8), 3802-3835.

147. Wang, T.; Tian, X.; Kim, H. B.; Jang, Y.; Huang, Z.; Na, C. H.; Wang, J., Intracellular energy controls dynamics of stress-induced ribonucleoprotein granules. *Nat Commun* **2022,** *13* (1), 5584.

148. Poon, M. W.; Tsang, W. H.; Chan, S. O.; Li, H. M.; Ng, H. K.; Waye, M. M., Dyslexia-associated kiaa0319-like protein interacts with axon guidance receptor nogo receptor 1. *Cell Mol Neurobiol* **2011,** *31* (1), 27-35.

149. Schmid, R. S.; Maness, P. F., L1 and NCAM adhesion molecules as signaling coreceptors in neuronal migration and process outgrowth. *Curr Opin Neurobiol* **2008,** *18* (3), 245-50.

150. Stipp, C. S.; Kolesnikova, T. V.; Hemler, M. E., EWI-2 regulates alpha3beta1 integrin-dependent cell functions on laminin-5. *J Cell Biol* **2003,** *163* (5), 1167-77.

151. Wang, H. X.; Hemler, M. E., Novel impact of EWI-2, CD9, and CD81 on TGF-beta signaling in melanoma. *Mol Cell Oncol* **2015,** *2* (1).

152. Kunji, E. R. S.; King, M. S.; Ruprecht, J. J.; Thangaratnarajah, C., The SLC25 Carrier Family: Important Transport Proteins in Mitochondrial Physiology and Pathology. *Physiology (Bethesda)* **2020,** *35* (5), 302-327.

153. Lei, I.; Tian, S.; Gao, W.; Liu, L.; Guo, Y.; Tang, P.; Chen, E.; Wang, Z., Acetyl-CoA production by specific metabolites promotes cardiac repair after myocardial infarction via histone acetylation. *Elife* **2021,** *10*.

154. Pouikli, A.; Parekh, S.; Maleszewska, M.; Nikopoulou, C.; Baghdadi, M.; Tripodi, I.; Folz-Donahue, K.; Hinze, Y.; Mesaros, A.; Hoey, D.; Giavalisco, P.; Dowell, R.; Partridge, L.; Tessarz, P., Chromatin remodeling due to degradation of citrate carrier impairs osteogenesis of aged mesenchymal stem cells. *Nat Aging* **2021,** *1* (9), 810-825.

155. Kay, E. J.; Paterson, K.; Riera-Domingo, C.; Sumpton, D.; Dabritz, J. H. M.; Tardito, S.; Boldrini, C.; Hernandez-Fernaud, J. R.; Athineos, D.; Dhayade, S.; Stepanova, E.; Gjerga, E.; Neilson, L. J.; Lilla, S.; Hedley, A.; Koulouras, G.; McGregor, G.; Jamieson, C.; Johnson, R. M.; Park, M.; Kirschner, K.; Miller, C.; Kamphorst, J. J.; Loayza-Puch, F.; Saez-Rodriguez, J.; Mazzone, M.; Blyth, K.; Zagnoni, M.; Zanivan, S., Cancer-associated fibroblasts require proline synthesis by PYCR1 for the deposition of pro-tumorigenic extracellular matrix. *Nat Metab* **2022,** *4* (6), 693-710.

156. Yang, F.; Chung, A. C.; Huang, X. R.; Lan, H. Y., Angiotensin II induces connective tissue growth factor and collagen I expression via transforming growth factor-beta-dependent and -independent Smad pathways: the role of Smad3. *Hypertension* **2009,** *54* (4), 877-84.

157. Nyyssönen, T.; Lantto, I.; Lüthje, P.; Selander, T.; Kröger, H., Drug treatments associated with Achilles tendon rupture. A case-control study involving 1118 Achilles tendon ruptures. *Scand J Med Sci Sports* **2018,** *28* (12), 2625-2629.

158. Lacheta, L.; Gao, X.; Miles, J. W.; Murata, Y.; Fukase, N.; Utsunomiya, H.; Dornan, G.; Tashman, S.; Kashyap, R.; Altintas, B.; Ravuri, S.; Philippon, M.; Huard, J.; Millett, P. J., Losartan in Combination With Bone Marrow Stimulation Showed Synergistic Effects on Load to Failure and Tendon Matrix Organization in a Rabbit Model. *Arthroscopy: The Journal of Arthroscopic & Related Surgery* **2023,** *39* (12), 2408-2419.

159. Diop-Frimpong, B.; Chauhan, V. P.; Krane, S.; Boucher, Y.; Jain, R. K., Losartan inhibits collagen I synthesis and improves the distribution and efficacy of nanotherapeutics in tumors. *Proc Natl Acad Sci U S A* **2011,** *108* (7), 2909-14.

160. Hocevar, B. A.; Prunier, C.; Howe, P. H., Disabled-2 (Dab2) mediates transforming growth factor beta (TGFbeta)-stimulated fibronectin synthesis through TGFbeta-activated kinase 1 and activation of the JNK pathway. *J Biol Chem* **2005,** *280* (27), 25920-7.

161. Perez-Riverol, Y.; Bai, J.; Bandla, C.; Garcia-Seisdedos, D.; Hewapathirana, S.; Kamatchinathan, S.; Kundu, D. J.; Prakash, A.; Frericks-Zipper, A.; Eisenacher, M.; Walzer, M.; Wang, S.; Brazma, A.;

Vizcaino, J. A., The PRIDE database resources in 2022: a hub for mass spectrometry-based proteomics evidences. *Nucleic Acids Res* **2022,** *50* (D1), D543-D552.

162. Demichev, V.; Messner, C. B.; Vernardis, S. I.; Lilley, K. S.; Ralser, M., DIA-NN: neural networks and interference correction enable deep proteome coverage in high throughput. *Nature Methods* **2020,** *17* (1), 41-44.

163. Cox, J.; Hein, M. Y.; Luber, C. A.; Paron, I.; Nagaraj, N.; Mann, M., Accurate proteome-wide label-free quantification by delayed normalization and maximal peptide ratio extraction, termed MaxLFQ. *Mol Cell Proteomics* **2014,** *13* (9), 2513-26.

164. Bruderer, R.; Bernhardt, O. M.; Gandhi, T.; Miladinović, S. M.; Cheng, L.-Y.; Messner, S.; Ehrenberger, T.; Zanotelli, V.; Butscheid, Y.; Escher, C.; Vitek, O.; Rinner, O.; Reiter, L., Extending the Limits of Quantitative Proteome Profiling with Data-Independent Acquisition and Application to Acetaminophen-Treated Three-Dimensional Liver Microtissues*[S]. *Molecular & Cellular Proteomics* **2015,** *14* (5), 1400-1410.

165. Henderson, A. R., The bootstrap: A technique for data-driven statistics. Using computer-intensive analyses to explore experimental data. *Clinica Chimica Acta* **2005,** *359* (1), 1-26.

166. Wenstrup, R. J.; Smith, S. M.; Florer, J. B.; Zhang, G.; Beason, D. P.; Seegmiller, R. E.; Soslowsky, L. J.; Birk, D. E., Regulation of collagen fibril nucleation and initial fibril assembly involves coordinate interactions with collagens V and XI in developing tendon. *J Biol Chem* **2011,** *286* (23), 20455-65.

167. Schmidt, L.; Saynisch, M.; Hoegsbjerg, C.; Schmidt, A.; Mackey, A.; Lackmann, J. W.; Müller, S.; Koch, M.; Brachvogel, B.; Kjaer, M.; Antczak, P.; Krüger, M., Spatial proteomics of skeletal muscle using thin cryosections reveals metabolic adaptation at the muscle-tendon transition zone. *Cell Rep* **2024,** *43* (7), 114374.

168. Rappsilber, J.; Mann, M.; Ishihama, Y., Protocol for micro-purification, enrichment, pre-fractionation and storage of peptides for proteomics using StageTips. *Nat Protoc* **2007,** *2* (8), 1896-906.

169. Rappsilber, J.; Ishihama, Y.; Mann, M., Stop and go extraction tips for matrix-assisted laser desorption/ionization, nanoelectrospray, and LC/MS sample pretreatment in proteomics. *Anal Chem* **2003,** *75* (3), 663-70.

170. Demichev, V.; Messner, C. B.; Vernardis, S. I.; Lilley, K. S.; Ralser, M., DIA-NN: neural networks and interference correction enable deep proteome coverage in high throughput. *Nat Methods* **2020,** *17* (1), 41-44.

171. Cox, J.; Mann, M., MaxQuant enables high peptide identification rates, individualized p.p.b.-range mass accuracies and proteome-wide protein quantification. *Nature Biotechnology* **2008,** *26* (12), 1367-1372.

172. Aryee, M. J.; Gutiérrez-Pabello, J. A.; Kramnik, I.; Maiti, T.; Quackenbush, J., An improved empirical bayes approach to estimating differential gene expression in microarray time-course data: BETR (Bayesian Estimation of Temporal Regulation). *BMC Bioinformatics* **2009,** *10* (1), 409.

173. Hughes, G.; Kopetzky, J.; McRoberts, N., Mutual Information as a Performance Measure for Binary Predictors Characterized by Both ROC Curve and PROC Curve Analysis. *Entropy (Basel)* **2020,** *22* (9).

174. McHugh, M. L., Multiple comparison analysis testing in ANOVA. *Biochem Med (Zagreb)* **2011,** *21* (3), 203-9.

175. Polla, B.; D'Antona, G.; Bottinelli, R.; Reggiani, C., Respiratory muscle fibres: specialisation and plasticity. *Thorax* **2004,** *59* (9), 808-17.

176. Oliver, K. A.; Ashurst, J. V., Anatomy, Thorax, Phrenic Nerves. In *StatPearls*, Treasure Island (FL) ineligible companies. Disclosure: John Ashurst declares no relevant financial relationships with ineligible companies., 2024.

177. Gonzalez-Freire, M.; de Cabo, R.; Studenski, S. A.; Ferrucci, L., The Neuromuscular Junction: Aging at the Crossroad between Nerves and Muscle. *Front Aging Neurosci* **2014,** *6*, 208.

178. Shi, L.; Fu, A. K.; Ip, N. Y., Molecular mechanisms underlying maturation and maintenance of the vertebrate neuromuscular junction. *Trends Neurosci* **2012,** *35* (7), 441-53.

179. Octavian, I.; Emilia, M.; Mihaela, G.; Bogdan, O. P.; Laura Cristina, C., Non-Myelinating Schwann Cells in Health and Disease. In *Demyelination Disorders*, Stavros, J. B.; Fabian, H. R.; Welwin, L., Eds. IntechOpen: Rijeka, 2020; p Ch. 4.

180. Engel, A. G.; Shen, X. M.; Selcen, D.; Sine, S. M., Congenital myasthenic syndromes: pathogenesis, diagnosis, and treatment. *Lancet Neurol* **2015,** *14* (4), 420-34.

181. Wang, W.; Wang, L.; Lu, J.; Siedlak, S. L.; Fujioka, H.; Liang, J.; Jiang, S.; Ma, X.; Jiang, Z.; da Rocha, E. L.; Sheng, M.; Choi, H.; Lerou, P. H.; Li, H.; Wang, X., The inhibition of TDP-43 mitochondrial localization blocks its neuronal toxicity. *Nature Medicine* **2016,** *22* (8), 869-878.

182. Kelley, R. C.; McDonagh, B.; Ferreira, L. F., Advanced aging causes diaphragm functional abnormalities, global proteome remodeling, and loss of mitochondrial cysteine redox flexibility in mice. *Experimental Gerontology* **2018,** *103*, 69-79.

183. Can, T.; Faas, L.; Ashford, D. A.; Dowle, A.; Thomas, J.; O'Toole, P.; Blanco, G., Proteomic analysis of laser capture microscopy purified myotendinous junction regions from muscle sections. *Proteome Sci* **2014,** *12*, 25.

184. Doncheva, N. T.; Morris, J. H.; Gorodkin, J.; Jensen, L. J., Cytoscape StringApp: Network Analysis and Visualization of Proteomics Data. *J Proteome Res* **2019,** *18* (2), 623-632.

185. Huber, L. A.; Pimplikar, S.; Parton, R. G.; Virta, H.; Zerial, M.; Simons, K., Rab8, a small GTPase involved in vesicular traffic between the TGN and the basolateral plasma membrane. *J Cell Biol* **1993,** *123* (1), 35-45.

186. Yamasaki, A.; Tani, K.; Yamamoto, A.; Kitamura, N.; Komada, M., The Ca2+-binding protein ALG-2 is recruited to endoplasmic reticulum exit sites by Sec31A and stabilizes the localization of Sec31A. *Mol Biol Cell* **2006,** *17* (11), 4876-87.

187. Nesbit, M. A.; Hannan, F. M.; Howles, S. A.; Reed, A. A.; Cranston, T.; Thakker, C. E.; Gregory, L.; Rimmer, A. J.; Rust, N.; Graham, U.; Morrison, P. J.; Hunter, S. J.; Whyte, M. P.; McVean, G.; Buck, D.; Thakker, R. V., Mutations in AP2S1 cause familial hypocalciuric hypercalcemia type 3. *Nat Genet* **2013,** *45* (1), 93-7.

188. Benavides Damm, T.; Egli, M., Calcium's role in mechanotransduction during muscle development. *Cell Physiol Biochem* **2014,** *33* (2), 249-72.

189. Lipp, S. N.; Jacobson, K. R.; Colling, H. A.; Tuttle, T. G.; Miles, D. T.; McCreery, K. P.; Calve, S., Mechanical loading is required for initiation of extracellular matrix deposition at the developing murine myotendinous junction. *Matrix Biol* **2023,** *116*, 28-48.

190. Roach, A.; Takahashi, N.; Pravtcheva, D.; Ruddle, F.; Hood, L., Chromosomal mapping of mouse myelin basic protein gene and structure and transcription of the partially deleted gene in shiverer mutant mice. *Cell* **1985,** *42* (1), 149-155.

191. Lepore, E.; Casola, I.; Dobrowolny, G.; Musarò, A., Neuromuscular Junction as an Entity of Nerve-Muscle Communication. *Cells* **2019,** *8* (8).

192. Doi, M.; Iwasaki, K., Na+/K+ ATPase regulates the expression and localization of acetylcholine receptors in a pump activity-independent manner. *Mol Cell Neurosci* **2008,** *38* (4), 548-58.

193. Diaz, J.; Gérard, X.; Emerit, M. B.; Areias, J.; Geny, D.; Dégardin, J.; Simonutti, M.; Guerquin, M. J.; Collin, T.; Viollet, C.; Billard, J. M.; Métin, C.; Hubert, L.; Larti, F.; Kahrizi, K.; Jobling, R.; Agolini, E.; Shaheen, R.; Zigler, A.; Rouiller-Fabre, V.; Rozet, J. M.; Picaud, S.; Novelli, A.; Alameer, S.; Najmabadi, H.; Cohn, R.; Munnich, A.; Barth, M.; Lugli, L.; Alkuraya, F. S.; Blaser, S.; Gashlan, M.; Besmond, C.; Darmon, M.; Masson, J., YIF1B mutations cause a post-natal neurodevelopmental syndrome associated with Golgi and primary cilium alterations. *Brain* **2020,** *143* (10), 2911-2928.

194. Schroeter, C. B.; Nelke, C.; Stascheit, F.; Huntemann, N.; Preusse, C.; Dobelmann, V.; Theissen, L.; Pawlitzki, M.; Räuber, S.; Willison, A.; Vogelsang, A.; Marina, A. D.; Hartung, H.-P.; Melzer, N.; Konen, F. F.; Skripuletz, T.; Hentschel, A.; König, S.; Schweizer, M.; Stühler, K.; Poschmann, G.; Roos, A.; Stenzel, W.; Meisel, A.; Meuth, S. G.; Ruck, T., Inter-alpha-trypsin inhibitor heavy chain H3 is a potential biomarker for disease activity in myasthenia gravis. *Acta Neuropathologica* **2024,** *147* (1), 102.

195. Evans, W. J., Skeletal muscle loss: cachexia, sarcopenia, and inactivity. *Am J Clin Nutr* **2010,** *91* (4), 1123s-1127s.

196. Volpi, E.; Nazemi, R.; Fujita, S., Muscle tissue changes with aging. *Curr Opin Clin Nutr Metab Care* **2004,** *7* (4), 405-10.

197. Li, L.; Xiong, W. C.; Mei, L., Neuromuscular Junction Formation, Aging, and Disorders. *Annu Rev Physiol* **2018,** *80*, 159-188.

198. Jonas, A. M., The mouse in biomedical research. *Physiologist* **1984,** *27* (5), 330-46.

199. Wokke, J. H.; Jennekens, F. G.; van den Oord, C. J.; Veldman, H.; Smit, L. M.; Leppink, G. J., Morphological changes in the human end plate with age. *J Neurol Sci* **1990,** *95* (3), 291-310.

200. Siu, P. M.; Alway, S. E., Response and adaptation of skeletal muscle to denervation stress: the role of apoptosis in muscle loss. *Front Biosci (Landmark Ed)* **2009,** *14* (2), 432-52.

201. Borkum, J. M., The Tricarboxylic Acid Cycle as a Central Regulator of the Rate of Aging: Implications for Metabolic Interventions. *Adv Biol (Weinh)* **2023,** *7* (7), e2300095.

202. Bader, B. L.; Smyth, N.; Nedbal, S.; Miosge, N.; Baranowsky, A.; Mokkapati, S.; Murshed, M.; Nischt, R., Compound Genetic Ablation of Nidogen 1 and 2 Causes Basement Membrane Defects and Perinatal Lethality in Mice. *Molecular and Cellular Biology* **2005,** *25* (15), 6846-6856.

203. Grimpe, B.; Probst, J. C.; Hager, G., Suppression of nidogen-1 translation by antisense targeting affects the adhesive properties of cultured astrocytes. *Glia* **1999,** *28* (2), 138-49.

204. Reed, M. J.; Damodarasamy, M.; Banks, W. A., The extracellular matrix of the blood–brain barrier: structural and functional roles in health, aging, and Alzheimer's disease. *Tissue Barriers* **2019,** *7* (4), 1651157.

205. Walker, A. K.; Spiller, K. J.; Ge, G.; Zheng, A.; Xu, Y.; Zhou, M.; Tripathy, K.; Kwong, L. K.; Trojanowski, J. Q.; Lee, V. M., Functional recovery in new mouse models of ALS/FTLD after clearance of pathological cytoplasmic TDP-43. *Acta Neuropathol* **2015,** *130* (5), 643-60.

206. Tian, Y.; Chang, J. C.; Fan, E. Y.; Flajolet, M.; Greengard, P., Adaptor complex AP2/PICALM, through interaction with LC3, targets Alzheimer's APP-CTF for terminal degradation via autophagy. *Proc Natl Acad Sci U S A* **2013,** *110* (42), 17071-6.

207. Tziortzouda, P.; Steyaert, J.; Scheveneels, W.; Sicart, A.; Stoklund Dittlau, K.; Barbosa Correia, A. M.; Burg, T.; Pal, A.; Hermann, A.; Van Damme, P.; Moens, T. G.; Van Den Bosch, L., PP2A and GSK3 act as modifiers of FUS-ALS by modulating mitochondrial transport. *Acta Neuropathol* **2024,** *147* (1), 41.

208. Flinn, L. J.; Keatinge, M.; Bretaud, S.; Mortiboys, H.; Matsui, H.; De Felice, E.; Woodroof, H. I.; Brown, L.; McTighe, A.; Soellner, R.; Allen, C. E.; Heath, P. R.; Milo, M.; Muqit, M. M.; Reichert, A. S.; Köster, R. W.; Ingham, P. W.; Bandmann, O., TigarB causes mitochondrial dysfunction and neuronal loss in PINK1 deficiency. *Ann Neurol* **2013,** *74* (6), 837-47.

209. López, K. L. R.; Simpson, J. E.; Watson, L. C.; Mortiboys, H.; Hautbergue, G. M.; Bandmann, O.; Highley, J. R., TIGAR inclusion pathology is specific for Lewy body diseases. *Brain Res* **2019,** *1706*, 218-223.

210. Gascón, E.; Zaragoza, P.; Calvo, A. C.; Osta, R., Sporadic Amyotrophic Lateral Sclerosis Skeletal Muscle Transcriptome Analysis: A Comprehensive Examination of Differentially Expressed Genes. *Biomolecules* **2024,** *14* (3).

211. Jia, Y.; Gao, M. D.; Liu, Y. F.; Lu, L.; Chen, G.; Chen, Y., Genetic dissection of glutathione S-transferase omega-1: identification of novel downstream targets and Alzheimer's disease pathways. *Neural Regen Res* **2022,** *17* (11), 2452-2458.

212. Iwahara, N.; Azekami, K.; Hosoda, R.; Nojima, I.; Hisahara, S.; Kuno, A., Activation of SIRT1 promotes membrane resealing via cortactin. *Sci Rep* **2022,** *12* (1), 15328.

213. Kopp, D. M.; Trachtenberg, J. T.; Thompson, W. J., Glial growth factor rescues Schwann cells of mechanoreceptors from denervation-induced apoptosis. *J Neurosci* **1997,** *17* (17), 6697-706.

214. Sternberger, N. H.; McFarlin, D. E.; Traugott, U.; Raine, C. S., Myelin basic protein and myelin-associated glycoprotein in chronic, relapsing experimental allergic encephalomyelitis. *Journal of Neuroimmunology* **1984,** *6* (4), 217-229.

215. Jacob, C.; Lötscher, P.; Engler, S.; Baggiolini, A.; Varum Tavares, S.; Brügger, V.; John, N.; Büchmann-Møller, S.; Snider, P. L.; Conway, S. J.; Yamaguchi, T.; Matthias, P.; Sommer, L.; Mantei, N.; Suter, U., HDAC1 and HDAC2 control the specification of neural crest cells into peripheral glia. *J Neurosci* **2014,** *34* (17), 6112-22.

216. Poitelon, Y.; Kopec, A. M.; Belin, S., Myelin Fat Facts: An Overview of Lipids and Fatty Acid Metabolism. *Cells* **2020,** *9* (4).

217. Kister, A.; Kister, I., Overview of myelin, major myelin lipids, and myelin-associated proteins. *Front Chem* **2022,** *10*, 1041961.

218. Taetzsch, T.; Valdez, G., NMJ maintenance and repair in aging. *Curr Opin Physiol* **2018,** *4*, 57-64.

219. Zhuo, L.; Kimata, K., Structure and function of inter-alpha-trypsin inhibitor heavy chains. *Connect Tissue Res* **2008,** *49* (5), 311-20.

220. Adair, J. E.; Stober, V.; Sobhany, M.; Zhuo, L.; Roberts, J. D.; Negishi, M.; Kimata, K.; Garantziotis, S., Inter-alpha-trypsin inhibitor promotes bronchial epithelial repair after injury through vitronectin binding. *J Biol Chem* **2009,** *284* (25), 16922-16930.

221. Trougakos, I. P.; Gonos, E. S., Clusterin/apolipoprotein J in human aging and cancer. *Int J Biochem Cell Biol* **2002,** *34* (11), 1430-48.

222. Meneses, A.; Koga, S.; O'Leary, J.; Dickson, D. W.; Bu, G.; Zhao, N., TDP-43 Pathology in Alzheimer's Disease. *Mol Neurodegener* **2021,** *16* (1), 84.

223. Yang, C. F.; Tsai, W. C., Calmodulin: The switch button of calcium signaling. *Tzu Chi Med J* **2022,** *34* (1), 15-22.

224. Xia, Z.; Storm, D. R., The role of calmodulin as a signal integrator for synaptic plasticity. *Nature Reviews Neuroscience* **2005,** *6* (4), 267-276.

225. Ureshino, R. P.; Rocha, K. K.; Lopes, G. S.; Bincoletto, C.; Smaili, S. S., Calcium signaling alterations, oxidative stress, and autophagy in aging. *Antioxid Redox Signal* **2014,** *21* (1), 123-37.

226. Morales, P. E.; Monsalves-Álvarez, M.; Tadinada, S. M.; Harris, M. P.; Ramírez-Sagredo, A.; Ortiz-Quintero, J.; Troncoso, M. F.; De Gregorio, N.; Calle, X.; Pereira, R. O.; Lira, V. A.; Espinosa, A.; Abel, E. D.; Lavandero, S., Skeletal muscle type-specific mitochondrial adaptation to high-fat diet relies on differential autophagy modulation. *Faseb j* **2021,** *35* (10), e21933.

227. Zappia, L.; Oshlack, A., Clustering trees: a visualization for evaluating clusterings at multiple resolutions. *GigaScience* **2018,** *7* (7).

228. Reingold, E. M.; Tilford, J. S., Tidier Drawings of Trees. *IEEE Transactions on Software Engineering* **1981,** *SE-7* (2), 223-228.

229. Stekhoven, D. J.; Bühlmann, P., MissForest--non-parametric missing value imputation for mixed-type data. *Bioinformatics* **2012,** *28* (1), 112-8.

230. Lazar, C.; Gatto, L.; Ferro, M.; Bruley, C.; Burger, T., Accounting for the Multiple Natures of Missing Values in Label-Free Quantitative Proteomics Data Sets to Compare Imputation Strategies. *J Proteome Res* **2016,** *15* (4), 1116-25.

231. Rath, S.; Sharma, R.; Gupta, R.; Ast, T.; Chan, C.; Durham, T. J.; Goodman, R. P.; Grabarek, Z.; Haas, M. E.; Hung, W. H. W.; Joshi, P. R.; Jourdain, A. A.; Kim, S. H.; Kotrys, A. V.; Lam, S. S.; McCoy, J. G.; Meisel, J. D.; Miranda, M.; Panda, A.; Patgiri, A.; Rogers, R.; Sadre, S.; Shah, H.; Skinner, O. S.; To, T. L.; Walker, M. A.; Wang, H.; Ward, P. S.; Wengrod, J.; Yuan, C. C.; Calvo, S. E.; Mootha, V. K., MitoCarta3.0: an updated mitochondrial proteome now with sub-organelle localization and pathway annotations. *Nucleic Acids Res* **2021,** *49* (D1), D1541-d1547.

232. Otoda, T.; Takamura, T.; Misu, H.; Ota, T.; Murata, S.; Hayashi, H.; Takayama, H.; Kikuchi, A.; Kanamori, T.; Shima, K. R.; Lan, F.; Takeda, T.; Kurita, S.; Ishikura, K.; Kita, Y.; Iwayama, K.; Kato, K.; Uno, M.; Takeshita, Y.; Yamamoto, M.; Tokuyama, K.; Iseki, S.; Tanaka, K.; Kaneko, S., Proteasome dysfunction mediates obesity-induced endoplasmic reticulum stress and insulin resistance in the liver. *Diabetes* **2013,** *62* (3), 811-24.

233. Lin, K.; Cheng, W.; Shen, Q.; Wang, H.; Wang, R.; Guo, S.; Wu, X.; Wu, W.; Chen, P.; Wang, Y.; Ye, H.; Zhang, Q.; Wang, R., Lipid Profiling Reveals Lipidomic Signatures of Weight Loss Interventions. *Nutrients* **2023,** *15* (7).

234. van der Veen, J. N.; Kennelly, J. P.; Wan, S.; Vance, J. E.; Vance, D. E.; Jacobs, R. L., The critical role of phosphatidylcholine and phosphatidylethanolamine metabolism in health and disease. *Biochim Biophys Acta Biomembr* **2017,** *1859* (9 Pt B), 1558-1572.

235. Tábara, L. C.; Burr, S. P.; Frison, M.; Chowdhury, S. R.; Paupe, V.; Nie, Y.; Johnson, M.; Villar-Azpillaga, J.; Viegas, F.; Segawa, M.; Anand, H.; Petkevicius, K.; Chinnery, P. F.; Prudent, J., MTFP1 controls mitochondrial fusion to regulate inner membrane quality control and maintain mtDNA levels. *Cell* **2024,** *187* (14), 3619-3637.e27.

236. Stringer, C.; Wang, T.; Michaelos, M.; Pachitariu, M., Cellpose: a generalist algorithm for cellular segmentation. *Nat Methods* **2021,** *18* (1), 100-106.

237. Stirling, D. R.; Swain-Bowden, M. J.; Lucas, A. M.; Carpenter, A. E.; Cimini, B. A.; Goodman, A., CellProfiler 4: improvements in speed, utility and usability. *BMC Bioinformatics* **2021,** *22* (1), 433.

238. Bock, T.; Türk, C.; Aravamudhan, S.; Keufgens, L.; Bloch, W.; Rozsivalova, D. H.; Romanello, V.; Nogara, L.; Blaauw, B.; Trifunovic, A.; Braun, T.; Krüger, M., PERM1 interacts with the MICOS-MIB complex to connect the mitochondria and sarcolemma via ankyrin B. *Nat Commun* **2021,** *12* (1), 4900.

239. Parry, S. M.; Puthucheary, Z. A., The impact of extended bed rest on the musculoskeletal system in the critical care environment. *Extrem Physiol Med* **2015,** *4*, 16.

240. Faitg, J.; Leduc-Gaudet, J. P.; Reynaud, O.; Ferland, G.; Gaudreau, P.; Gouspillou, G., Effects of Aging and Caloric Restriction on Fiber Type Composition, Mitochondrial Morphology and Dynamics in Rat Oxidative and Glycolytic Muscles. *Front Physiol* **2019,** *10*, 420.

241. Denies, M. S.; Johnson, J.; Maliphol, A. B.; Bruno, M.; Kim, A.; Rizvi, A.; Rustici, K.; Medler, S., Diet-induced obesity alters skeletal muscle fiber types of male but not female mice. *Physiol Rep* **2014,** *2* (1), e00204.

242. de Wilde, J.; Mohren, R.; van den Berg, S.; Boekschoten, M.; Dijk, K. W.; de Groot, P.; Müller, M.; Mariman, E.; Smit, E., Short-term high fat-feeding results in morphological and metabolic adaptations in the skeletal muscle of C57BL/6J mice. *Physiol Genomics* **2008,** *32* (3), 360-9.

243. Asmussen, G.; Schmalbruch, I.; Soukup, T.; Pette, D., Contractile properties, fiber types, and myosin isoforms in fast and slow muscles of hyperactive Japanese waltzing mice. *Experimental Neurology* **2003,** *184* (2), 758-766.

244. Xu, L.; Tang, D.; Guan, M.; Xie, C.; Xue, Y., Effect of high-fat diet on peripheral neuropathy in C57BL/6 mice. *Int J Endocrinol* **2014,** *2014*, 305205.

245. Hyatt, J. P.; Nguyen, L.; Hall, A. E.; Huber, A. M.; Kocan, J. C.; Mattison, J. A.; de Cabo, R.; LaRocque, J. R.; Talmadge, R. J., Muscle-Specific Myosin Heavy Chain Shifts in Response to a Long-Term High Fat/High Sugar Diet and Resveratrol Treatment in Nonhuman Primates. *Front Physiol* **2016,** *7*, 77.

246. Koves, T. R.; Ussher, J. R.; Noland, R. C.; Slentz, D.; Mosedale, M.; Ilkayeva, O.; Bain, J.; Stevens, R.; Dyck, J. R.; Newgard, C. B.; Lopaschuk, G. D.; Muoio, D. M., Mitochondrial overload and incomplete fatty acid oxidation contribute to skeletal muscle insulin resistance. *Cell Metab* **2008,** *7* (1), 45-56.

247. Bonnard, C.; Durand, A.; Peyrol, S.; Chanseaume, E.; Chauvin, M. A.; Morio, B.; Vidal, H.; Rieusset, J., Mitochondrial dysfunction results from oxidative stress in the skeletal muscle of diet-induced insulin-resistant mice. *J Clin Invest* **2008,** *118* (2), 789-800.

248. Fabbrizi, E.; Fiorentino, F.; Carafa, V.; Altucci, L.; Mai, A.; Rotili, D., Emerging Roles of SIRT5 in Metabolism, Cancer, and SARS-CoV-2 Infection. *Cells* **2023,** *12* (6), 852.

249. Juszczak, F.; Arnould, T.; Declèves, A.-E., The Role of Mitochondrial Sirtuins (SIRT3, SIRT4 and SIRT5) in Renal Cell Metabolism: Implication for Kidney Diseases. *International Journal of Molecular Sciences* **2024,** *25* (13), 6936.

250. Polletta, L.; Vernucci, E.; Carnevale, I.; Arcangeli, T.; Rotili, D.; Palmerio, S.; Steegborn, C.; Nowak, T.; Schutkowski, M.; Pellegrini, L.; Sansone, L.; Villanova, L.; Runci, A.; Pucci, B.; Morgante,

E.; Fini, M.; Mai, A.; Russo, M. A.; Tafani, M., SIRT5 regulation of ammonia-induced autophagy and mitophagy. *Autophagy* **2015,** *11* (2), 253-70.

251. Hwang, I.; Kim, B. S.; Lee, H. Y.; Cho, S. W.; Lee, S. E.; Ahn, J. Y., PA2G4/EBP1 ubiquitination by PRKN/PARKIN promotes mitophagy protecting neuron death in cerebral ischemia. *Autophagy* **2024,** *20* (2), 365-379.

252. Tang, F.; Wang, B.; Li, N.; Wu, Y.; Jia, J.; Suo, T.; Chen, Q.; Liu, Y. J.; Tang, J., RNF185, a novel mitochondrial ubiquitin E3 ligase, regulates autophagy through interaction with BNIP1. *PLoS One* **2011,** *6* (9), e24367.

253. Ryu, S. W.; Choi, K.; Yoon, J.; Kim, S.; Choi, C., Endoplasmic reticulum-specific BH3-only protein BNIP1 induces mitochondrial fragmentation in a Bcl-2- and Drp1-dependent manner. *J Cell Physiol* **2012,** *227* (8), 3027-35.

254. Virtue, S.; Vidal-Puig, A., GTTs and ITTs in mice: simple tests, complex answers. *Nature Metabolism* **2021,** *3* (7), 883-886.

255. Blaauw, B.; Schiaffino, S.; Reggiani, C., Mechanisms modulating skeletal muscle phenotype. *Compr Physiol* **2013,** *3* (4), 1645-87.

256. Sarto, F.; Bottinelli, R.; Franchi, M. V.; Porcelli, S.; Simunic, B.; Pisot, R.; Narici, M. V., Pathophysiological mechanisms of reduced physical activity: Insights from the human step reduction model and animal analogues. *Acta Physiol (Oxf)* **2023,** *238* (3), e13986.

257. Bertile, F.; Habold, C.; Le Maho, Y.; Giroud, S., Body Protein Sparing in Hibernators: A Source for Biomedical Innovation. *Front Physiol* **2021,** *12*, 634953.

258. Lohuis, T. D.; Harlow, H. J.; Beck, T. D., Hibernating black bears (Ursus americanus) experience skeletal muscle protein balance during winter anorexia. *Comp Biochem Physiol B Biochem Mol Biol* **2007,** *147* (1), 20-8.

259. Laske, T. G.; Garshelis, D. L.; Iaizzo, P. A., Monitoring the wild black bear's reaction to human and environmental stressors. *BMC Physiol* **2011,** *11*, 13.

260. Toien, O.; Blake, J.; Edgar, D. M.; Grahn, D. A.; Heller, H. C.; Barnes, B. M., Hibernation in black bears: independence of metabolic suppression from body temperature. *Science* **2011,** *331* (6019), 906-9.

261. Evans, A. L.; Singh, N. J.; Friebe, A.; Arnemo, J. M.; Laske, T. G.; Frobert, O.; Swenson, J. E.; Blanc, S., Drivers of hibernation in the brown bear. *Front Zool* **2016,** *13*, 7.

262. Chazarin, B.; Ziemianin, A.; Evans, A. L.; Meugnier, E.; Loizon, E.; Chery, I.; Arnemo, J. M.; Swenson, J. E.; Gauquelin-Koch, G.; Simon, C.; Blanc, S.; Lefai, E.; Bertile, F., Limited Oxidative Stress Favors Resistance to Skeletal Muscle Atrophy in Hibernating Brown Bears (Ursus Arctos). *Antioxidants (Basel)* **2019,** *8* (9).

263. Luu, B. E.; Lefai, E.; Giroud, S.; Swenson, J. E.; Chazarin, B.; Gauquelin-Koch, G.; Arnemo, J. M.; Evans, A. L.; Bertile, F.; Storey, K. B., MicroRNAs facilitate skeletal muscle maintenance and metabolic suppression in hibernating brown bears. *J Cell Physiol* **2020,** *235* (4), 3984-3993.

264. Chanon, S.; Chazarin, B.; Toubhans, B.; Durand, C.; Chery, I.; Robert, M.; Vieille-Marchiset, A.; Swenson, J. E.; Zedrosser, A.; Evans, A. L.; Brunberg, S.; Arnemo, J. M.; Gauquelin-Koch, G.; Storey, K. B.; Simon, C.; Blanc, S.; Bertile, F.; Lefai, E., Proteolysis inhibition by hibernating bear serum leads to increased protein content in human muscle cells. *Sci Rep* **2018,** *8* (1), 5525.

265. Stewart, M. A.; Franks-Skiba, K.; Chen, S.; Cooke, R., Myosin ATP turnover rate is a mechanism involved in thermogenesis in resting skeletal muscle fibers. *Proc Natl Acad Sci U S A* **2010,** *107* (1), 430-5.

266. Chazarin, B.; Storey, K. B.; Ziemianin, A.; Chanon, S.; Plumel, M.; Chery, I.; Durand, C.; Evans, A. L.; Arnemo, J. M.; Zedrosser, A.; Swenson, J. E.; Gauquelin-Koch, G.; Simon, C.; Blanc, S.; Lefai, E.; Bertile, F., Metabolic reprogramming involving glycolysis in the hibernating brown bear skeletal muscle. *Front Zool* **2019,** *16*, 12.

267. Yu, H.; Chakravorty, S.; Song, W.; Ferenczi, M. A., Phosphorylation of the regulatory light chain of myosin in striated muscle: methodological perspectives. *Eur Biophys J* **2016,** *45* (8), 779-805.

268. Stienen, G. J.; Kiers, J. L.; Bottinelli, R.; Reggiani, C., Myofibrillar ATPase activity in skinned human skeletal muscle fibres: fibre type and temperature dependence. *J Physiol* **1996,** *493 (Pt 2)* (Pt 2), 299-307.

269. Lee, K. H.; Sulbaran, G.; Yang, S.; Mun, J. Y.; Alamo, L.; Pinto, A.; Sato, O.; Ikebe, M.; Liu, X.; Korn, E. D.; Sarsoza, F.; Bernstein, S. I.; Padron, R.; Craig, R., Interacting-heads motif has been conserved as a mechanism of myosin II inhibition since before the origin of animals. *Proc Natl Acad Sci U S A* **2018,** *115* (9), E1991-E2000.

270. Cussonneau, L.; Boyer, C.; Brun, C.; Deval, C.; Loizon, E.; Meugnier, E.; Gueret, E.; Dubois, E.; Taillandier, D.; Polge, C.; Béchet, D.; Gauquelin-Koch, G.; Evans, A. L.; Arnemo, J. M.; Swenson, J. E.; Blanc, S.; Simon, C.; Lefai, E.; Bertile, F.; Combaret, L., Concurrent BMP Signaling Maintenance and TGF-β Signaling Inhibition Is a Hallmark of Natural Resistance to Muscle Atrophy in the Hibernating Bear. *Cells* **2021,** *10* (8).

271. Cahill, T.; da Silveira, W. A.; Renaud, L.; Wang, H.; Williamson, T.; Chung, D.; Chan, S.; Overton, I.; Hardiman, G., Investigating the effects of chronic low-dose radiation exposure in the liver of a hypothermic zebrafish model. *Sci Rep* **2023,** *13* (1), 918.

272. Masiero, G.; Ferrarese, G.; Perazzolo, E.; Baraldo, M.; Nogara, L.; Tezze, C., Custom-made 3D-printed boot as a model of disuse-induced atrophy in murine skeletal muscle. *PLoS One* **2024,** *19* (5), e0304380.

273. Alkner, B. A.; Tesch, P. A., Knee extensor and plantar flexor muscle size and function following 90 days of bed rest with or without resistance exercise. *Eur J Appl Physiol* **2004,** *93* (3), 294-305.

274. Feng, H. Z.; Wang, Q.; Reiter, R. S.; Lin, J. L.; Lin, J. J.; Jin, J. P., Localization and function of Xinalpha in mouse skeletal muscle. *Am J Physiol Cell Physiol* **2013,** *304* (10), C1002-12.

275. Harlow, H. J.; Lohuis, T.; Beck, T. D.; Iaizzo, P. A., Muscle strength in overwintering bears. *Nature* **2001,** *409* (6823), 997.

276. Lohuis, T. D.; Harlow, H. J.; Beck, T. D.; Iaizzo, P. A., Hibernating bears conserve muscle strength and maintain fatigue resistance. *Physiol Biochem Zool* **2007,** *80* (3), 257-69.

277. Monti, E.; Reggiani, C.; Franchi, M. V.; Toniolo, L.; Sandri, M.; Armani, A.; Zampieri, S.; Giacomello, E.; Sarto, F.; Sirago, G.; Murgia, M.; Nogara, L.; Marcucci, L.; Ciciliot, S.; Simunic, B.; Pisot, R.; Narici, M. V., Neuromuscular junction instability and altered intracellular calcium handling as early determinants of force loss during unloading in humans. *J Physiol* **2021,** *599* (12), 3037-3061.

278. Lang, F.; Aravamudhan, S.; Nolte, H.; Tuerk, C.; Holper, S.; Muller, S.; Gunther, S.; Blaauw, B.; Braun, T.; Kruger, M., Dynamic changes in the skeletal muscle proteome during denervation-induced atrophy. *Dis Model Mech* **2017**.

279. Blaauw, B.; Canato, M.; Agatea, L.; Toniolo, L.; Mammucari, C.; Masiero, E.; Abraham, R.; Sandri, M.; Schiaffino, S.; Reggiani, C., Inducible activation of Akt increases skeletal muscle mass and force without satellite cell activation. *FASEB J* **2009,** *23* (11), 3896-905.

280. Perkins, W. J.; Han, Y. S.; Sieck, G. C., Skeletal muscle force and actomyosin ATPase activity reduced by nitric oxide donor. *J Appl Physiol (1985)* **1997,** *83* (4), 1326-32.

281. Staples, J. F.; Mathers, K. E.; Duffy, B. M., Mitochondrial Metabolism in Hibernation: Regulation and Implications. *Physiology (Bethesda)* **2022,** *37* (5), 0.

282. Liu, M.; Gomez, D., Smooth Muscle Cell Phenotypic Diversity. *Arteriosclerosis, Thrombosis, and Vascular Biology* **2019,** *39* (9), 1715-1723.

283. Zhu, X.; Guan, R.; Zou, Y.; Li, M.; Chen, J.; Zhang, J.; Luo, W., Cold-inducible RNA binding protein alleviates iron overload-induced neural ferroptosis under perinatal hypoxia insult. *Cell Death Differ* **2024,** *31* (4), 524-539.

284. Li, J.; Cao, F.; Yin, H.-l.; Huang, Z.-j.; Lin, Z.-t.; Mao, N.; Sun, B.; Wang, G., Ferroptosis: past, present and future. *Cell Death & Disease* **2020,** *11* (2), 88.

285. Sone, M.; Yamaguchi, Y., Cold resistance of mammalian hibernators ~ a matter of ferroptosis? *Front Physiol* **2024,** *15*, 1377986.

286. Pagano, A. M.; Rode, K. D.; Lunn, N. J.; McGeachy, D.; Atkinson, S. N.; Farley, S. D.; Erlenbach, J. A.; Robbins, C. T., Polar bear energetic and behavioral strategies on land with implications for surviving the ice-free period. *Nat Commun* **2024,** *15* (1), 947.

287. Canepari, M.; Maffei, M.; Longa, E.; Geeves, M.; Bottinelli, R., Actomyosin kinetics of pure fast and slow rat myosin isoforms studied by in vitro motility assay approach. *Exp Physiol* **2012,** *97* (7), 873-81.

288. Canepari, M.; Rossi, R.; Pansarasa, O.; Maffei, M.; Bottinelli, R., Actin sliding velocity on pure myosin isoforms from dystrophic mouse muscles. *Muscle Nerve* **2009,** *40* (2), 249-56.

289. Stull, J. T.; Kamm, K. E.; Vandenboom, R., Myosin light chain kinase and the role of myosin light chain phosphorylation in skeletal muscle. *Arch Biochem Biophys* **2011,** *510* (2), 120-8.

290. Muthu, P.; Kazmierczak, K.; Jones, M.; Szczesna-Cordary, D., The effect of myosin RLC phosphorylation in normal and cardiomyopathic mouse hearts. *J Cell Mol Med* **2012,** *16* (4), 911-9.

291. MacIntosh, B. R., Role of calcium sensitivity modulation in skeletal muscle performance. *News Physiol Sci* **2003,** *18*, 222-5.

292. Pemrick, S. M., The phosphorylated L2 light chain of skeletal myosin is a modifier of the actomyosin ATPase. *J Biol Chem* **1980,** *255* (18), 8836-41.

293. Sweeney, H. L.; Bowman, B. F.; Stull, J. T., Myosin light chain phosphorylation in vertebrate striated muscle: regulation and function. *Am J Physiol* **1993,** *264* (5 Pt 1), C1085-95.

294. Padron, R.; Ma, W.; Duno-Miranda, S.; Koubassova, N.; Lee, K. H.; Pinto, A.; Alamo, L.; Bolanos, P.; Tsaturyan, A.; Irving, T.; Craig, R., The myosin interacting-heads motif present in live tarantula muscle explains tetanic and posttetanic phosphorylation mechanisms. *Proc Natl Acad Sci U S A* **2020,** *117* (22), 11865-11874.

295. Phung, L. A.; Karvinen, S. M.; Colson, B. A.; Thomas, D. D.; Lowe, D. A., Age affects myosin relaxation states in skeletal muscle fibers of female but not male mice. *PLoS One* **2018,** *13* (9), e0199062.

296. Caremani, M.; Brunello, E.; Linari, M.; Fusi, L.; Irving, T. C.; Gore, D.; Piazzesi, G.; Irving, M.; Lombardi, V.; Reconditi, M., Low temperature traps myosin motors of mammalian muscle in a refractory state that prevents activation. *J Gen Physiol* **2019,** *151* (11), 1272-1286.

297. Fusi, L.; Huang, Z.; Irving, M., The Conformation of Myosin Heads in Relaxed Skeletal Muscle: Implications for Myosin-Based Regulation. *Biophys J* **2015,** *109* (4), 783-92.

298. Stenvinkel, P.; Jani, A. H.; Johnson, R. J., Hibernating bears (Ursidae): metabolic magicians of definite interest for the nephrologist. *Kidney Int* **2013,** *83* (2), 207-12.

299. Schneider, C. A.; Rasband, W. S.; Eliceiri, K. W., NIH Image to ImageJ: 25 years of image analysis. *Nat Methods* **2012,** *9* (7), 671-5.

300. Talmadge, R. J.; Roy, R. R., Electrophoretic separation of rat skeletal muscle myosin heavy-chain isoforms. *J Appl Physiol (1985)* **1993,** *75* (5), 2337-40.

301. Glyn, H.; Sleep, J., Dependence of adenosine triphosphatase activity of rabbit psoas muscle fibres and myofibrils on substrate concentration. *J Physiol* **1985,** *365*, 259-76.

302. Griffith, O. W., Determination of glutathione and glutathione disulfide using glutathione reductase and 2-vinylpyridine. *Anal Biochem* **1980,** *106* (1), 207-12.

303. Hilber, K.; Galler, S., Improvement of the measurements on skinned muscle fibres by fixation of the fibre ends with glutaraldehyde. *J Muscle Res Cell Motil* **1998,** *19* (4), 365-72.

304. Brenner, B., The cross-bridge cycle in muscle. Mechanical, biochemical, and structural studies on single skinned rabbit psoas fibers to characterize cross-bridge kinetics in muscle for correlation with the actomyosin-ATPase in solution. *Basic Res Cardiol* **1986,** *81 Suppl 1*, 1-15.

305. Xu, D.; Wan, B.; Qiu, K.; Wang, Y.; Zhang, X.; Jiao, N.; Yan, E.; Wu, J.; Yu, R.; Gao, S.; Du, M.; Liu, C.; Li, M.; Fan, G.; Yin, J., Single-Cell RNA-Sequencing Provides Insight into Skeletal Muscle Evolution during the Selection of Muscle Characteristics. *Adv Sci (Weinh)* **2023,** *10* (35), e2305080.

306. Ismaeel, A.; Van Pelt, D. W.; Hettinger, Z. R.; Fu, X.; Richards, C. I.; Butterfield, T. A.; Petrocelli, J. J.; Vechetti, I. J.; Confides, A. L.; Drummond, M. J.; Dupont-Versteegden, E. E., Extracellular vesicle distribution and localization in skeletal muscle at rest and following disuse atrophy. *Skelet Muscle* **2023,** *13* (1), 6.

307. Li, H.; Capetanaki, Y., Regulation of the mouse desmin gene: transactivated by MyoD, myogenin, MRF4 and Myf5. *Nucleic Acids Res* **1993,** *21* (2), 335-43.

308. Montarras, D.; L'Honoré, A.; Buckingham, M., Lying low but ready for action: the quiescent muscle satellite cell. *Febs j* **2013,** *280* (17), 4036-50.

309. Hagen, K. M.; Gordon, P.; Frederick, A.; Palmer, A. L.; Edalat, P.; Zonta, Y. R.; Scott, L.; Flancia, M.; Reid, J. K.; Joel, M.; Ousman, S. S., CRYAB plays a role in terminating the presence of pro-inflammatory macrophages in the older, injured mouse peripheral nervous system. *Neurobiology of Aging* **2024,** *133*, 1-15.

310. Li, X.; Prudente, A. S.; Prato, V.; Guo, X.; Hao, H.; Jones, F.; Figoli, S.; Mullen, P.; Wang, Y.; Tonello, R.; Lee, S. H.; Shah, S.; Maffei, B.; Berta, T.; Du, X.; Gamper, N., Peripheral gating of mechanosensation by glial diazepam binding inhibitor. *J Clin Invest* **2024**.

311. Cappellari, O.; Cossu, G., Pericytes in Development and Pathology of Skeletal Muscle. *Circulation Research* **2013,** *113* (3), 341-347.

312. van Nieuwenhoven, F. A.; Munts, C.; op't Veld, R. C.; González, A.; Díez, J.; Heymans, S.; Schroen, B.; van Bilsen, M., Cartilage intermediate layer protein 1 (CILP1): A novel mediator of cardiac extracellular matrix remodelling. *Sci Rep-Uk* **2017,** *7* (1), 16042.

313. Ito, N.; Miyagoe-Suzuki, Y.; Takeda, S.; Kudo, A., Periostin Is Required for the Maintenance of Muscle Fibers during Muscle Regeneration. *Int J Mol Sci* **2021,** *22* (7).

314. Lopes, F. M.; Roberts, N. A.; Zeef, L. A.; Gardiner, N. J.; Woolf, A. S., Overactivity or blockade of transforming growth factor-β each generate a specific ureter malformation. *J Pathol* **2019,** *249* (4), 472-484.

315. Rysz, J.; Franczyk, B.; Rysz-Górzyńska, M.; Gluba-Brzózka, A., Pharmacogenomics of Hypertension Treatment. *Int J Mol Sci* **2020,** *21* (13).

316. Shnitsar, V.; Li, J.; Li, X.; Calmettes, C.; Basu, A.; Casey, J. R.; Moraes, T. F.; Reithmeier, R. A. F., A substrate access tunnel in the cytosolic domain is not an essential feature of the solute carrier 4 (SLC4) family of bicarbonate transporters. *J Biol Chem* **2013,** *288* (47), 33848-33860.

317. Ungsupravate, D.; Sawasdee, N.; Khositseth, S.; Udomchaiprasertkul, W.; Khoprasert, S.; Li, J.; Reithmeier, R. A.; Yenchitsomanus, P. T., Impaired trafficking and intracellular retention of mutant kidney anion exchanger 1 proteins (G701D and A858D) associated with distal renal tubular acidosis. *Mol Membr Biol* **2010,** *27* (2-3), 92-103.

318. Jones, R. A.; Harrison, C.; Eaton, S. L.; Llavero Hurtado, M.; Graham, L. C.; Alkhammash, L.; Oladiran, O. A.; Gale, A.; Lamont, D. J.; Simpson, H.; Simmen, M. W.; Soeller, C.; Wishart, T. M.; Gillingwater, T. H., Cellular and Molecular Anatomy of the Human Neuromuscular Junction. *Cell Rep* **2017,** *21* (9), 2348-2356.

319. Murthy, A.; Shao, Y. W.; Narala, S. R.; Molyneux, S. D.; Zúñiga-Pflücker, J. C.; Khokha, R., Notch activation by the metalloproteinase ADAM17 regulates myeloproliferation and atopic barrier immunity by suppressing epithelial cytokine synthesis. *Immunity* **2012,** *36* (1), 105-19.

320. de Bivort, B. L.; Guo, H. F.; Zhong, Y., Notch signaling is required for activity-dependent synaptic plasticity at the Drosophila neuromuscular junction. *J Neurogenet* **2009,** *23* (4), 395-404.

321. Sorkaç, A.; DiIorio, M. A.; O'Hern, P. J.; Baskoylu, S. N.; Graham, H. K.; Hart, A. C., LIN-12/Notch Regulates GABA Signaling at the Caenorhabditis elegans Neuromuscular Junction. *G3 Genes|Genomes|Genetics* **2018,** *8* (8), 2825-2832.

322. Li, P.; Collins, K. M.; Koelle, M. R.; Shen, K., LIN-12/Notch signaling instructs postsynaptic muscle arm development by regulating UNC-40/DCC and MADD-2 in Caenorhabditis elegans. *Elife* **2013,** *2*, e00378.

323. Fleck, D.; van Bebber, F.; Colombo, A.; Galante, C.; Schwenk, B. M.; Rabe, L.; Hampel, H.; Novak, B.; Kremmer, E.; Tahirovic, S.; Edbauer, D.; Lichtenthaler, S. F.; Schmid, B.; Willem, M.; Haass, C., Dual cleavage of neuregulin 1 type III by BACE1 and ADAM17 liberates its EGF-like domain and allows paracrine signaling. *J Neurosci* **2013,** *33* (18), 7856-69.

324. La Marca, R.; Cerri, F.; Horiuchi, K.; Bachi, A.; Feltri, M. L.; Wrabetz, L.; Blobel, C. P.; Quattrini, A.; Salzer, J. L.; Taveggia, C., TACE (ADAM17) inhibits Schwann cell myelination. *Nature Neuroscience* **2011,** *14* (7), 857-865.

325. Gros-Louis, F.; Larivière, R.; Gowing, G.; Laurent, S.; Camu, W.; Bouchard, J. P.; Meininger, V.; Rouleau, G. A.; Julien, J. P., A frameshift deletion in peripherin gene associated with amyotrophic lateral sclerosis. *J Biol Chem* **2004,** *279* (44), 45951-6.

326. Ham, A. S.; Lin, S.; Tse, A.; Thürkauf, M.; Oliveri, F.; Rüegg, M. A., Single-nuclei sequencing of skeletal muscle reveals subsynaptic-specific transcripts involved in neuromuscular junction maintenance. *bioRxiv* **2024**, 2024.05.15.594276.

327. Zhao, Z.; Yang, X., Inhibition of SMYD2 attenuates paraquat-induced pulmonary fibrosis by inhibiting the epithelial-mesenchymal transition through the GLIPR2/ERK/p38 axis. *Pestic Biochem Physiol* **2024,** *202*, 105971.

328. Lewis, P. A., Vesicular dysfunction and pathways to neurodegeneration. *Essays Biochem* **2021,** *65* (7), 941-948.

329. Todorov-Völgyi, K.; González-Gallego, J.; Müller, S. A.; Beaufort, N.; Malik, R.; Schifferer, M.; Todorov, M. I.; Crusius, D.; Robinson, S.; Schmidt, A.; Körbelin, J.; Bareyre, F.; Ertürk, A.; Haass, C.; Simons, M.; Paquet, D.; Lichtenthaler, S. F.; Dichgans, M., Proteomics of mouse brain endothelium uncovers dysregulation of vesicular transport pathways during aging. *Nat Aging* **2024,** *4* (4), 595-612.

330. Cao, W.; Fan, D., Neutrophils: a subgroup of neglected immune cells in ALS. *Front Immunol* **2023,** *14*, 1246768.

331. Evans, C. S.; Holzbaur, E. L. F., Autophagy and mitophagy in ALS. *Neurobiol Dis* **2019,** *122*, 35-40.

332. Squatrito, M.; Mancino, M.; Sala, L.; Draetta, G. F., Ebp1 is a dsRNA-binding protein associated with ribosomes that modulates eIF2alpha phosphorylation. *Biochem Biophys Res Commun* **2006,** *344* (3), 859-68.

333. Plotkin, D. L.; Roberts, M. D.; Haun, C. T.; Schoenfeld, B. J., Muscle Fiber Type Transitions with Exercise Training: Shifting Perspectives. *Sports (Basel)* **2021,** *9* (9).

334. Ciciliot, S.; Rossi, A. C.; Dyar, K. A.; Blaauw, B.; Schiaffino, S., Muscle type and fiber type specificity in muscle wasting. *Int J Biochem Cell Biol* **2013,** *45* (10), 2191-9.

335. Medler, S., Mixing it up: the biological significance of hybrid skeletal muscle fibers. *J Exp Biol* **2019,** *222* (Pt 23).